

# Site U1324<sup>1</sup>

Expedition 308 Scientists<sup>2</sup>

## Chapter contents

Background and objectives .....	1
Summary of operations .....	2
Lithostratigraphy .....	4
Biostratigraphy .....	7
Paleomagnetism .....	11
Geochemistry and microbiology .....	12
Physical properties .....	14
Downhole measurements .....	17
References .....	24
Figures .....	25
Tables .....	107

## Background and objectives

### Geological setting of Mars-Ursa Basin

The geological framework of Mars-Ursa Basin is treated in detail in the “Site U1322” chapter. The reader is referred to this chapter regarding detailed background information, and a more extensive compilation of the data available before drilling operations began (Figs. F1, F2, F3, F4 in the “Site U1322” chapter; Table T1 in the “Site U1322” chapter).

### Overview of seismically mapped surfaces

Site U1324 is the westernmost of the sites drilled in Ursa Basin during Expedition 308 (see Figs. F2, F3 in the “Site U1322” chapter), is at the shallowest water depth (1057 meters below sea level [mbsl]), and has the deepest sediment penetration (612 meters below seafloor [mbsf]). It is located within Mississippi Canyon Lease Block 897. Eight seismic surfaces are mapped along the Ursa Basin transect (Fig. F1; see also Fig. F4 and Table T1 in the “Site U1322” chapter). Among those, seismic Reflectors S10, S20, S30, and S80 are regional surfaces that span all three drill sites. Seismic Reflector S10 at 1458 ms two-way travelttime (TWT) (35 mbsf) represents the probable base of the hemipelagic drape sediments. Seismic Reflector S20 at 1548 ms TWT (105 mbsf) separates distal levee muds from the underlying fine-grained clastics of the eastern Southwest Pass Canyon levee. Seismic Reflector S30 (1623 ms TWT; 165 mbsf) is a detachment surface that underlies one of the mass transport deposits (MTDs). Between seismic Reflectors S30 and S60-1324 (2136 ms TWT; 612 mbsf) horizontal parallel reflectors alternate with chaotic zones. The top of the Blue Unit (S80) is delineated by a weak, negative polarity reflector of irregular geometry ~20 ms TWT beneath the terminal depth (TD) of Holes U1324A and U1324B.

### Local summary of borehole expectations

Latest Pleistocene to Holocene sedimentation at Site U1324 is characterized (from youngest to oldest) by a hemipelagic drape underlain by a packet of muddy sediments belonging to distal levee deposits. Beneath this, the deposits of the eastern levee of Southwest Pass Canyon are underlain by sediments belonging to the western levee of Ursa Canyon. The Ursa Canyon levee deposits cut into the underlying sand-dominated Blue Unit (Fig. F1; see also Fig. F4 in the “Site U1322” chapter).

<sup>1</sup>Expedition 308 Scientists, 2006. Site U1324. In Flemings, P.B., Behrmann, J.H., John, C.M., and the Expedition 308 Scientists, *Proc. IODP, 308: College Station TX (Integrated Ocean Drilling Program Management International, Inc.). doi:10.2204/iodp.proc.308.108.2006*

<sup>2</sup>Expedition 308 Scientists’ addresses.



## Drilling objectives

The primary drilling objectives at this site were the following:

- Characterize temperature and pressure as a function of depth in this part of the Ursa Basin sediment wedge.
- Characterize porosity and other key physical and geotechnical properties as a function of depth.
- Elucidate controls on slope stability, especially in the slumped lithostratigraphic intervals.
- Understand the timing of hemipelagic and muddy turbidite background sedimentation and the slumping events.
- Characterize lithology and depositional processes within the Southwest Pass canyon and Ursa channelized turbidite systems.

To fully achieve these objectives, Hole U1324B was continuously cored to TD at 608 mbsf. Advanced piston coring (APC) was used to 357.90 mbsf, followed by extended core barrel (XCB) coring to 368 mbsf. From there, further APC coring was carried out to 394.50 mbsf, again followed by XCB coring to TD. Special tool deployments included five deployments of the temperature/dual pressure (T2P) probe and seven deployments of the Davis-Villinger Temperature-Pressure Probe (DVTTP). Before coring operations, a dedicated hole (Hole U1324A) was drilled to conduct logging-while-drilling/measurement-while-drilling (LWD/MWD) operations to a TD of 612 mbsf. This was followed by wireline logging and a vertical seismic profile to generate a complete set of logging parameters for correlation with core data and observations from Hole U1324A. After coring in Hole U1324B, a dedicated third hole (Hole U1324C) was drilled to 511.8 mbsf in order to obtain additional temperature and pressure measurements, followed by one spot core at each measurement station. There were five T2P probe and three DVTTP deployments in Hole U1324C.

## Summary of operations

### Hole U1324A

A summary of operations in Hole U1324A is found in Table [T1](#). A beacon was deployed at Site U1324 at 1040 h on 17 June 2005. Hole U1324A was spudded at 1610 h when the driller tagged the seafloor at 1066.0 meters below rig floor (mbrf) (precision depth recorder [PDR] = 1078.0 mbrf). After the bit was washed ahead to 5.0 mbsf, MWD drilling advanced without incident to 333.4 mbsf at a rate of penetration (ROP) of 30 m/h, where a wiper trip was made back to 60.8 mbsf. MWD drilling resumed to 477.7 mbsf, where another wiper trip was made back to

330.4 mbsf. Because of the potential for interbedded levee sands below 481 mbsf, we used heavy mud from this depth to the TD of 612 mbsf (20 m above the top of the Blue Unit). At ~2045 h on 18 June, MWD drilling advanced slowly at an ROP of 20 m/h, gradually increasing to 30 m/h while “pumping and dumping” 10.0 ppg mud. Drilling advanced to the depth objective of 612 mbsf by 0410 h the next morning. The hole was plugged with cement and heavy mud and abandoned. A free-fall funnel (FFF) was made up and deployed at 0808 h on 19 June with the bit at ~80 mbsf. The vibration-isolated television (VIT) camera was deployed and a visual inspection confirmed that there was no flow emanating from the top of the FFF and that the funnel was upright. The bit was pulled free of the seafloor at 0853 h. It was decided in view of the good hole conditions that wireline logging should be attempted in Hole U1324A. A logging/cementing bottom-hole assembly (BHA) was made up with the 9 $\frac{7}{8}$  inch polycrystalline diamond bit, bit, bit sub, controlled-length drill collar (CLDC), modified top sub, four CLDCs, tapered drill collar, six joints of 5 $\frac{1}{2}$  inch drill pipe, and a crossover sub (length = 116.6 m). The second reentry of the expedition was made at 1828 h on 19 June, and the bit placed at the logging depth of 54.2 mbsf. A tool string consisting of the Hostile Environment Gamma Ray Sonde (HNGS), Dipole Sonic Imager (DSI), and General Purpose Inclinometer Tool (GPIT) was deployed. A more detailed description of wireline logging and LWD/MWD operations in Hole U1324A can be found in [“Downhole measurements.”](#)

### Hole U1324B

A summary of operations in Hole U1324B is found in Table [T2](#). The BHA was reconfigured to an APC/XCB array by replacing two of the CLDCs with a seal bore drill collar and nonmagnetic drill collar. This array was identical to the BHA used to core the Brazos-Trinity sites. After a VIT camera survey of the seafloor, the driller tagged the bottom at 1066.8 mbrf. Hole U1324B was spudded with the APC at 0250 h on 21 June 2005. The recovery of the first core established the seafloor depth at 1067.5 mbrf. Piston coring advanced without incident to 17.8 mbsf, where the corer did not achieve a complete stroke but did recover 9.91 m (recovery = 104%). APC coring continued to 357.9 mbsf by advancing by recovery. We observed that downhole pressure measurements from the previous day indicated pressures below hydrostatic, and the readings were consistent between both the T2P probe and the DVTTP. Comparing these abnormal readings with the deformation seen at the base of the APC cores, it was inferred that the suction applied to retrieve the piston cores may have



deformed the material sufficiently to influence pressure readings in the formation. Hence, one XCB core was obtained prior to a deployment of the DVTTP and T2P probe. However, XCB coring did not improve pressure measurements; the subhydrostatic pressure readings continued to afflict most of the subsequent DVTTP measurements up to the eighth run in the hole. Just prior to the eighth measurement, a small interior leak in the DVTTP unit was discovered and repaired. This fixed the problem.

Piston coring continued to a TD of 394.5 mbsf by advancing by recovery. A total of 48 piston cores were shot in order to penetrate to this depth, and the average recovery was 101.3%. Nonmagnetic core barrels were used for all piston cores. The cores were oriented starting with Core 4H. The APC temperature (APCT) tool was deployed at Cores 6H, 9H, 12H, and 15H (see Tables [T2](#), [T16](#)). Fluorescent microspheres were deployed in the core catchers of Cores 1H–11H, 13H, 15H, 17H, 19H, 21H–23H, 26H, 29H–32H, 35H, 38H–41H, 44H, 47H, and 50H (see Table [T2](#)). The Fugro cutting shoe that was sent out on the work boat was deployed on Cores 4H and 7H and odd-numbered piston cores up to and including Core 49H (see Table [T2](#)).

Coring resumed with the XCB and deepened the hole to 608.2 mbsf. The XCB-cored portion of the hole was 223.8 m (average recovery = 80.8%). The total cored interval was 608.2 m (average recovery = 93.7%). In compliance with the operational protocol, heavy mud (10.5 ppg) was continuously pumped starting at 481 mbsf until the bottom of the hole. Fluorescent microspheres were deployed in 10 XCB cores: 53X, 56X, 59X, 62X, 64X, 66X, 68X, 70X, 72X, and 74X (see Table [T2](#)).

When drill pipe connections were made to recover or deploy tools or core barrels, the heavy mud would “U-tube,” creating a large air gap in the pipe. The impact of the core barrel at the top of the mud level in the pipe tended to shatter the core liner as a result of the sudden deceleration. To avoid this, the core barrels were lowered on the coring line and then intentionally jarred and released by the core winch operator after the barrel landed. The sinker bars were then removed from the drill string to prevent oil saver leakage from spraying mud over the rig floor and derrick. Once the core was cut, the sinker bars were stabbed and the core barrel recovered. This resulted in two coring line roundtrips for each core.

The DVTTP was deployed 10 times in this hole (229.1, 362.4, 387.9, 464.3, 493.1, 522.0, 541.2, 560.4, 589.2, and 608.3 mbsf) (see Table [T16](#)). The pressure data prior to DVTTP Deployment 8 were not usable. The T2P probe was deployed 10 times (~30 min each; 51.3, 89.3, 117.8, 136.3, 368.0, 394.5, and 593.2 mbsf). Because of deployment and electronic

problems, none of the data obtained from the T2P in this hole were usable. It was observed that an additional benefit of filling the hole with heavy mud made DVTTP and T2P deployments easier because the tools and BHA became easier to extract from the bottom of the hole after sustained periods without rotation during the deployment process.

Because it was not possible to measure the equivalent circulating density (ECD) of the mud, as was effectively done in Hole U1324A, the conservative measure of pumping 10.5 ppg mud was adopted. The mud engineer calculated that we expended 3880 bbl of 10.5 ppg mud while drilling this hole. In accordance with the operating protocol, the hole was plugged with 44 bbl of 11.0 ppg neat cement, forming a plug of ~145 m. The cement was followed by 40 bbl of 10.5 ppg mud and then chased with 50 bbl of seawater. The hole was observed using the VIT camera with the bit at ~80 mbsf and no flow was detected. The bit was pulled free of the hole at 0025 h on 26 June. As the vessel was moved off location, a subsea release dart was pumped down to swab the inside of the pipe. This was followed by extensive seawater flushing of the drill string.

## Hole U1324C

A summary of operations in Hole U1324C is found in Table [T3](#). The vessel was repositioned 20 m west of Hole U1324A in dynamic positioning (DP) mode. After a VIT camera survey of the seafloor indicated no obstructions, Hole U1324C was spudded when the driller tagged the seafloor at 1066.5 mbfr. The hole was then drilled ahead to 50.0 mbsf, where the T2P probe was deployed with good results. Following the retrieval of the probe, a single APC core was obtained for physical property analyses. Following this procedure, three more T2P deployments were made at 100, 150.0, and 200.0 mbsf, each measurement followed by a single APC core. The hole was then drilled to 250.0 mbsf, where a DVTTP measurement was made, followed by a single piston core. Once again the hole was drilled from 250.0 to 300.0 mbsf, where the fourth T2P deployment was made, followed by a single APC core. The hole was then drilled to 405.0 and 505.0 mbsf, followed each time by a single piston core. The last piston cored advanced to a TD of 511.8 mbsf. When the driller advanced beyond 481.0 mbsf, heavy mud (10.5 ppg) was continuously pumped in accordance with the operating protocol for this site. A total of eight piston cores were obtained, the last seven were advanced by recovery. The cored interval was 55.1 m (average recovery = 100.9%). The cores were not oriented and were all obtained with the nonmagnetic core barrel. The Fugro cutting shoe was deployed on even-numbered core barrels. Before the drill string

was withdrawn from Hole U1324C, the hole was observed with the VIT camera and no flow was evident. Because penetration in the hole was terminated above the sand layers, it was not necessary to plug this hole with cement. The bit was pulled free of the seafloor at 0135 h on 28 June and positioned 204 m above the seafloor. The vessel was then offset in DP mode to Site U1322. The beacon was recovered before departing location at 0240 h.

## Lithostratigraphy

Drilling at Site U1324 penetrated Ursa Basin where the sediments above the Blue Unit are thicker than either to Site U1323 or Site U1322. Hole U1324B sampled the entire eastern levee deposits of the Southwest Pass Canyon channel-levee system and the overlying hemipelagic drape and distal turbidites of younger channel-levee systems (Fig. F4 in the “Site U1322” chapter). Sediment was recovered to 608 mbsf in Hole U1324B using APC and XCB coring with overall recovery >90%. The TD of 608 mbsf ties closely with seismic Reflector S60-1324, the top of the Ursa Canyon western levee. Therefore, sediment recovered at Site U1324 records the entire evolution of the eastern levee of Southwest Pass Canyon. Hole U1324C was spot-cored with the APC between 0 and 511.8 mbsf (Cores 308-U1324C-1H to 7H), but these cores were used primarily for geotechnical whole-round samples and were not used to define lithostratigraphic units.

The sedimentary succession at Site U1324 is dominated by clay and mud in the upper 360 m and by interbedded silt, sand, and mud in the lower 250 m. Thus, we divided the succession into two lithostratigraphic units based on this distinction (Table T4). Both units were further divided into subunits based on the occurrence of intervals composed of contorted and faulted sediment and intervals composed of undeformed sediment.

Cores 308-U1324B-4H to 44H were oriented, which allowed for detailed measurements of inclination and orientation of faults and dip of bedding planes (Table T5). Figure F2 summarizes the lithostratigraphic column, and Figures F3, F4, F5, F6, F7, F8, F9, F10, F11, F12, F13, F14, and F15 illustrate the range of features and variations in each of the lithostratigraphic units and subunits.

### Description of lithostratigraphic units

#### Unit I

Interval: Sections 308-U1324B-1H-1, 0 cm, through 46X-2, 75 cm

Depth: 0–364.7 mbsf

Age: Holocene/late Pleistocene

Lithology: clay and mud

Lithostratigraphic Unit I extends from the seafloor to 364.7 mbsf and includes seven subunits (IA–IG). Lithostratigraphic Unit I is predominantly composed of terrigenous clay and mud with a marked paucity of silt and sand. Subunit divisions are based on the observation of distinct intervals composed of contorted and faulted sediment. Other than this distinction, the lithology throughout Unit I is very similar. The base of lithostratigraphic Unit I is defined as the top of a silt bed at 364.7 mbsf, marking a fundamental change in lithology to interbedded silt and very fine sand below, characteristic of lithostratigraphic Unit II.

#### *Subunit IA (0.0–43.9 mbsf)*

Lithostratigraphic Subunit IA is 43.9 m thick and is composed primarily of olive-green and reddish brown clay interbedded with centimeter- to decimeter-thick thin beds and laminae of black clay. Black clay is organic rich and shows transitions from black at the base to greenish gray at the top. The uppermost 0.38 m of this subunit is rich in nannofossils and foraminifers (Fig. F3). The base at 43.9 mbsf is marked by a fault that offsets parallel bedding surfaces (Table T5; Fig. F4A).

#### *Subunit IB (43.9–59.7 mbsf)*

Lithostratigraphic Subunit IB is composed of contorted and faulted greenish gray and reddish brown clay and centimeter- to decimeter-thick beds and laminae of black clay (Fig. F4). This lithology is similar to the lithology of Subunit IA but is deformed. Characteristics of faults were measured on the split core face and are summarized in Table T5. Generally, these are reverse faults with dips of ~30°. The top of this subunit corresponds closely to seismic Reflector S10 (Fig. F2). The seismic character of this subunit is chaotic with low-amplitude reflections and is distinct from the otherwise laterally continuous seismic reflections above and below this subunit (Fig. F4 in the “Site U1322” chapter). This is discussed further in “Core-seismic intergration.”

#### *Subunit IC (59.7–107.0 mbsf)*

Lithostratigraphic Subunit IC is composed of couplets of greenish gray and brownish gray laminae and beds up to 2–3 cm thick (Fig. F5). A minor component of silt occurs throughout this subunit as thin, discontinuous lenses and burrow fills a millimeter in diameter. Burrow fills are dominated by quartz grains with minor amounts of carbonate fragments and sponge spicules, as determined by smear slide analyses (Fig. F14).

***Subunit ID (107.0–151.0 mbsf)***

Lithostratigraphic Subunit ID is composed of faulted and contorted reddish brown and greenish gray clay couplets (Fig. F6). Bed dips are typically ~20°, and faults are mostly normal faults with small offset. Resistivity-at-the-bit (RAB) images of the formation in this subunit reveal dipping beds (5°–55°) throughout the interval (see “[Downhole measurements](#)”). The base of this subunit occurs just above the prominent seismic Reflector S30.

***Subunit IE (151.0–264.8 mbsf)***

Lithostratigraphic Subunit IE is a thick interval composed of 1–2 cm thick couplets of dark gray to light gray clay laminae and thin beds (Fig. F7). At the base of each couplet, dark gray clay has a slightly higher content of silt and organic matter than light gray clay; the couplets are normally graded. Black clay layers are commonly irregular and mottled rather than forming continuous laminae (Fig. F7). This sub-unit contains scattered white silt specks (burrow fills), burrows highlighted by black iron sulfides, and rare silt laminae. An interval enriched in foraminifers and nannofossils occurs between 165.0 and 167.2 mbsf, which corresponds closely with seismic Reflector S30.

***Subunit IF (264.8–286.1 mbsf)***

Lithostratigraphic Subunit IF is composed of faulted and contorted couplets of green and brownish green clay. Beds are steeply dipping (up to 70°) with small-offset faults and folding (Fig. F8). RAB images confirm the occurrence of deformed sediments in this subunit (see “[Downhole measurements](#)”).

***Subunit IG (286.1–364.7 mbsf)***

Lithostratigraphic Subunit IG is composed of greenish gray, reddish brown, and black mottled clay (Fig. F9) commonly arranged in couplets 2–7 cm thick with black clay grading to brownish gray and greenish gray clay. The black clay has a slightly higher component of silt than the greenish gray and brownish gray clay, and each couplet is normally graded. Black color is possibly caused by precipitation of iron sulfides and red/brown color by precipitation of iron oxides. A single bed of massive gray medium sand occurs from 305.7 to 306.8 mbsf, but otherwise this subunit is dominated by clay (Fig. F9).

**Unit II**

Interval: Sections 308-U1324B-46X-2, 75 cm, through 74X-7, 40 cm

Depth: 364.7–600.8 mbsf

Age: late Pleistocene

Lithology: silt and very fine sand

Lithostratigraphic Unit II extends from 364.7 to 600.8 mbsf and includes four subunits (IIA–IID). The top of this unit is defined at the top of a normally graded thin bed of silt at 364.7 mbsf that marks a fundamental change in lithology in Hole U1324B. The unit predominantly includes interbedded silt and very fine sand with beds and laminae of mud and clay. Subunit divisions were distinguished by distinct intervals of contorted sediment.

***Subunit IIA (364.7–445.5 mbsf)***

Lithostratigraphic Subunit IIA is composed of bioturbated and mottled laminae and beds of greenish gray and reddish brown mud interbedded with normally graded reddish brown silt and very fine sand (Fig. F10). Laminae and bed thicknesses range from 1 to 45 cm. X-ray diffraction (XRD) analyses of green and red clay show that the samples are dominated by quartz and contain calcite, dolomite, feldspars, mica (illite), kaolinite, and chlorite; the X-ray diffractograms are similar in the two types of clay (Fig. F15). Carbon analyses show total carbon content of 2.4 and 2.5 wt% for the red and green clay, respectively. Thus, the variations from reddish brown, greenish gray, and blackish gray appear to be related primarily to precipitation of iron oxides or sulfides, depending on the redox conditions within the sediment.

***Subunit IIB (445.5–481.9 mbsf)***

Lithostratigraphic Subunit IIB is composed of contorted interbeds of brown and gray silty sand and contorted beds of green and red clay (Fig. F11). Rare burrows filled with sandy silt occur throughout this subunit. Deformed beds are well expressed in Cores 308-U1324B-57X through 59X.

***Subunit IIC (481.9–578.9 mbsf)***

Lithostratigraphic Subunit IIC is composed of interbedded greenish gray and reddish brown mud with thin beds and light gray silt laminae (Fig. F12). Silt beds are normally graded with sharp bases and gradational tops to mud. A few silt beds have scoured bases. Very fine lower sand occurs in thin, discontinuous light gray and tan laminae. Figure F12E shows a photomicrograph of silt from this subunit that is dominated by quartz with abundant mica grains. Drilling mud was observed to penetrate silt/mud interbeds, and it lined the outside margins of the core sections.

***Subunit IID (578.9–600.8 mbsf)***

Lithostratigraphic Subunit IID is composed of contorted interbeds of silty sand with greenish gray mud (Fig. F13). Folds and tilted beds are observed in cores



but XCB disturbance and biscuiting mask the original structures (Fig. F13). RAB images of this subunit reveal a striking three-dimensional (3-D) view of a fold with the fold axis trending north-south (see “[Downhole measurements](#)”).

### Interpretation of lithostratigraphy

Lithostratigraphic Unit I (0–364.7 mbsf) is interpreted to record a succession of rapidly deposited levee turbidite clay and mud with discrete intervals of MTDs. Lithostratigraphic Subunit IA is interpreted to be hemipelagic drape and very distal turbidites from the Old and Young Timbalier Canyon channel-levee systems to the west (Winker and Shipp, 2002). The subtly graded couplets of light and dark gray clay in each subunit throughout lithostratigraphic Unit I may record fine-grained turbidity current overspill on the east levee of the Southwest Pass Canyon. Sedimentation rates for lithostratigraphic Unit I are estimated to be ~0.4–0.6 cm/y (see “[Biostratigraphy](#)”). Considering that the average thickness of clay laminae couplets is ~2 cm, the overspill events recorded at Site U1324 would occur, on average, every 4 y. Similar color bands and laminations in mud and clay sediment from the Amazon Fan levees were interpreted to record turbidity current overspill events occurring every 1–3 y (Piper and Deptuck, 1997; Pirmez and Isram, 2003). Lithostratigraphic Subunits IB, ID, and IF are only different compared to the other subunits within lithostratigraphic Unit I by being composed of tilted, contorted, and faulted beds. This suggests that these intervals have been remobilized downslope and they are thus interpreted as MTDs. We infer that the relatively mild deformation observed in these subunits indicates that they have remained relatively intact during transport and probably have not moved significant distances from their original deposition location.

The base of lithostratigraphic Unit I and top of lithostratigraphic Unit II at 364.7 mbsf marks a distinct lithologic change separating mud and clay above from interbedded sand, silt, and mud below. This boundary ties closely to seismic Reflector S40-1324, which also marks a fundamental change in seismic facies (Fig. F2). In lithostratigraphic Unit I, the seismic facies is predominantly characterized by intervals of continuous subparallel reflections and by transparent intervals. The seismic facies of lithostratigraphic Unit II is very chaotic and discontinuous. This major boundary also marks distinct character changes in the gamma ray and resistivity logs (Fig. F2; see “[Downhole measurements](#)”). Above this boundary, both logs do not show major variations. Below this boundary, resistivity varies frequently and ties well with the thin beds and laminae

of silt and sand observed in lithostratigraphic Unit II. Gamma radiation indicates the presence of more silt and sand below this boundary as well.

A marked change in the evolution of the Southwest Pass Canyon is interpreted to be recorded at the lithostratigraphic Unit I/II boundary. Before a single confining channel was established in the Southwest Pass Canyon system, there were probably numerous low-relief channels that were unable to completely confine the turbidity currents, leading to abundant overspill of sand and silt. Thus, the sedimentary succession of lithostratigraphic Unit II is dominated by thin beds of silt and sand interbedded with mud representing overbank deposits. The sands and silts tie to discontinuous reflectors and lenses in seismic data and are not regionally extensive. Lithostratigraphic Subunits IIB and IID are interpreted to be MTDs consistent with a dynamic environment with high sedimentation rate and extensive overspill. It is possible that the triggering mechanisms for the MTDs in lithostratigraphic Unit I and those in lithostratigraphic II are different. The MTDs of lithostratigraphic Unit I were potentially related to low effective stresses developed in the thick levee assemblage above the Blue Unit. The MTDs of lithostratigraphic Unit II were probably associated with the dynamic depositional environment of the young Southwest Pass Canyon channel-levee system.

### Core-seismic integration

Comparison of 3-D seismic survey Line 150 (Fig. F4 in the “Site U1322” chapter) with Site U1324 lithostratigraphy suggests a strong correlation between seismic facies and lithostratigraphic units. Lithostratigraphic Unit I extends from the seafloor to just below seismic Reflector S40-1324 at 364.7 mbsf and is characterized overall by intervals of laterally continuous, high-amplitude reflectors and intervals of acoustically transparent and/or chaotic and discontinuous reflectors.

Lithostratigraphic Subunits IB, ID, and IF are characterized by faulted and contorted bedding and tie closely to the transparent/chaotic seismic facies (Fig. F2; see also Fig. F4 in the “Site U1322” chapter). Such acoustically transparent/chaotic intervals are interpreted to be MTDs that were not transported very far but rather slumped and faulted during a short transport. The strong regional seismic Reflector S30 at the base of a thick transparent/chaotic interval ties to just below the base of lithostratigraphic Subunit ID. It is interpreted that this subunit represents a regional-scale MTD (Fig. F4 in the “Site U1322” chapter). This MTD can be correlated to Sites U1323 and U1322 in the seismic section.

Lithostratigraphic Unit II extends from the base of lithostratigraphic Unit I just below seismic Reflector S40-1324 to the TD at 608 mbsf and is characterized by intervals of high-amplitude chaotic facies and high-amplitude continuous reflections. Seismic Reflectors S50-1324 and S60-1324 occur within this unit.

Lithostratigraphic Subunits IIB and IID are characterized by faulted and contorted sediment and tie closely with the intervals of high-amplitude chaotic zones (Fig. F2). These subunits are interpreted to be MTDs but are not seismically transparent like the MTDs of lithostratigraphic Unit I. The high-amplitude signature may be related to the abundance of thin bedded silt, sand, and mud observed throughout lithostratigraphic Unit II. These subunits are not regionally extensive and do not correlate to Sites U1323 or U1322.

Lithostratigraphic Subunits IIA and IIC tie closely to high-amplitude continuous reflectors between seismic Reflectors S40-1324 and S60-1324 (Fig. F2). These subunits are not characterized by faulted and contorted sediment and contain interbedded silt, sand, and mud and thin laterally to the east and are truncated by MTDs (Fig. F4 in the "Site U1322" chapter).

## Summary interpretation

Site U1324B recovered a thick sedimentary succession overlying the Blue Unit and records the evolution of the eastern levee of the Southwest Pass Canyon channel-levee system. Lithostratigraphic Unit I is composed of clay, mud, and three MTDs. Lithostratigraphic Unit II is composed of interbedded silt, sand, and mud and two MTDs. The boundary between these units reflects a fundamental change in the development of the Southwest Pass Canyon channel-levee system. Below this boundary, a transitional period characterized by relatively unconfined deposition of sand, silt, and mud reflects a young developing channel-levee system. Above this boundary, the Southwest Pass Canyon channel-levee system was firmly established west of Site U1324 and was effective in confining sands and silts to a main channel corridor. Overspill of mud and clay developed the thick levee assemblage recorded in lithostratigraphic Unit I. Core-seismic integration suggests that acoustically transparent intervals are regional MTDs composed of faulted and contorted mud and clay. However, close examination reveals that these MTDs contain levee clay and mud that are only mildly deformed and tilted and were not transported very far from their in situ position.

## Biostratigraphy

Calcareous nannofossils and foraminifers were studied in all core catcher samples from Holes U1324B and U1324C plus several samples from Cores 308-U1324B-9H, 14H, 19H, and 27H. Rare to common calcareous nannofossils and foraminifers with good to moderate preservation occur in samples above 350 mbsf, with reduced abundance toward the bottom of the holes.

We identified nannofossil Zone QAZ1 *Emiliania huxleyi* Acme with Subzones A and B, as well as planktonic foraminifer Zones Z and Y (including Subzones Y1–Y5) (Fig. F16). Nannofossil and planktonic foraminifer data indicate that, similar to Site U1322, the sediment sequence recovered at Site U1324 was deposited during the last 60 k.y. However, the average sedimentation rate of ~10 m/k.y., is 2.5 times higher than that for Site U1322. Benthic foraminifers are dominated by infaunal species that prefer low-oxygen "stress" environments, which is expected for such rapid sedimentation rates.

## Calcareous nannofossils

Calcareous nannofossils were encountered in all samples from Holes U1324B and U1324C (Figs. F17, F18, F19, F20). Samples 308-U1324B-7H-2, 30 cm, and 27H-1, 13–18 cm, contain abundant nannofossils. Preservation ranges from good to moderate throughout the holes. Coarse-grained samples typically contain poorly preserved nannofossils with low to barren overall abundance. Nannofossils in samples below 238.65 mbsf in Hole U1324B are less abundant, but it is unclear why. Nannoplankton assemblages contain rare to common in situ and reworked species. *E. huxleyi* is the dominant in situ species. Other species, *Braarudosphaera bigelowii*, *Calcidiscus leptoporus*, *Coccolithus pelagicus*, *Discosphaera tubifera*, *Gephyrocapsa aperta*, *Gephyrocapsa caribbeanica*, *Gephyrocapsa ericsonii*, *Gephyrocapsa oceanica*, *Gephyrocapsa sinuosa*, *Helicosphaera carteri*, *Helicosphaera wallichii*, *Pontosphaera multipora*, *Reticulofenestra productella*, *Rhabdosphaera clavigera*, *Rhabdosphaera procera*, *Scapholithus fossilis*, *Syracosphaera histrica*, *Thoracosphaera* spp., and *Umbilicosphaera sibogae* were sporadically encountered. *G. oceanica* is always more abundant than *G. caribbeanica*, although both rarely constitute 10% of the total abundance. The majority of reworked species are Cretaceous in age (>99%) and occur throughout the section (Figs. F17, F19, F20). Samples 308-U1324B-1H-CC, 19–24 cm, through 7H-CC, 29–34 cm, contain high numbers of other reworked Mesozoic species.

Generally, species abundances vary significantly from sample to sample. This could be due to cyclic



fluctuations in sediment input from turbidity currents in Ursula Basin. This is supported by the relationship that we observed: the more abundant the in situ assemblages, the less abundant the reworked Mesozoic assemblages are, and vice versa (Fig. F17). We found that in situ nannofossils are better preserved in hemipelagic deposits, whereas deposits with higher terrigenous content are richer in reworked Mesozoic assemblages. Lower abundances of nannofossils toward the bottom of the holes point to the possibility that sedimentation rates (Subzone B) were very high in comparison to the upper section (Subzone A).

Based on the nannofossil stratigraphic subdivision of Hine and Weaver (1998), we recognized QAZ1 *E. huxleyi* Acme Zone in the sediment sequence recovered at Site U1324. The zone can be subdivided into Subzones A and B, which correlates well to Holes U1324B and U1324C.

### QAZ1 *E. huxleyi* Acme Zone

We identified this zone in Samples 308-U1324B-1H-CC, 7–12 cm, through 74X-CC, 36–43 cm, based on the high abundance of *E. huxleyi* (70% or more). According to Berggren et al. (1995), the first occurrence datum of *E. huxleyi* acme is at 90 ka. In situ species have sporadic distribution throughout the holes. Reworked Mesozoic assemblages form >50% of the total nannofossil abundance in most samples from Site U1324. They typically have higher values in MTDs (Fig. F18), lithostratigraphic Subunits IB, ID, IF, IIB, and IID (see “[Lithostratigraphy](#)”).

#### **Subzone A**

We distinguished Subzone A in samples above 352.74 mbsf of Holes U1324B (308-U1324B-1H-CC through 43H-CC) and U1324C (308-U1324C-1H-CC through 6H-CC). This interval is characterized by higher abundances of both in situ and reworked nannofossils relative to the lower section. The in situ species *E. huxleyi* has a cyclic distribution throughout Subzone A. Subzone A correlates with lithostratigraphic Unit I between seismic Reflectors S10 and S40-1324.

#### **Subzone B**

Subzone B, with low abundances of in situ assemblages, was identified in samples below 357.79 mbsf in Holes U1324B (Samples 308-U1324B-44H-CC through 74X-CC) and U1324C (Samples 308-U1324C-7H-CC through 8H-CC). Reworked Mesozoic assemblages are less abundant relative to Subzone A. Two peaks of reworked Mesozoic assemblages are associated with MTDs. Subzone B

correlates with lithostratigraphic Unit II between seismic Reflectors S50-1324 and S60-1324.

### **Planktonic foraminifers**

Planktonic foraminifers are frequent to abundant in samples from core catchers and selected cores above Cores 308-U1324B-29H and 308-U1324C-4H (above ~250 mbsf). Further downhole, planktonic foraminifer abundances are rare to trace and even barren in Samples 308-U1324B-48H-CC, 52X-CC, and 71X-CC through 74X-CC. In most samples, the preservation was good to excellent overall, and only a few specimens exhibit abraded features indicative of reworking. Semiquantitative data for planktonic foraminifers in Hole U1324B are presented in Table T6.

As at other Expedition 308 sites, the planktonic foraminifer assemblage found in samples from Site U1324 is dominated by typical subtropical to temperate taxa. The most abundant species is *Globigerinoides ruber* (both the pink and white forms), averaging 50% or more. Species found frequently include *Globigerinoides sacculifer*, *Globigerinoides conglobatus*, *Neogloboquadrina dutertrei*, *Globorotalia truncatulinoides*, *Globorotalia inflata* (older than 10 ka), *Globorotalia crassaformis*, *Globigerinella siphonifera*, *Orbulina universa*, *Globigerina falconensis*, and *Globigerina quinqueloba*. *Globorotalia menardii* and *Globorotalia tumida* are found only in Sample 308-U1324B-1H-CC, 19–24 cm, whereas *Pulleniatina obliquiloculata* not only occurs in the same sample, but a single specimen of this species was also observed in three other widely separated samples from the lower part of the core: Samples 308-U1324B-40H-CC, 31–36 cm, 56X-CC, 36–41 cm, and 61X-CC, 37–42 cm (Fig. F21). Other species, including *Globigerina bulloides*, *Globigerinita glutinata*, *Hastigerina pelagica*, and *Globigerinella calida*, are very rare and may occur sporadically.

Planktonic foraminifer assemblage Zones Z and Y (including Subzones Y1, Y2, Y3, and Y3–Y6?) (Kennett and Huddlestun, 1972) were identified, suggesting that the sediment recovered at Site U1324 was deposited mainly during the last 60 k.y., during marine isotope Stages (MIS) 1–3 (4?) (Fig. F21). The bottom of the core cannot be dated because of the absence of planktonic foraminifers. The last occurrence datum of *G. flexuosa* at 68 ka and the temporary last occurrence of consistent *P. obliquiloculata* at ~65 ka (Kennett and Huddlestun, 1972) were not found at Site U1324. Therefore, the sediments recovered at Site U1324 are likely younger than 65 ka. Abundant planktonic foraminifers found in Samples 308-U1324B-10H-CC, 29–34 cm, and 19H-3, 53–58 cm, may have been influenced by warm interstadial events 2.1 and 3.1, respectively.



## Zone Z

This zone is represented only by Sample 308-U1324B-1H-CC, 19–24 cm (Fig. F21). The planktonic foraminifer assemblage is characterized by abundant warm-water species including *G. menardii*, *G. sacculifer*, *G. crassaformis*, *P. obliquiloculata*, and *G. ruber*. The absence of the cool-water species *G. inflata* indicates an age younger than 10.5 ka (Kennett and Huddlestun, 1972).

## Zone Y

From Cores 308-U1324B-2H through 74X and 308-U1324C-1H through 8H, planktonic foraminifer assemblages are dominated by *G. ruber* and *G. inflata*, and the absence of warm-water species *G. menardii* (Zones X and Z), *G. flexuosa* (lower Subzone Y6 and below), and *P. obliquiloculata* (middle Subzone Y6 and below), collectively suggests that the sediment section spans Subzones Y1–Y6(?). Samples from Core 308-U1324B-43H with very rare planktonic foraminifers are grouped together as representing an interval from the lower part of Subzone Y5 to probably Y6 (Fig. F21), approximately equating to lithostratigraphic Unit II (see “[Lithostratigraphy](#)”). Because of the semiquantitative nature of our work on board, the subdivision of Zone Y requires further studies to be confirmed or modified.

### Subzone Y1

Samples 308-U1324B-2H-CC, 15–20 cm, and 3H-CC, 19–24 cm, having abundant *G. ruber* and frequent *G. crassaformis* and *G. siphonifera* but reduced *G. inflata*, are assigned to Subzone Y1. According to Kennett and Huddlestun (1972), Subzone Y1 represents a short interval at the MIS 1/2 transition between ~10.5 and 16 ka.

### Subzone Y2

Although *G. ruber* remains frequent, the cool-water species *G. inflata* becomes frequent to common, especially in the lower part of the Subzone Y2, in Cores 308-U1324B-13H through 16H. *G. crassaformis* and *G. siphonifera* are also consistently present and may become frequent only occasionally. Between Cores 308-U1324B-4H and 9H, *G. truncatulinoides* is very rare or absent. An increase in the number of planktonic foraminifers, especially *G. crassaformis*, *G. falconensis*, and *G. conglobatus*, in Sample 308-U1324B-10H-CC, 29–34 cm, may signal the influence of warmer climatic conditions such as those during MIS 2.21. Subzone Y2 represents deposition during MIS 2 (Kennett and Huddlestun, 1972) and spans the last 16–24 k.y. based on the timescale of Bassinot et al. (1994).

### Subzone Y3

Cores 308-U1324B-17H through 29H are assigned to Subzone Y3 based on the consistent occurrence of many planktonic foraminifers, particularly *G. sacculifer* and *G. inflata* without *G. menardii* and its allied species. *G. conglobatus*, a species preferring warmer water conditions, occurs in three intervals: from Sample 308-U1324B-19H-2, 52–57 cm, through 19H-3, 53–58 cm; 22H-CC, 29–34 cm, through 25H-CC, 36–41 cm; and 28H-CC, 43–48 cm, through 29H-CC, 50–55 cm. Dominated by subtropical species, the planktonic foraminifer assemblage from Sample 308-U1324B-25H-CC, 36–41 cm, shows all the characteristics of warm conditions within Subzone Y3 (Fig. F21; Table T7). Subzone Y3 represents deposition during the later part of MIS 3 (Kennett and Huddlestun, 1972) and has an age of 24–42 ka based on the timescale of Bassinot et al. (1994).

### Subzone Y4

Subzone Y4, characterized by frequent *G. inflata* and *G. falconensis*, spans Samples 308-U1324B-30H-CC, 19–24 cm, through 38H-CC, 40–45 cm. *G. sacculifer* and *G. crassaformis* are rare, and *G. conglobatus* is absent. The upper part of Subzone Y4 corresponds to lithostratigraphic Subunit ID (see “[Lithostratigraphy](#)”). Subzone Y4 represents deposition in the middle part of MIS 3 (Kennett and Huddlestun, 1972), which lasted from ~42 to 48 ka on the timescale of Bassinot et al. (1994).

### Subzone Y5

Samples 308-U1324B-39H-CC, 40–45 cm, through 42H-CC, 31–36 cm, with frequent *G. sacculifer* and *G. crassaformis*, can be assigned to Subzone Y5. Other species including *G. ruber*, *G. sacculifer*, *G. siphonifera*, *G. inflata*, and *N. dutertrei* are frequent or common. However, rare *G. conglobatus* occurs only in Sample 308-U1324B-39H-CC, 40–45 cm, whereas a single specimen of *P. obliquiloculata* is found in Sample 40H-CC, 31–36 cm. Overall, the planktonic foraminifer assemblage from Subzone Y5 supports interpretation of a gradually warming trend across the MIS 3/4 boundary (Kennett and Huddlestun, 1972) at ~48–57 ka (Bassinot et al., 1994).

### Subzone Y5–Y6?

Planktonic foraminifers are very rare or barren in samples from Cores 308-U1324B-43H through 74X in lithostratigraphic Unit II, characterized by interbedded thin silt and mud layers and MTDs (see “[Lithostratigraphy](#)”). The interval is collectively assigned to Subzone Y5–Y6? pending further studies. The absence of *G. menardii* (Zone X, 85 ka and older) and *G. flexuosa* (lower Subzone Y6, 68 ka and older)



suggests that the sediment section must be younger than 68 ka. The temporary last occurrence of consistent *P. obliquiloculata* was ~65 k.y. ago, in Subzone Y6 (Kennett and Huddlestun, 1972; Mallarino et al., in press). Solid evidence of this event was not found at Site U1324, but sporadic *P. obliquiloculata* occurs in Samples 308-U1324B-56X-CC, 36–41 cm, and 61X-CC, 37–42 cm (as well as 40H-CC, 31–36 cm, mentioned above) and may bear an age close to 65 ka, although we cannot rule out that these single specimens were reworked.

### Benthic foraminifers

Benthic foraminifers are rare to common in core catcher samples from Cores 308-U1324B-1H through 43H and 308-U1324C-1H through 6H, above ~350 mbsf, but are very rare or barren further downhole (Fig. F22). Preservation in most samples varies from good to very good except for displaced or reworked specimens. The assemblages include mainly calcareous taxa and only few species and specimens of porcelaneous taxa. The benthic foraminifers generally represent well-known neritic to “deepwater” taxa that prefer oxygen-poor, nutrient-rich environments. The *Bolivina-Bulimina* assemblage, which was described at Sites U1319 and U1320, is also found at Site U1324 (above 330 mbsf). A *Valvulineria* assemblage characterized by common occurrences of *Valvulineria bradyana* is newly identified in Sample 308-U1324B-40H-CC, 31–36 cm. Below 350 mbsf, no assemblages can be recognized because few or no benthic foraminifers are present. Rare *Ammonia beccarii*, representing reworked inner neritic species, only occurs in Samples 308-U1324B-17H-CC, 33–38 cm, and 18H-CC, 31–36 cm. Semiquantitative data of benthic foraminifers from Hole U1324B are listed in Table T6.

### *Bolivina-Bulimina* assemblage

The *Bolivina-Bulimina* assemblage was recovered from Cores 308-U1324B-1H through 39H and 308-U1324C-1H through 6H. As already described from Sites U1319 and U1320, this assemblage is characterized by abundant small thin-shelled species including *Bolivina spissa*, *Bolivina* spp., *Bulimina aculeata*, *Uvigerina* spp., *Fursenkoina bradyi*, *Stainforthia complanata*, and *Chilostomella ovoidea*. Other species that also occur are *Globobulimina affinis*, *Quinqueloculina* spp., *Gyroidina* spp., *Cibicidoides* spp., *Sphaeroidina bulloides*, and *Oridorsalis tenera*. This infauna-dominated assemblage indicates upper slope to lower bathyal depths greater than 400 m with low oxygen content. Fluctuations in the relative abundance of these species, especially above 260 mbsf (Fig. F22), may reflect cyclic changes in sediment load and bottom water circulation.

### *Valvulineria* assemblage

We recognized the *Valvulineria* assemblage in Sample 308-U1324B-40H-CC, 31–36 cm. Although species of the *Bolivina-Bulimina* assemblage remain frequent, the common occurrence of *Valvulineria bradyana* in Sample 308-U1324B-40H-CC, 31–36 cm, warrants a separation. Like many infaunal *Bolivina* and *Bulimina* species, the epifaunal *Valvulineria* spp. are also stress markers (van Hinsbergen et al., 2005), but the latter’s epifaunal living mode suggests that the stress conditions were probably not caused by fast sediment loading and low oxygen content, as indicated by infaunal species, but were more likely a result of circulation change in the later part of Subzone Y5, across the MIS 3/4 boundary, as described above.

### Age model and sedimentation rates

The age models developed during the expedition are preliminary. Biostratigraphic dating of Pleistocene sediments is difficult, and we had to rely on several assumptions to constrain age models and sedimentation rates. In the case of Site U1324, we took into consideration planktonic foraminifer biostratigraphic data and some magnetostratigraphic tie points (Table T8; Fig. F23). The magnetostratigraphic tie points were derived by matching the rock magnetic record with a global  $\delta^{18}\text{O}$  curve (see “**Paleomagnetism**” in the “Methods” chapter), and they are thus very interpretive. The biostratigraphic age constraints are mainly derived from the modified ages for the boundaries between planktonic foraminifer subzones according to the timescale of Bassinot et al. (1994) (see “**Biostratigraphy**” in the “Methods” chapter). The estimated sedimentation rates (Fig. F23) are 0.86 m/k.y. between the seafloor and 8.65 mbsf (last occurrence [LO] of *G. inflata*), 10.0 m/k.y. between 8.65 and 163.0 mbsf (Subzone Y2/Y3 boundary), 5.5 m/k.y. between 163.0 and 252.0 mbsf (Subzone Y3/Y4 boundary), and 12.0 m/k.y. between 252.0 and 323.0 mbsf (Subzone Y4/Y5 boundary). The interval between 163.0 and 252.0 mbsf corresponds to lithostratigraphic Unit I, a unit with few MTDs. This can explain the comparatively low sedimentation rates for this interval (5.5 m/k.y.). Below 323.0 mbsf, no biostratigraphic datum was recovered. However, considering that we did not retrieve *P. obliquiloculata* specimens, we infer that the oldest sediment recovered is younger than the LO of this species (Subzone Y6, ~65 ka for the LO of consistent *P. obliquiloculata* [Kennett and Huddlestun, 1972; Mallarino et al., in press]). Thus, assuming that the oldest sediment recovered is 65 ka, we estimate a sedimentation rate >25 m/k.y., but this could be even greater (up to 50 m/k.y.) if we assumed that the sediment was deposited starting in Subzone Y6. We



note that magnetic tie points 3 (10 mbsf; 26 ka) and 4 (470 mbsf; 52 ka) are in relative good agreement with the proposed age model (Table T8; Fig. F23). More rigorous postcruise work is needed to confirm this interpretation.

## Paleomagnetism

Archive halves were measured in the pass-through cryogenic magnetometer to a peak alternating-field (AF) demagnetization of 20 mT (see Table T9). APC coring was used from Cores 308-U1324B-1H to 50H; Cores 4H to 50H were oriented using the Tensor tool. The XCB drilling system was deployed (see “[Summary of operations](#)”) beginning with Core 308-U1324B-51X. The special geotechnical cutting shoe from Fugro Inc. was deployed in some cores (Table T9), which resulted in a considerable magnetic overprint (see discussion below).

### Paleomagnetic intervals

Hole U1324B was divided into five intervals based on paleomagnetic measurements (Fig. F24).

#### Interval 1 (0–260 mbsf)

Paleomagnetic Interval 1 includes lithostratigraphic Subunits IA–IE. Natural remanent magnetization after 20 mT AF demagnetization ( $\text{NRM}_{20\text{mT}}$ ) in this interval averages 0.006 mA/m (Fig. F24A). This interval can be separated into two paleomagnetic subintervals (1A and 1B) corresponding to lithostratigraphic Subunits IA–IC and ID–IE, respectively. In paleomagnetic Subinterval 1A (0–110 mbsf)  $\text{NRM}_{20\text{mT}}$  has a lower mean value (0.004 mA/m) than in Subinterval 1B (~0.008 mA/m).

Declination in paleomagnetic Interval 1 is scattered between 0° and 360°. The average declination in this interval changes from 90° at 0 mbsf to 270° at 260 mbsf (Fig. F24B). In general, the declination signal is very noisy and therefore unreliable. Inclination in paleomagnetic Interval 1 shows an average normal polarity of 20° (Fig. F24C). The inclination signal exhibits the same level of noise as the declination data and is therefore not considered reliable in this interval. Two trends can be observed; inclination directions decrease from 60° to –30° between 0 and 180 mbsf and revert to ~30° at 180 to 260 mbsf.

#### Interval 2 (260–365 mbsf)

Paleomagnetic Interval 2 spans lithostratigraphic Subunits IF–IG (260–365 mbsf) and has  $\text{NRM}_{20\text{mT}}$  intensity values ~2.5 times greater than those in Interval 1 (0.015 mA/m) (Fig. F24A). The average declination of 330° is comparatively stable in Interval 2 (Fig.

F24B). The same stable trend is observed in inclination, showing directions with an average value of 30° (Fig. F24C).

#### Interval 3 (365–440 mbsf)

$\text{NRM}_{20\text{mT}}$  values in paleomagnetic Interval 3 (corresponding to lithostratigraphic Subunit IIA) average 0.015 mA/m and are comparable to those of Interval 2 (Fig. F24A). However, the noise level of  $\text{NRM}_{20\text{mT}}$  in Interval 3 is higher than in Interval 2. This may be due to changes in lithology (see “[Lithostratigraphy](#)”) from mud and clay-rich sediments in lithostratigraphic Unit I to sand-silt interbedded facies in lithostratigraphic Unit II. Declination across Interval 2 to Interval 3 shows a sudden change from 330° to 50° (Fig. F24B), which clearly coincides with the change from APC to XCB coring. The Tensor tool is not deployed with XCB and hence declination data below Core 308-U1324B-51X could not be corrected. The inclination signal shows a relatively stable normal polarity of 40° throughout Interval 3 (Fig. F24C).

#### Interval 4 (440–490 mbsf)

Paleomagnetic Interval 4 includes the highest variations of  $\text{NRM}_{20\text{mT}}$  in Hole U1324B. The upper part of Interval 4 (440–460 mbsf) reaches a maximum of 0.03 mA/m, which is 10 times that in the lower part of the interval (460–490 mbsf;  $\text{NRM}_{20\text{mT}} = \sim 0.003$  mA/m). This feature can be correlated with the sandy MTD of lithostratigraphic Subunit IIB. Declination in Interval 4 has a relatively stable average direction of ~50° (Fig. F24B). Inclination values have stable normal polarities of 65° throughout Interval 4 (Fig. F24C).

#### Interval 5 (490–608 mbsf)

Paleomagnetic Interval 5 has an average  $\text{NRM}_{20\text{mT}}$  intensity of 0.01 mA/m (Fig. F24A). This interval corresponds to lithostratigraphic Subunits IIC and IID. The noise level in the  $\text{NRM}_{20\text{mT}}$  signal is comparable to that in Interval 3. Declination shows relatively stable directions, slightly higher than 50°, and thus is similar to those in Interval 4 (Fig. F24B). Inclination values have stable normal polarities, very similar to those of Interval 4 (Fig. F24).

The Mono Lake Excursion, Lake Mungo Event, and Lachamps Excursion (Clark and Kennett, 1973; Freed and Healy, 1974; Stupavsky and Gravenor, 1984; Flood, Piper, Klaus, et al., 1995; Cisowski and Hall, 1997) were not identified in Hole U1324B.

Observed deviations of inclination and declination data in Hole U1324B often correspond to cores taken with the geotechnical cutting shoe from Fugro Inc.



(applied during APC coring), which is magnetic (for more details see “[Summary of operations](#)”) (Table [T9](#); Fig. [F24](#)). The shoe caused a considerable magnetic overprint on the recovered sediments, resulting in inclination and declination outliers. Hence, data points from cores recovered using the Fugro cutting shoe are plotted in red in Figure [F24](#) and not included in the data analysis. The drilling overprint in inclination and declination was not removed by the applied peak field of 20 mT.

## Magnetostratigraphy

In general, the major trends in the  $\text{NRM}_{20\text{mT}}$  intensity correlate with magnetic volume susceptibility ( $\kappa$ ), although detailed features are often expressed differently between the two records (Fig. [F25](#)). As  $\kappa$  is a measure of the bulk sediment, large amounts of paramagnetic clay minerals tend to increase the values, whereas diamagnetic components, such as quartz, dilute the signal of the ferrimagnetic mineral fraction. In comparison, the  $\text{NRM}_{20\text{mT}}$  intensity is carried exclusively by the ferrimagnetic particle fraction of the sediment. For example, the double peak occurring in  $\text{NRM}_{20\text{mT}}$  between 140 and 180 mbsf is damped in the  $\kappa$  signal. Therefore, magnetostratigraphic tie points (MTP1, MTP2, MTP3, and MTP4; for details see “[Paleomagnetism](#)” in the “Methods” chapter) are primarily identified using the  $\text{NRM}_{20\text{mT}}$  intensity peaks.

The preliminary and tentative magnetostratigraphic interpretation in Hole U1324B is achieved by correlation of the identified magnetostratigraphic tie points to MIS 1.1–3.3 (Fig. [F25A](#), [F25B](#), [F25C](#), [F25D](#)) (Bassinot et al., 1994). Comparison of the  $\kappa$  signal of Hole U1324B with the Subtropical South Atlantic susceptibility (SUSAS) stack (von Dobeneck and Schmieder, 1999) (Fig. [F25A](#)) also supports our tentative correlation. MTP1 and MTP2 are primarily defined by  $\text{NRM}_{20\text{mT}}$  intensity but are not clearly identified in  $\kappa$ . MTP3 and MTP4 are identified in  $\text{NRM}_{20\text{mT}}$  intensity as well as  $\kappa$ .

MTP4 lies within an MTD belonging to lithostratigraphic Subunit IIB. Because this deposit is composed of interbedded sandy and silty layers (see “[Lithostratigraphy](#)”), the ferromagnetic fraction in this interval may be concentrated at ~450 mbsf and diluted at ~470 mbsf. Average values as extreme as those in paleomagnetic Interval 4 are not observed elsewhere in Hole U1324B, nor are they observed in sandy layers or other identified MTDs. Within the possible time frame estimated by biostratigraphic analysis in Hole U1324B (see “[Biostratigraphy](#)”) magnetostratigraphic tie point MTP4 is thought to coincide with MIS 3.3. This is also consistent with the age of the base of the underlying Blue Unit to MIS 4 (Winker and Shipp, 2002). MTP3 and MTP4

are the only two tie points that are clearly expressed in both magnetic parameters and were therefore included in the age model (see Fig. [F22](#); Table [T10](#)).

## Geochemistry and microbiology

### Inorganic geochemistry

#### Interstitial water geochemistry

Interstitial water chemical data are listed in Table [T11](#) and shown in Figures [F26](#), [F27](#), [F28](#), and [F29](#). Interstitial water alkalinity shows limited variation between 4.61 and 11.35 mM (Table [T11](#)). A down-hole increase in alkalinity is observed with local maxima at 43, 131, 226, 411, 467, 507, and 584 mbsf (Fig. [F26](#)). The pH of the interstitial water varies between 6.59 and 7.60. The acidic nature of the interstitial water ( $\text{pH} < 7.0$ ) above 200 mbsf in this hole is peculiar and rare for pore water from deep-sea marine sediments. Below 200 mbsf to the bottom of the sampled section, the pH values are higher and center around  $7.3 \pm 0.2$  (Fig. [F26](#)).

Salinity varies between 3.3 and 3.8 parts per hundred (pph) (Table [T11](#)). At depths above 50 mbsf, the salinity is higher and centers at 3.7–3.8 pph. Between 50 and 94 mbsf, salinity decreases from 3.8 to 3.4 pph, and then it remains constant to the bottom of the hole. Interstitial water chlorinity varies from 554 to 570 mM, quite similar to the standard seawater value (International Association of Physical Sciences of the Ocean [IAPSO] = 559 mM), but a clear decrease in chlorinity is observed at 438 mbsf (Fig. [F26](#)).

Dissolved sulfate increases slightly from 30.6 mM at the seafloor to a maximum of 37.3 mM at ~35 mbsf (seismic Reflector S10). Below this depth,  $\text{SO}_4^{2-}$  decreases to 0 mM at 94 mbsf (Fig. [F27](#)), the sulfate/methane interface (SMI) depth. Interstitial water ammonium concentrations are very high, from 1109 to 6820  $\mu\text{M}$ , and a general downhole increase is observed within lithostratigraphic Unit I. Variations of ammonium contents occur in lithostratigraphic Unit II, but the values are generally high. Dissolved phosphate concentrations are very low (<4.0  $\mu\text{M}$ ) with one exception (9.2  $\mu\text{M}$ ) at 507 mbsf (Table [T11](#)). The interstitial water data also show elevated concentrations of dissolved silica ( $\text{H}_4\text{SiO}_4$ ) from 185 to 601 nM. Fluctuations similar to those in ammonium are also observed in dissolved silica, and both elements show a slightly antithetical relationship (Fig. [F27](#)). Although ammonium and silica contents are higher at greater depths, at shallower depths ammonium, silica, and sulfate show local maxima at the same depth of ~25 mbsf (Fig. [F27](#)).

$\text{Na}^+$  concentrations of the interstitial water did not show significant downhole variation. However, significant increases of  $\text{Mg}^{2+}$  and  $\text{Ca}^{2+}$  and decreases of



K<sup>+</sup> are observed from the seafloor to ~35 mbsf (i.e., seismic Reflector S10). Below 35 mbsf to 165 mbsf (seismic Reflector S30), concentrations of Mg<sup>2+</sup>, Ca<sup>2+</sup>, and K<sup>+</sup> decrease. Between 240 and 280 mbsf, local maxima are obvious for Na<sup>+</sup>, K<sup>+</sup>, Ca<sup>2+</sup>, and Mg<sup>2+</sup>. Below 280 mbsf, the elemental concentrations stay relatively constant, except at 411 and 603 mbsf, where samples show significantly lower Na<sup>+</sup> and Mg<sup>2+</sup> values (Fig. F28).

Downhole variations of Li<sup>+</sup>, B<sup>3+</sup>, and Sr<sup>2+</sup> mimic those of Ca<sup>2+</sup> and Mg<sup>2+</sup>. Concentrations of Ba<sup>2+</sup> are generally low (<1.7 µM) above 75 mbsf in Hole U1324B. Ba<sup>2+</sup> peaks at 23.2 µM at 112 mbsf (just below seismic Reflector S20) and decreases to 9.9 µM at 150 mbsf. Between 150 mbsf and seismic Reflector S40, Ba<sup>2+</sup> concentrations are constant at ~10–12 µM. Below seismic Reflector S40, Ba<sup>2+</sup> concentrations fluctuate between 9 and 21 µM. The deepest sample (603 mbsf) shows significantly lower Sr<sup>2+</sup> and Ba<sup>2+</sup> and higher Li<sup>+</sup> concentrations (Fig. F29). Dissolved Mn<sup>2+</sup> concentrations decrease from 22.9 µM at the seafloor to a minimum of 5.7 µM by ~25 mbsf. Below 75 mbsf Mn<sup>2+</sup> concentrations remain generally low, although the deepest sample shows an unusually high value of 25.2 µM. The interstitial water contains high concentrations of dissolved Fe<sup>2+</sup> at shallow depths with local maxima of 479 and 354 µM at 18 and 94 mbsf, respectively (Fig. F29). High dissolved Fe<sup>2+</sup> caused iron oxyhydroxide precipitation (lepidocrocite, FeO[OH], as deduced from XRD analyses of the precipitates) from the pore waters immediately after squeezing in the laboratory.

Eight pore water samples from Hole U1324C were also analyzed and show similar trends as the data from Hole U1324B.

In summary, the interstitial water chemistry at Site U1324 shows the largest variations at depths <100 mbsf. Below 100 mbsf, only limited changes are observed. Pronounced pore water chemical changes are particularly important from the seafloor to seismic Reflector S10 (~35 mbsf). Li<sup>+</sup>, B<sup>3+</sup>, and Sr<sup>2+</sup> maxima and a Mn<sup>2+</sup> minimum occur at ~35–40 mbsf, whereas H<sub>4</sub>SiO<sub>4</sub> and Fe<sup>2+</sup> maxima occur between ~20 and 25 mbsf. Between seismic Reflectors S10 and S30, salinity, Li<sup>+</sup>, B<sup>3+</sup>, and Sr<sup>2+</sup> decrease; Ba<sup>2+</sup>, Fe<sup>2+</sup>, and NH<sub>4</sub><sup>+</sup> increase; and Cl<sup>-</sup>, Mn<sup>2+</sup>, and H<sub>4</sub>SiO<sub>4</sub> remain constant. The extremely high NH<sub>4</sub><sup>+</sup> content (up to 6820 µM) is consistent with more reducing conditions at this site in comparison with the sites drilled in Brazos-Trinity Basin IV. The general downhole increase in NH<sub>4</sub><sup>+</sup> likely reflects enhanced organic degradation at depth. The vertical profile, especially the surficial maximum and minimum in dissolved Fe<sup>2+</sup> and Mn<sup>2+</sup>, are consistent with the hierarchy of redox reactions often observed in deep-marine sediments (Froelich

et al., 1979). Elevated Fe<sup>2+</sup> concentrations within shallow depths may reflect enhanced iron reduction and/or greater availability of detrital iron oxides/oxyhydroxides or simply Fe-rich clays. The pore water chemistry at the seafloor is probably dominated by dissolution rather than organic matter degradation, which enhances alkalinity, Ca<sup>2+</sup>, Mg<sup>2+</sup>, Sr<sup>2+</sup>, B<sup>3+</sup>, and Li<sup>+</sup> concentrations at ~35 mbsf. The causes for the acidic nature of the pore water (pH < 7) at depths above 200 mbsf are unclear.

### Solid-phase chemistry

Initial results for total inorganic carbon (TIC), calcium carbonate (CaCO<sub>3</sub>), total organic carbon (TOC), total nitrogen, molar ratio of organic carbon to total nitrogen (C/N), and total hydrogen analyses on sediment squeeze cakes are listed in Table T12 and presented in Figure F30. With the exception of total hydrogen concentrations above 205 mbsf, Hole U1324C elemental data are coincident with concentration data from Hole U1324B.

TIC concentrations range from 0.60 to 2.92 wt% (average = 1.85 wt%). The organic-rich clays described in lithostratigraphic Subunit IA in the upper 15 mbsf contain <10 wt% CaCO<sub>3</sub>. The color-banded laminations of green and red mud and clay within the remaining sections of lithostratigraphic Unit I are typically calcite rich, composed of ~15 wt% CaCO<sub>3</sub>. The TIC and CaCO<sub>3</sub> curves exhibit a smooth transition between low and high concentrations from 49.3 to 332.1 mbsf. The excursion in inorganic carbon content observed in Section 308-U1324B-19H-3 at 166.5 mbsf is likely related to increased contribution of iron, indicated by the reddish color of the sediment (see Fig. F7). Inorganic carbon contents generally decrease with depth from 300 mbsf to 608 mbsf.

TOC contents are fairly uniform, ranging between 0.22 and 2.24 wt% (average = 0.75 wt%). Results ≤0 wt% for Sections 308-U1324B-3H-3, 5H-5, 13H-3, and 69X-2 and 308-U1324C-6H-2 are an artifact of the method used to calculate TOC, where

$$\text{TOC} = \text{TC} - \text{TIC},$$

and are not included in the data analysis. TOC concentrations remain relatively constant downhole, with exception of a maximum in the upper 50 m that corresponds to organic-rich, black clays in lithostratigraphic Subunit IA. Mottled black sediments were observed throughout the color-banded laminations of lithostratigraphic Unit I and are likely related to increases in TOC concentrations at 198–227, 294–323, and 361 mbsf.

Nitrogen ranges from 0.10 to 0.53 wt% (average = 0.15 wt%). The total nitrogen curve is similar to the TOC curve, with the highest concentrations in or-



ganic-rich layers. Hydrogen contents of the sediments range between 0.17 and 1.00 wt% (average = 0.64 wt%).

Molar C/N ratio ranges between 2.46 and 9.24 (average = 5.85) (omitting results from Sections 308-U1324B-3H-3, 5H-5, 13H-3, and 69X-2 and 308-U1324C-6H-2). The broad range suggests fluctuations between hemipelagic and marine organic matter. The greatest C/N variability in lithostratigraphic Unit I occurs within the organic-rich layers of Sub-units IA and ID. C/N is fairly uniform within the carbonate-rich sediments. The jagged ratio trace below 300 mbsf is associated with highly interbedded sand and silt layers in the lower portions of lithostratigraphic Unit I and throughout lithostratigraphic Unit II.

### **Solid-phase initial interpretations**

TOC contents at Site U1324 are slightly higher than concentrations observed within sediments at Sites U1319 and U1320 (Brazos-Trinity Basin IV). An increase in available organic matter based on trends in the TOC, total nitrogen, and C/N curves at 0–50 and 320–608 mbsf suggests isolated periods of intensified organic matter sequestration possibly related to glacial-interglacial cycles and oxidation fronts associated with rapid sedimentation rates. The upper 60 m represents the Holocene/Pleistocene boundary (see Fig. F22). Within the top 50 m, the maximum C/N value of 9.09 suggests increased input of terrigenous material during sea level rise. Provenance of sedimentary organic matter may be better assessed with carbon and nitrogen isotopic analysis (Jasper and Gagosian, 1990). Rapid sedimentation rates estimated at >25 m/k.y. (see Fig. F22) may be responsible for the preservation of organic matter below 320 mbsf.

## **Organic geochemistry**

### **Hydrocarbon gas composition**

Headspace methane is shown in Figure F31. Rapid increases in methane concentration begin in the middle of lithostratigraphic Unit I, whereas there are only minor amounts of methane from seafloor to 160 mbsf. Methane was the predominant hydrocarbon species determined in Hole U1324B. Concentrations of hydrocarbon gas components are shown in Table T13. The calculated SMI depth is 94 mbsf (Fig. F32). This inverse correlation may suggest that methane results from methanogenesis, which is inhibited in the presence of sulfate. Minor amounts of ethane (<3.5 ppmv) and ethylene (<1.5 ppmv) were detected below 100 mbsf, coincident with localized peak methane concentrations (100–320 mbsf and/or 600 mbsf) (Fig. F31). No higher hydrocarbons were

detected in Hole U1324B. When interpreting  $C_1/C_2$  ratios, we need to consider that minor amounts of  $C_2$  (and  $C_3$ ,  $C_4$ , and  $C_5$ ) compounds can also be generated in situ during early (low temperature) diagenesis of organic matter (e.g., Kvenvolden and Barnard, 1983). The  $C_1/C_2$  ratios at Site U1324 are generally high, suggesting biogenic origin of the methane, which may be derived by in situ microbial activities or hydrogeologically driven migration. The almost exclusive presence of methane suggests that the hydrocarbon gases found at Site U1324 are of biogenic, not thermogenic, origin.

Methane concentrations fluctuate with depth. The two highest concentrations of methane were observed in the range of 40,339–41,620 ppmv at depths of 212 and 261 mbsf. According to the lithologic description, gas-bearing strata from 198 to 278 mbsf are a mixed association of muds and clays within lithostratigraphic Unit I. These strata are positively correlated with slight increases in diagenetic ethane. In situ methanogenesis is expected to be minor considering the low abundance of subsurface microbes. Hence, the anomalously high concentrations in the middle part of lithostratigraphic Unit I are inferred to reflect fluid flow and transport. Stratigraphic accumulations occur in relatively permeable sediments and form largely from bacterial methane generated in situ or slowly migrated from depth in the section.

## **Microbiology**

### **Biomass enumeration**

The prokaryotic cell distribution in Hole U1324B was determined using whole-round core samples. The sampling frequency was one sample every 4–7 m between 2.8 and 27.2 mbsf, one sample every 8–10 m between 27.2 and 111.7 mbsf, and one sample every 15–30 m between 111.7 and 603.1 mbsf. The maximum cell density, which was  $2.0 \times 10^5$  cells/mL, was observed at 2.8 mbsf. Cell density decreases with depth and was below detection limit ( $1.0 \times 10^4$  cells/mL) within ~100 mbsf with the exception of one sample at 131.8 mbsf ( $2.8 \times 10^4$  cells/mL) (Fig. F33). The biomass of microbial cells at Site U1324 was unexpectedly small considering the location and high sedimentation rate of this site. The predominance of clay-rich sediment at Site U1324 is interpreted to explain the low microbial abundance (Table T14).

## **Physical properties**

A downhole profile of physical properties was established for Site U1324 where the overburden above the Blue Unit is thickest relative to Sites U1322 and U1323. Physical properties are compared with those



from Site U1322, where overburden above the Blue Unit is thinnest, and Site U1323, which has an intermediate overburden.

All cores were processed through the multisensor track (MST) before splitting. Initially, noncontact resistivity (NCR) and magnetic susceptibility measurements were taken at 2 cm intervals. *P*-wave logger (PWL) and gamma ray attenuation (GRA) densitometer measurements were taken at 4 cm intervals. All MST measurements were taken at 6 cm intervals from Core 308-U1324B-5H. PWL measurements were aborted after Core 308-U1324B-26H because of voids and cracks created by gas expansion.

Moisture and density (MAD) samples were selected from undisturbed cores at regularly spaced intervals ~50 cm from the top of each section. They were used to calculate water content, bulk density, grain density, and porosity. An extra sample was taken ~100 cm from the top of each section from Cores 308-U1324B-46X through 52X. The dry volume of these extra samples was not measured and, hence, grain density was not calculated because of time constraints and equipment capacity. Instead, the grain density of the sample from the MAD measurement at 50 cm in the same section was used to estimate the bulk density and porosity.

The discrete *P*-wave velocity (PWS) measurements only provided good data for cores above Core 308-U1324B-28H due to extensive voids and fractures in the cores.

## Density and porosity

Bulk density was determined from GRA on whole sections and from MAD measurements on discrete samples. Image-derived density (IDRO) from LWD data are discussed for comparison. Bulk densities determined from different methods are in good agreement in lithostratigraphic Unit I (Fig. F34A). There was considerable scatter of the LWD (IDRO) bulk density in lithostratigraphic Unit II. This is interpreted to be due to borehole washout when drilling through sandy-silty layers. The LWD (IDRO) densities had low values because it was partially measuring the water density when the borehole was washed out. LWD porosities were calculated assuming a grain density of 2.7 g/cm<sup>3</sup> and a pore water density of 1.024 g/cm<sup>3</sup>. MAD porosities and LWD porosities are generally in good agreement.

MAD bulk densities rapidly increase from 1.27 to ~1.7 g/cm<sup>3</sup> from the seafloor to 35 mbsf. Consequently, porosity values decrease from 80% to 55%. A decrease in bulk density and increase in porosity at 35 mbsf correlates with seismic Reflector S10. From 35 to 160 mbsf, bulk density increases

slightly from 1.7 to 2.0 g/cm<sup>3</sup>. Correspondingly, porosity decreases from 55% to 45% (Fig. F34C). The sharp density decrease reflected by both the MAD and LWD data at ~160 mbsf may be related to the silt layer above seismic Reflector S30 (see “[Lithostratigraphy](#)”). Below seismic Reflector S30 there is little increase in bulk density with depth; values range from 1.95 g/cm<sup>3</sup> immediately below seismic Reflector S30 to 2.05 g/cm<sup>3</sup> at the bottom of the hole. Porosity from MAD and LWD data shows little variation below seismic Reflector S30, with values decreasing gently from 48% to 40% with depth. Slight variations from this trend are observed at the top of lithostratigraphic Subunit IIA, with a small sudden increase in density, and within lithostratigraphic Subunit IIC, with a negative peak.

## Noncontact resistivity (NCR)

NCR increases with depth from 0.36 Ωm at the seafloor to ~1.5 Ωm at the bottom of the borehole (Fig. F35). NCR values increase with depth in lithostratigraphic Subunits IA and IB from 0.36 Ωm at the seafloor to 0.80 Ωm at 59.7 mbsf. In lithostratigraphic Subunits IC to IIB (59.7–481.9 mbsf), NCR values are more scattered than within the overlying lithostratigraphic units; these values range from 0.60 to 1.20 Ωm. The scatter is more evident between 240 and 400 mbsf, which probably reflects gas voids and cracks, in addition to lithologic variability. The high variability in these intervals correlates with high methane concentrations in the pore water (see “[Geochemistry and microbiology](#)”).

The lowest part of lithostratigraphic Subunit IIC (550–578.9 mbsf) has the highest resistivity values, while the sandy/silty layers within Subunit IID (578.9–608.0 mbsf) have NCR values similar to those of the upper part of Subunit IIC.

The resistivities from wireline logging data show a similar trend to that of MST measurements. However, wireline logging resistivities are generally higher, which probably results from measurement conditions, especially temperature contrast between laboratory and in situ conditions.

## Magnetic susceptibility logger

Interpretations are based on uncorrected magnetic susceptibility (Fig. F36). Near-zero values or extremely high values were observed at the top and bottom of each section. These values are not included in the description of the data.

Lithostratigraphic Subunit IA shows an increase of magnetic susceptibility with depth from 0 to 22 mbsf that correlates with a rapid increase in bulk density (Fig. F34). From 22 mbsf to the base of litho-



stratigraphic Subunit IA at 43.9 mbsf, a slight decrease in magnetic susceptibility can be observed (Fig. F36).

Magnetic susceptibility within lithostratigraphic Subunits IB (43.9–59.7 mbsf), IC (59.7–107 mbsf), and ID (107–116.8 mbsf) increases rapidly with depth until 160 mbsf and then, in lithostratigraphic Subunit IE (116.8–264.6 mbsf), decreases. The maximum value of magnetic susceptibility is correlated with a thin silt-rich interval that corresponds to seismic Reflector S30 (Fig. F36) almost at the top of lithostratigraphic Subunit IE. The lowest part of lithostratigraphic Unit I, including Subunits IF (264.8–288 mbsf) and IG (288–364.7 mbsf), shows again an increase in magnetic susceptibility from  $\sim 65 \times 10^{-5}$  to  $95 \times 10^{-5}$  SI. Magnetic susceptibility in lithostratigraphic Subunit IIA (364.7–445.5 mbsf) continues the trend of the interval above. This unit, corresponding to a thick interval of fining-upward silt/sand-rich turbidites alternating with muddy intervals (see “[Lithostratigraphy](#)”), does not display excursions as might be expected from the alternating lithologies.

Lithostratigraphic Subunit IIB (445.5–481.9 mbsf) is mainly composed of material deformed and remolded within MTDs (see “[Lithostratigraphy](#)”). This unit is characterized by very low magnetic susceptibility values, on the order of  $45 \times 10^{-5}$  SI (Fig. F36). However, the rest of the MTDs at Site U1324 do not show similar excursions. The top of lithostratigraphic Subunit IIC shows values on the order of  $100 \times 10^{-5}$  SI, comparable to those in the lower part of Subunit IIA, and has decreasing values with increasing depth.

### Thermal conductivity

Thermal conductivity increases rapidly with depth within lithostratigraphic Subunit IA and continues to increase with depth but less rapidly in lithostratigraphic Subunits IB and IC. Below lithostratigraphic Subunit IC, at 107 mbsf, there is almost no increase in thermal conductivity with depth, although the profile oscillates between 1 and 1.4 W/(m·K), centered around a mean of 1.2 W/(m·K) (Fig. F37). The trend in thermal conductivity mirrors that of the porosity: a rapid porosity decrease through lithostratigraphic Subunits IA-ID and a relatively constant porosity profile thereafter (Fig. F34).

### P-wave velocity

The data from the PWS probes and the PWL correspond well (Fig. F38). The velocity rapidly and smoothly increases from 0 to 60 mbsf and then increases more moderately from 60 to 190 mbsf (Fig.

F38). No major shifts in P-wave velocity are observed when crossing from one lithostratigraphic unit to another. Velocity peaks in PWS data are relatively small in the uppermost 100 m and, from this depth downhole, the profile shows a more jagged pattern. The most important excursion recorded by PWS and PWL data is related to seismic Reflector S30, at ~160 mbsf. This low-velocity excursion is also evident in wireline logging data (Fig. F38).

P-wave velocities from wireline logging in Hole U1324B show substantial disagreement above seismic Reflector S20. Below this reflector the wireline logging values converge with PWS and PWL data (Fig. F38). This mismatch most probably results from the large borehole diameter above seismic Reflector S20, at 107 mbsf. The caliper log from LWD data in Hole U1324A shows a large hole diameter above 120 mbsf.

Below 220 mbsf, the wireline logging data show significant deviations from the smooth increase in velocity observed above. The first occurs between 220 and 260 mbsf, where wireline P-wave velocity decreases by ~50 m/s (Fig. F38). The caliper tool in Hole U1324A measured a large diameter in this interval, indicating that this decrease may be at least partially due to borehole washout. From 260 to 350 mbsf, near the top of lithostratigraphic Unit II, P-wave velocities continue to increase smoothly (Fig. F38). The wireline P-wave velocity log shows more irregular behavior from 350 mbsf downhole (lowest part of lithostratigraphic Subunit IG and lithostratigraphic Unit II). This is probably related to the alternating silt-sand-clay layers within this unit. Nevertheless, two intervals can be observed in Unit II. In the upper one (350–425 mbsf), velocities decrease from 1675 to 1650 m/s. The second one shows increasing velocities from 1675 to 1750 m/s.

P-wave velocity anisotropy was derived from PWS measurements. It is relatively small, with values ~1%, within lithostratigraphic Subunits IA, IB, and IC but increases in lithostratigraphic Subunit ID, especially below seismic Reflector S20, with mean anisotropies of ~2%.

### Undrained shear strength

The undrained shear strengths measured by the AVS consistently match those measured with the pocket penetrometer (Fig. F39). Below 240 mbsf, the values measured by the penetrometer are systematically higher than those measured by the AVS, probably because the penetrometer measurements do not generate fractures whereas those of the AVS do.

Peak undrained shear strength increases downhole from near zero at the top of lithostratigraphic Unit I



to ~250 kPa at 220 mbsf (Fig. F39). The undrained shear strength is more scattered in lithostratigraphic Unit II. This is interpreted to be associated with the voids and fractures formed before and during measurements and the highly variable lithology. The upper part of the MTDs (440–480 mbsf) has higher undrained shear strength. This may result from a higher consolidation state of the sediments due to recompaction during the landslide process. An overall trend of decreasing shear strength with depth is shown in lithostratigraphic Subunits IIB and IIC. The shear strength increases from 540 to 580 mbsf and then decreases to the bottom of the hole. The decrease in shear strength at the base of lithostratigraphic Subunit IIB is correlated to the presence of silty layers, whereas within lithostratigraphic Subunit IID, the low shear strengths correlate with the presence of sand layers within clay (measurements were always performed on the mudstone lithology).

Residual shear strength is highly variable (Fig. F39). This is partly explained by the difference in failure pattern after the shear vane reaches the undrained peak shear strength. Brittle failures isolate a plug around the shear vane, and the undrained residual shear strength is then very low. If the failure is caused without fracture the residual shear strengths are observed to be generally higher.

The sensitivity is generally intermediate (5–10) with a few peak values that indicate high sensitivity (Fig. F39). These peak values are associated with low residual shear strengths and reflect brittle failure rather than low disturbed shear strength.

In Figure F40, the peak shear strength is plotted and compared with iso-lines of the ratio between peak shear strength and the vertical hydrostatic effective stress (see “Physical properties” in the “Methods” chapter). The relation between the iso-lines and the peak undrained shear strength gives an indication of the consolidation state of the clay. At Site U1324 the peak undrained shear strength is not parallel to a particular iso-line. Within lithostratigraphic Subunits IA and IB, the undrained peak shear strength follows the 0.1 iso-line (Fig. F40). In Lithostratigraphic Subunit IC the peak shear strength moves toward the lower iso-lines 0.05 and 0.025.

## Summary

Variations in physical properties correlate with lithostratigraphic units (see “Lithostratigraphy”). The interbedded silt, sand, mud, and MTDs in lithostratigraphic Unit II are characterized by highly variable bulk density and porosity. Physical

properties show much less scatter within the uniform hemipelagic mud and clay in lithostratigraphic Unit I.

Bulk density, porosity, noncontact resistivity, thermal conductivity, and *P*-wave velocity data are mutually dependent. Porosity decreases rapidly from the seafloor to 35 mbsf and then slowly to 160 mbsf. There is only a slight decrease in porosity below 160 mbsf to the bottom of the hole. This trend is also reflected on the bulk density, NCR, *P*-wave velocity, and thermal conductivity data. Almost no decrease in porosity with depth below 160 mbsf suggests that these sediments are underconsolidated and overpressured. This explanation is supported by the high sedimentation rates described in “Biostratigraphy.”

There is no significant difference in physical properties between the MTDs and the nondeformed sedimentary successions in lithostratigraphic Unit I at Site U1324, suggesting that these MTDs remained relatively intact during transport and probably have not moved significant distances from their original deposition location. This explanation is supported by the mild deformation observed in these intervals (see “Lithostratigraphy”).

Undrained peak shear strength shows larger oscillations within lithostratigraphic Unit II. It generally increases with depth from a low at the boundary between lithostratigraphic Units I and II until the bottom of the hole. However, major reductions in shear strength occur at ~520 mbsf, at the base of a major MTD, and at ~590 mbsf.

Lithostratigraphic Subunits IB and ID correspond to MTDs at Sites U1322 and U1324. The trends in porosity and undrained shear strength are similar at both sites. However, the porosity and undrained shear strength profiles at Site U1324 (Figs. F34C, F40B) show more subdued variations (or no variation at all) between MTDs and undisturbed units than those at Site U1322 (Figs. F34C, F40B). It is possible that at Site U1324, upslope on the Mississippi Canyon levee, the velocity of landslides might have been lower than that at Site U1322, in the center of the basin, and thus the amount of shearing and deformation might also have been lower. Higher shearing at Site U1322 would then translate into a higher degree of consolidation.

## Downhole measurements

Downhole measurements at Site U1324 were used to characterize pressure, temperature, and rock properties within the mudstone-dominated sedimentary section above the Blue Unit.



## Logging while drilling and measurement while drilling

### Operations

LWD/MWD operations in Hole U1324A used the same BHA, tool configuration, and protocols as those for at Sites U1322 and U1323. (see “[Downhole measurements](#)” and “[Summary of operations](#)” in the “Site 1322” chapter). Batteries were replaced in the LWD tools prior to drilling. The hole was initiated with a rapid jet-in to 8 mbsf before retrieving the VIT camera. After the VIT camera was recovered, bit rotation and pump rates of 50 rpm and 60 gpm were used to 25 mbsf while maintaining an ROP of 30 m/h. From 25 to 35 mbsf, pump rates were increased gradually to 400 gpm. Below 35 to ~612 mbsf, an ROP of 30 m/h and pump rates of at least 400 gpm were maintained. The interval from 472 to 612 mbsf was drilled using 10.5 ppg mud (seawater, sepiolite, and barite). One sand interval >1.5 m was encountered, and as result the hole was cemented according to IODP Expedition 308 operations protocol.

### Logging data quality

Figure F41 shows the LWD quality control logs. The target ROP of 30 m/h ( $\pm 5$  m/h) was achieved except during jet-in (Fig. F41). The density-derived caliper log (DCAV) documents good borehole conditions from 130 to 612 mbsf (Fig. F41). Enlarged borehole dimensions, however, existed from 378 to 420 and 509 to 520 mbsf. The bulk density correction (IDDR) for the entire borehole varies from -0.1 to 0.2 g/cm<sup>3</sup> (mean = 0.02 g/cm<sup>3</sup>) (Fig. F41), which was larger than in previous holes. The largest variations are concentrated in enlarged borehole intervals.

LWD logs were depth-shifted by identifying the seafloor in the gamma ray data. For Hole U1324B, the gamma ray pick for the seafloor was at 1466.5 mbrf, 0.4 m deeper than the drillers depth. The rig floor logging datum was located 10.6 m above sea level.

### Annular pressure while drilling and equivalent circulating density

Pressure within the borehole was monitored during MWD/LWD operations (see discussion in “[Array resistivity compensated tool](#)” in “Downhole measurements” in the “Methods” chapter) as annular pressure while drilling in excess of hydrostatic (APWD\*) and equivalent circulating density referenced to the seafloor (ECD<sub>rf</sub>). ECD<sub>rf</sub> decreases from 0 to 300 mbsf and then gradually increases from 300 to 470 mbsf (Fig. F42). APWD\* gradually increases with depth from 0 to 470 mbsf. At 470 mbsf, 10.5

ppg mud (seawater, sepiolite, and barite) was circulated while drilling. The weighted mud created step increases in ECD<sub>rf</sub> and APWD\*.

### LWD results

Operations in Hole U1324A drilled through a series of interbedded clay, mud, and sand units as well as several MTDs from 0 to 612 mbsf. The hole quality from 0 to 65 mbsf is highly variable, with caliper measurements reaching at least 42 cm. Below 65 mbsf, the caliper measured an average hole diameter of 25.9 cm, with washouts at ~244, 328, 378, and 509 mbsf.

The GeoVision Resistivity (GVR) tool gamma ray log has minor variations through lithostratigraphic Unit I. Lithostratigraphic Unit I was predominantly composed of clay and mud with rare occurrences of silt and sand. Gamma radiation in lithostratigraphic Unit I increases with depth, and the most significant deviation occurs at ~160 mbsf, which corresponds to seismic Reflector S30 (Fig. F43). This interval is characterized by lower gamma radiation and is interpreted as a silty sand layer. Lithostratigraphic Unit II, predominantly composed of interbedded silt and very fine sand with beds and laminae of mud and clay, shows more gamma ray variability than lithostratigraphic Unit I. Gamma radiation ranges from 26.4 to 92.4 gAPI, which suggests distinct changes in lithology from sand-rich to mud intervals (Fig. F43).

GVR deep button resistivity increases from 0.3 to 2.2 Ωm from the seafloor to 365 mbsf (Fig. F43). Variations in deep resistivity are interpreted as occurrences of sand and silt within lithostratigraphic Unit I. The GVR shallow button resistivity shows larger variations above 100 mbsf, due to variable hole conditions that are most likely caused by drilling disturbances (Fig. F43). Deep resistivity measurements show a wider range of values within lithostratigraphic Unit II (365–608 mbsf), where resistivity varies from 0.5 to 3.6 Ωm (mean = 1.5 Ωm). These variations reflect greater sand content within lithostratigraphic Unit II.

Vision Density Neutron (VDN) bulk density increases from 1.0 g/cm<sup>3</sup> near the seafloor to 2.2 g/cm<sup>3</sup> near the bottom of the hole (Fig. F43). A comparison of LWD bulk density with core MAD measurements shows an excellent correlation throughout most of the hole except for washed-out intervals in lithostratigraphic Subunits IIA and IIC (Fig. F43). Neutron porosity decreases from 86.5% to 38%, with the largest downhole porosity fluctuations occurring in sand-rich intervals within lithostratigraphic Subunit IIA (Fig. F43). The photoelectric factor log from Hole



U1324B follows similar trends as those observed in the gamma ray profile except below 472 mbsf, when of heavy mud containing barite affected the measurements (Fig. F43).

Resistivity images show deformation in the hemipelagic drape and distal turbidites drilled in Hole U1324A (Fig. F43). Lithostratigraphic Subunit ID is composed of faulted and contorted reddish brown and greenish gray clay (see “[Lithostratigraphy](#)”). Resistivity images in Subunits ID and IE reveal dipping beds ( $5^{\circ}$ – $55^{\circ}$ ) throughout these intervals that are consistent with core observations (Fig. F44). Steep deformed beds with dips as high as  $65^{\circ}$ , corresponding to the top of lithostratigraphic Subunit IE, exist just above seismic Reflector S30 (Fig. F44).

Lithostratigraphic Unit II shows large amounts of deformation as contorted and faulted beds indicative of downslope remobilization (Fig. F45). This unit is interpreted as MTDs (see “[Lithostratigraphy](#)”). Steep dips and folds in the resistivity images suggest the presence of overturned beds in lithostratigraphic Subunit IIA. Scoured surfaces, interpreted as erosional episodes, are imaged in lithostratigraphic Subunit IIC (Fig. F46). A fold with an east-west-trending axis found in lithostratigraphic Subunit IID confirms significant deformation in this subunit (Fig. F47). Most of the deformation features observed within Hole U1324A trend in an east-west direction, with the majority dipping to the north.

## Wireline logging

### Operations

Wireline tools were deployed in Hole U1324A to obtain velocity data (Fig. F48). A tool string consisting of the HNGS, DSI, and GPIT was deployed first (see “[Downhole measurements](#)” in the “Methods” chapter), with the drill pipe at ~54 mbsf. A down-hole log was recorded at 550 m/h from the seafloor to 59 mbsf. The tool string was then stuck either with the lower DSI centralizer on the lockable float valve or the go-devil at the end of the tool string hitting the borehole wall. We pulled the pipe up 5 m and then successfully lowered the tool string into the borehole. The pipe was left at 49 mbsf. We started the first logging pass from 507 mbsf. We measured gamma radiation, including spectral data, and P- and S-wave (P&S) mode at 15 Hz sampling rate. Logging proceeded at 275 m/h to 84 mbsf. We then lowered the tool string for a second pass starting from 509.5 mbsf. The second pass recorded gamma radiation, P&S, low-frequency lower dipole, and Stoneley modes at 15 Hz sampling rate.

The second wireline tool string deployed consisted of the Well Seismic Tool for a check shot survey (see “[Downhole logging](#)” in the “Methods” chapter).

Sixteen stations were targeted at ~25 m intervals (Table T15). The generator-injector gun had a 45 in<sup>3</sup> generator chamber volume and a 105 in<sup>3</sup> injector chamber volume and a total pressure of 2000 psi. The recording length was 5 s with a 1 ms sampling rate and a 40 ms delay. The rig floor preparations for wireline logging operations began on 19 June 2005 at 1905 h and were completed by 20 June at 1255 h.

### Logging data quality

The wireline data were depth-shifted based on a sea-floor depth of 1066.5 mbsf determined by gamma ray logs. HNGS data were not corrected for borehole diameter variations or mud weight.

### Wireline results

HNGS gamma ray measurements are in good agreement with those of the GVR. The spectral measurements ( $^{40}\text{K}$ ,  $^{232}\text{Th}$ , and  $^{238}\text{U}$  isotopes) show that the decay of  $^{232}\text{Th}$  is the primary gamma ray contributor (Fig. F48.) The range of  $^{232}\text{Th}$  values measured in Hole U1324A fall within values reported for illite and smectite (Rider, 1996).

In Hole U1324A we collected wireline sonic data and check shot data to evaluate velocity between 83.8 and 498.9 mbsf (Table T15; Fig. F48). Compressional wave velocities (wireline log) to 501.9 mbsf generally increase from 1486 to 1834 m/s with depth, whereas the interval velocities from the check shot increase from 1583 to 1852 m/s (Fig. F48).

Before obtaining velocity measurements at Site U1324, the only available time-depth information for the Ursula Basin site was based on nearby check shot surveys (see [Equation 1](#) in the “Site U1322” chapter). This time-to-depth conversion is plotted with check shot and sonic log data (Fig. F49).

### Core-log-seismic integration

Lithostratigraphic Unit I (0–364.7 mbsf) is described as hemipelagic drape and very distal turbidites from channel-levee systems to the west and is divided into seven subunits (see “[Lithostratigraphy](#)”). Lithostratigraphic Unit II (364.7–600.8 mbsf) includes four subunits and marks a change in lithology that includes interbedded silt and very fine sand with beds and laminae of mud and clay. Several MTDs within this unit are potentially associated with the depositional environment of the Southwest Pass Canyon channel-levee system (see “[Lithostratigraphy](#)”).



Most of the lithostratigraphic subdivisions correlate with log responses (Fig. F50). Based on gamma radiation, resistivity, bulk density, and compressional wave velocity log responses, five fining-upward and fining-downward sequences were identified within lithostratigraphic Unit II. This correlates well with variations in sand content in cores. Four out of five of these zones correlate closely with the tops of lithostratigraphic subunits; the exception is from 400 to 422 mbsf within lithostratigraphic Subunit IIA and seems to be the thickest sand sequence (Fig. F51).

We used LWD density data and the wireline sonic log to construct a synthetic seismogram for Hole U1324B (Fig. F50). Reflection coefficients were calculated using the LWD density data and a constant compressional wave velocity of 1600 m/s from 0 to 50 mbsf and the wireline velocity below 50 mbsf. A 150 Hz minimum-phase, Ricker wavelet was convolved with the reflection coefficients to create the synthetic seismogram. The correlation of events between the synthetic seismogram and the high-resolution seismic indicates that the time-depth model is appropriate for these sediments. An accurate time-depth model allows correlation of seismic reflections with observations in core and logging data.

A decrease in gamma radiation and bulk density correlates with seismic Reflector S10 (Figs. F24, F51). The top of lithostratigraphic Subunit ID is defined by an increase in velocity and a subtle change in resistivity (Figs. F50, F51). The top of lithostratigraphic Subunit IE is interpreted as a transition from an overlying MTD to a series clay laminae and thin beds enriched in foraminifers and nannofossils (see “[Lithostratigraphy](#)”). The upper part of this subunit is characterized by high gamma radiation, low density, and low velocity. A low-density zone correlates with seismic Reflector S30 (Figs. F50, F51). Seismic reflectors S40-1324 and S50-1324 correlate with zones interpreted as potential low-relief channels containing silt and sand deposits. The synthetic seismogram shows an apparent offset with the regional seismic data suggesting that the shallow velocity may have been too fast (Fig. F50). The synthetic seismogram matches the frequency and amplitude of signals observed in the seismic data except in lithostratigraphic Unit II, where the high-amplitude reflections, due to low densities, are frequent. These low densities may be the result of degraded borehole conditions.

## Temperature and pressure measurements

In situ measurements made with the APCT tool, the T2P, and the DVTTP documented overpressure and a low thermal gradient relative to Site U1322.

## Advanced piston corer temperature tool

The APCT tool was deployed four times in Hole U1324B (Table T16). Temperature was measured in the sediment for 10 min to establish the temperature decay curve. Extrapolation of the temperature decay curve with an assumed thermal conductivity of 1.2 W/(m·K) was used to estimate in situ formation temperatures. The first deployment at 51.3 mbsf (Core 308-U1324B-6H) provided an in situ temperature of 5.66°C (Fig. F52). The second deployment (79.8 mbsf; Core 308-U1324B-9H) yielded an equilibrium temperature of 6.32°C (Fig. F53). The third deployment was at 108.3 mbsf (Core 308-U1324B-12H) and yielded an equilibrium temperature of 6.40°C (Fig. F54). The final deployment occurred at 136.3 mbsf (Core 308-U1324B-15H) and provided a formation temperature of 7.50°C (Fig. F55).

## Temperature/Dual Pressure Probe

Twelve deployments of the T2P were completed at Site 1324 (Table T16). These measurements provided numerous constraints on in situ temperature and some constraints on formation pressures.

### T2P Deployment 5

All sensors recorded an increase during penetration into the formation during T2P Deployment 5 (Table T17; Fig. F56). The tip pressure decreased after penetration and achieved nearly constant pressure at 11.0 MPa. The hydrostatic reference was 11.13 MPa. The shaft sensor recorded a small pressure increase followed by minimal dissipation to 11.9 MPa. A pressure difference between the tip and shaft was recorded while lowering the tool downhole. The temperature record was continuous and smooth to its final temperature of 5.57°C. Data recording stopped upon pulling the tool out of the formation. At the rig floor, it was noted that the T2P tip was bent and the thermistor and bottom porous stone were missing from the tool. We believe the tool was bent during penetration and broken when pulling the tool out of the formation. Data may not reflect in situ conditions because of probe damage.

### T2P Deployment 6

Pressure and temperature data for T2P Deployment 6 show multiple pulses and decays (Table T18; Fig. F57). The first increase in all sensors occurred when the CDS landed in the BHA, the second increase in the tip and shaft pressure coincided with pushing into the formation, and the third increase occurred when circulation began (Table T18; Fig. F57). The tip pressure went subhydrostatic (hydrostatic pressure = 11.51 MPa), after which it slowly increased to 11.7



MPa. Subhydrostatic pressure may have resulted from an internal leak or a small void near the tip caused when the drill bit was picked up. The shaft pressure dissipated to 12.7 MPa. The temperature was decreasing when the tool was recovered and did not reach an equilibrium value. This continual decrease in temperature suggested there was a leak in the system that removed heat.

#### **T2P Deployment 7**

During T2P Deployment 7, pressure and temperature responded to initial landing of the CDS in the BHA, pushing into to the formation, and circulation of drilling fluid (Table T19; Fig. F58). The tip pressure decreased to 12.0 MPa; however, the response was erratic. The shaft had a small pressure increase and declined to a final pressure of 13.3 MPa. Hydrostatic pressure was 11.80 MPa. The small shaft pressure increase may have indicated incomplete penetration into the formation. The temperature data provided an in situ temperature estimate of 6.81°C.

#### **T2P Deployment 8**

The tip pressure and temperature increased with penetration during T2P Deployment 8 (Table T20; Fig. F59). The tip pressure eventually increased to 12.4 MPa. The hydrostatic reference was 11.99 MPa. The temperature profile equilibrated to a formation temperature of 7.20°C. The shaft pressure response was erratic throughout the deployment, with multiple step increases and decreases in pressure that were not associated with deployment events. Because of the poor pressure readings the tool was disassembled and reassembled to establish good seals and electrical connections.

#### **T2P Deployment 9**

T2P Deployment 9 exhibited large pressure and temperature responses when the tool landed in the BHA and when it penetrated the formation (Table T21; Fig. F60). These responses were immediately followed by decreases. We interpreted that the tool was coupled with the drill bit; therefore, when the bit was picked up, the tool was pulled out of the sediment. A large offset between the tip and shaft pressure was also a problem. Because of deployment and calibration problems, no in situ conditions could be evaluated.

#### **T2P Deployment 10**

T2P Deployment 10 is documented in Table T22. An electronic problem that occurred after placing the tool on the rig floor precluded collection of any downhole data. Upon recovery of the tool, it was determined that the connection between the sensors

and the data acquisition system was poor. To remedy this problem, the tool was dismantled, all connections were cleaned, and the tool was reassembled.

#### **T2P Deployment 11**

T2P Deployment 11 tested the sensors and data acquisition system. The probe was not pushed into the sediment (Table T23). Data recorded for the deployment show excellent agreement between the tip and shaft pressure sensors (Fig. F61). Two pressure decreases occurred at the tip. These may have been caused by the tip being partly embedded in the sediment. The shaft did not penetrate the formation. Overall, the Deployment 10 confirmed that the electronic failure from T2P deployment had been fixed.

#### **T2P Deployment 12**

T2P Deployment 12 showed pressure and temperature increases during landing of the CDS in the BHA and during penetration into the formation (Table T24; Fig. F62). The tip pressure decreased rapidly and then slowly dissipated to 11.0 MPa (hydrostatic pressure = 11.10 MPa). The shaft pressure increased and then dissipated to 11.4 MPa. From the slow dissipation of shaft pressure we inferred low permeability of the sediments. The temperature profile recorded a final temperature of 5.46°C, which was assumed to represent in situ conditions.

#### **T2P Deployment 13**

All sensors increased with penetration into the sediment during T2P Deployment 13 (Table T25; Fig. F63). Pressures then dissipated until the tool was pulled out of the formation. The tip had a pressure decrease coincident with picking up the bit. End pressures of 12.0 MPa (tip) and 12.2 MPa (shaft) exceeded hydrostatic pressure (11.61 MPa). The temperature profile exhibited decay to an estimated in situ temperature of 6.40°C.

#### **T2P Deployment 14**

Similar to Deployment 13, pressure and temperature increased with penetration into the sediment, followed by dissipation curves during T2P Deployment 14 (Table T26; Fig. F64). All sensors recorded a perturbation while in the formation that could not be attributed to deployment activities (Table T26). After this perturbation, temperature and shaft pressure continued to dissipate. The tip pressure had a larger decrease followed by a pressure increase. The end pressures of 12.7 MPa (tip) and 13.0 MPa (shaft) exceed hydrostatic (12.11 MPa). The temperature (7.31°C) appeared to be in equilibrium with the formation.

### T2P Deployment 15

T2P Deployment 15 provided useful shaft pressure and temperature data; however, tip pressure data were less reliable. All data increased during penetration followed by dissipation curves (Table T27; Fig. F65). No data were recorded during retrieval of the tool from the sediment. The tip pressure decreased after penetration, then recovered and dissipated to 13.8 MPa. The shaft pressure dissipated to 14.3 MPa. Hydrostatic pressure was 12.61 MPa. The temperature decay was rapid to 8.27°C. We interpreted this to be the formation temperature. When the tool reached the rig floor, it was confirmed that the tip was bent and the drive tube was loose. The loosening of the drive tube most likely caused the failure to record data during tool retrieval.

### T2P Deployment 16

The pressure and temperature data are excellent for T2P Deployment 16 (Table T28; Fig. F66). Pressure and temperature increased during penetration, which was followed by continuous dissipation curves. The end pressure of 13.9 MPa (tip) may have been in equilibrium with the formation. The hydrostatic reference was 13.62 MPa. Temperature equilibrated with the formation at 9.97°C.

### Davis-Villinger Temperature-Pressure Probe

Thirteen DVTTP deployments were completed at Site U1324 (229.1–608.1 mbsf) to provide additional constraints on formation pressure and temperature (Table T16).

### DVTTP Deployment 3

After penetration during DVTTP Deployment 3, the pressure rapidly decreased followed by a slow pressure increase (Fig. F67). It was believed an internal leak or a pressure drop caused by a void when picking up the drill string, caused this response. The slow, continuous pressure increase most likely indicated the latter. A final pressure of 13.1 MPa was nearly constant and may be near in situ conditions; hydrostatic pressure was 12.92 MPa. The temperature profile provided an equilibrium temperature of 9.52°C (Fig. F67).

### DVTTP Deployment 4

Similar to DVTTP Deployment 3, the temperature record provided in situ conditions during DVTTP Deployment 4 (11.68°C), whereas the pressure record was problematic (Fig. F68). Pressure decreased rapidly after insertion and then had increase/decrease cycles. We interpreted this was caused by an internal leak; as the pressure reached a high value, fluid pres-

sure leaked into the tool pressure housing, which in turn caused a rapid decrease; the pressure then slowly increased until it leaked again. This prompted a rebuild of the DVTTP to seal internal leaks.

### DVTTP Deployment 5

No data were recorded for DVTTP Deployment 5.

### DVTTP Deployment 6

DVTTP Deployment 6 provided an equilibrium temperature (12.96°C) (Fig. F69). Pressure increased with penetration and then decreased rapidly when the bit was picked up from the bottom of the hole. A slow pressure rebound was then recorded. It was believed the tool was partly pulled up with the drill bit, and this created a void around the pressure sensor. As the void equilibrated with the formation, pressure increased to 14.9 MPa, which is less than hydrostatic pressure (15.28 MPa). Pressure was still increasing when the DVTTP was retrieved.

### DVTTP Deployment 7

During DVTTP Deployment 7 the temperature profile had a type dissipation curve but the pressure profile exhibited a low-pressure excursion after picking up the bit off the bottom of the hole (Fig. F70). The equilibrium temperature was estimated to be 13.46°C. The pressure decreased to a value significantly below hydrostatic (hydrostatic pressure = 15.57 MPa) and then slowly increased to 12.9 MPa. The increase may have reflected charging of a void with formation fluids. Fluid pressure was still increasing at the end of the experiment.

### DVTTP Deployment 8

In DVTTP Deployment 8 the temperature spiked at penetration followed by decay to an in situ temperature of 13.84°C (Fig. F71). The pressure record for this deployment was significantly less than hydrostatic (hydrostatic = 15.86 MPa) and did not record any penetration pressure or dissipation (Fig. F71). This poor pressure result prompted a change in the DVTTP being deployed while the tool used in this deployment was rebuilt.

### DVTTP Deployment 9

A programming error occurred during DVTTP Deployment 9. No data were recorded.

### DVTTP Deployment 10

Pressure and temperature dissipation profiles increased with penetration and then decreased during DVTTP Deployment 10 (Fig. F72). Temperature followed a decay curve to a formation temperature of



15.81°C. Pressure dissipated while the tool was in the formation, but only to 19.9 MPa, in contrast to hydrostatic pressure of 16.75 MPa. The pressure dissipation was far from reaching equilibrium.

#### DVTTP Deployment 11

The temperature and pressure sensors recorded unreliable data during DVTTP Deployment 11 (Fig. F73).

#### DVTTP Deployment 12

During DVTTP Deployment 12, pressure increased during penetration, then quickly declined, and then recovered rapidly. The pressure ultimately dissipated to 18.9 MPa (Fig. F74). This dissipation was not yet in equilibrium with the formation. The temperature increased rapidly during penetration and then dissipated. The equilibrium temperature was 17.16°C (Fig. F74).

#### DVTTP Deployment 13

Pressure and temperature profiles were recorded during and after penetration during DVTTP Deployment 13 (Fig. F75). Temperature decayed to an in situ value of 11.11°C. The pressure profile dissipated to 14.7 MPa but had not yet equilibrated with the formation. Hydrostatic pressure was 13.12 MPa.

#### DVTTP Deployment 14

During DVTTP Deployment 14, pressure and temperature data had regular profiles. Pressure increased slightly during penetration and then dropped rapidly to 15.8 MPa (Fig. F76), which exceeded hydrostatic (14.67 MPa). Temperature increased rapidly and then decreased rapidly when the bit was picked up off the bottom of the hole. Near the end of the deployment, temperature increased to a final value of 11.2°C. No explanation was available for the small temperature increase at the end of the deployment.

#### DVTTP Deployment 15

Similar to DVTTP Deployment 14, during DVTTP Deployment 15, pressure increased, then decreased, and slowly increased to 16.9 MPa (Fig. F77), which exceeded hydrostatic pressure (15.68 MPa). The temperature reading was more problematic than DVTTP Deployment 14. The end temperature of 13.63°C most likely is not representative of in situ conditions.

#### Temperature and pressure summary

APCT, T2P, and DVTTP measurements help constrain the thermal gradient and the pressure field at Site U1324. Temperature measurements increased approximately linearly with depth (Fig. F78). Regression of temperatures provided a thermal gradient of

18.4°C/km. The largest scatter between the data and the average gradient occurred between 200 and 400 mbsf and below 550 mbsf. In the 200–400 mbsf interval, deviations may reflect lithology variation, deployment duration, or coupling between the probe and the sediment.

Two summaries of the pressure field were extracted from pressure measurements. The first included the pressure data (Fig. F79) where both pressure increases during penetration and dissipation curves were recorded. These data provided a maximum estimate of pressure, as complete dissipation was not achieved. Deviations of the last measured pressure (Fig. F79) and the in situ pressure were a function of the initial pressure spike (a function of probe geometry) and the amount of time the tool was left in the formation (Table T16).

The second pressure interpretation included reliable dissipation pressures (Fig. F79) and pressures measured that were interpreted as recovery from a void created near the tip of the probe. In multiple deployments, it was interpreted that a void was created near the tip of the probe when the drill bit was picked up. The pressure then rebounded as the void started to equilibrate with the formation fluid. The pressures (Fig. F80) were the final pressures measured by the probe prior to removal from the formation and represent a minimum bound on pressure. These data, although not finalized, were interpreted to document fluid overpressure from 50 to 608 mbsf at Site U1324.

#### Summary

Site U1324 logging data provided a detailed picture of the bedding style and lithofacies overlying the Blue Unit. Detailed core-log data integration at Sites U1322 and U1323 will enable refinement of the interpretation, but our preliminary interpretation provided the following insights:

- The main lithostratigraphic units defined in cores correlate with variations in LWD and wireline logs responses.
- Gamma ray, resistivity, bulk density, and compressional wave velocity log responses define five intervals within lithostratigraphic Unit II that are associated with fining-upward and fining-downward sequences.
- Resistivity images show significant deformation (dipping beds from 5° to 55°) of the overlying hemipelagic drape and distal turbidites from the Southwest Pass Canyon sediments. Steeply deformed beds with dips as high as 65° and folded and faulted beds suggest downslope remobilization as MTDs. Resistivity images show evidence of these MTDs in lithostratigraphic Subunit IIA,

where steep dips and folds suggest a succession of sand-silt-mud laminae. Most of the deformation features observed in Hole U1324A trend in an east-west direction with the majority dipping to the north.

- A correlation between seismic data, well logs, and synthetic seismograms shows a good match between seismic reflectors. In the case of lithostratigraphic Subunit IE, faulted and contorted clay units with steeply dipping beds show an acoustically transparent nature in both the seismic data and the synthetic model.
- In situ temperature and pressure measurements documented overpressure and a low thermal gradient at Site U1324. Successful fluid pressure measurements yield  $\lambda^*$  values between 0.2 and 0.6 at the end of the deployment:

$$\lambda^* = (P - P_h) / (\sigma_v - P_h),$$

where

$P$  = pressure,

$P_h$  = hydrostatic pressure, and

$\sigma_v$  = total vertical stress.

- A thermal gradient of 18.4°C/km was established for temperature data.

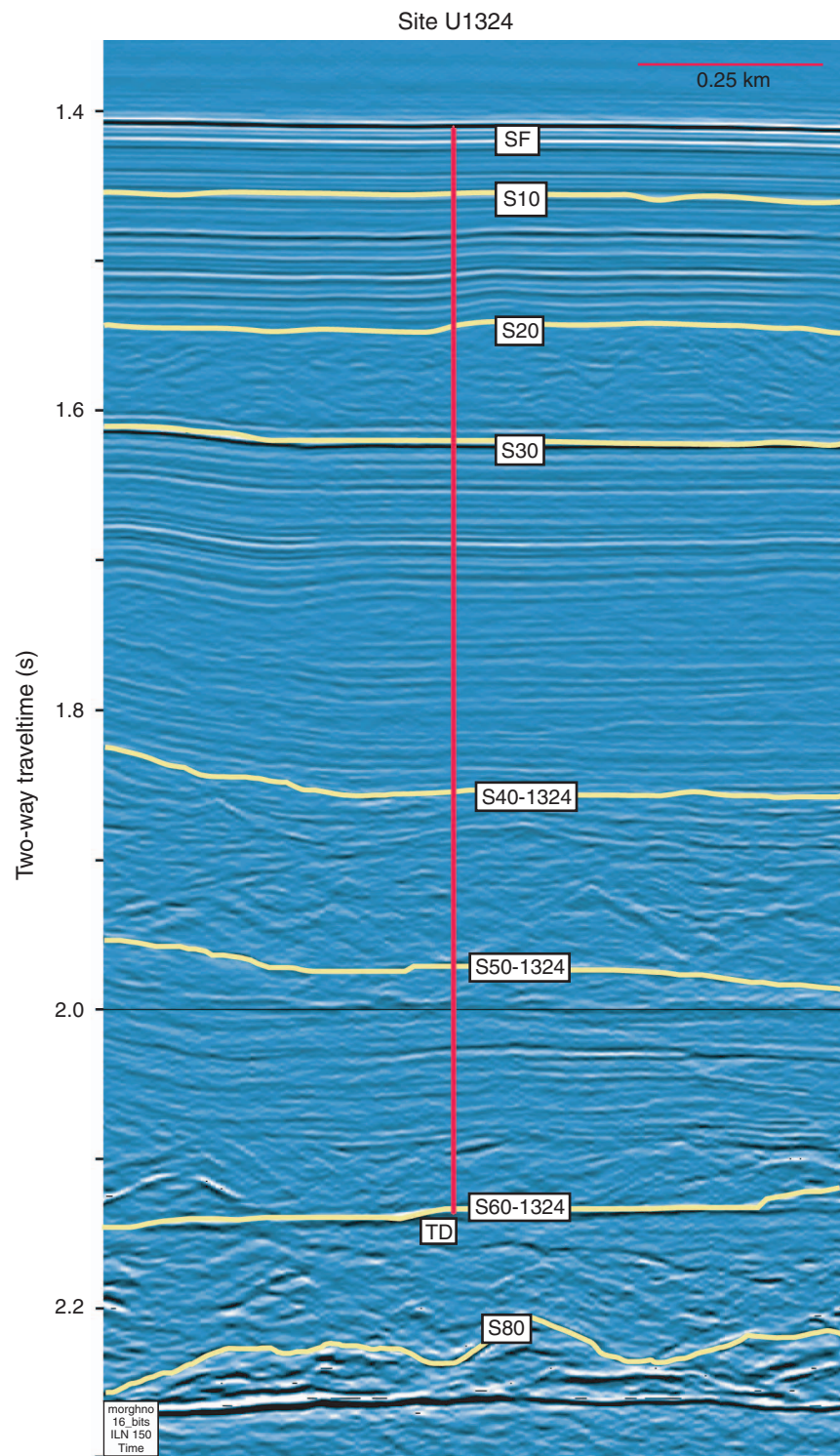
## References

- Bassinot, F.C., Labeyrie, L.D., Vincent, E., Quidelleur, X., Shackleton, N.J., and Lancelot, Y., 1994. The astronomical theory of climate and the age of the Brunhes-Matuyama magnetic reversal. *Earth Planet. Sci. Lett.*, 126:91–108. doi:10.1016/0012-821X(94)90244-5
- Berggren, W.A., Hilgen, F.J., Langereis, C.G., Kent, D.V., Obradovich, J.D., Raffi, I., Raymo, M.E., and Shackleton, N.J., 1995. Late Neogene chronology: new perspectives in high-resolution stratigraphy. *Geol. Soc. Am. Bull.*, 107:1272–1287. doi:10.1130/0016-7606(1995)107<1272:LNCNPI>2.3.CO;2
- Cisowski, S.M., and Hall, F.R., 1997. An examination of the paleointensity record and geomagnetic excursions recorded in Leg 155 cores. In Flood, R.D., Piper, D.J.W., Klaus, A., and Peterson, L.C. (Eds.), *Proc. ODP, Sci. Results*, 155: College Station, TX (Ocean Drilling Program), 231–243.
- Clark, H.C., and Kennett, J.P., 1973. Paleomagnetic excursions recorded in latest Pleistocene deep-sea sediments, Gulf of Mexico. *Earth Planet. Sci. Lett.*, 19(2):267–274. doi:10.1016/0012-821X(73)90127-1
- Flood, R.D., Piper, D.J.W., Klaus, A., et al., 1995. *Proc. ODP, Init. Repts.*, 155: College Station, TX (Ocean Drilling Program).
- Freed, W.K., and Healy, N., 1974. Excursions of the Pleistocene geomagnetic field recorded in Gulf of Mexico sediments. *Earth Planet. Sci. Lett.*, 24:99–104. doi:10.1016/0012-821X(74)90013-2
- Froelich, P.N., Klinkhammer, G.P., Bender, M.L., Luedtke, N.A., Heath, G.R., Cullen, D., Dauphin, P., Hammond, D., Hartman, B., and Maynard, V., 1979. Early oxidation of organic matter in pelagic sediments of the eastern equatorial Atlantic: suboxic diagenesis. *Geochim. Cosmochim. Acta*, 43(7):1075–1090. doi:10.1016/0016-7037(79)90095-4
- Hine, H., and Weaver, P.P., 1998. Quaternary. In Bown, P.R. (Ed.), *Calcareous Nannofossil Biostratigraphy*: Dordrecht, The Netherlands (Kluwer Academic Publ.), 266–283.
- Jasper, J.P., and Gagosian, R.B., 1990. The sources and deposition of organic matter in the Late Quaternary Pigmy Basin, Gulf of Mexico. *Geochim. Cosmochim. Acta*, 54:1117–1132. doi:10.1016/0016-7037(90)90443-O
- Kennett, J.P., and Huddlestun, P., 1972. Late Pleistocene paleoclimatology, foraminiferal biostratigraphy, and tephrochronology, western Gulf of Mexico. *Quat. Res.*, 2:38–69. doi:10.1016/0033-5894(72)90004-X
- Kvenvolden, K.A., and Barnard, L.A., 1983. Gas hydrates of the Blake Outer Ridge, Site 533, Deep Sea Drilling Project Leg 76. In Sheridan, R.E., Gradstein, F.M., et al., *Init. Repts. DSDP*, 76: Washington (U.S. Govt. Printing Office), 353–365.
- Mallarino, G., Droxler, A.W., Beaubouef, R.T., Abreu, V., and Laberye, L., in press. Sea level influence on the nature and timing of a mini-basin sedimentary fill (northwestern slope of the Gulf of Mexico). *AAPG Bull.*
- Piper, D.J.W., and Deptuck, M., 1997. Fined-grained turbidites of the Amazon Fan: facies characterization and interpretation. In Flood, R.D., Piper, D.J.W., Klaus, A., and Peterson, L.C. (Eds.), *Proc. ODP, Sci. Results*, 155: College Station, TX (Ocean Drilling Program), 79–108.
- Pirmez, C., and Isram, J., 2003. Reconstruction of turbidity currents in Amazon Channel. *Mar. Petrol. Geol.*, 20(6–8):823–849. doi:10.1016/j.marpetgeo.2003.03.005
- Rider, M., 1996. *The Geological Interpretation of Well Logs* (2nd ed.): Caithness (Whittles Publishing).
- Stupavsky, M., and Gravenor, C.P., 1984. Paleomagnetic dating of Quaternary sediments: a review. In Mahaney, W.C. (Ed.), *Quaternary Dating Methods*: Amsterdam (Elsevier).
- van Hinsbergen, D.J.J., Kouwenhoven, T.J., and van der Zwaan, G.J., 2005. Paleobathymetry in the backstripping procedure: correction for oxygenation effects on depth estimates. *Palaeogeogr., Palaeoclimatol., Palaeocol.*, 221(3–4):245–265. doi:10.1016/j.palaeo.2005.02.013
- von Dobeneck, T., and Schmieder, F., 1999. Using rock magnetic proxy records for orbital tuning and extended time series analysis into the super- and sub-Milankovitch bands. In Fischer, G., and Wefer, G. (Eds.), *Use of Proxies in Paleoceanography: Examples from the South Atlantic*: Heidelberg (Springer-Verlag), 601–633.
- Winker, C.D., and Shipp, R.C., 2002. Sequence stratigraphic framework for prediction of shallow water flow in the greater Mars-Ursa area, Mississippi Canyon area, Gulf of Mexico continental slope [22nd Annual GCSSEPM Foundation Bob F. Perkins Research Conference, Houston, TX, 8–11 December, 2002]. (Abstract)

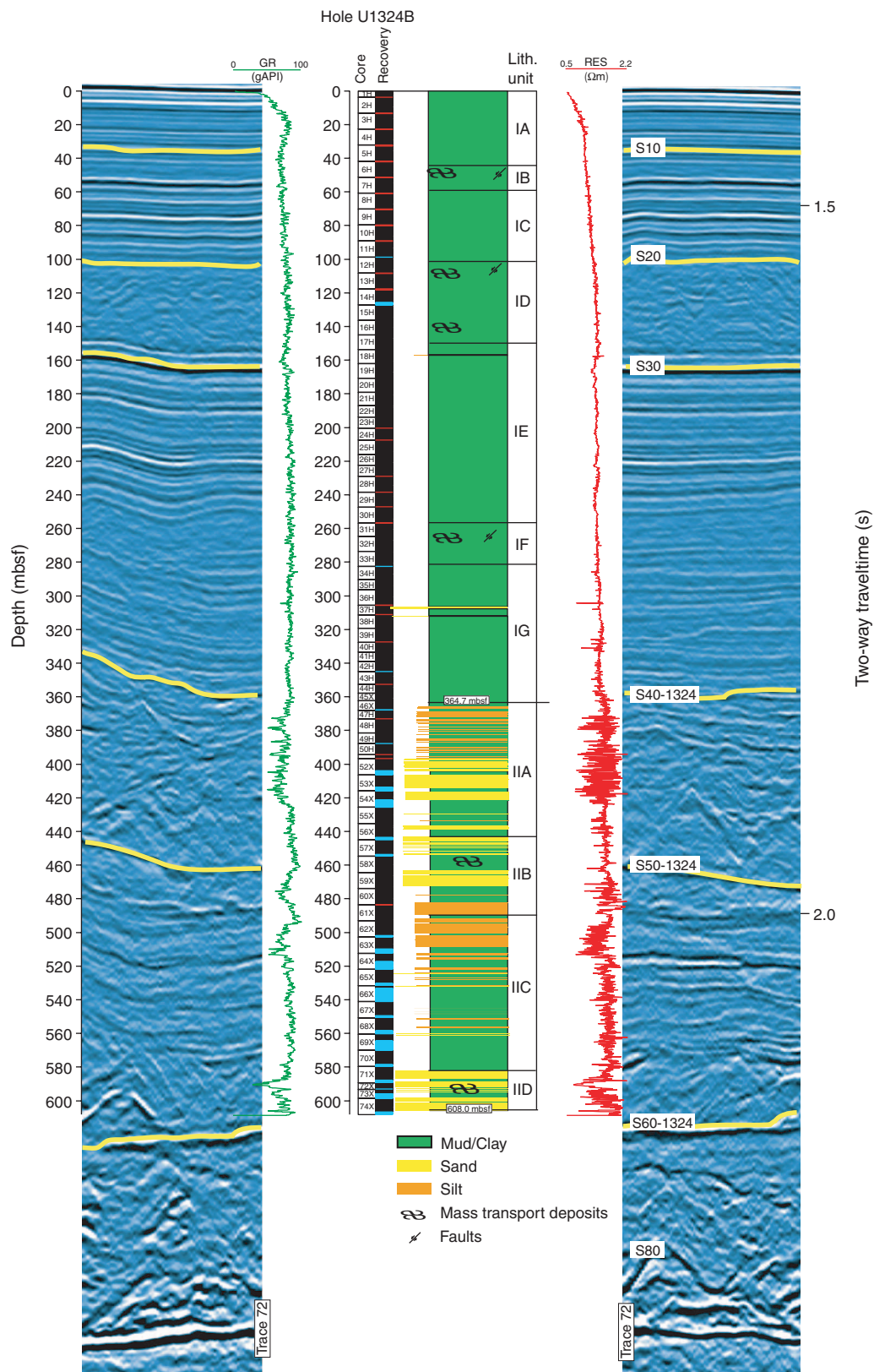
Publication: 8 July 2006  
MS 308-108



Figure F1. Seismic strip chart, Site U1324. TD = total depth.



**Figure F2.** Lithostratigraphic summary with gamma ray (GR) and resistivity (RES) logs (LWD/MWD). Seismic panel was split at the location of Hole U1324B at Trace 72. Seismic data are approximately zero phase with peaks (black) and troughs (white) and are plotted in depth using the check shot generated from wireline logging in Hole U1324A. Key seismic reflectors are yellow/labeled.



**Figure F3.** Lithostratigraphic Subunit IA. A. Greenish brown to reddish brown clay interpreted to be hemipelagic deposits (Section 308-U1324B-1H-1; DIS image). B. Light greenish gray near the top and greenish gray at the bottom (interval 308-U1324B-1H-1, 18–42 cm). (Continued on next page.)

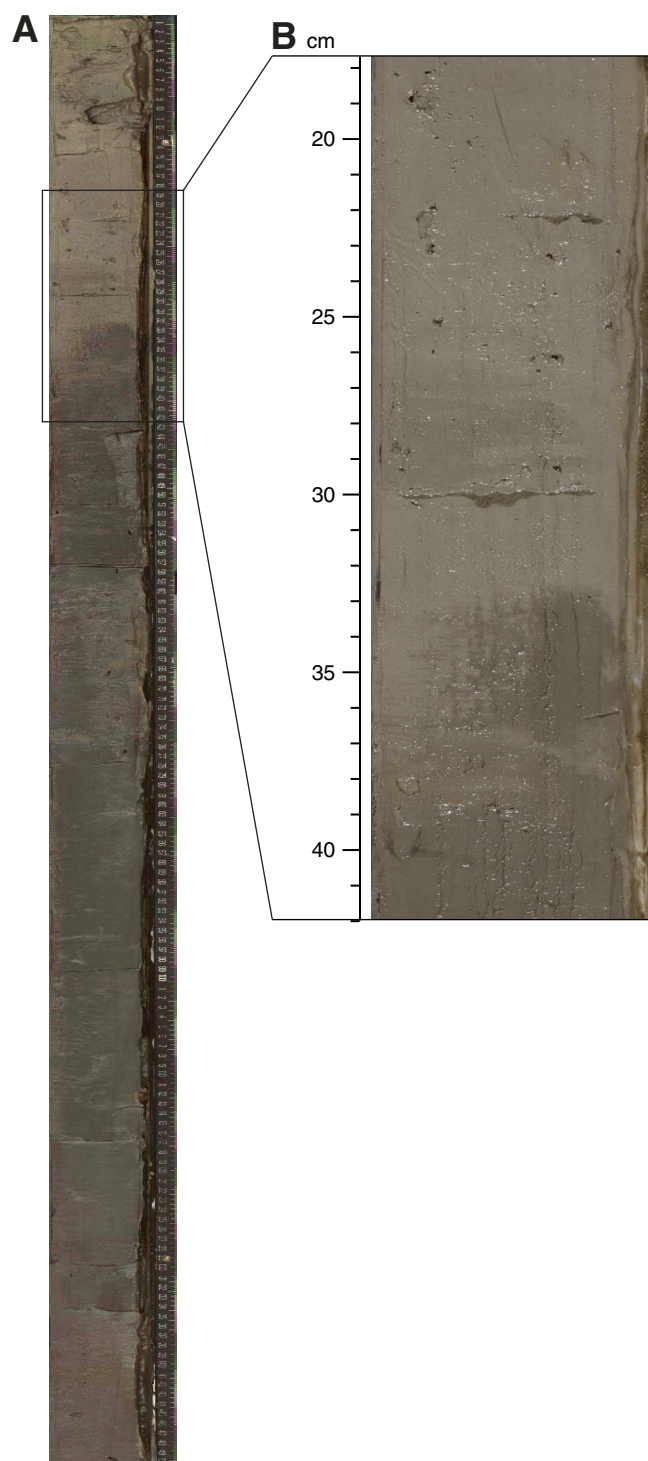


**Figure F3 (continued).** C. *Globigerina falconensis* in a foraminifer-rich clay (Sample 308-U1324B-1H-1, 20 cm). D. Foraminifer-rich clay with *Globigerina quinqueloba* in Subunit IA (Sample 308-U1324B-1H-1, 20 cm). E. Foraminifer-rich clay with *Globorotalia quinqueloba*, *Globorotalia siphonifera*, and *Bolivina spissa* in Subunit IA (Sample 308-U1324B-1H-1, 20 cm). F. Clay with sponge spicules in Subunit IA (Sample 308-U1324B-4H-4, 99.5 cm).

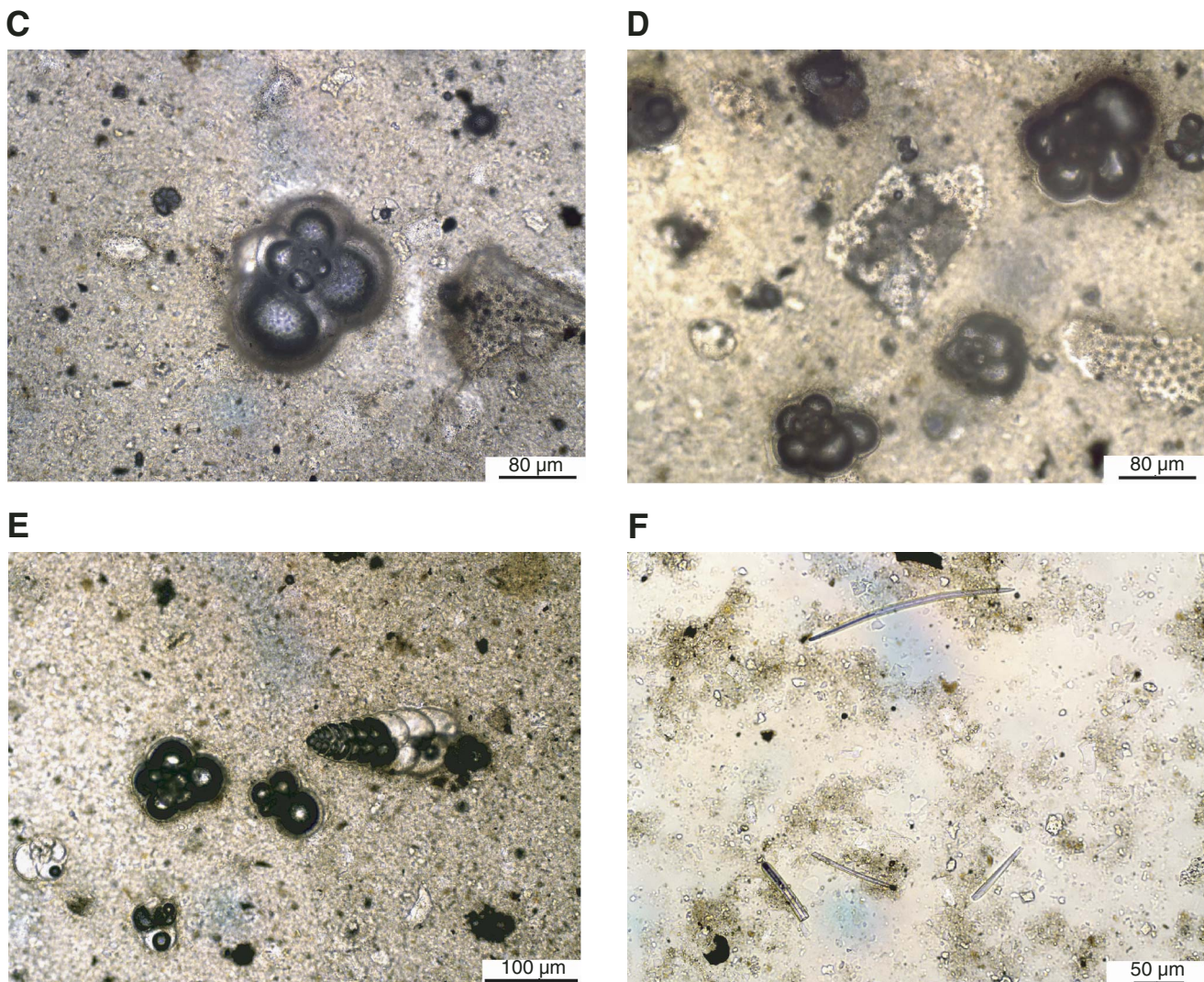


**Figure F4.** Gradation from dark gray to greenish gray and light gray clay in lithostratigraphic Subunit IB. A. Fault strike is  $124^\circ$  (interval 308-U1324B-6H-2, 41–64 cm). B. Fault strike is  $150^\circ$  with a dip of  $60^\circ$  NW (interval 308-U1324B-6H-5, 93–117 cm).



**Figure F5.** Alternation of greenish gray clay bands and light/dark clay laminae and thin beds in lithostratigraphic Subunit IC. A. Silt occurs as disrupted laminae (58 cm) and 44.5, 49.5, and 52 cm filled burrows (interval 308-U1324B-8H-4, 28–63 cm). B. Color-banded clay in interval 308-U1324B-10H-2, 72–108 cm.

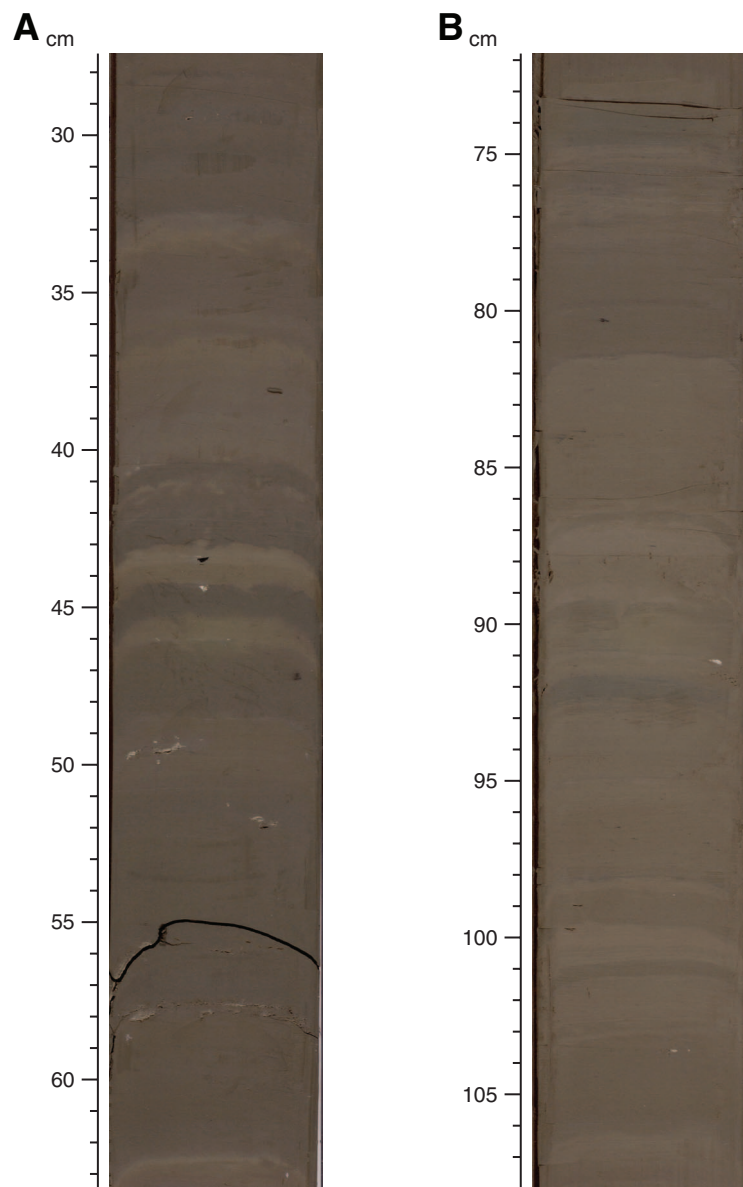


**Figure F6.** Couplets of greenish gray and brownish gray dipping beds in lithostratigraphic Subunit ID. A, B. Faults (intervals 308-U1324B-15H-2, 29–64 cm, and 15H-2, 8–32 cm). C. Dipping beds (interval 308-U1324B-13H-2, 98–134 cm).

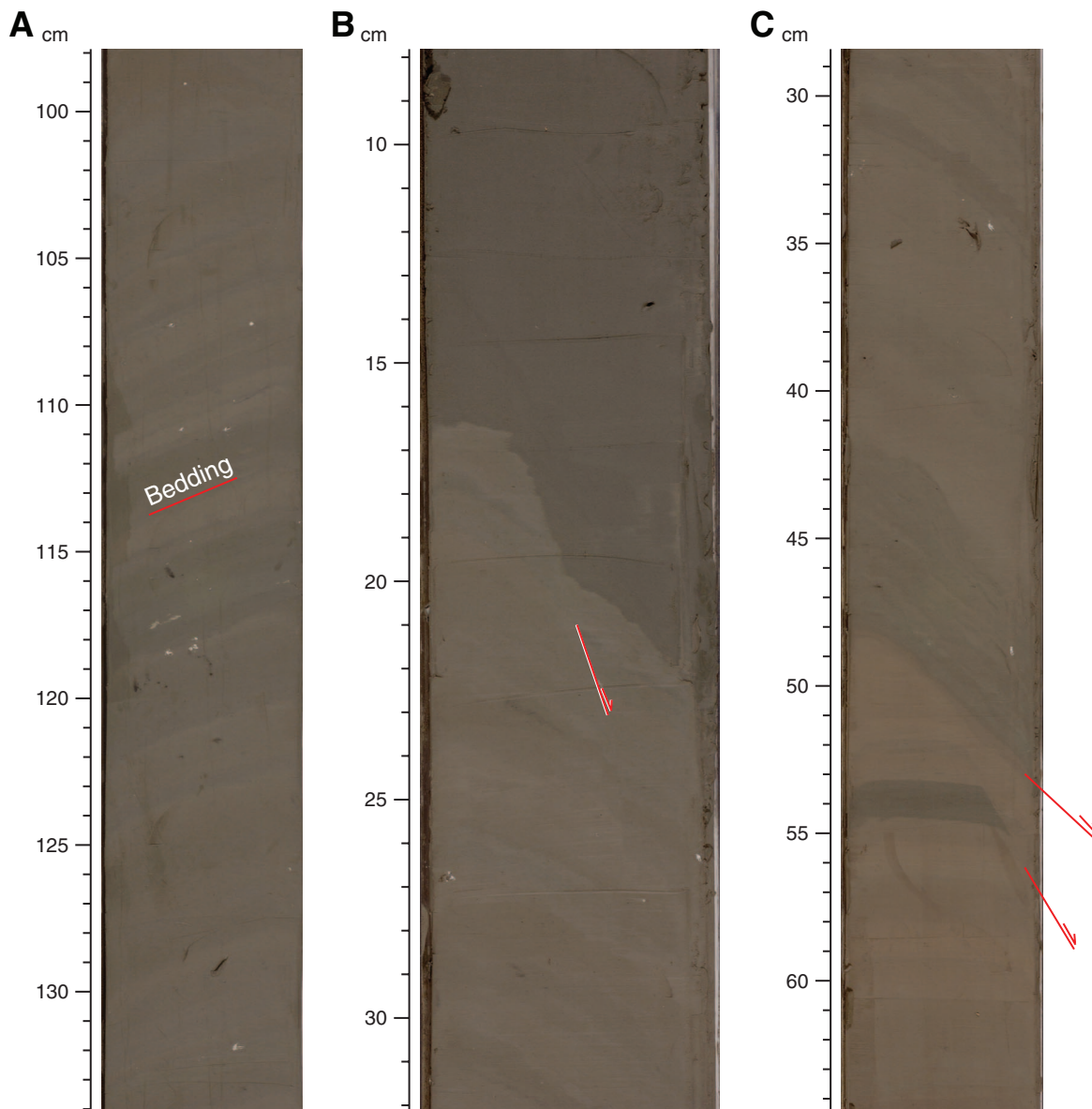


**Figure F7.** Fine-scale color banding in lithostratigraphic Subunit IE. A. Dark gray and brown (interval 308-U1324B-17H-4, 26–61 cm). B. Color changes at seismic Reflector S30 to reddish brown (308-U1324B-19H-3, 58–92 cm). C. Alternation of dark greenish gray and brownish clay layers (interval 308-U1324B-21H-4, 25–60 cm). D. Greenish brown clay, a reddish brown clay band at 60–74 cm with gradational color change, and mottled black clay (interval 308-U1324B-28H-2, 51–90 cm).

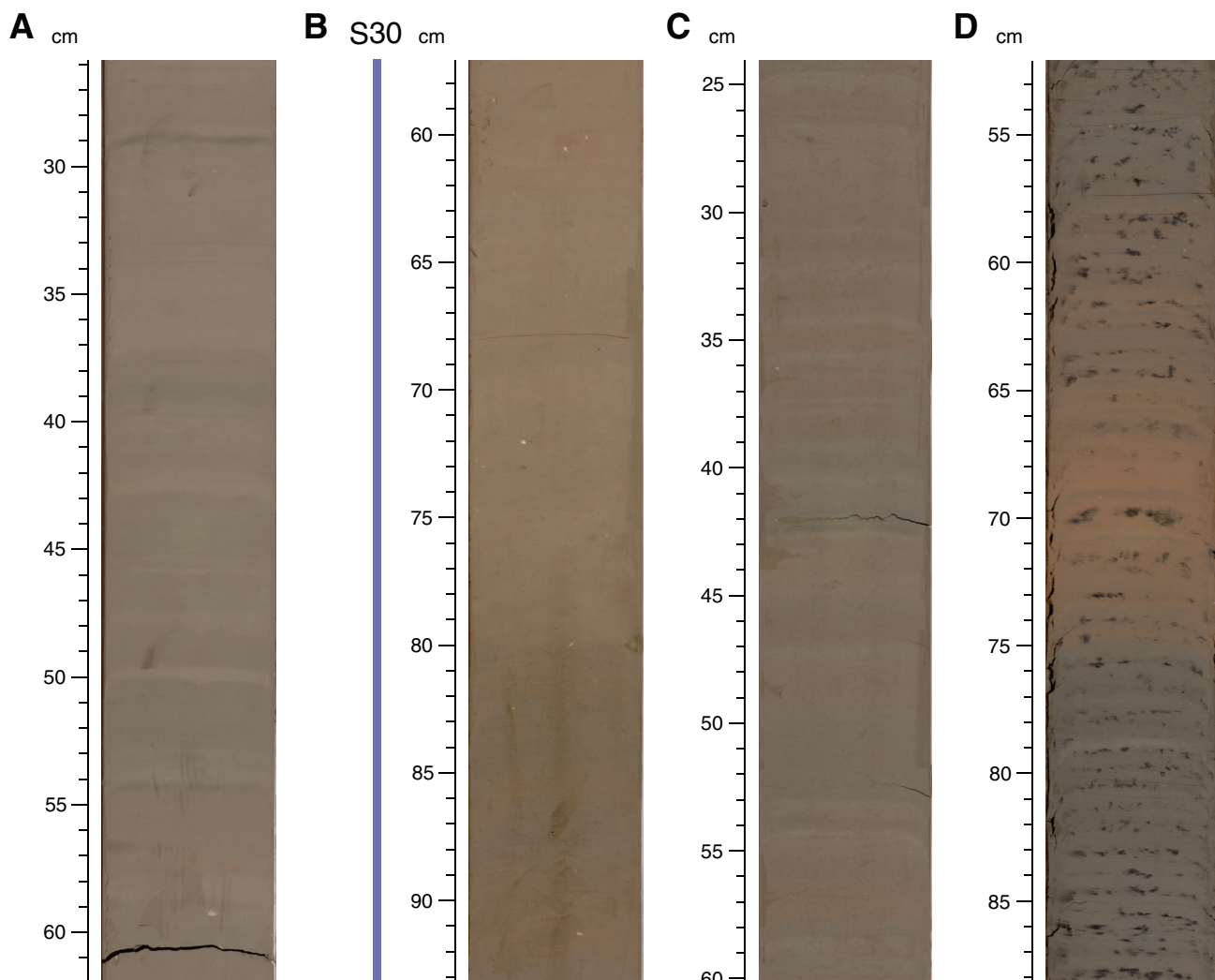


**Figure F8.** Green and brownish green clay alternating with black laminae in lithostratigraphic Subunit IF. A. Composite DIS image of Sections 308-U1324B-32H-1 through 32H-3, showing inclined beds strike N120E (upper), N140E (middle), and N125E (bottom) with a dip of 50°. B. Composite DIS image of Sections 308-U1324B-34H-2 through 34H-3, showing inclined beds that strike N150E (upper) to N40E (lower) with a dip of 90° (horizontal). Note that the composite DIS images do not display correct angles because it is vertically compressed. See Table T5 for measurements.

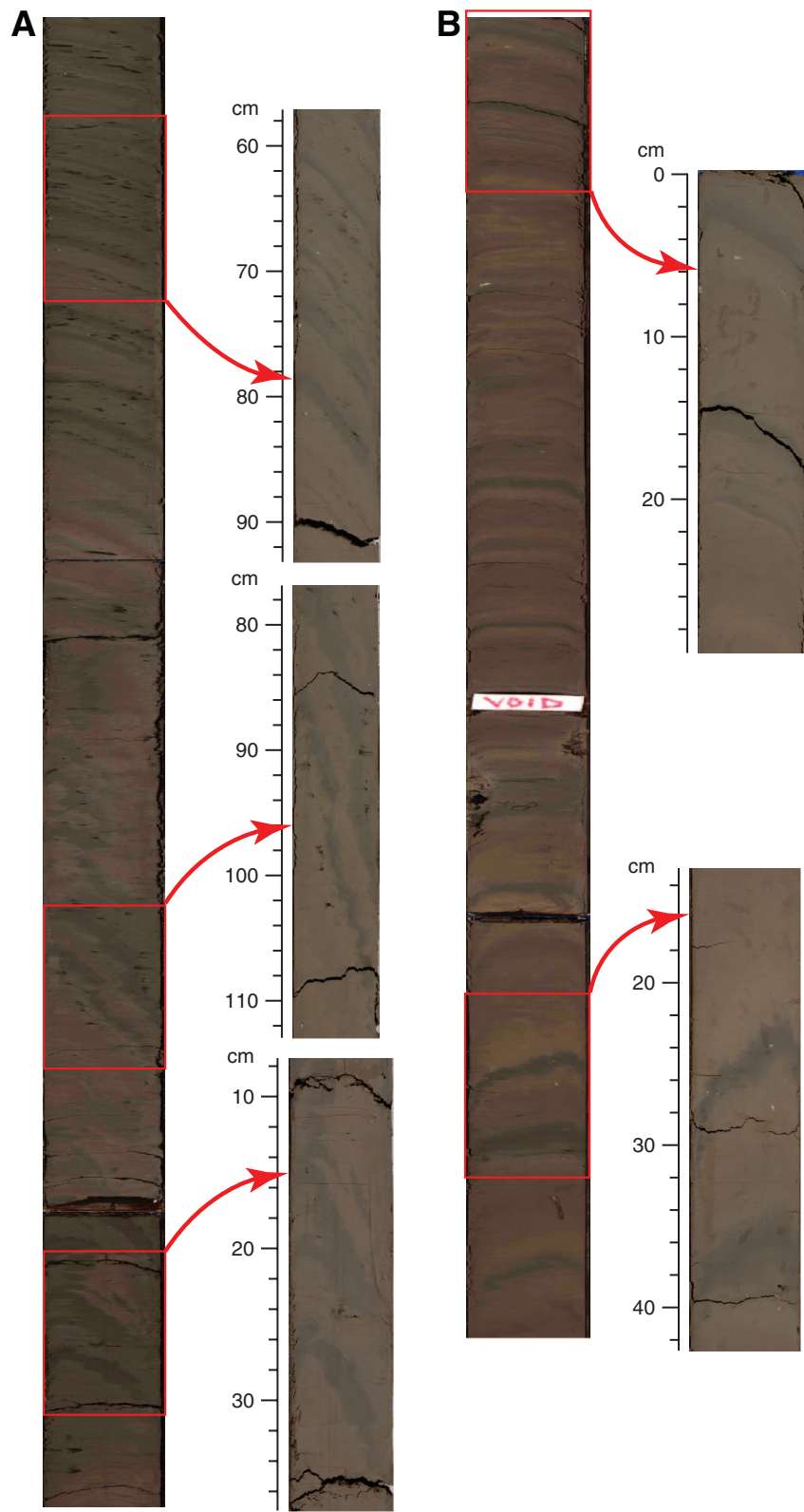


**Figure F9.** Lithostratigraphic Subunit IG. A. Lower medium sand (top), which could have resulted from flow-in from a thinner layer, and greenish gray clay with dark gray laminae (base) (Section 308-U1324B-37H-1; DIS image). B. Couplets of dark gray and lighter gray/brown clay with reddish bands with lighter gray clay and mottling throughout (Section 308-U1324B-40H-2; DIS image). C. Laminated silt bed with sharp base and top at 53–58 cm (interval 308-U1324B-40H-2, 40–76 cm). D. Lamination of greenish gray and reddish brown clay (interval 308-U1324B-44H-1, 68–103 cm). Note that DIS images do not reproduce exact sediment color.

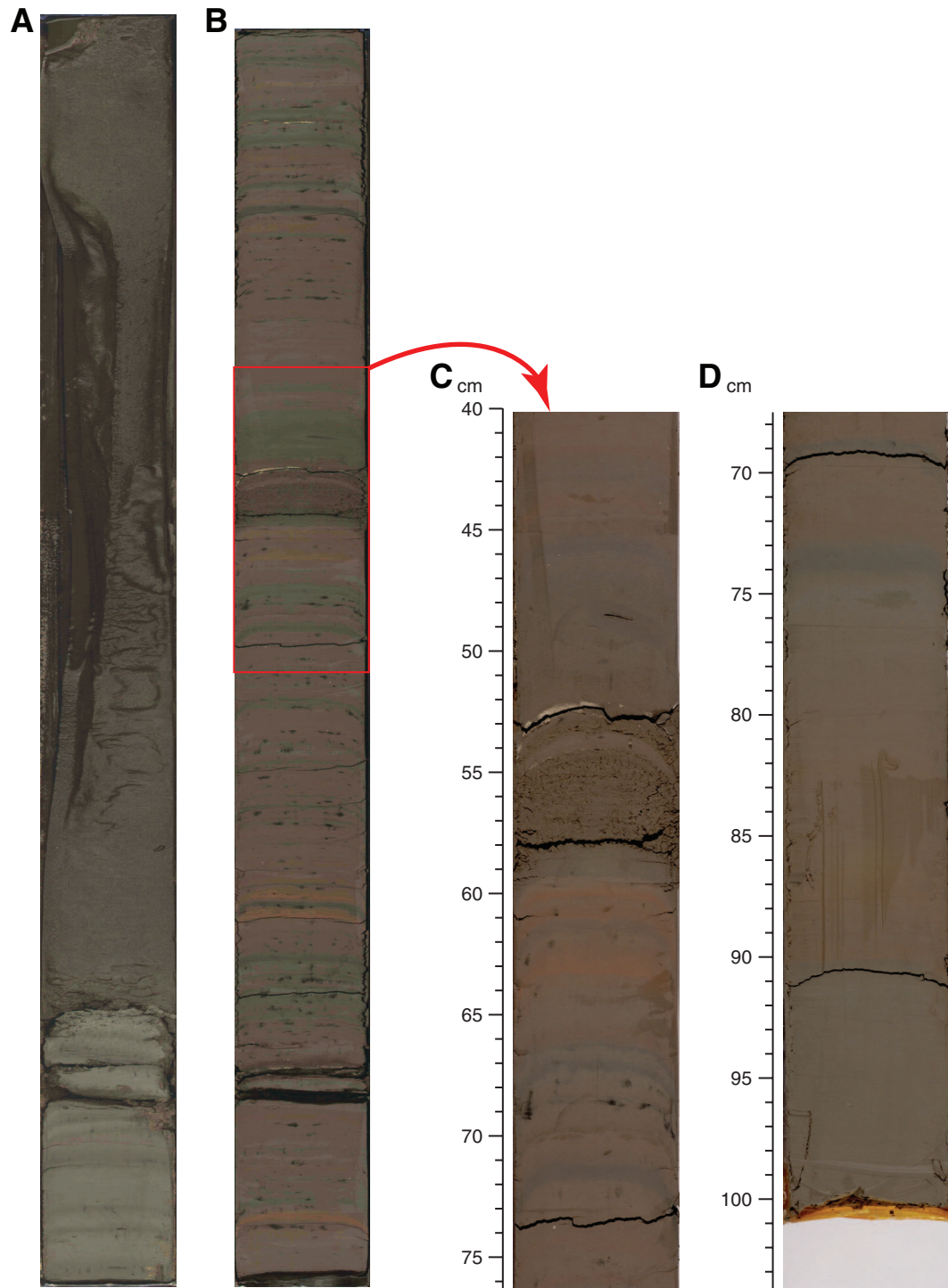


**Figure F10.** Lithostratigraphic Subunit IIA. A. Dark greenish gray and brown mud and silt as fining-upward beds with couplets of silt and mud (Core 308-U1324B-46X). B. Laminated silt bed interpreted as a distal turbidite at 109–132 cm (interval 308-U1324B-46X-2, 102–138 cm). C. Photographic detail of silt (Core 308-U1324B-50X). D. Interbedded clay and silt in gray and medium brown clay (interval 308-U1324B-50X-2, 71–106 cm; DIS image). Note that DIS images do not reproduce exact sediment color.

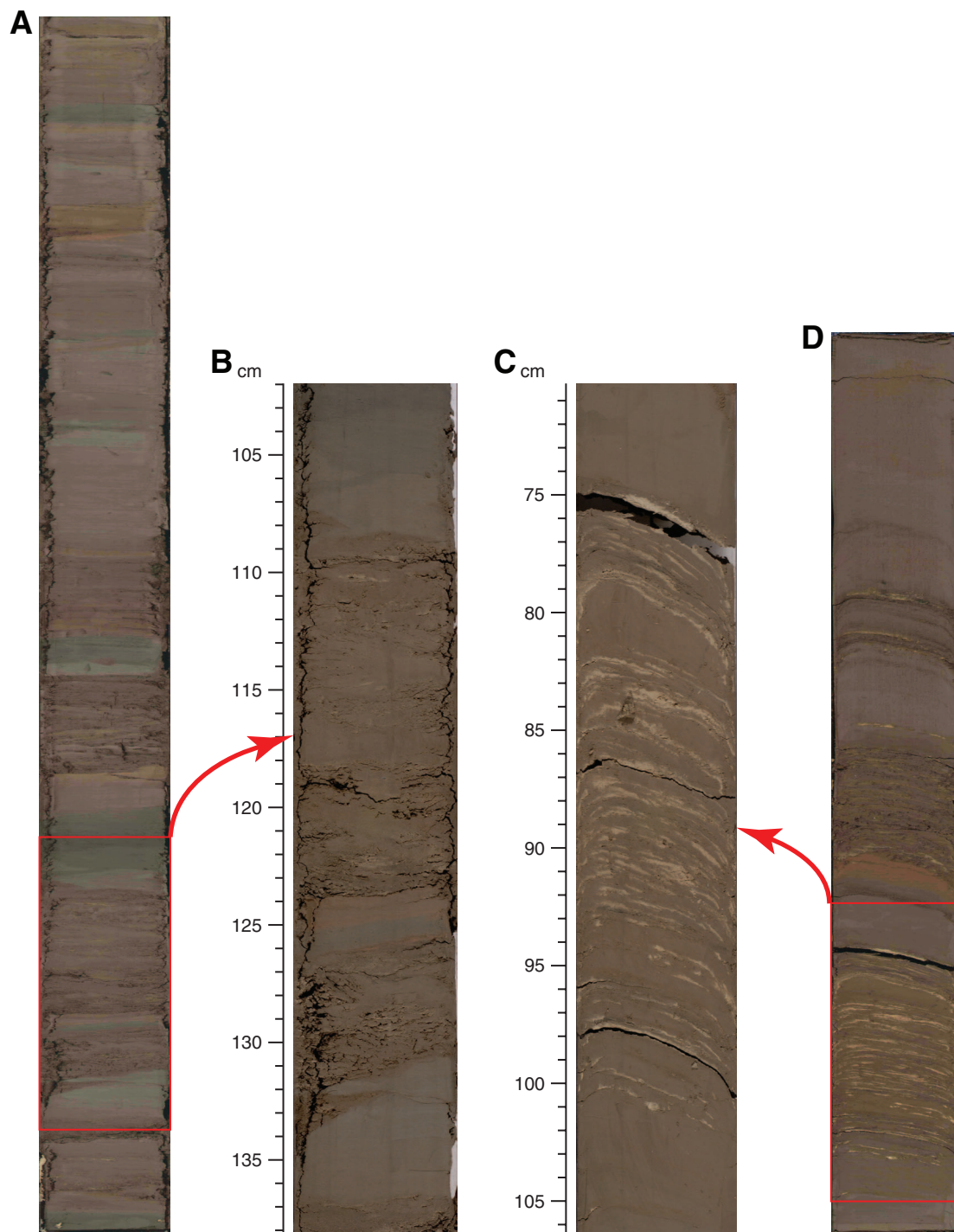


**Figure F11.** Mass transport deposits showing biscuits by drilling disturbance and folds in all sections of lithostratigraphic Subunit IIB. A, B. Interbedding of silty sand and gray and brownish clay (intervals 308-U1324B-57X-1, 35–75 cm, and 57X-2, 118–150 cm). C, D. Greenish gray mud, showing contorted bedding and interbedded silt and sand (intervals 308-U1324B-59X-2, 48–83 cm, and 59X-7, 98–132 cm).

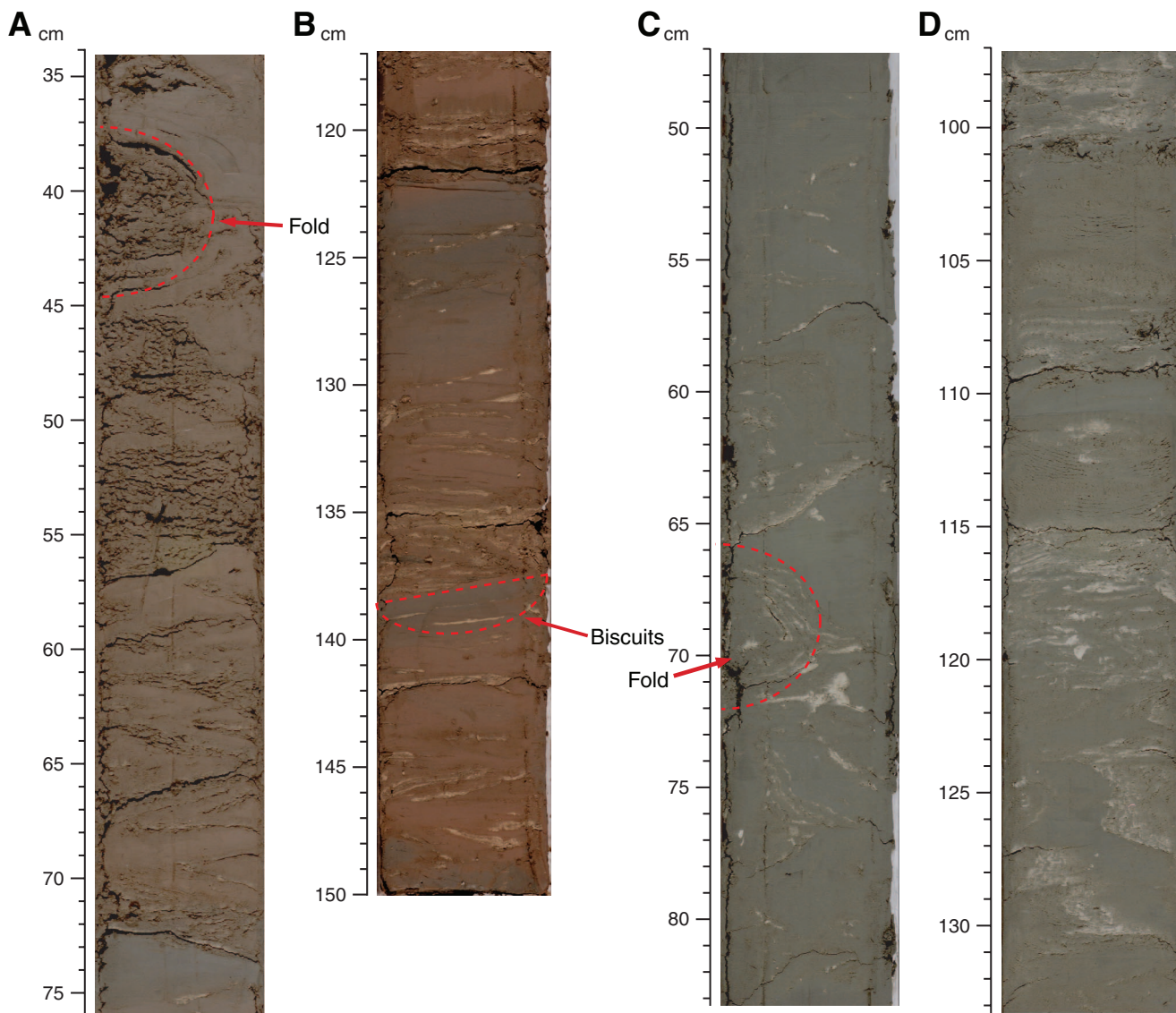


**Figure F12.** Lithostratigraphic Subunit IIC. A. Green and reddish brown clay interbedded with silt beds (Core 308-U1324B-62X; DIS image). B. Sequence consisting of brown silt with a sharp base at 74 cm, fining upward to greenish mud with laminae and reddish mud at the top (interval 308-U1324B-62X-5, 44–80 cm). C. Interbeds of greenish gray mud and silt (Core 308-U1324B-64X; DIS image). D. Normally graded silt beds and laminae at 122–128 cm (interval 308-U1324B-64X-4, 114–137 cm). E. Laminated silty sand bed with quartz and calcite in Subunit IIC (Sample 308-U1324B-63X-5, 82 cm).

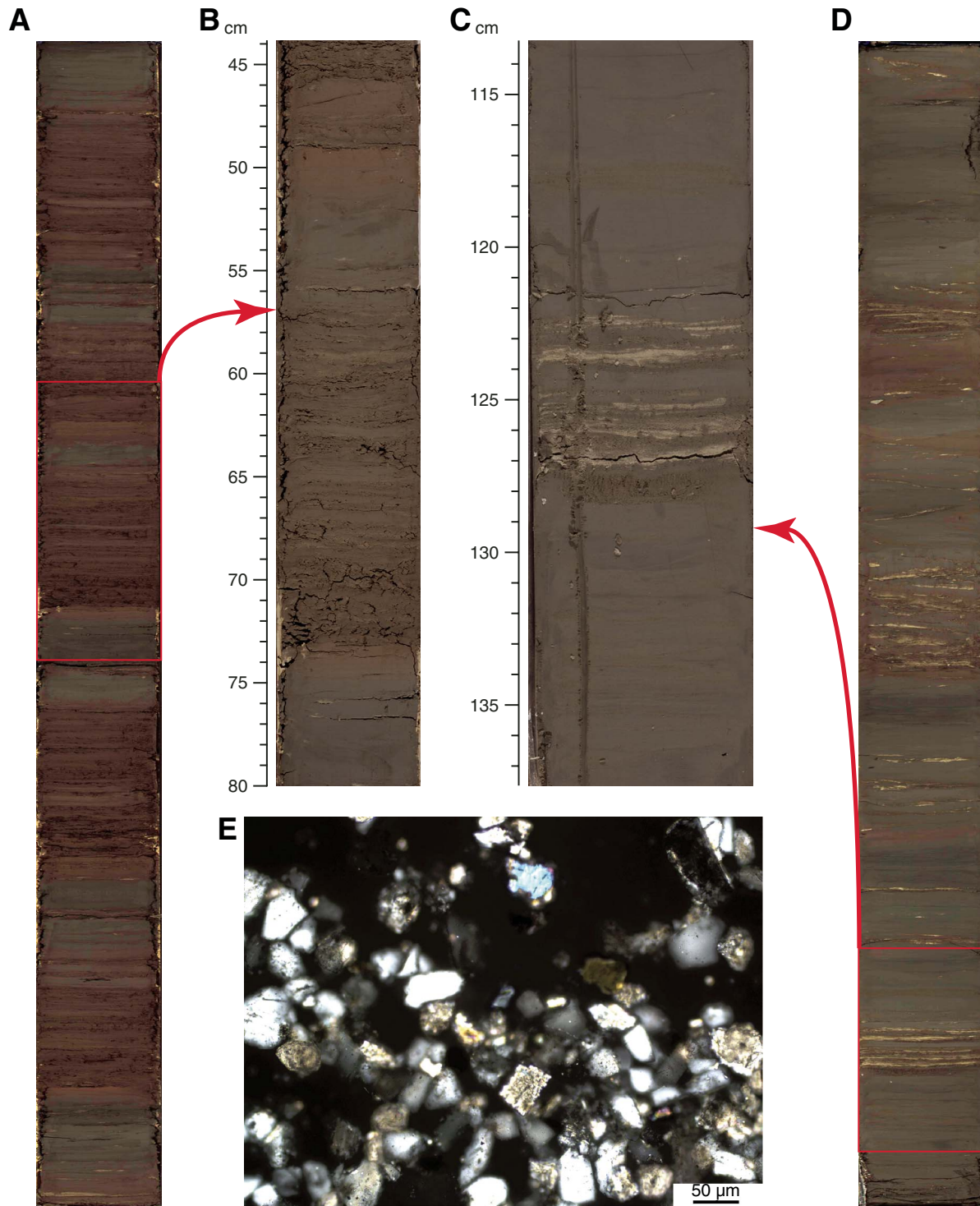


**Figure F13.** Mass transport deposits characterized by greenish gray contorted mud bedding and sand as irregular lenses and laminae in lithostratigraphic Subunit IID. A, B. Intervals 308-U1324B-73X-1, 38–67 cm, and 73X-1, 118–140 cm. C, D. Intervals 308-U1324B-74X-1, 88–120 cm, and 74X-2, 96–132 cm. XCB biscuiting is particularly pronounced in these images.

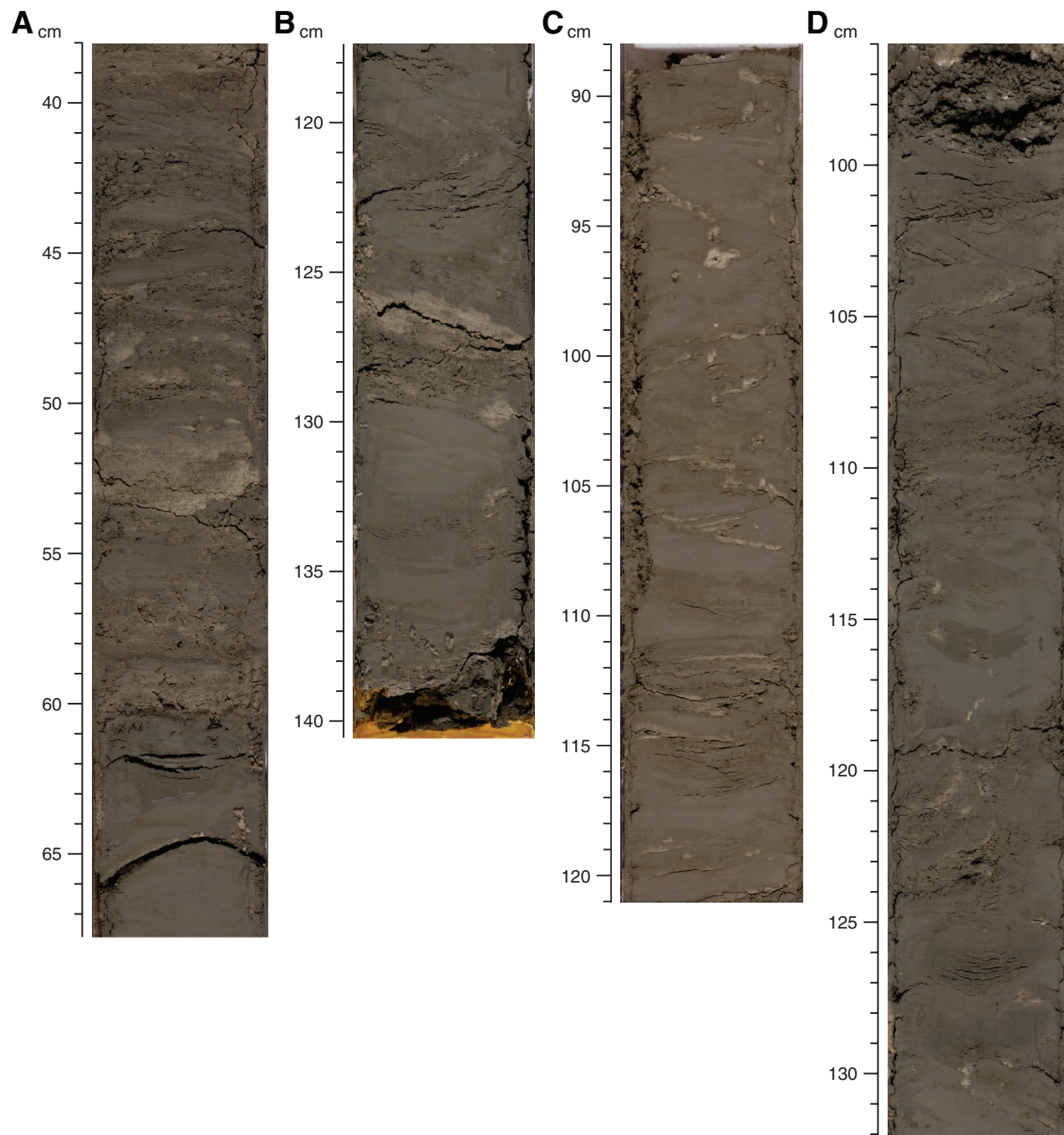


**Figure F14.** Summary of smear slide analysis showing dominant and minor lithologic components.

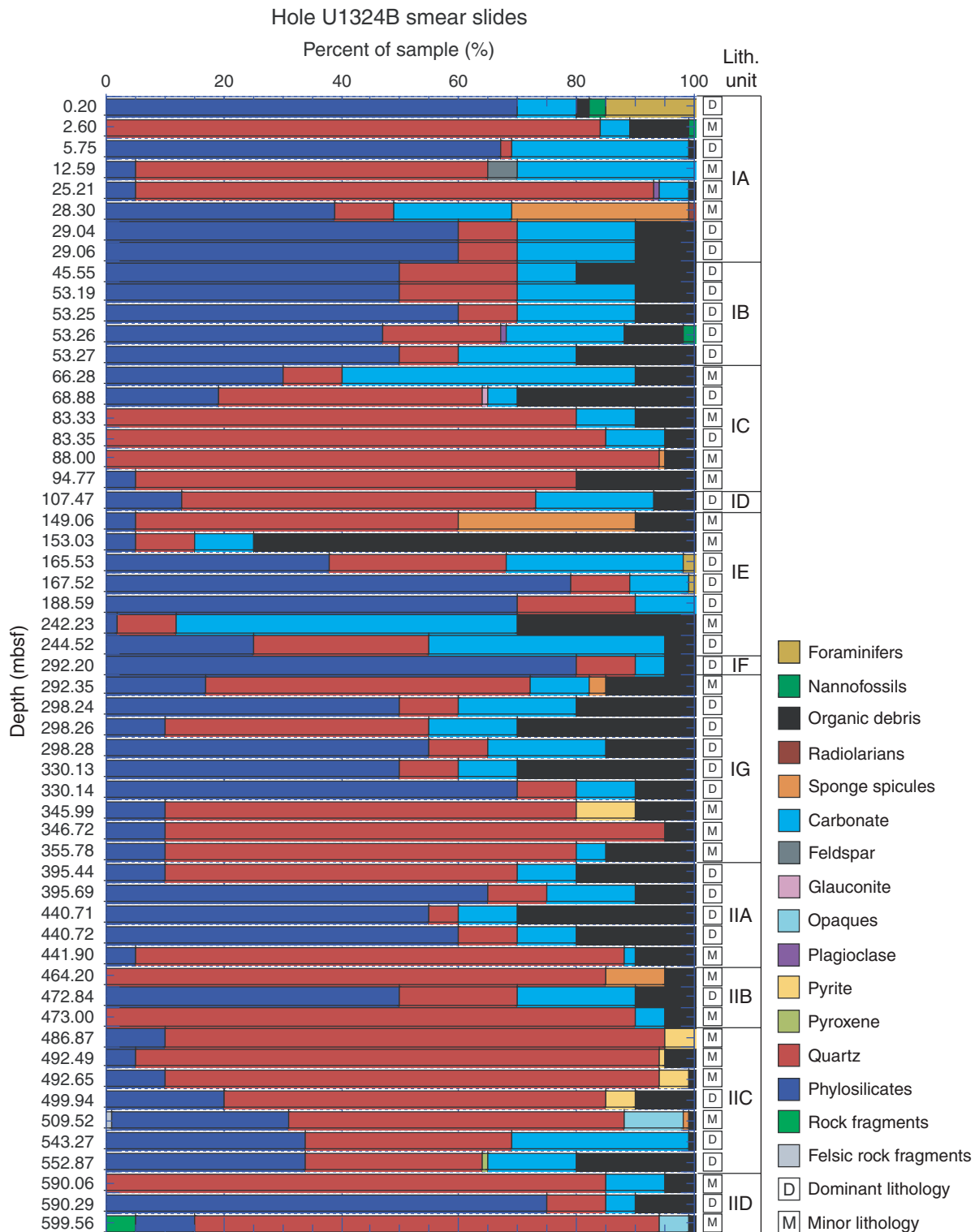


**Figure F15.** Results of the XRD analysis of two samples from Subunit IC. A. Boundary between greenish and reddish clay (Section 308-U1324B-10H-6). B. XRD multiple diagram shows nearly identical results for single samples from the green clay and from the red clay. Note that the black line has background counts removed and green line has background counts retained in order to compare the two curves.

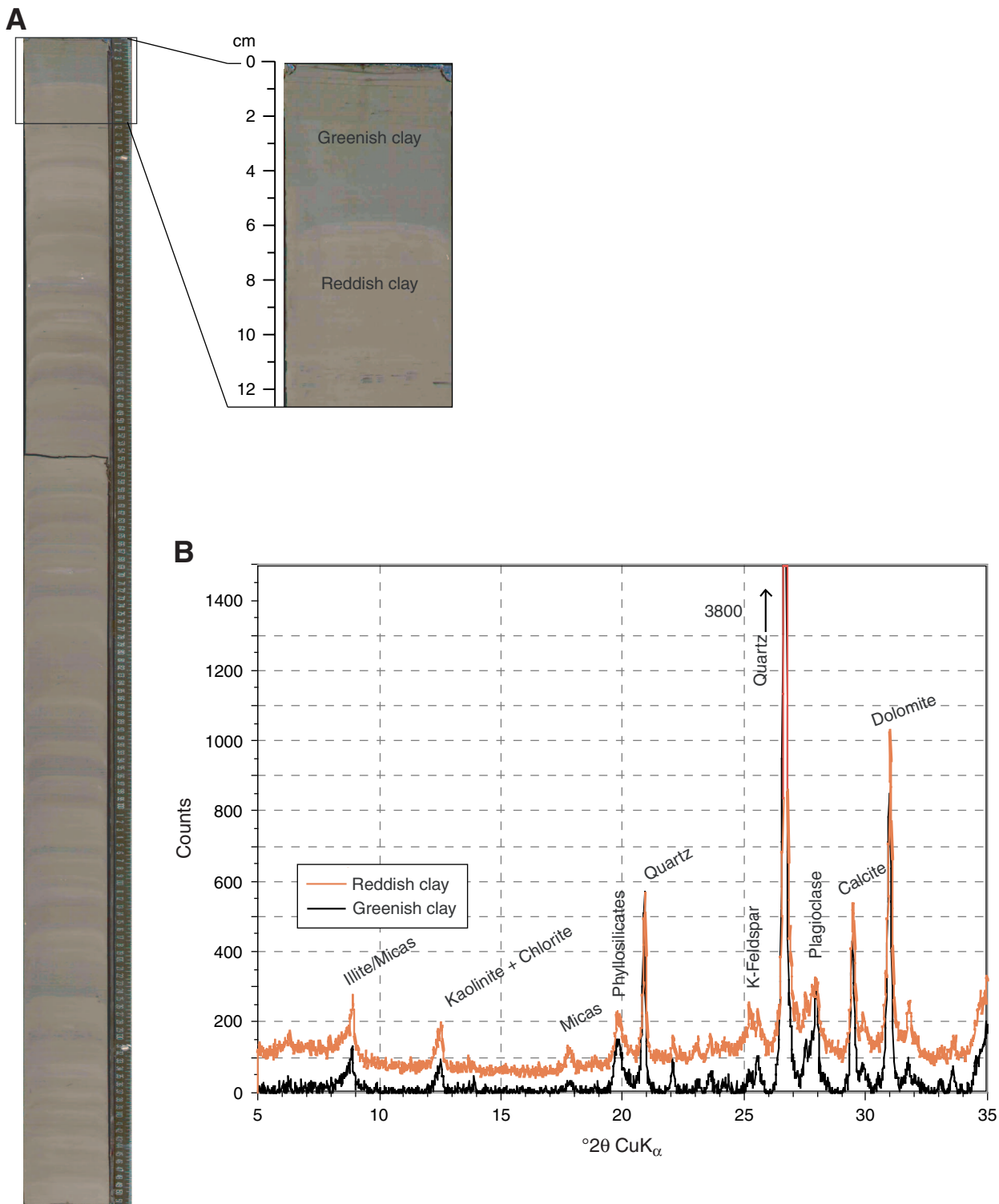


**Figure F16.** Biostratigraphic summary for Site U1324 with nannofossil and planktonic foraminifer zones and benthic foraminifer assemblages, gamma ray (GR) and resistivity (RES), seismic reflectors, natural remanent magnetization after 20 mT AF demagnetization ( $NRM_{20mT}$ ), and lithostratigraphy (see “[Lithostratigraphy](#)” and “[Paleomagnetism](#)”).

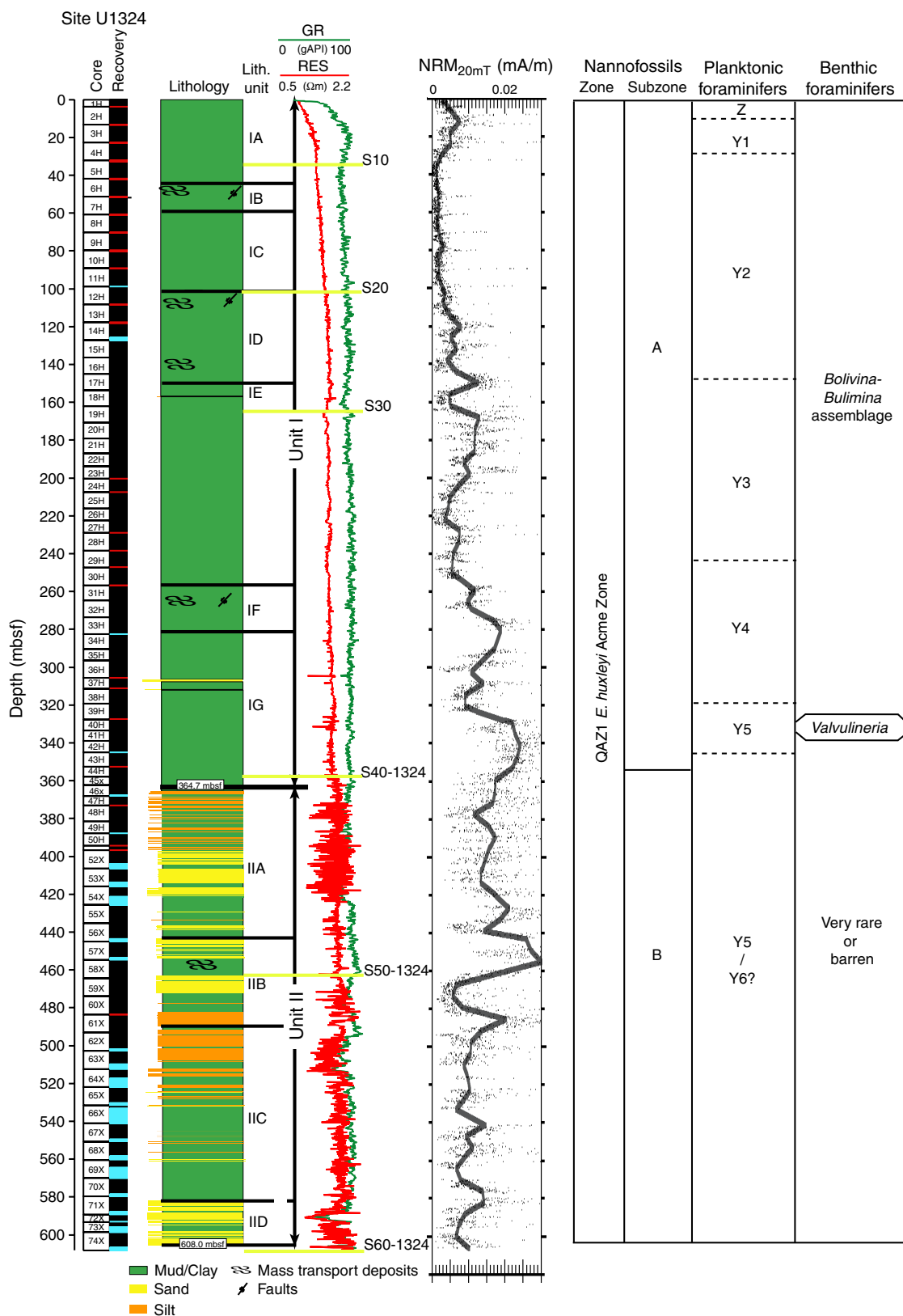
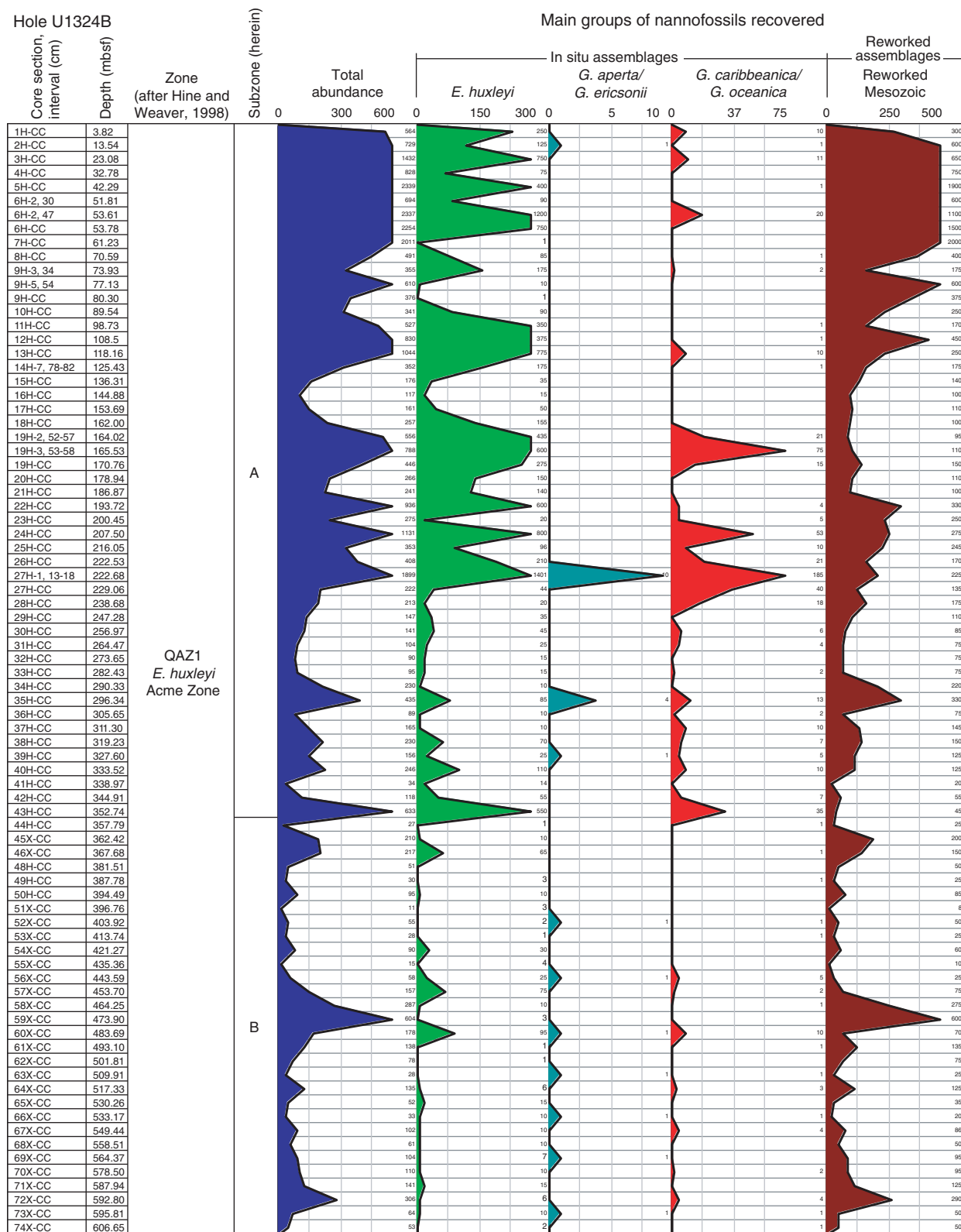
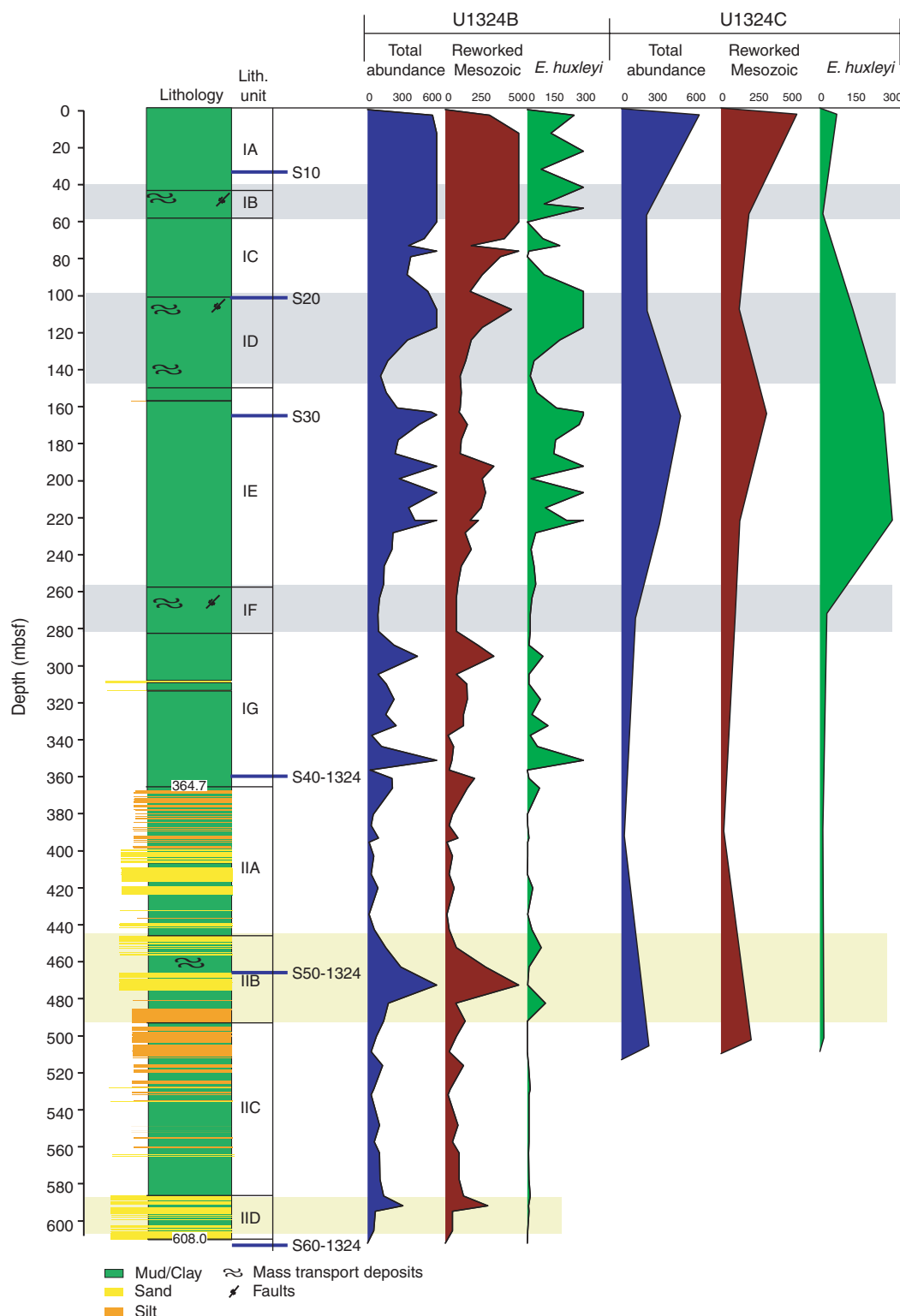


Figure F17. Distribution of stratigraphically important nannofossil groups in Hole U1324B.



**Figure F18.** Distribution of stratigraphically important nannofossil groups in Holes U1324B and U1324C with lithostratigraphy from Hole U1324B. Note that high abundances of reworked Mesozoic nannofossils correlate well with mass transport deposits (shaded).



**Figure F19.** General distribution of nannofossils from Hole U1324B, showing the sporadic pattern for most species. Nannofossil zonation is given.

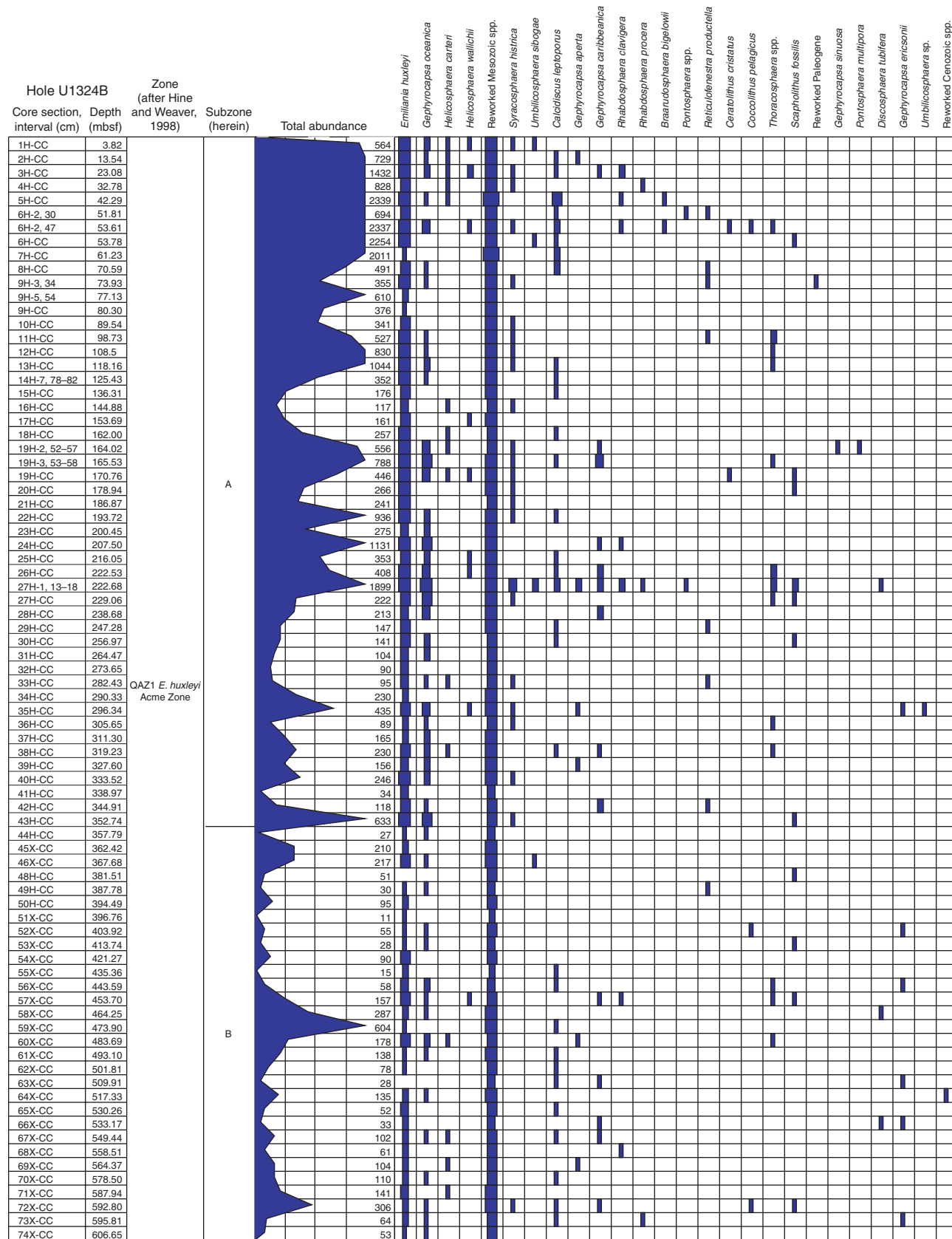


**Figure F20.** General distribution of nannofossils from Hole U1324C, showing the sporadic pattern for most species. Nannofossil zonation is given.

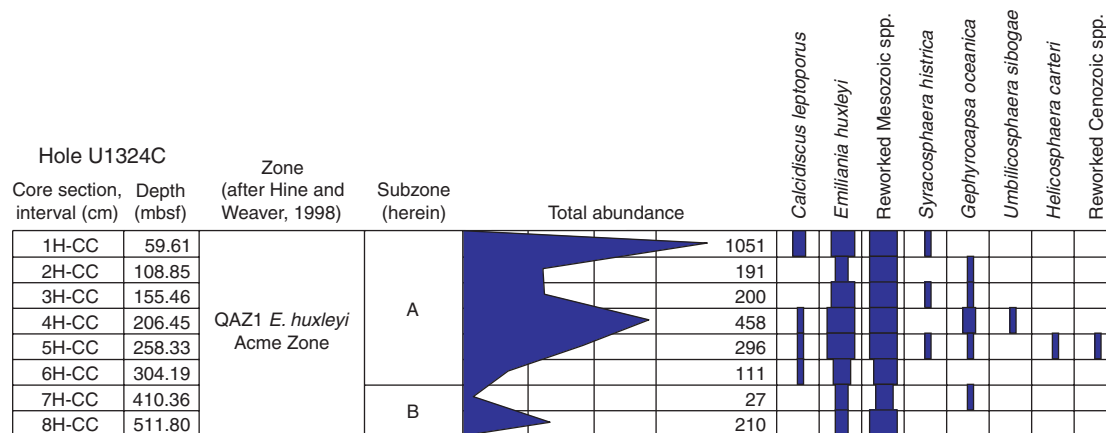


**Figure F21.** Planktonic foraminifer biostratigraphy and abundance of selected taxa from Hole U1324B along with lithostratigraphic units, seismic reflectors, and marine isotopic stages (MIS).

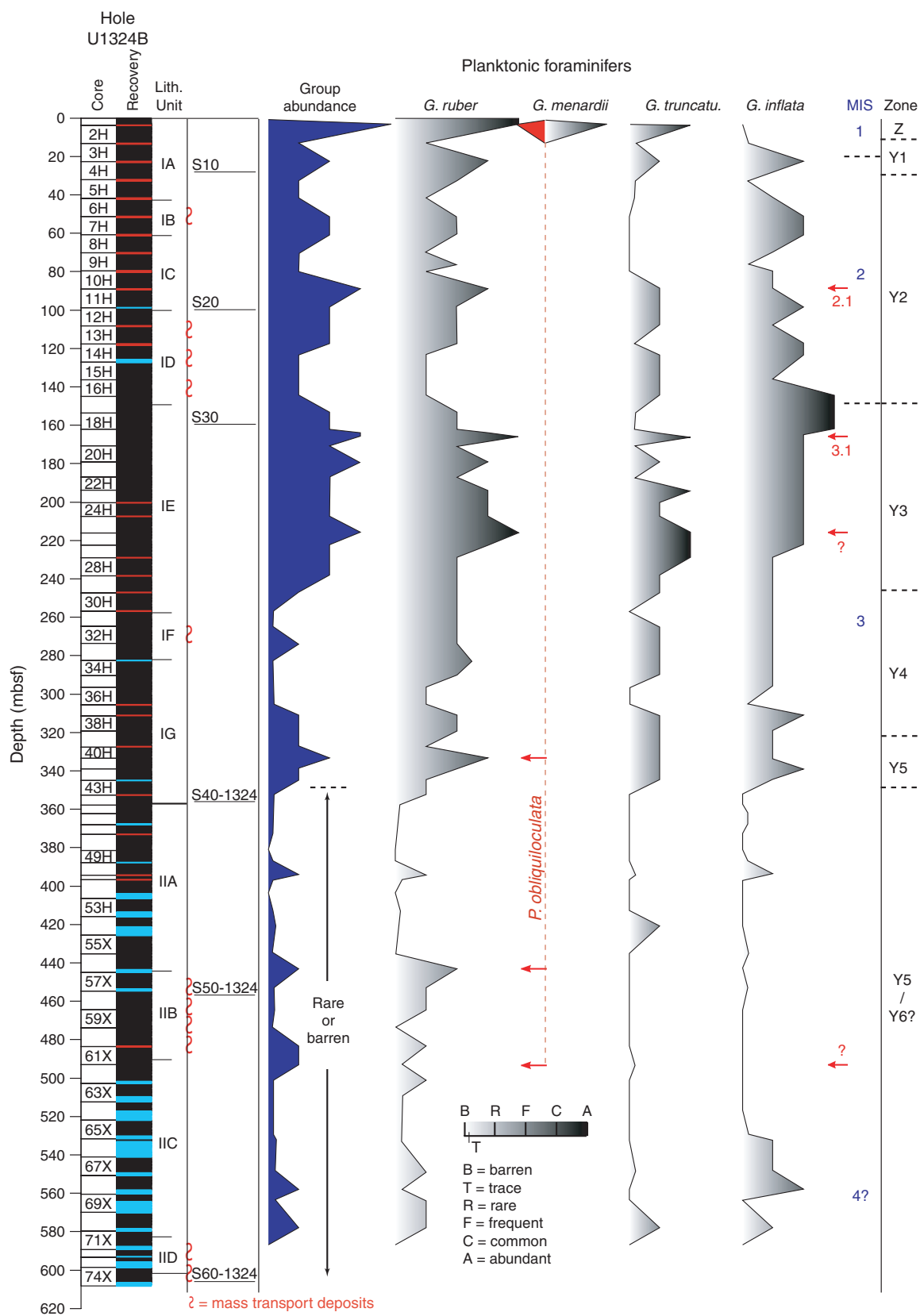


**Figure F22.** Distribution of selected epifaunal and infaunal benthic foraminifer species from Hole U1324B along with lithostratigraphic units, seismic reflectors, and marine isotopic stages (MIS).

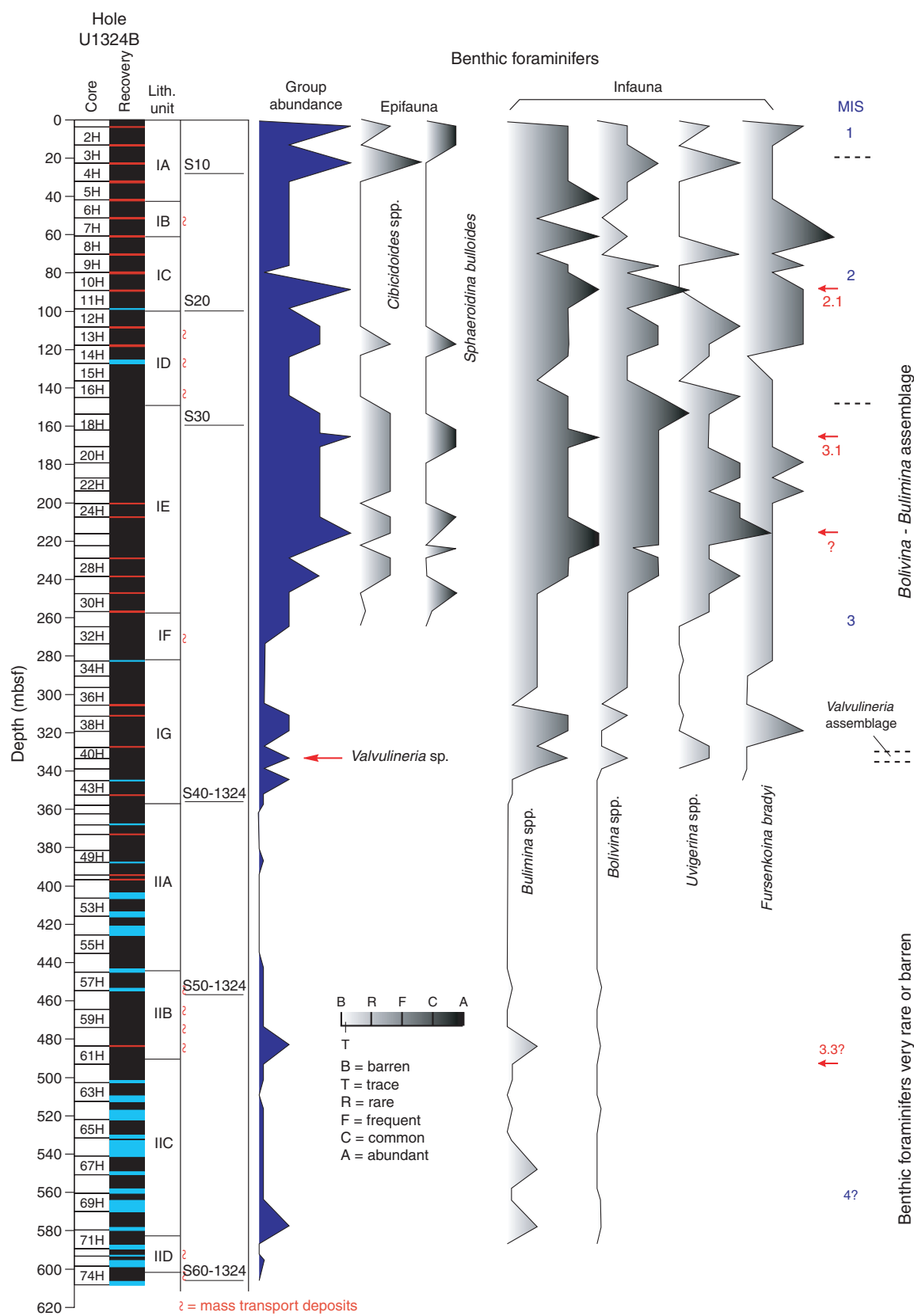


**Figure F23.** Microfossil and magnetostratigraphic datums and calculated sedimentation rates for Site U1324. Lithostratigraphy and seismic reflectors (SR) are described in “[Background and objectives](#)” and “[Lithostratigraphy](#),” respectively. LO = last occurrence.

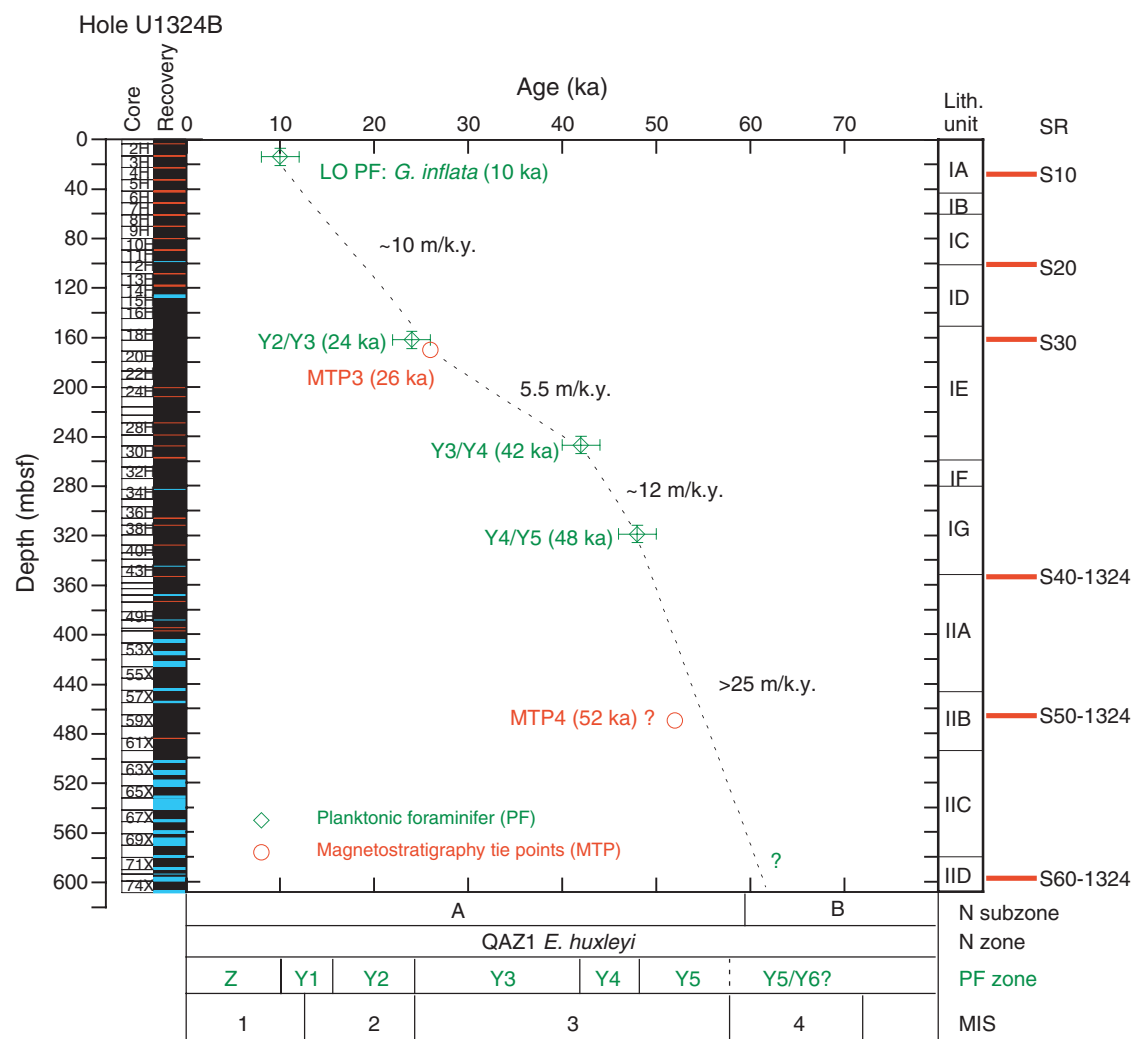


**Figure F24.** Uncorrected shipboard measurements (black dots) and running average (gray line) on archive-half core sections of (A) natural remanent magnetization after 20 mT AF demagnetization ( $\text{NRM}_{20\text{mT}}$ ), (B) declination (black = cores recovered using a nonmagnetic APC cutting shoe, red = cores recovered with the Fugro cutting shoe), and (C) inclination (black = APC cutting shoe, red = Fugro cutting shoe). Depths have been corrected for voids in the core; paleomagnetic intervals, lithostratigraphic units, and seismic reflectors (SF = seafloor) are also shown.

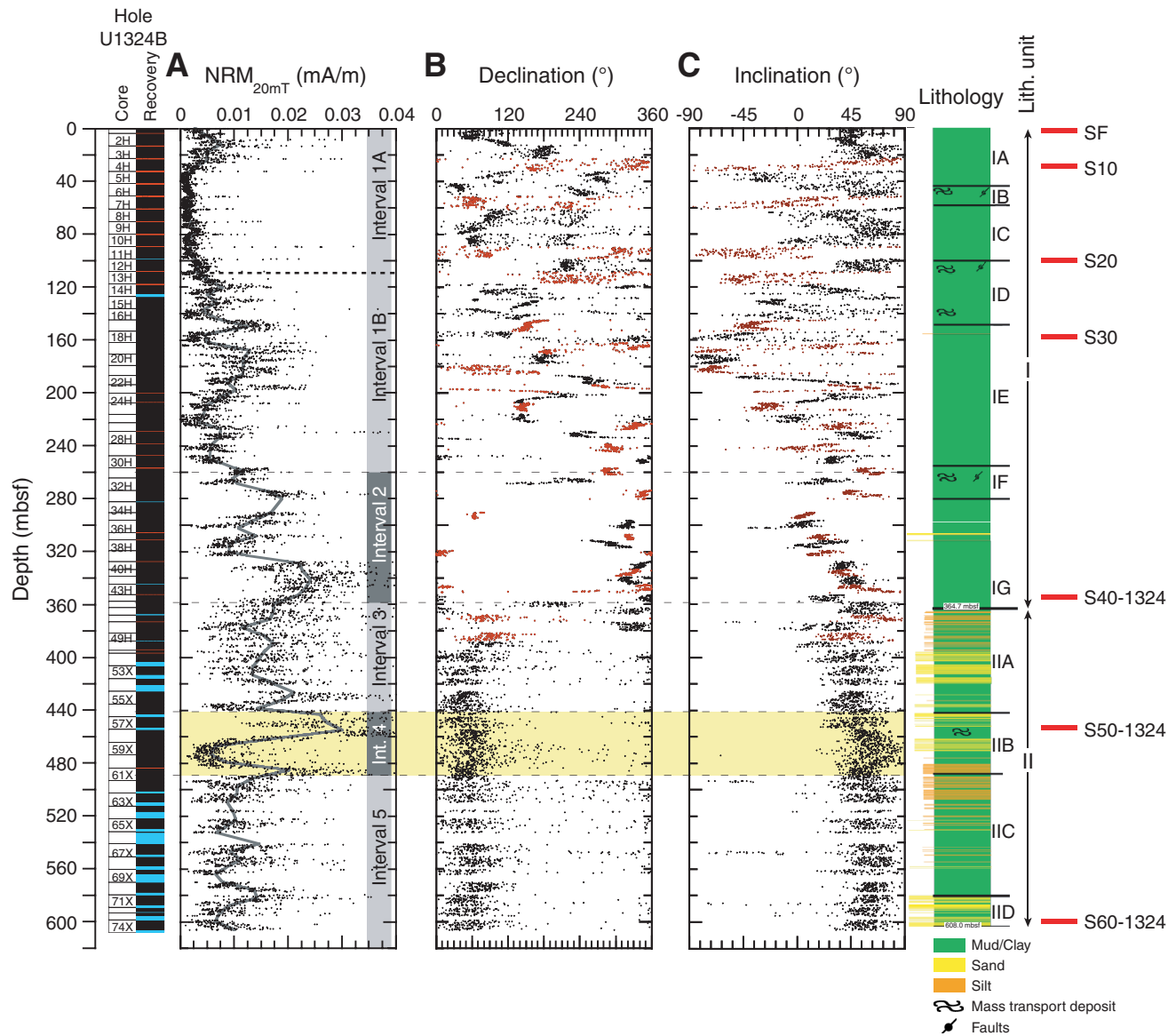


**Figure F25.** Magnetostatigraphic data (black dots) and running average (gray lines) of Hole U1324B. A.  $\delta^{18}\text{O}$  record (Bassinot et al., 1994, solid line) and Subtropical South Atlantic Susceptibility stack (von Dobeneck and Schmiedert, 1999, dashed line) vs. age, and marine isotope stages (MIS) 1.1, 2.2, 3.1, 3.3. B. Natural remanent magnetization after 20 mT AF demagnetization ( $\text{NRM}_{20\text{mT}}$ ), showing the graphical correlation of the magnetostatigraphic tie points (MTP1–MTP4) with marine isotopic stages. C. MS2F sensor magnetic point susceptibility ( $\kappa$ ) performed on archive halves at 10 cm resolution. D. Multisensor track (MST)  $\kappa$  measured on whole cores at 6 cm resolution. Depths have been corrected for voids in the core; lithostratigraphic units, magnetostatigraphic intervals, and seismic reflectors (SF = seafloor) are also shown.

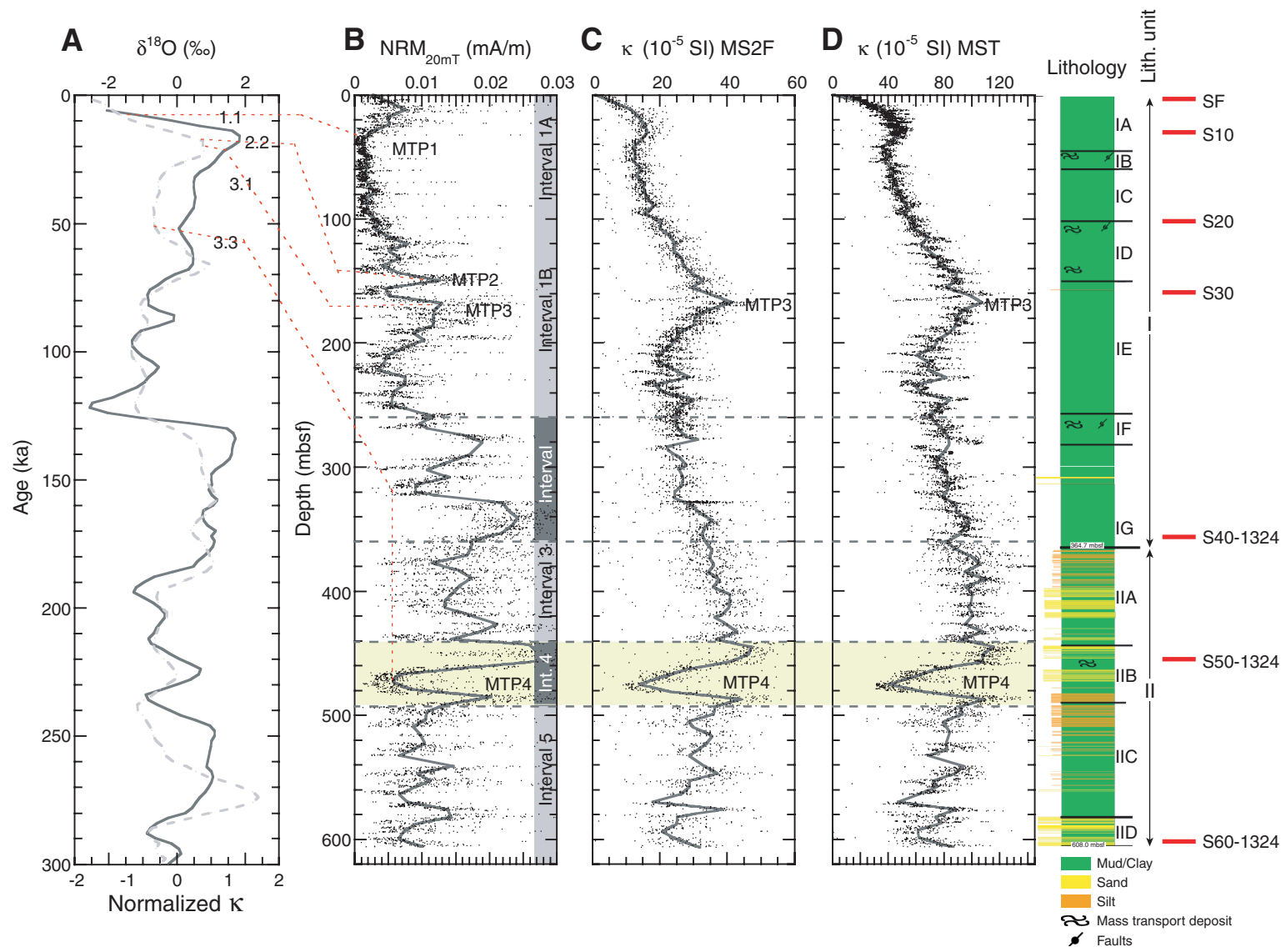


**Figure F26.** Interstitial water concentration profiles for alkalinity, pH, salinity, and chlorinity (black symbols = Hole U1324B, gray symbols = Hole U1324C) along with seismic reflectors (SF = seafloor) and lithostratigraphic units.

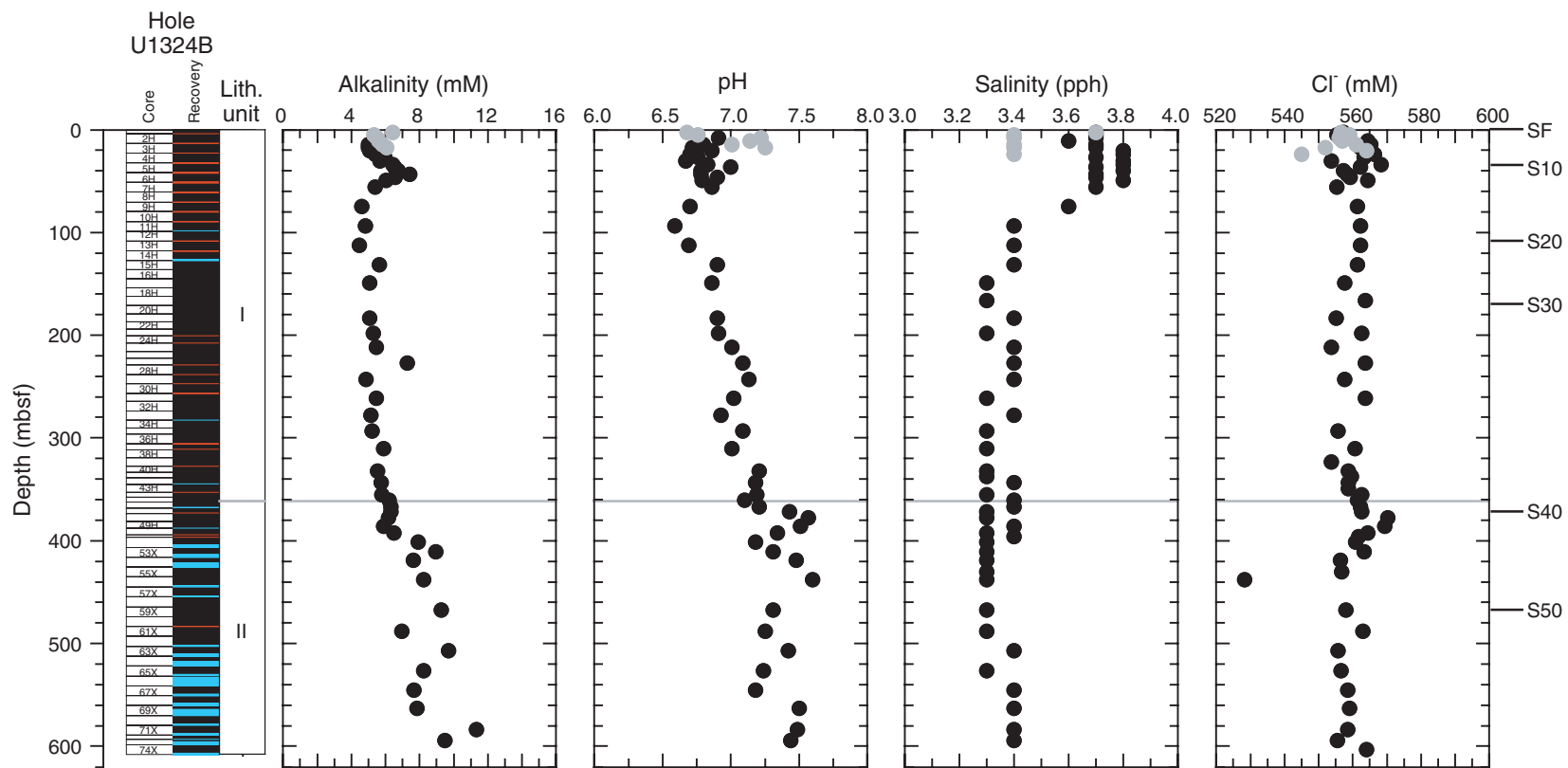




**Figure F27.** Interstitial water concentration profiles  $\text{SO}_4^{2-}$ ,  $\text{NH}_4^+$ ,  $\text{PO}_4^{3-}$ , and  $\text{H}_4\text{SiO}_4$  (black symbols = Hole U1324B, gray symbols = Hole U1324C) along with seismic reflectors (SF = seafloor) and lithostratigraphic units.

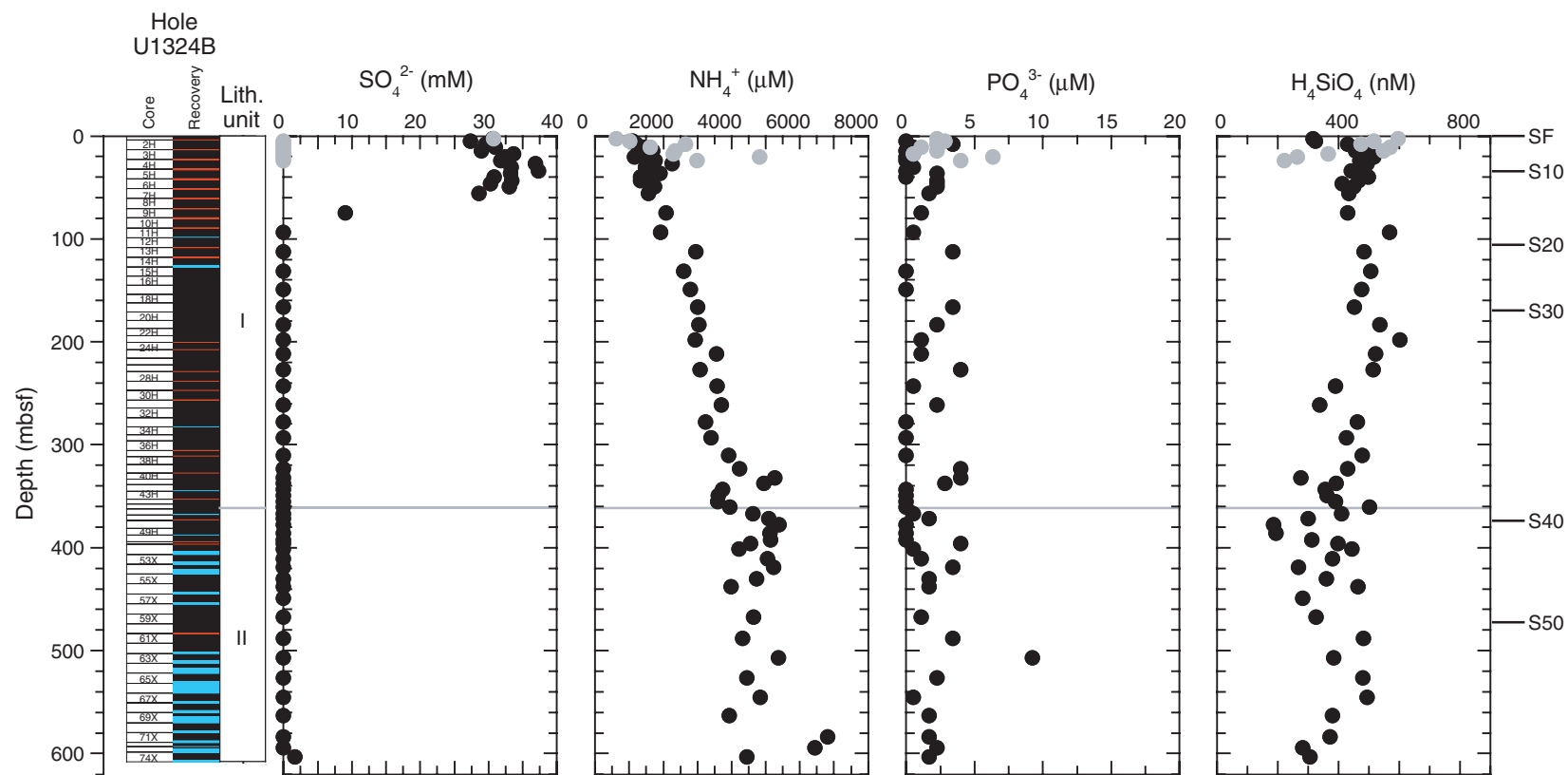


**Figure F28.** Interstitial water concentration profiles for major cations  $\text{Na}^+$ ,  $\text{K}^+$ ,  $\text{Ca}^{2+}$ ,  $\text{Mg}^{2+}$  (black symbols = Hole U1324B, gray symbols = Hole U1324C) along with seismic reflectors (SF = seafloor) and lithostratigraphic units.

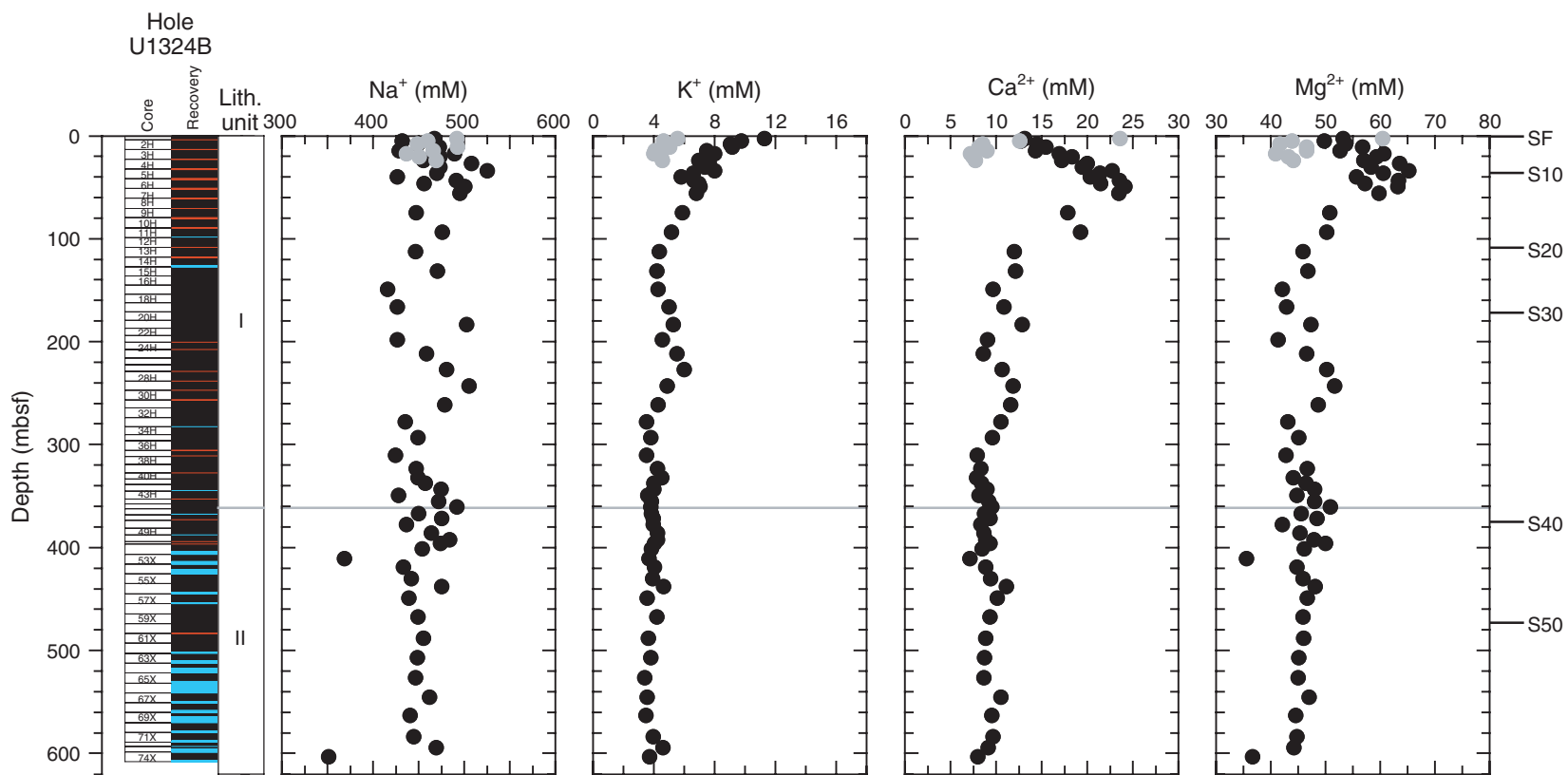


**Figure F29.** Interstitial water concentration profiles for trace metals (black symbols = Hole U1324B, gray symbols = Hole U1324C) along with seismic reflectors (SF = seafloor) and lithostratigraphic units.  $B^{3+}$ ,  $Li^+$ , and  $Sr^{2+}$  (continued on next page).

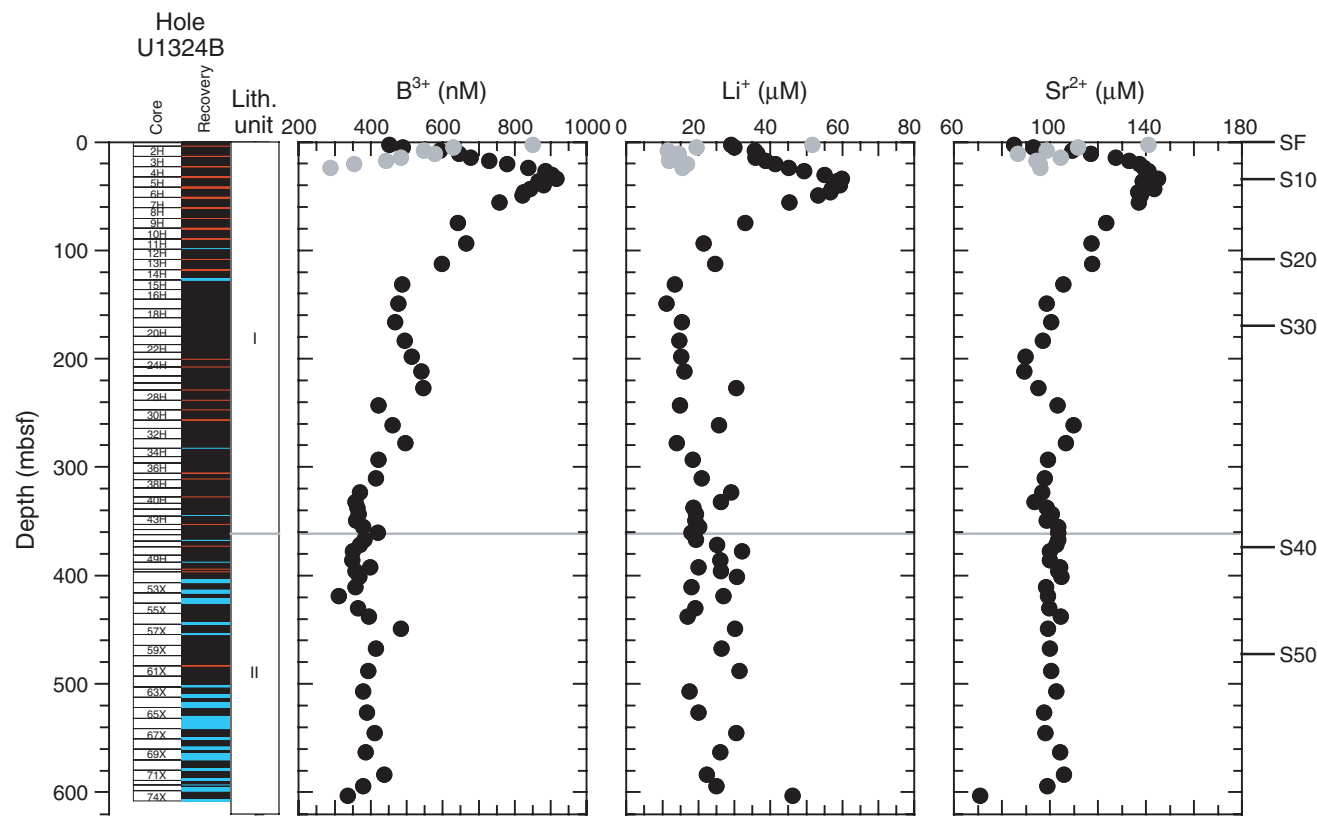
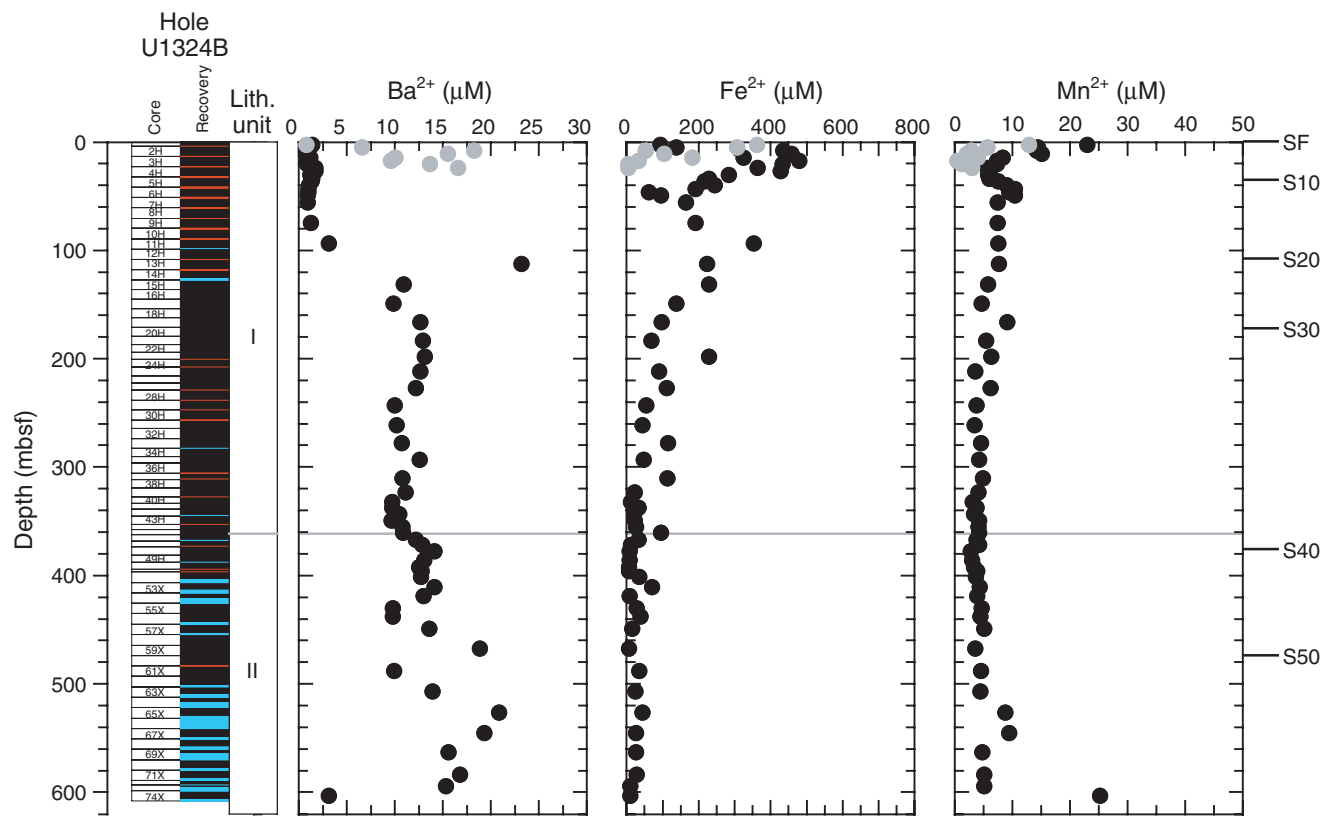
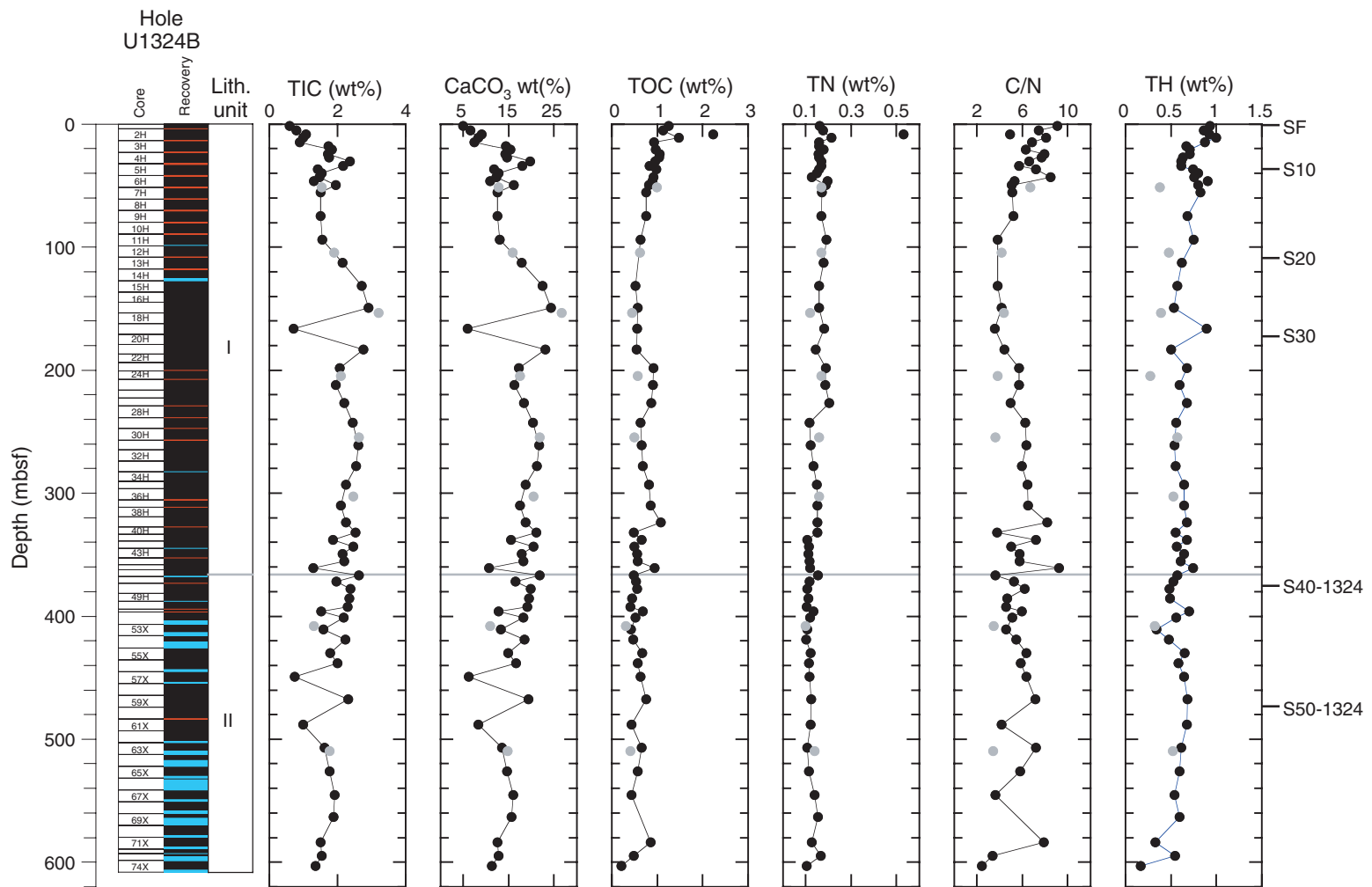
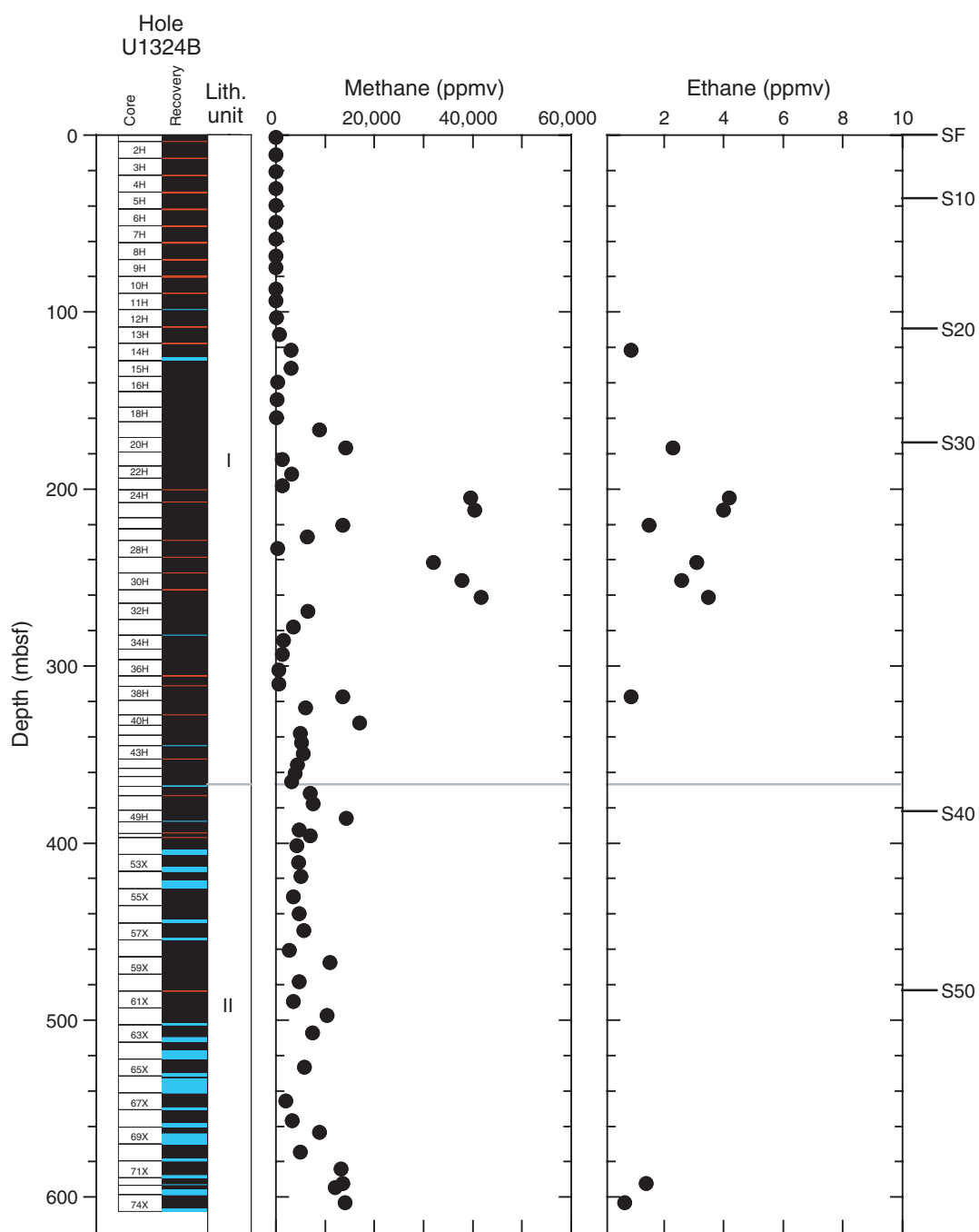


Figure F29 (continued). Ba<sup>2+</sup>, Fe<sup>2+</sup>, and Mn<sup>2+</sup>.

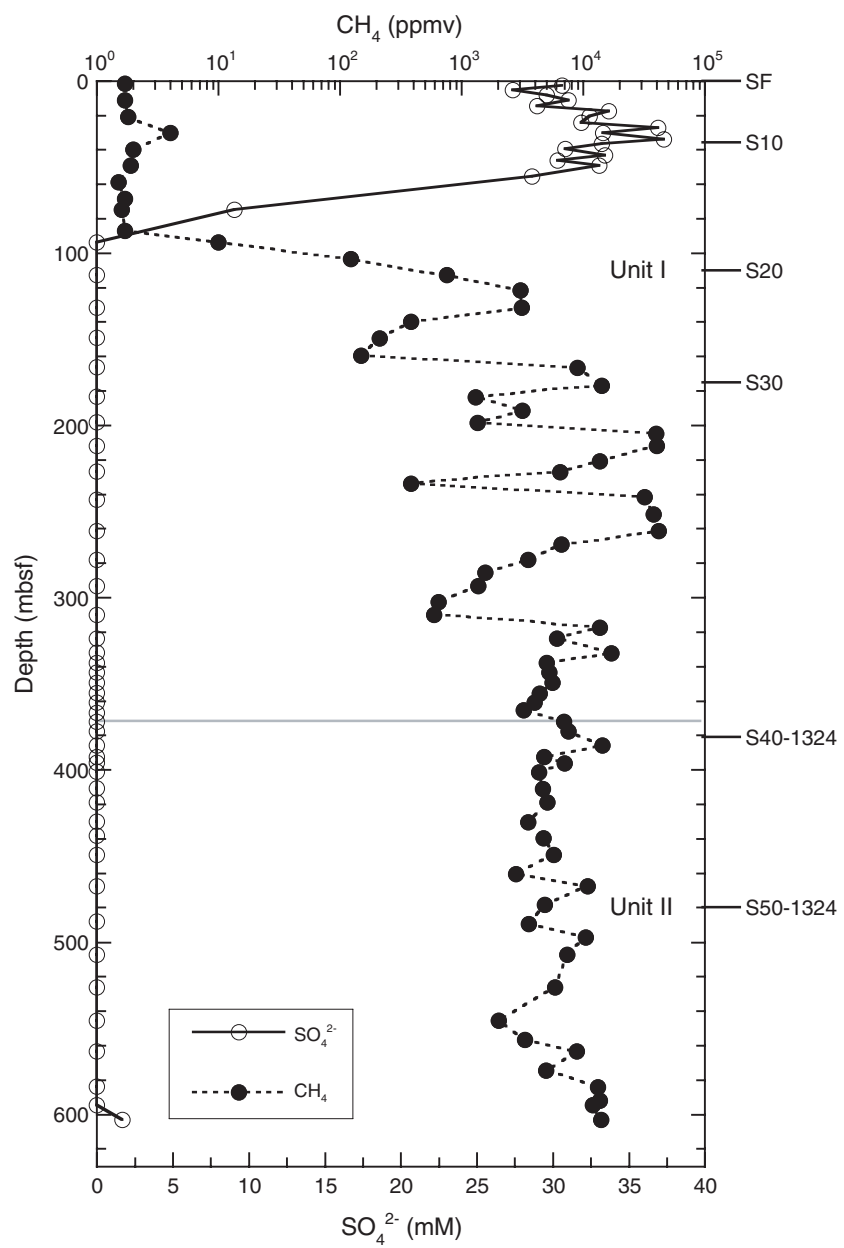
**Figure F30.** Downhole variations in total inorganic carbon (TIC), calcium carbonate ( $\text{CaCO}_3$ ), total organic carbon (TOC), total nitrogen (TN), molar ratio of organic carbon to total nitrogen (C/N), and total hydrogen (TH) in sediments at Site U1324 (black symbols = Hole U1324B, gray symbols = Hole U1324C) along with seismic reflectors (SF = seafloor) and lithostratigraphic units.



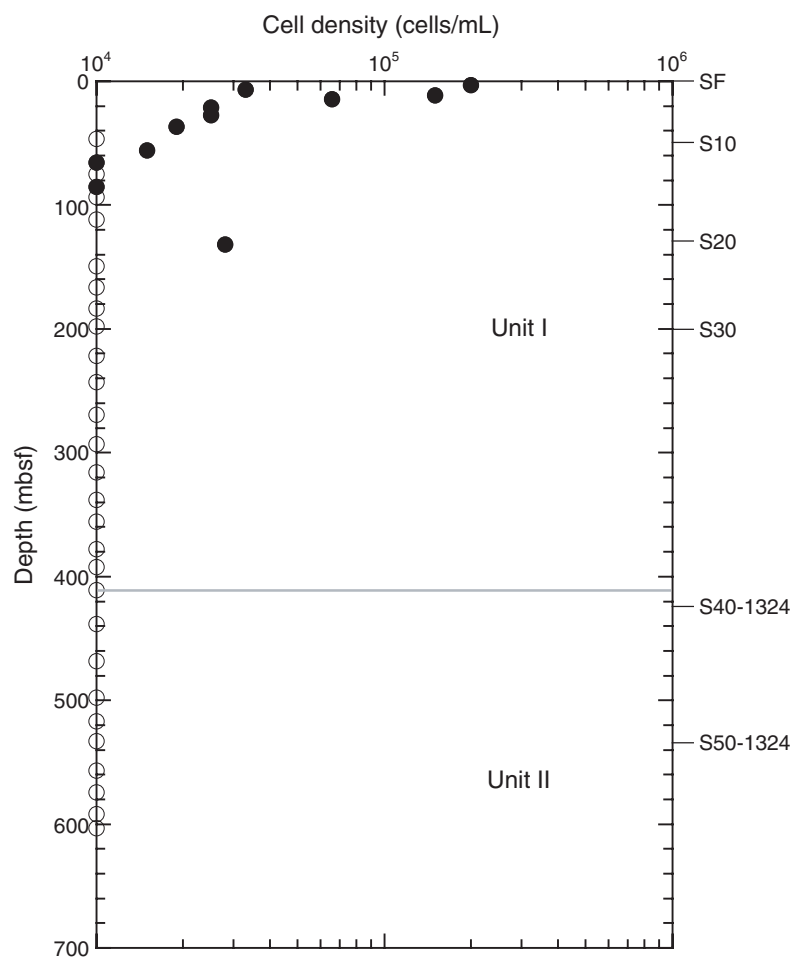
**Figure F31.** Headspace gas concentrations of methane and ethane in Hole U1324B along with seismic reflectors (SF = seafloor) and lithostratigraphic units.



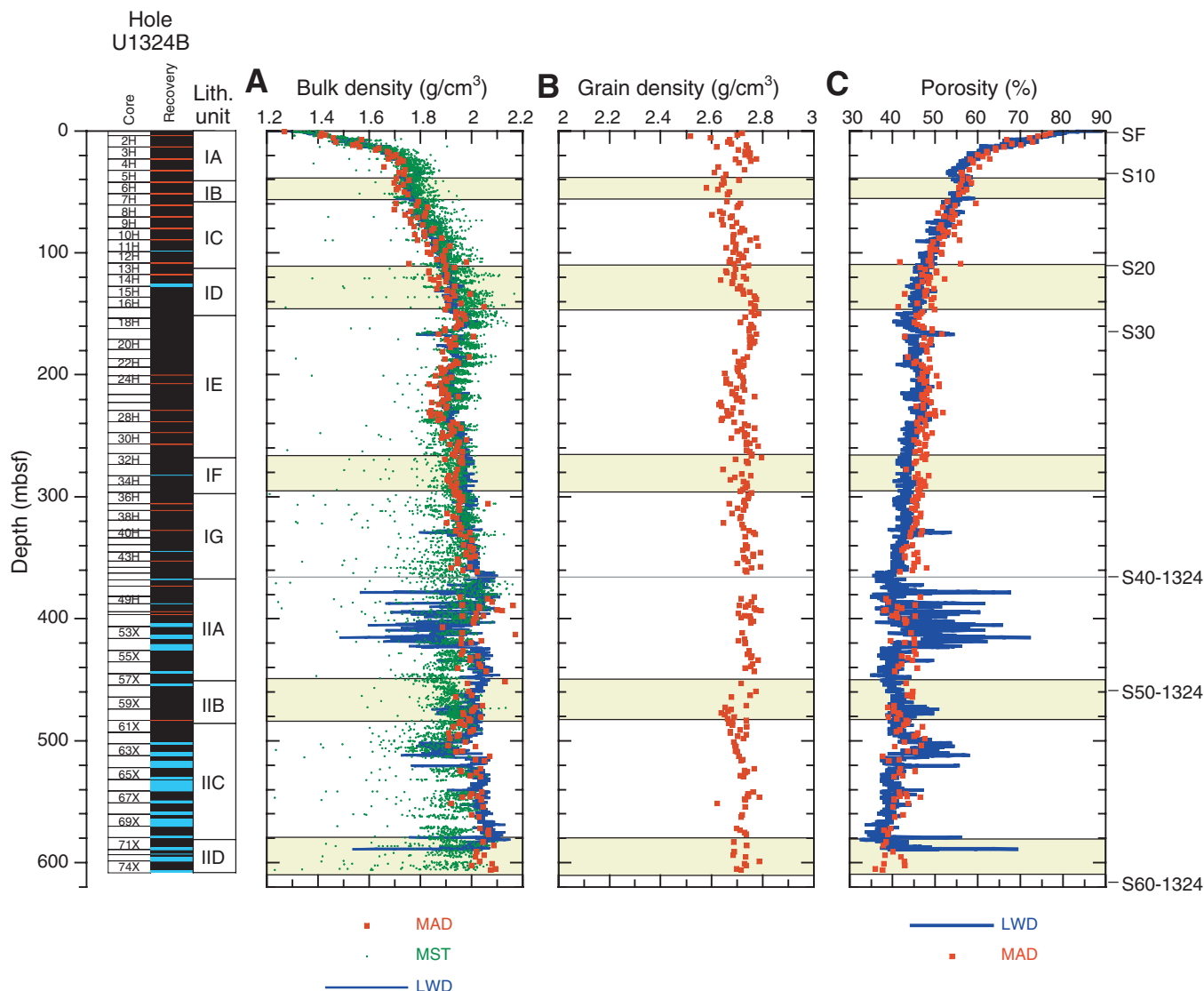
**Figure F32.** Methane and sulfate concentration profiles in Hole U1324B along with seismic reflectors (SF = seafloor) and lithostratigraphic units.



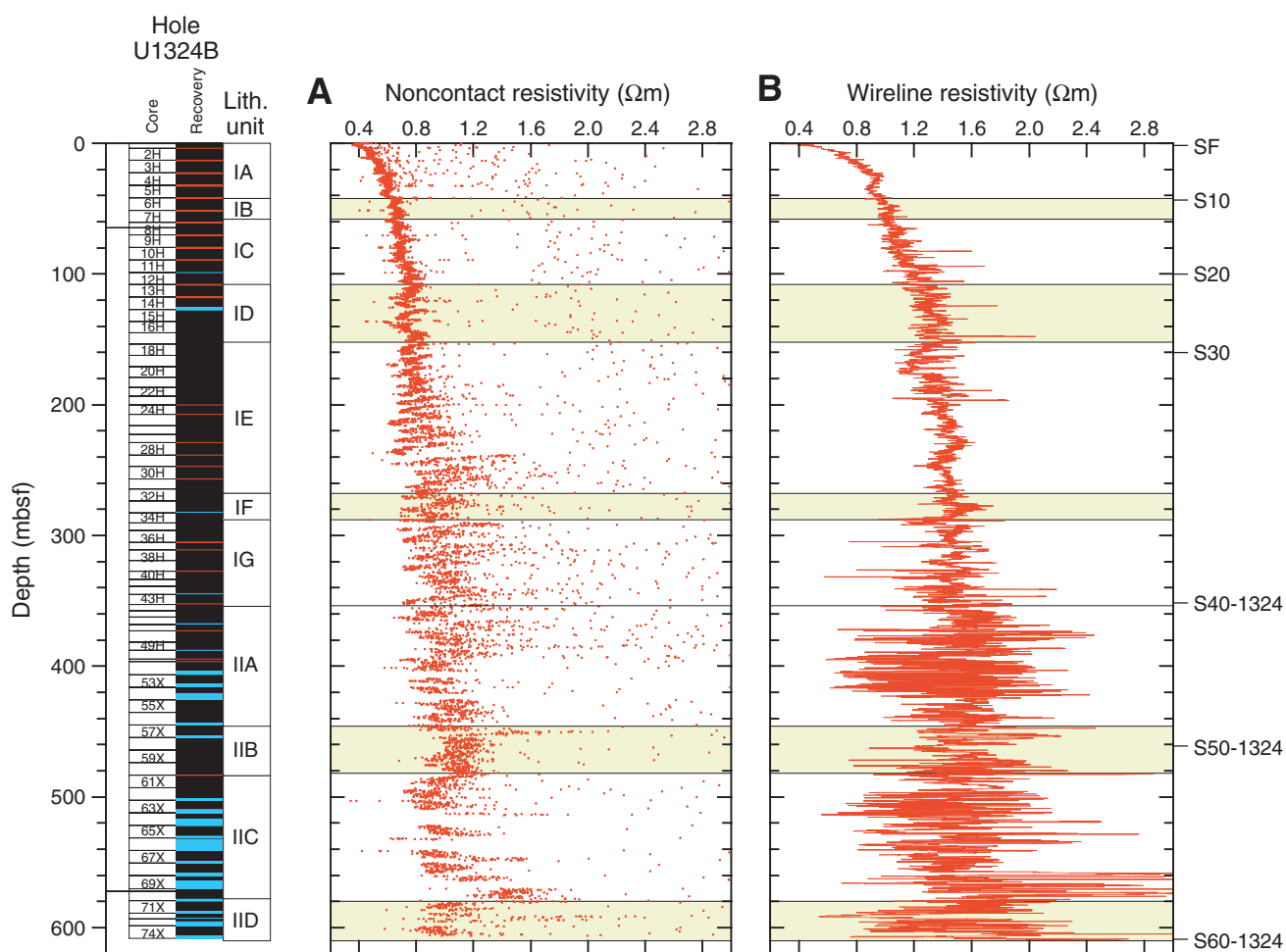
**Figure F33.** Vertical profile of cell density in Hole U1324B (solid symbols = cell density, open symbols = not detected or not significant amounts) along with seismic reflectors (SF = seafloor) and lithostratigraphic units.



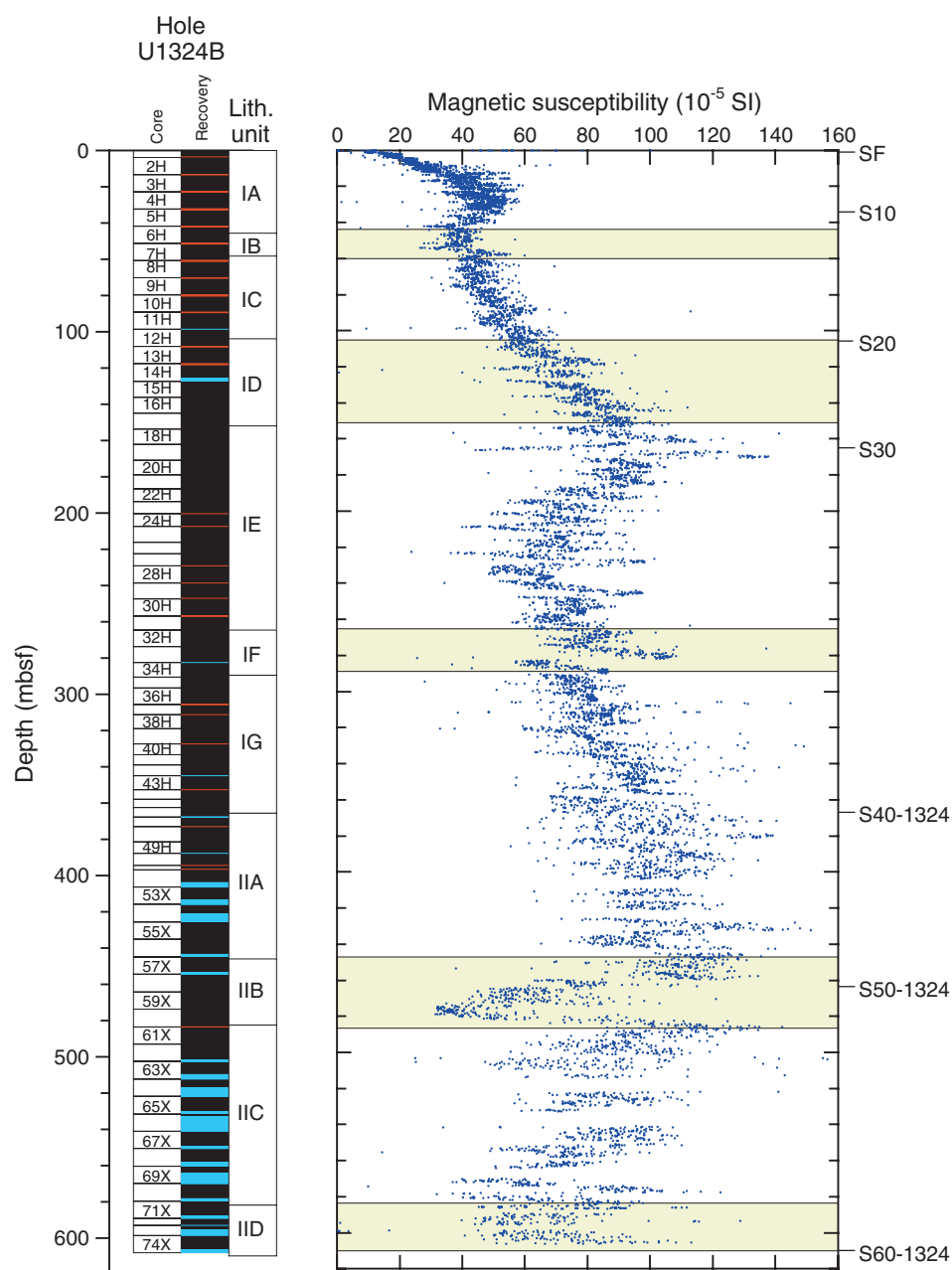
**Figure F34.** A. Bulk density determined from gamma ray attenuation (GRA) on unsplit cores and from moisture and density (MAD) measurements on discrete samples. Image-derived density (IDRO) from logging-while-drilling (LWD) data are overlain for comparison. B. Grain density profile determined from MAD measurements. C. Porosity obtained from MAD measurements and porosity calculated from IDRO density assuming a constant grain density of  $2.7 \text{ g/cm}^3$  and a pore water density of  $1.024 \text{ g/cm}^3$ . Yellow = mass transport deposits (see “[Lithostratigraphy](#)”). SF = seafloor.



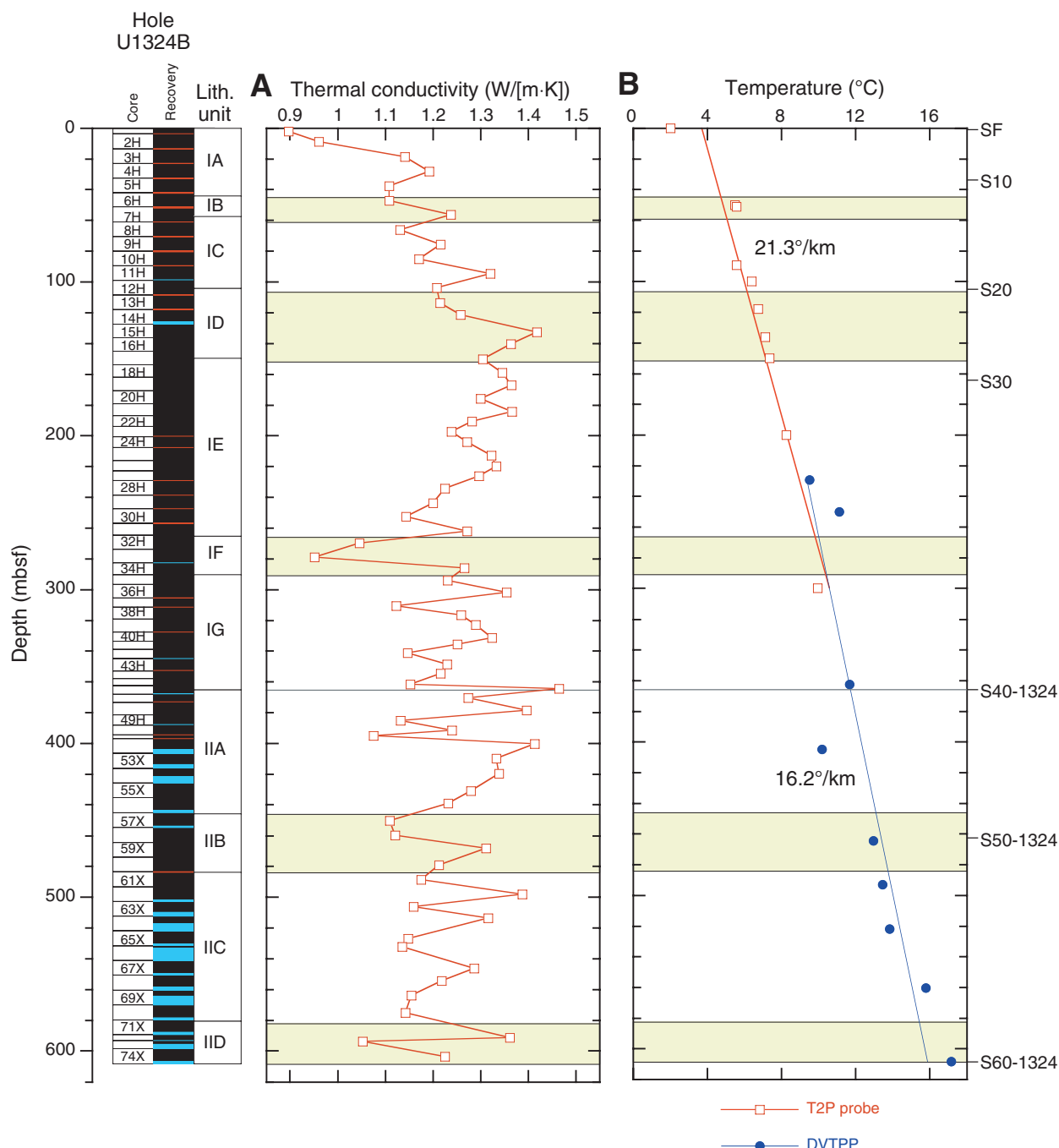
**Figure F35.** A. Noncontact resistivity (from MST core logging). B. Resistivity from wireline logging plotted along with seismic reflectors (SF = seafloor; see “[Background and objectives](#)”) and lithostratigraphic units.



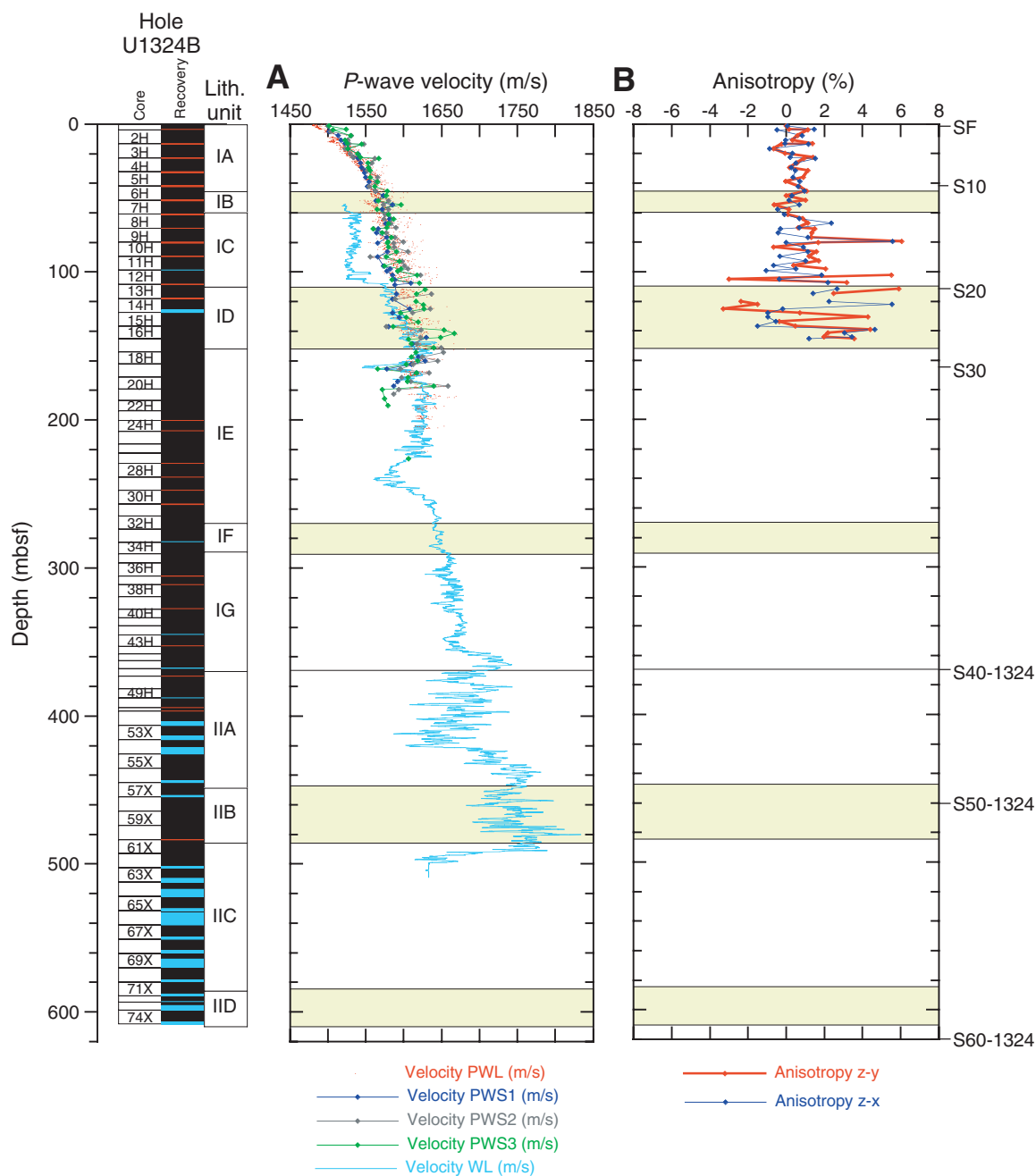
**Figure F36.** Magnetic susceptibility (MS) plotted along with seismic reflectors (SF = seafloor; see “[Background and objectives](#)”). Yellow = mass transport deposits.



**Figure F37.** A. Thermal conductivity. B. In situ temperatures measured using the temperature/dual pressure (T2P) probe and Davis-Villinger Temperature-Pressure Probe (DVTPP), plotted along with seismic reflectors (SF = seafloor). Yellow = mass transport deposits.

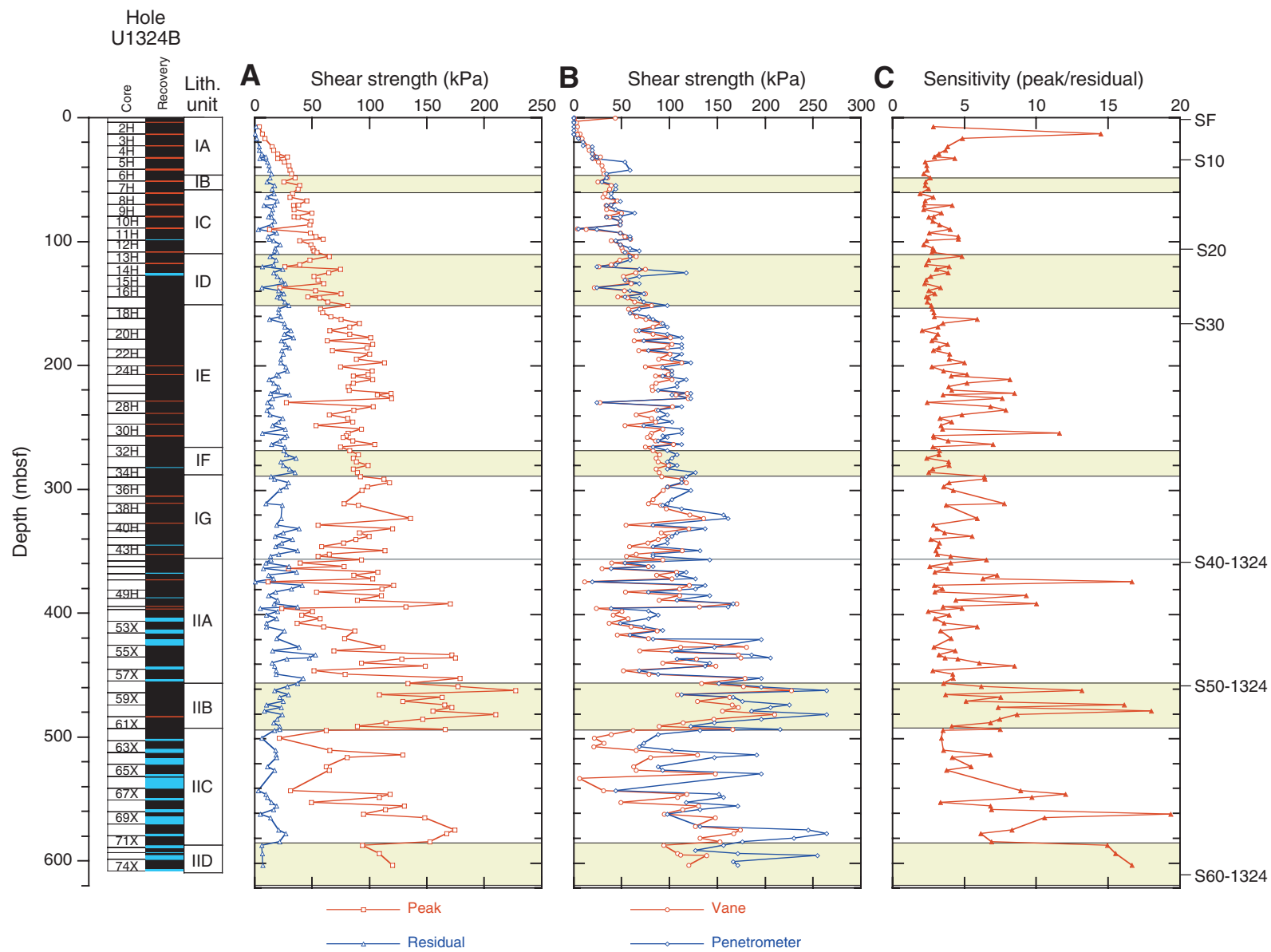


**Figure F38.** A.  $P$ -wave velocity vs. depth. B.  $P$ -wave anisotropy vs. depth, with seismic reflectors (SF = sea-floor). Yellow = mass transport deposits. PWL =  $P$ -wave logger on the MST, PWS = contact probe system, WL = wireline logging.

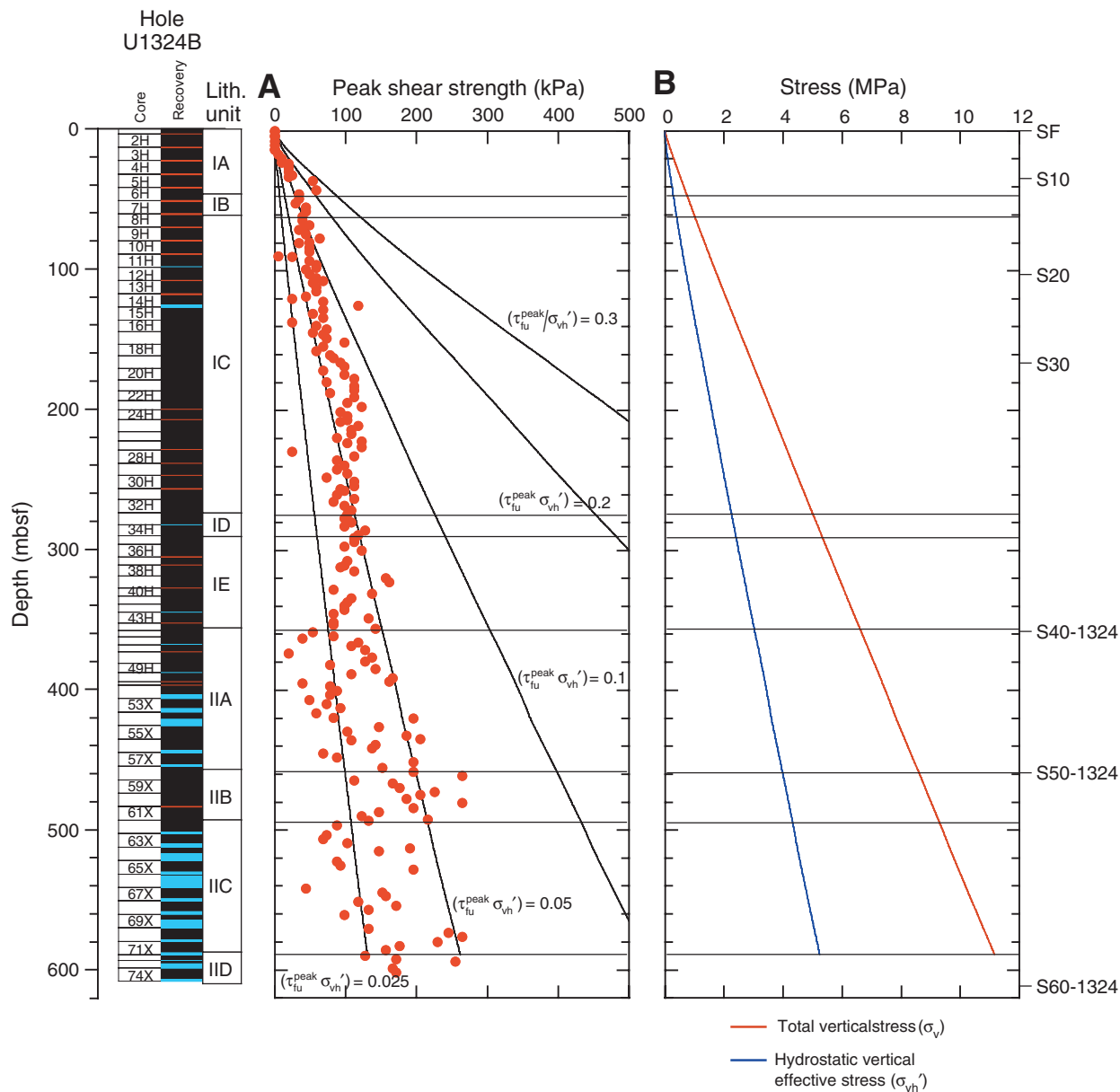




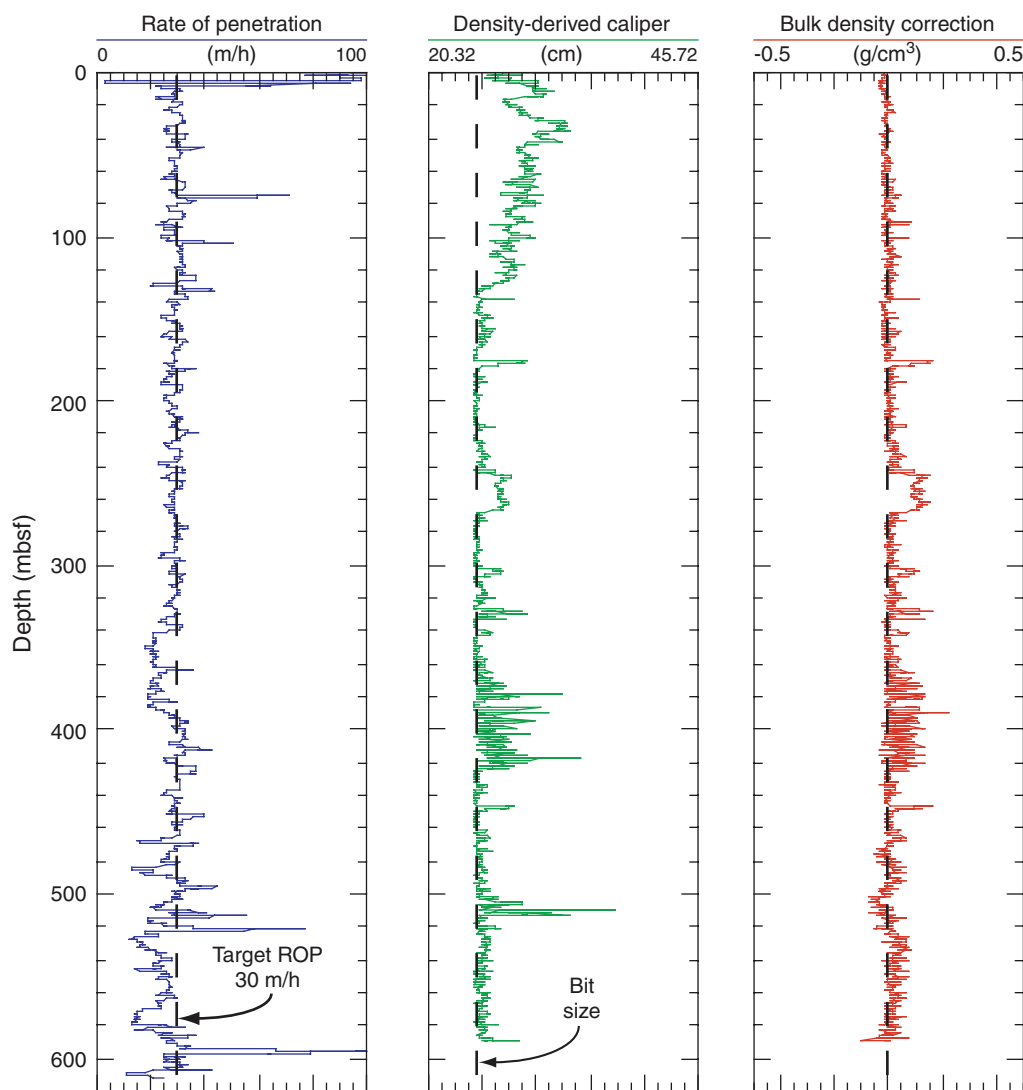
**Figure F39.** A. Peak and residual undrained shear strength from vane shear tests. B. Comparison of the peak undrained shear strengths measured by the shear vane and the pocket penetrometer. C. Sensitivity. Seismic reflectors (SF = seafloor; see “[Background and objectives](#)”) are shown. Yellow = mass transport deposits.



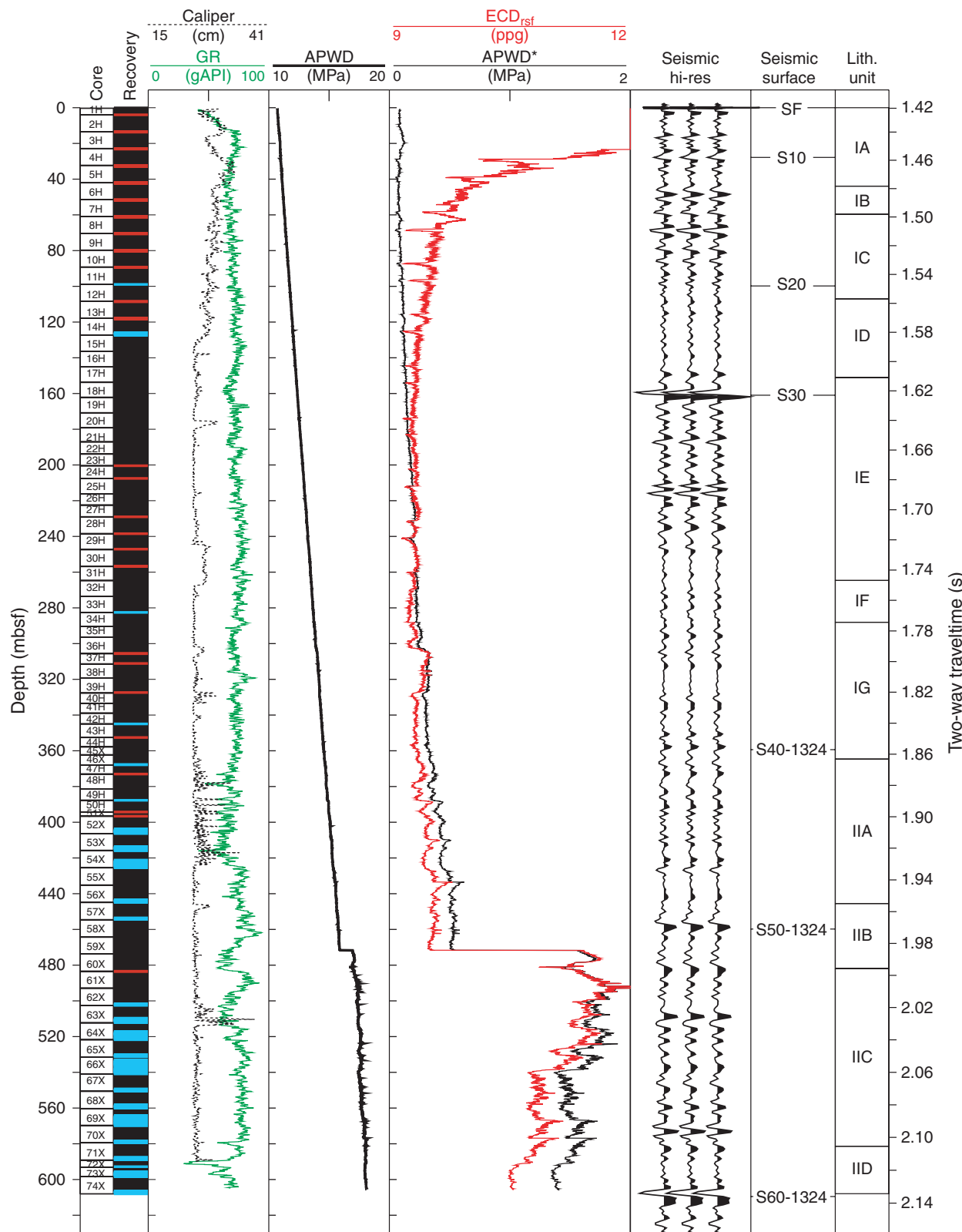
**Figure F40.** A. Comparison between the undrained peak shear strength and the ratio between the peak shear strength ( $\tau_{fu}^{\text{peak}}$ ) and the vertical hydrostatic effective stress ( $\sigma_{vh}'$ ). B. Lithostatic stress and vertical hydrostatic effective stress calculated from LWD (IDRO) bulk density profile (see “Physical properties” in the “Methods” chapter). Seismic reflectors (SF = seafloor) are shown.



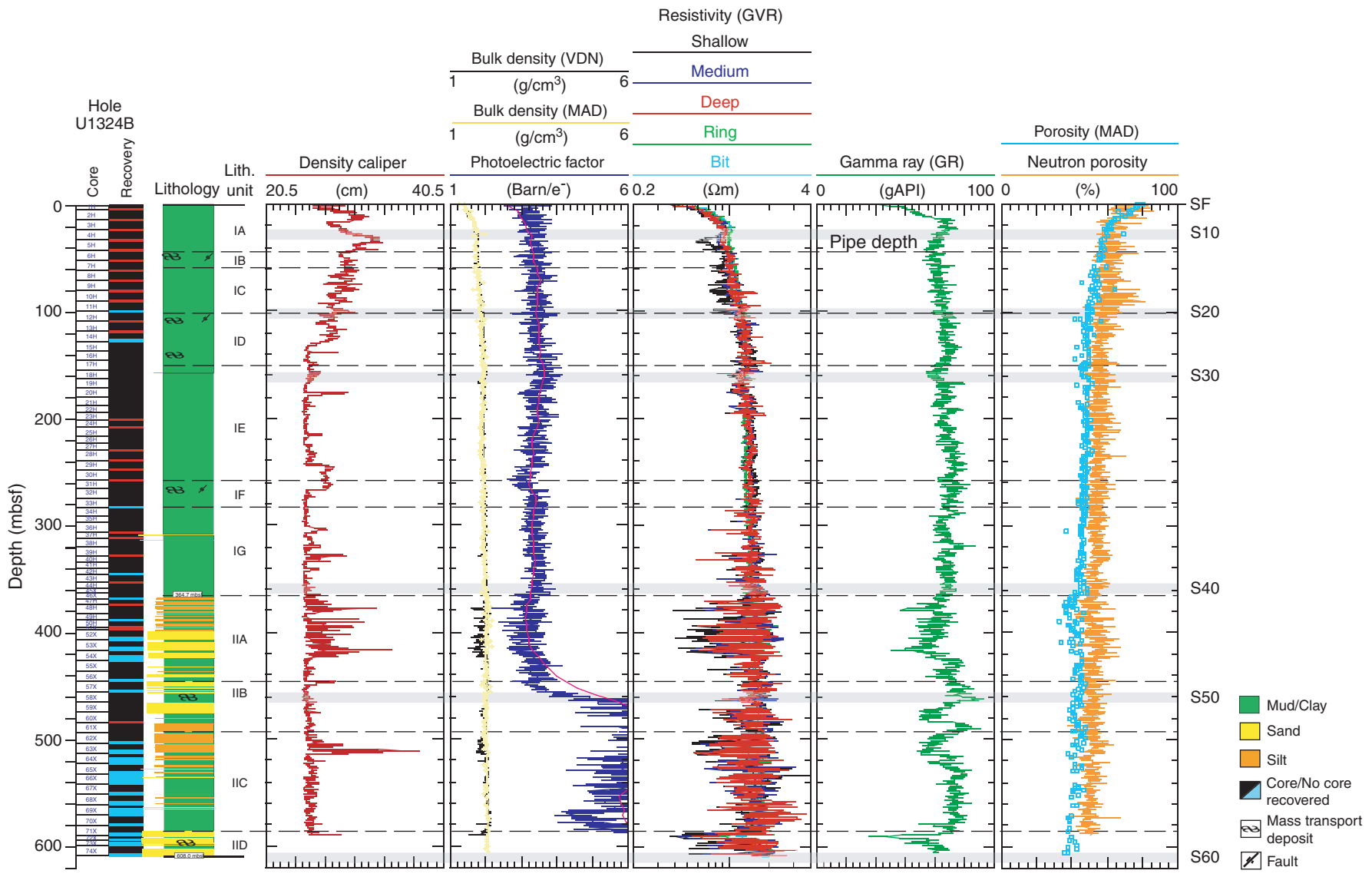
**Figure F41.** Data quality of curves for LWD/MWD measurements from Hole U1324B showing the rate of penetration (ROP), density-derived caliper, and bulk density correction.



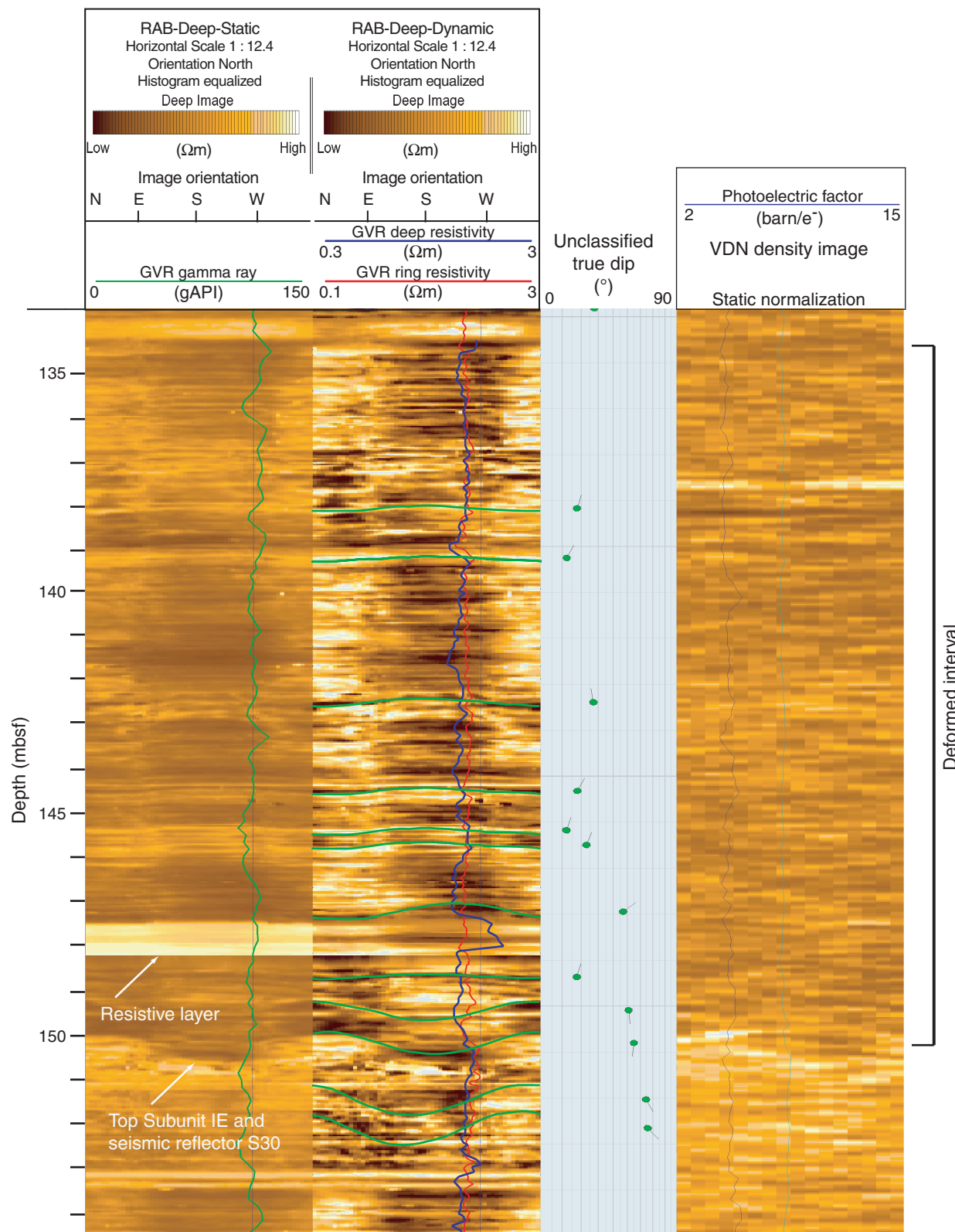
**Figure F42.** Pressure monitoring of Hole U1324A along with seismic reflectors (SF = seafloor), gamma radiation (GR), and lithostratigraphic units. The near-linear increase in annular pressure whole drilling (APWD) is interpreted as stable borehole conditions without shallow-water flow problems. Variations in annular overpressure in excess of hydrostatic (APWD\*) and equivalent circulating density referenced to seafloor ( $ECD_{rsf}$ ) at 470–608 mbsf are due to continuous circulation of 10 ppg mud (seawater, sepiolite, and barite).



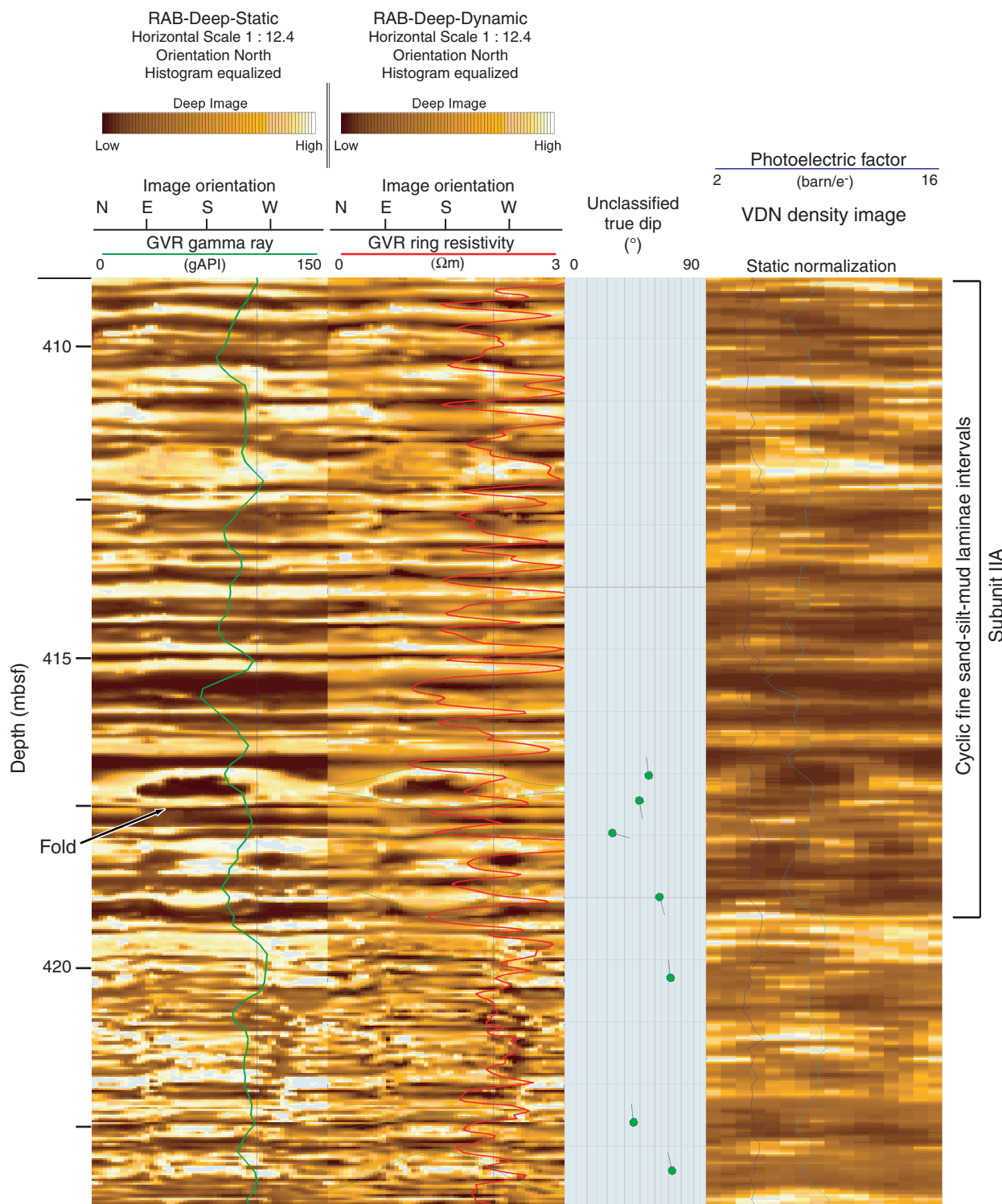
**Figure F43.** LWD logs recorded in Hole U1324A. Density caliper, photoelectric factor (PEF), and neutron porosity were recorded with the Vision Density Neutron (VDN) tool. Gamma ray and resistivity measurements were obtained with the GeoVision Resistivity (GVR) tool. The red line superimposed on the (PEF) log is a five-point average curve. The lithologic column is based on core descriptions made from Holes U1324B and U1324C. Lithostratigraphic subunit boundaries are denoted with dashed lines. Seismic reflectors (SF = seafloor) are shown. Both laboratory measurements of porosity and density (MAD) are compared to the neutron porosity data.



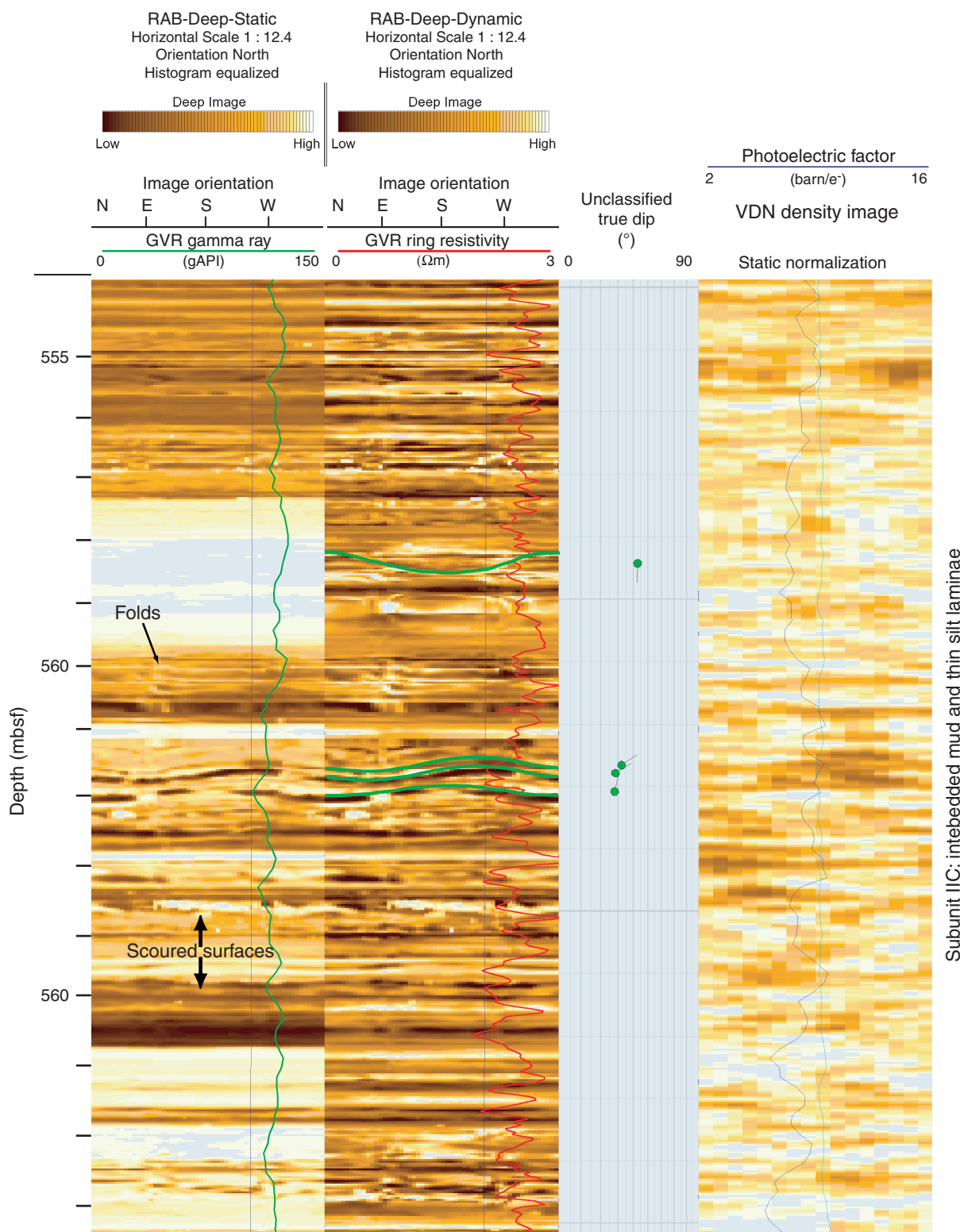
**Figure F44.** Resistivity images showing numerous deformed and dipping beds throughout Subunits ID and IE. Dips range from 5° to 55° and the top of Subunit IE correlates with seismic Reflector S30. RAB = resistivity at the bit. GVR = GeoVision Resistivity, VDN = Vision Density Neutron.



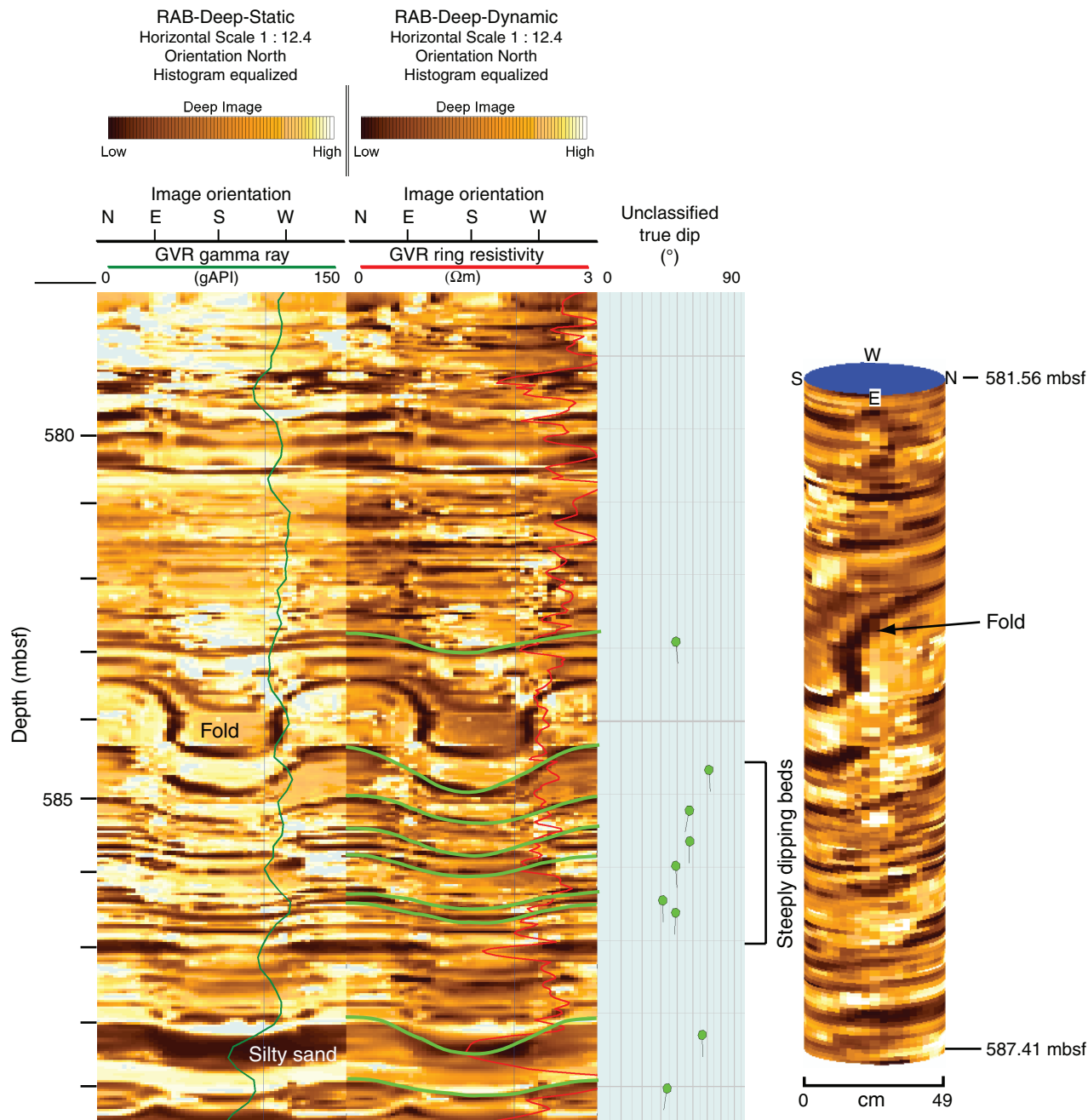
**Figure F45.** Resistivity images showing evidence of mass transport deposits in lithostratigraphic Subunit IIA and the presence of overturned beds. A series of cyclic intervals are interpreted as a succession of sand-silt-mud laminae. RAB = resistivity at the bit. GVR = GeoVision Resistivity, VDN = Vision Density Neutron.



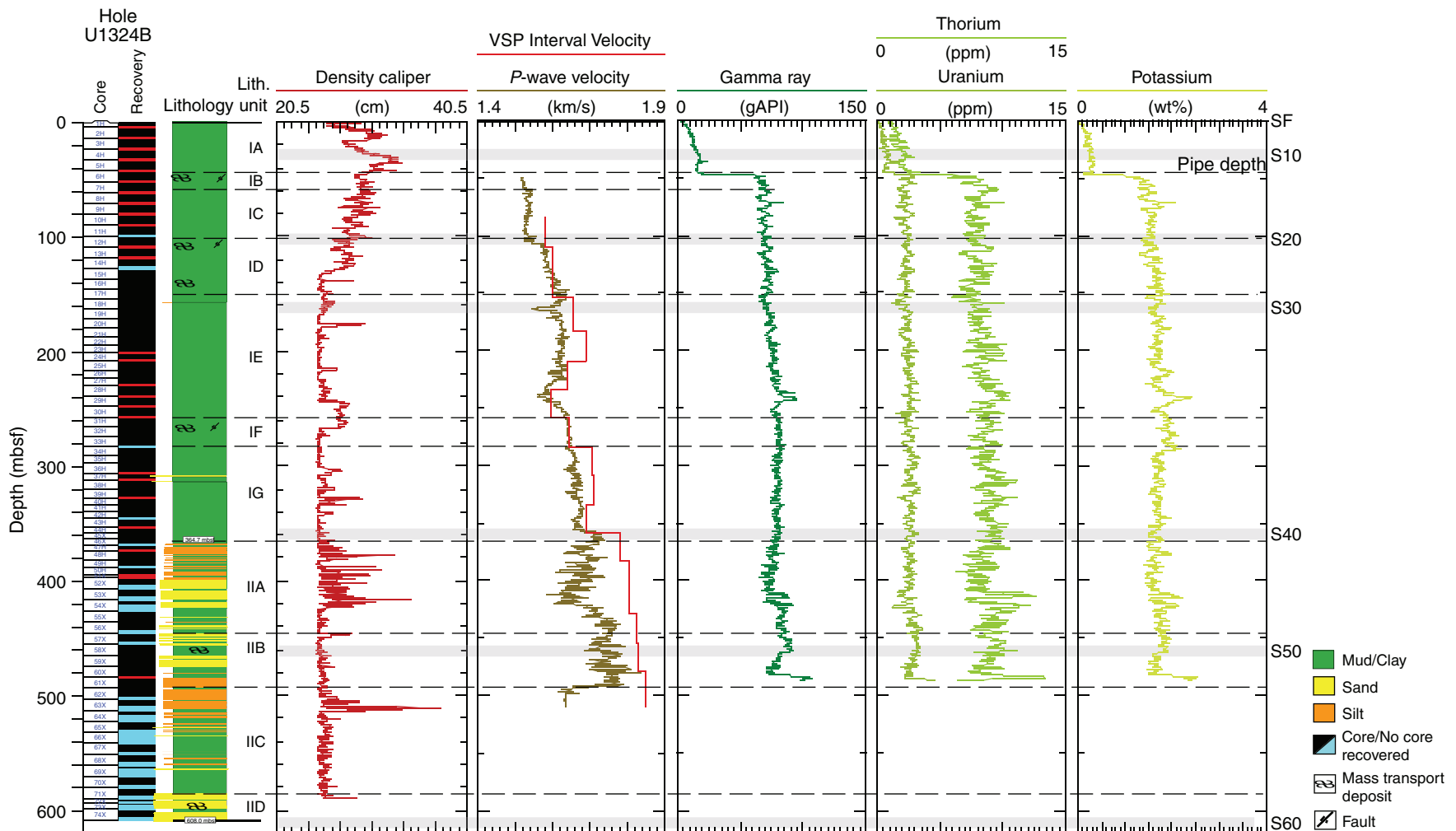
**Figure F46.** Resistivity images showing scoured surfaces in lithostratigraphic Subunit IIC, suggesting erosion. RAB = resistivity at the bit. GVR = GeoVision Resistivity, VDN = Vision Density Neutron.



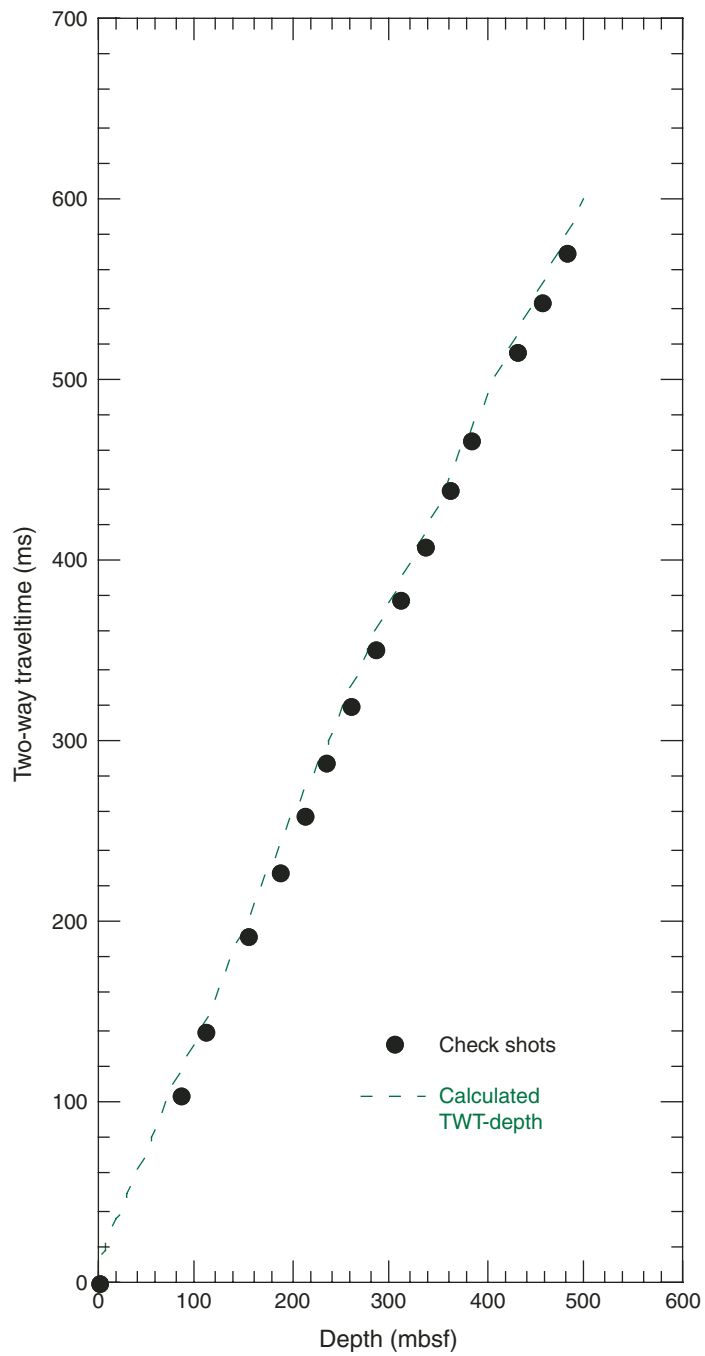
**Figure F47.** Resistivity images showing a fold with an east-west-trending fold axis within lithostratigraphic Subunit IID. Fold is overturned to the south, indicating mass transport in that direction. Most of the deformation features observed in Hole U1324A trend in an east-west direction with the majority dipping to the north. RAB = resistivity at the bit. GVR = GeoVision Resistivity.



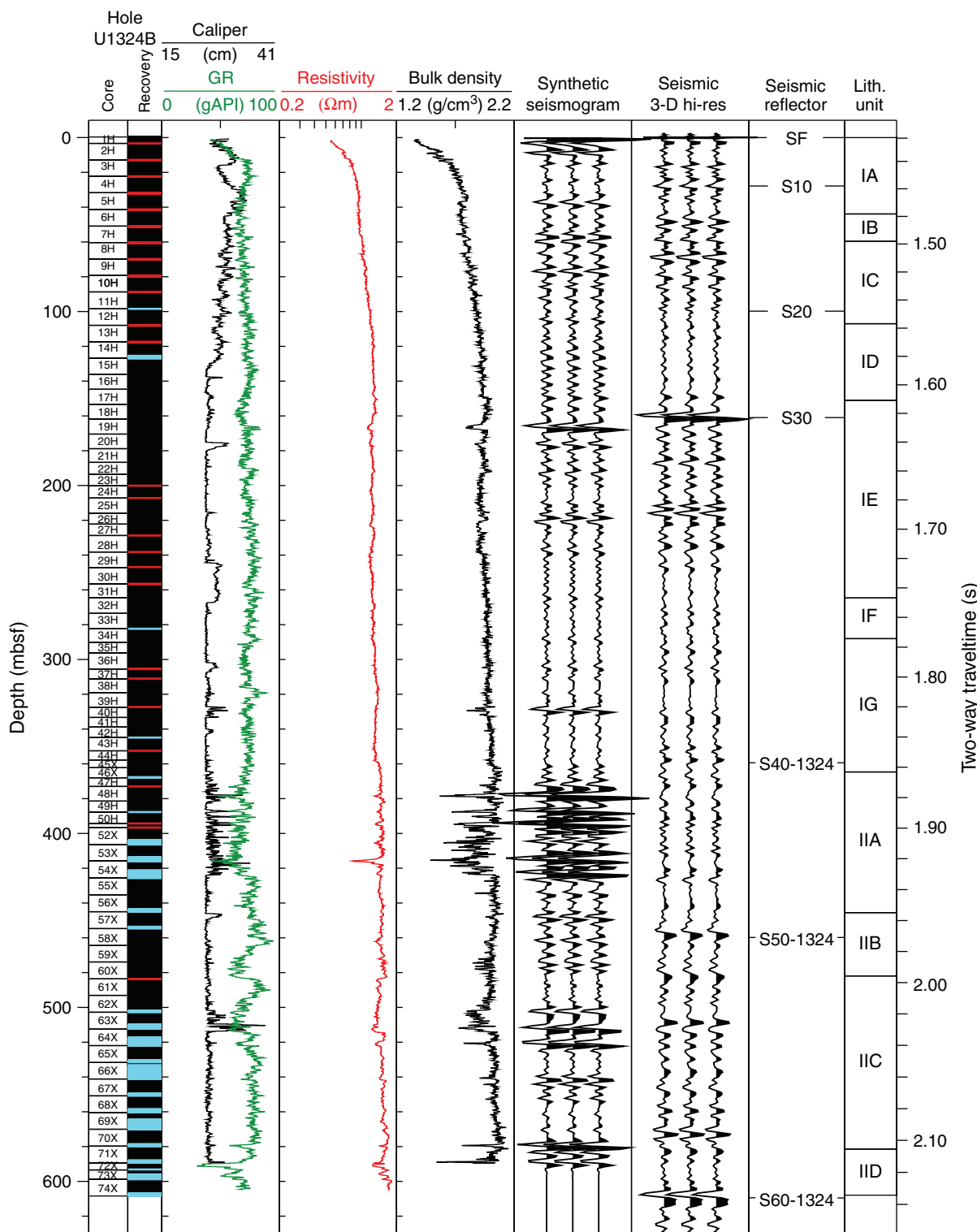
**Figure F48.** Wireline logs recorded in Hole U1324A include compressional wave velocity (*P*-wave velocity), gamma ray including spectral components, and interval velocities derived from check shots. The density caliper from LWD measurements is presented to show the quality of the borehole. Lithologic and core recovery columns are based on results from Hole U1324B. Seismic reflectors (SF = seafloor) are shown. VSP = vertical seismic profile.



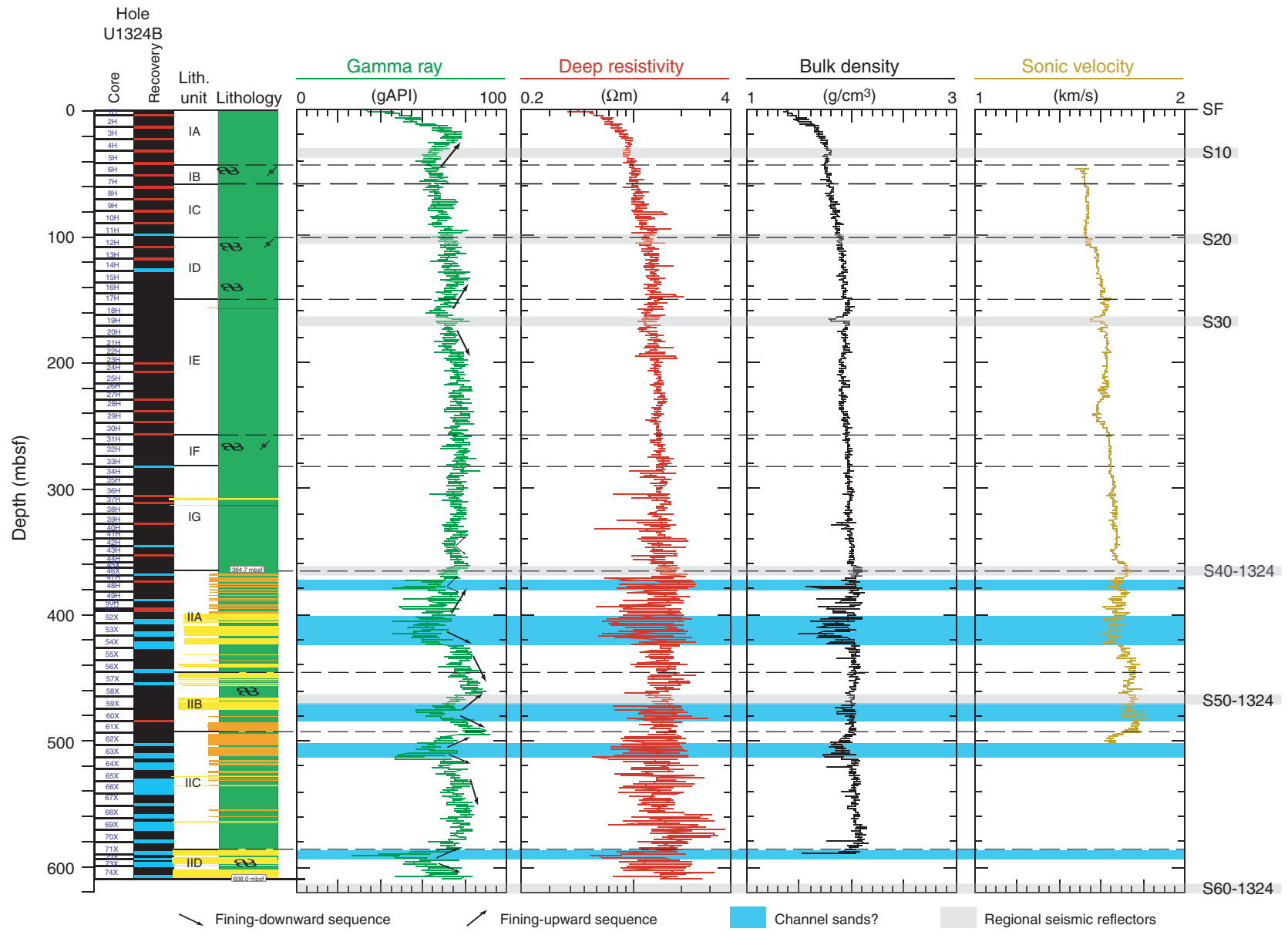
**Figure F49.** Calculated two-way traveltime (TWT) below seafloor vs. mbsf relationship for Hole U1324A including interval and sonic velocities. The function used for the conversion represents a polynomial fit (Equation E1 in the “Site U1322” chapter) through the nearby check shot data (see text for details). All data are referenced to seafloor assuming a velocity of 1490 m/s through the water column.



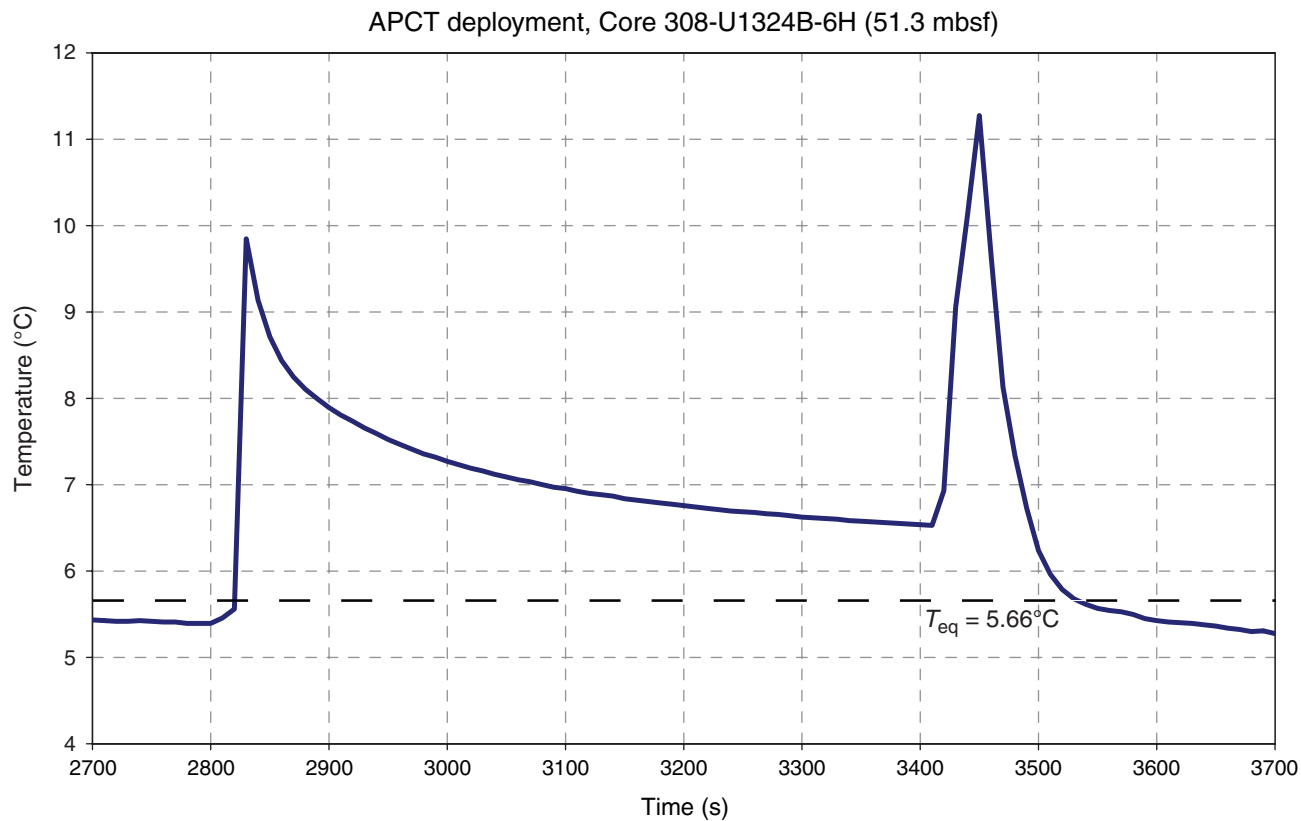
**Figure F50.** Core-log-seismic correlation for Site U1324. Synthetic seismogram was constructed by convolving a 150 Hz minimum-phase Ricker wavelet with the reflection coefficient series based on LWD bulk density and velocity log data. A seismic high-resolution trace (Hi-Res) is extracted from three-dimensional (3-D) high-resolution multichannel seismic (MCS) data at the location of Site U1324. GR = gamma ray, SF = seafloor.



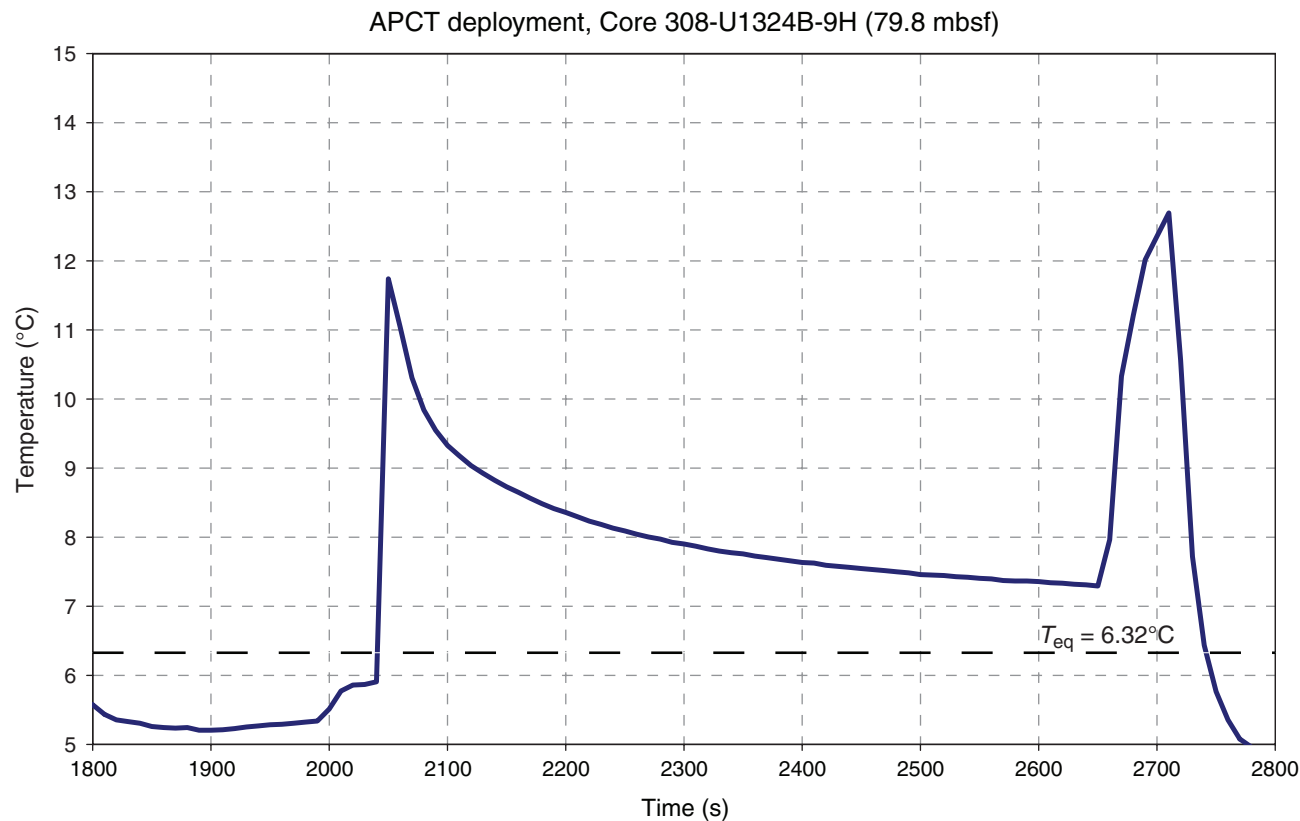
**Figure F51.** Logs from Hole U1324A used for the definition of low-relief channel deposits and changes in grain size with depth. Lithostratigraphic units and regional seismic reflectors (SF = seafloor) are shown.



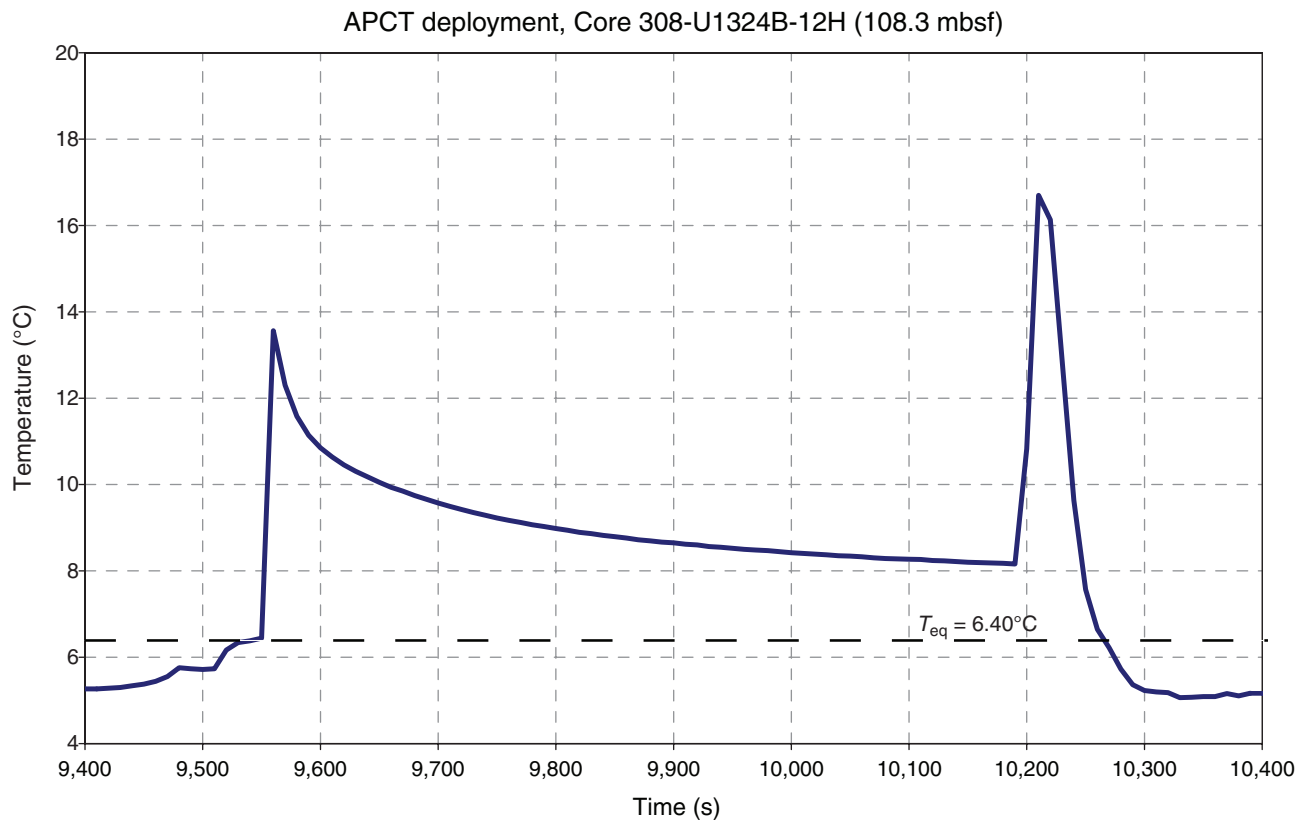
**Figure F52.** Result for the APCT tool deployment for Core 308-U1324B-6H (51.3 mbsf). Temperature was measured in the sediment for 10 min to establish the temperature decay curve (blue). Extrapolation from the dissipation curve provided an equilibrium temperature of  $5.66^{\circ}\text{C}$  (dashed line). See “Downhole” in “Supplementary material.”



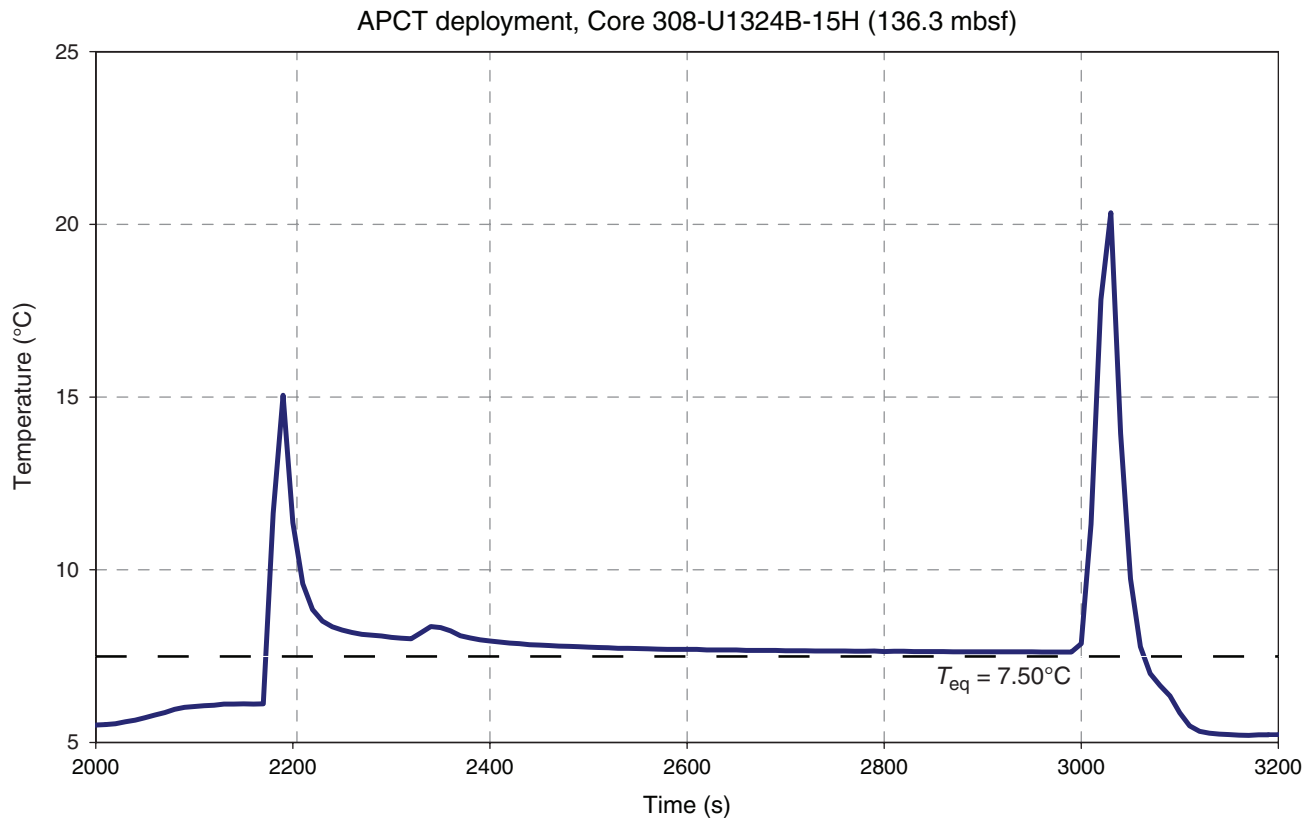
**Figure F53.** Result for the APCT tool deployment for Core 308-U1324B-9H (79.8 mbsf). Temperature was measured in the sediment for 10 min to establish the temperature decay curve (blue). Extrapolation from the dissipation curve provided an equilibrium temperature of  $6.32^{\circ}\text{C}$  (dashed line). See “Downhole” in “Supplementary material.”



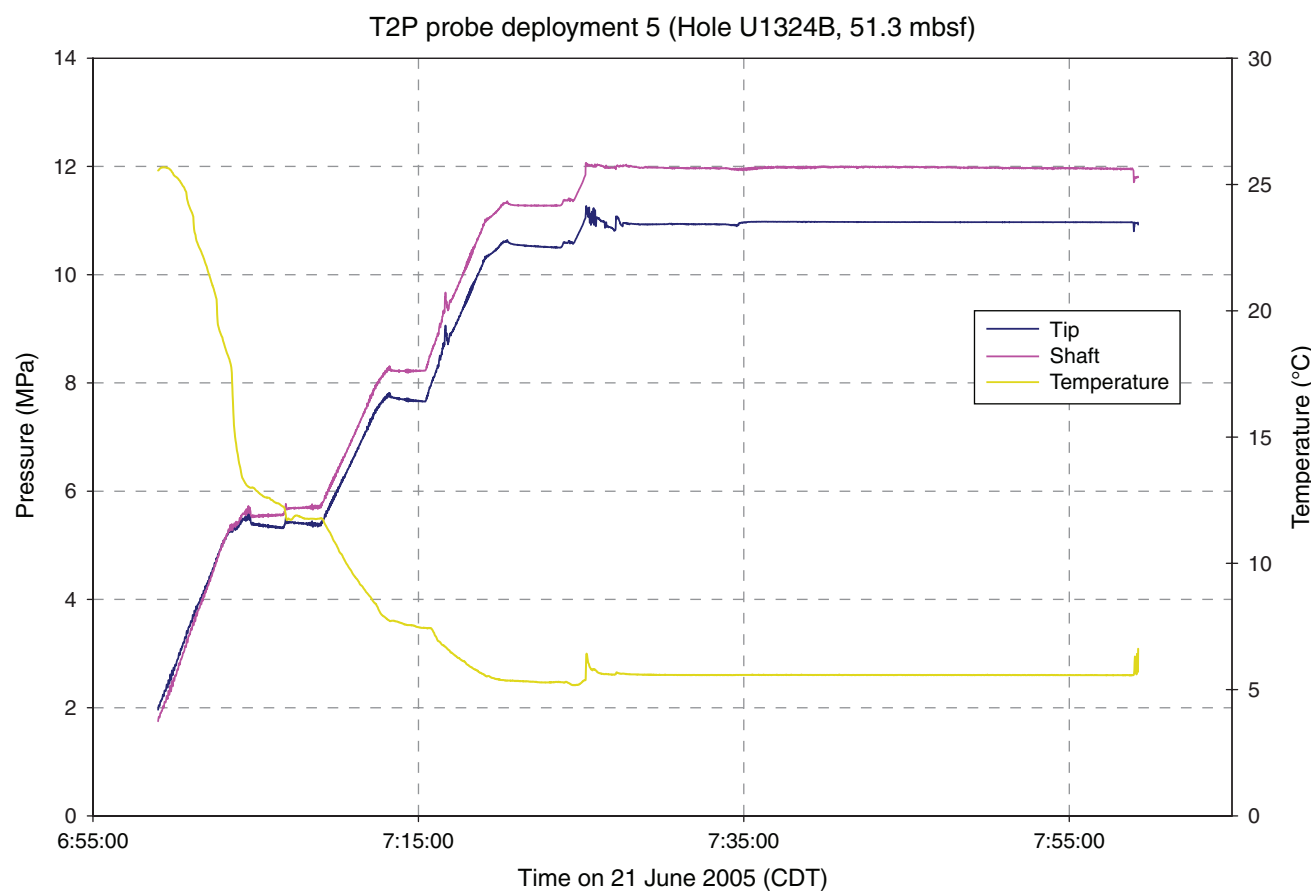
**Figure F54.** Result for the APCT tool deployment for Core 308-U1324B-12H (108.3 mbsf). Temperature was measured in the sediment for 10 min to establish the temperature decay curve (blue). Extrapolation from the dissipation curve provided an equilibrium temperature of 6.40°C (dashed line). See “Downhole” in “[Supplementary material](#).”



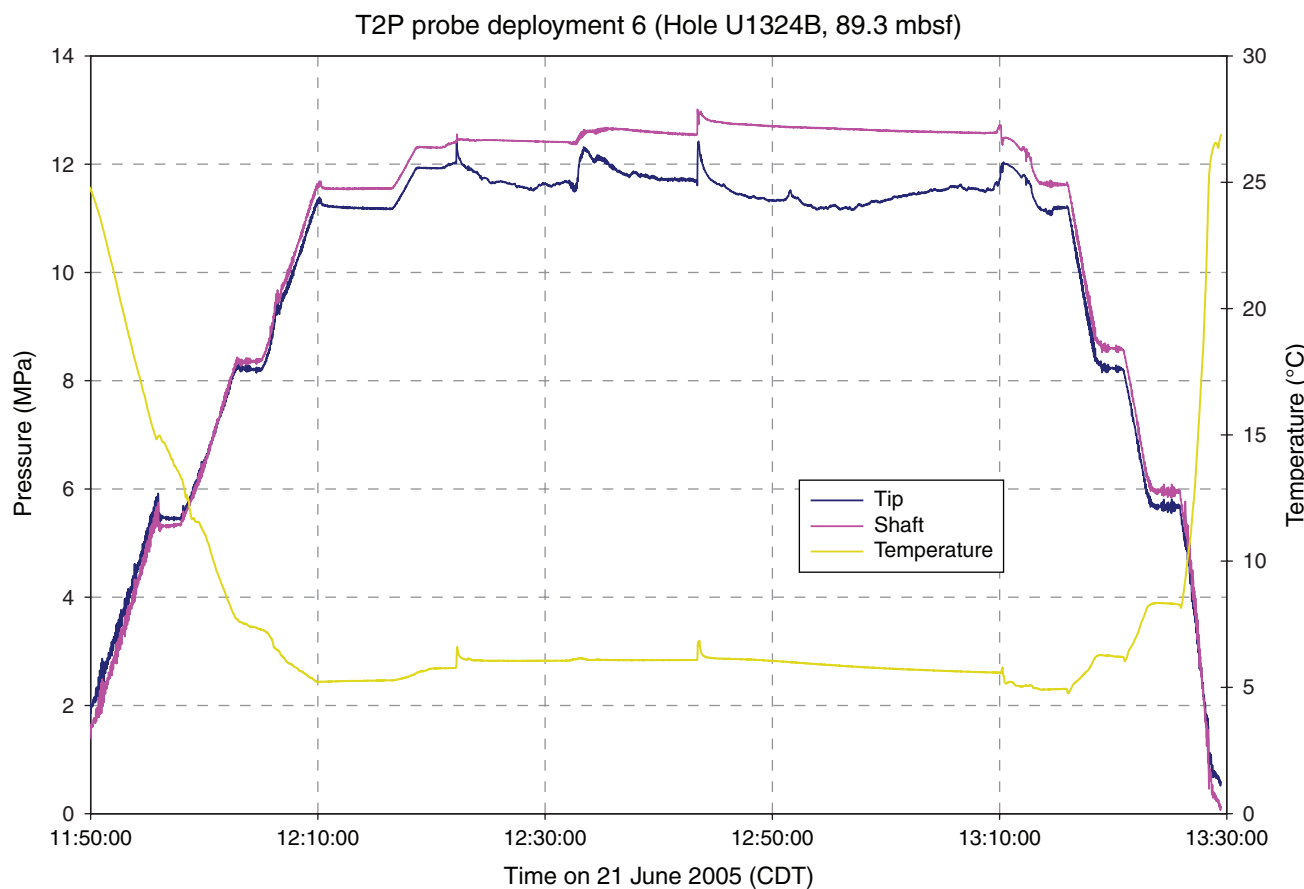
**Figure F55.** Result for the APCT tool deployment for Core 308-U1324B-15H (127.3 mbsf). Temperature was measured in the sediment for 10 min to establish the temperature decay curve (blue). Extrapolation from the dissipation curve provided an equilibrium temperature of 7.50°C (dashed line). See “Downhole” in “[Supplementary material](#).”



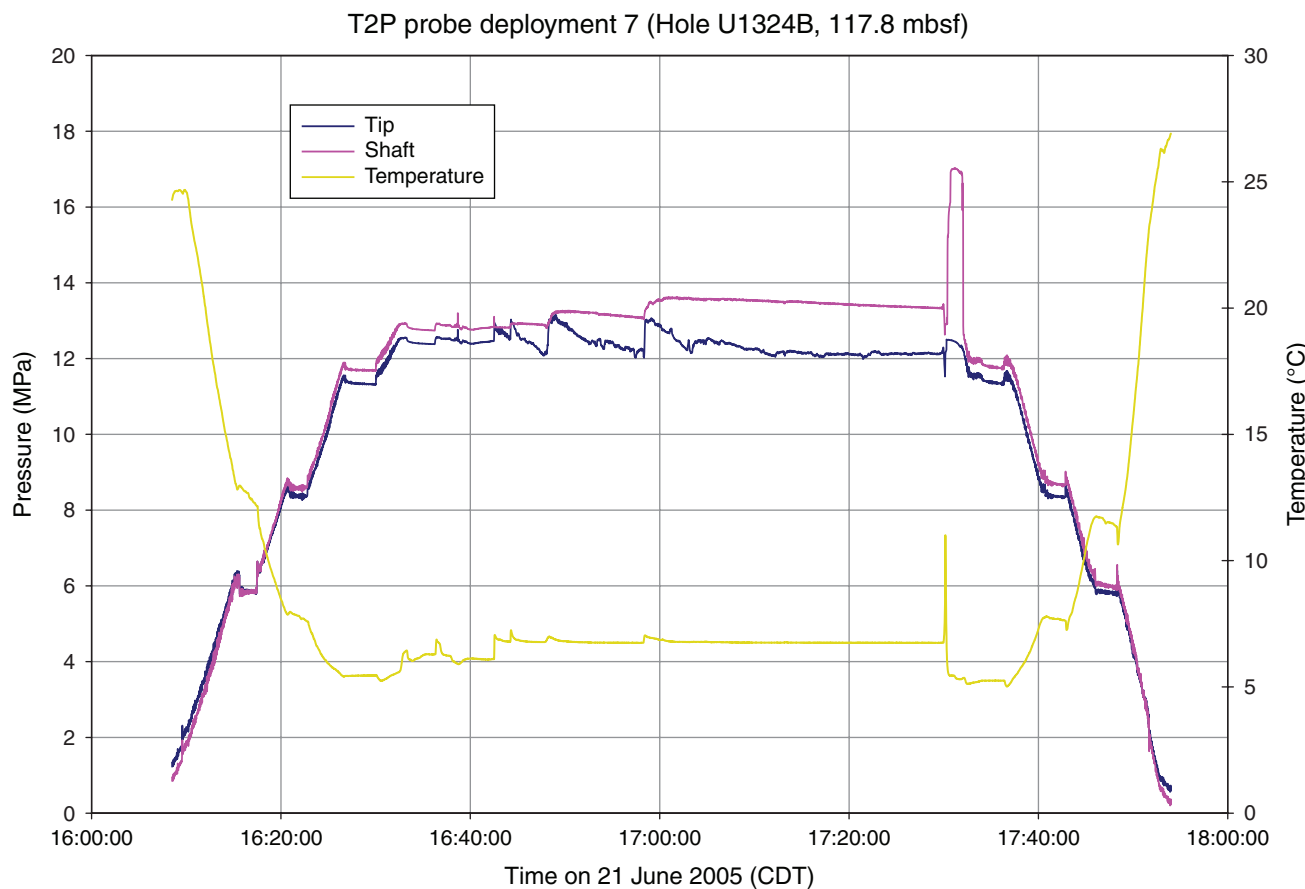
**Figure F56.** Fluid pressure and temperature measured by the temperature/dual pressure (T2P) probe during Deployment 5. CDT = central daylight time. See “Downhole” in “[Supplementary material](#).”



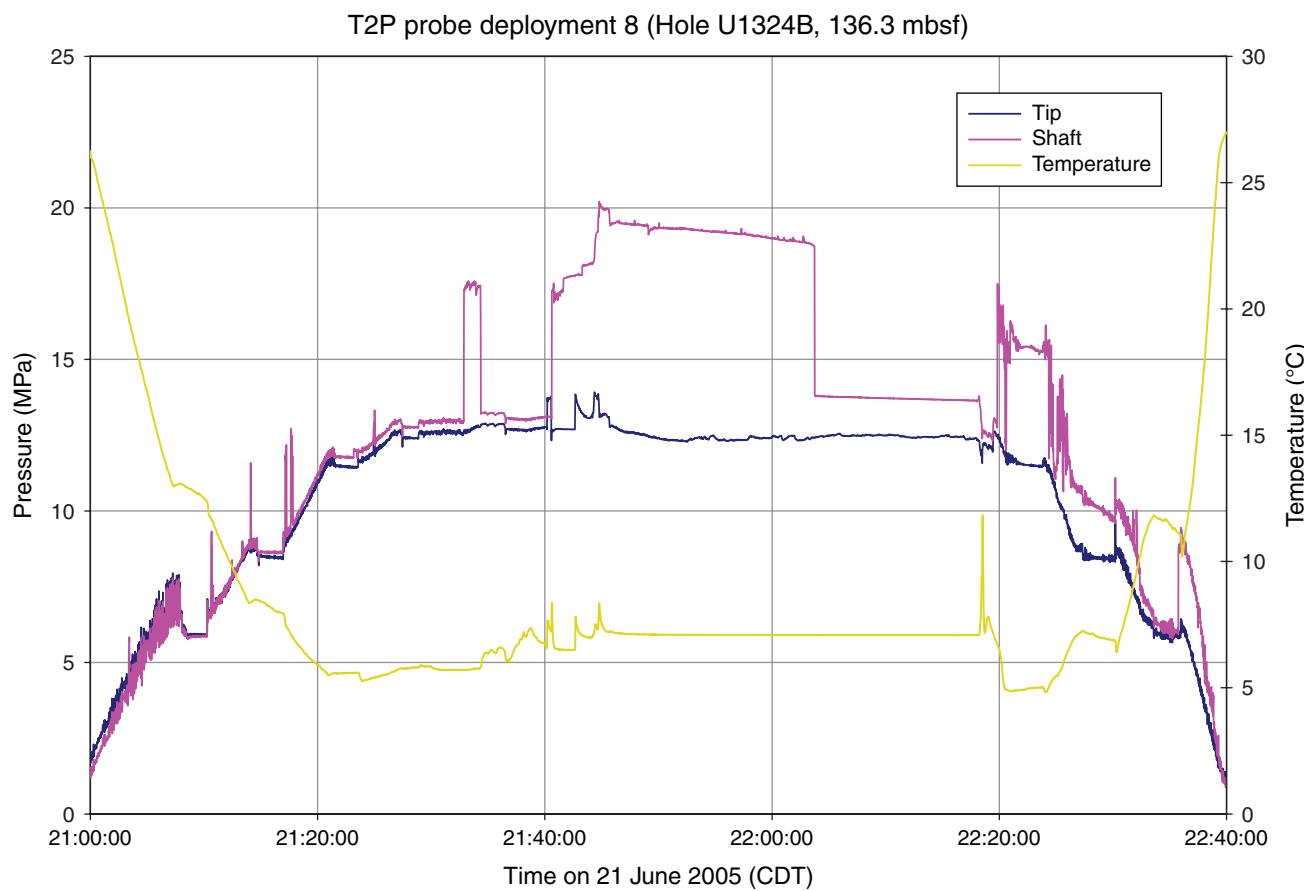
**Figure F57.** Fluid pressure and temperature measured by the temperature/dual pressure (T2P) probe during Deployment 6. CDT = central daylight time. See “Downhole” in “[Supplementary material](#).”



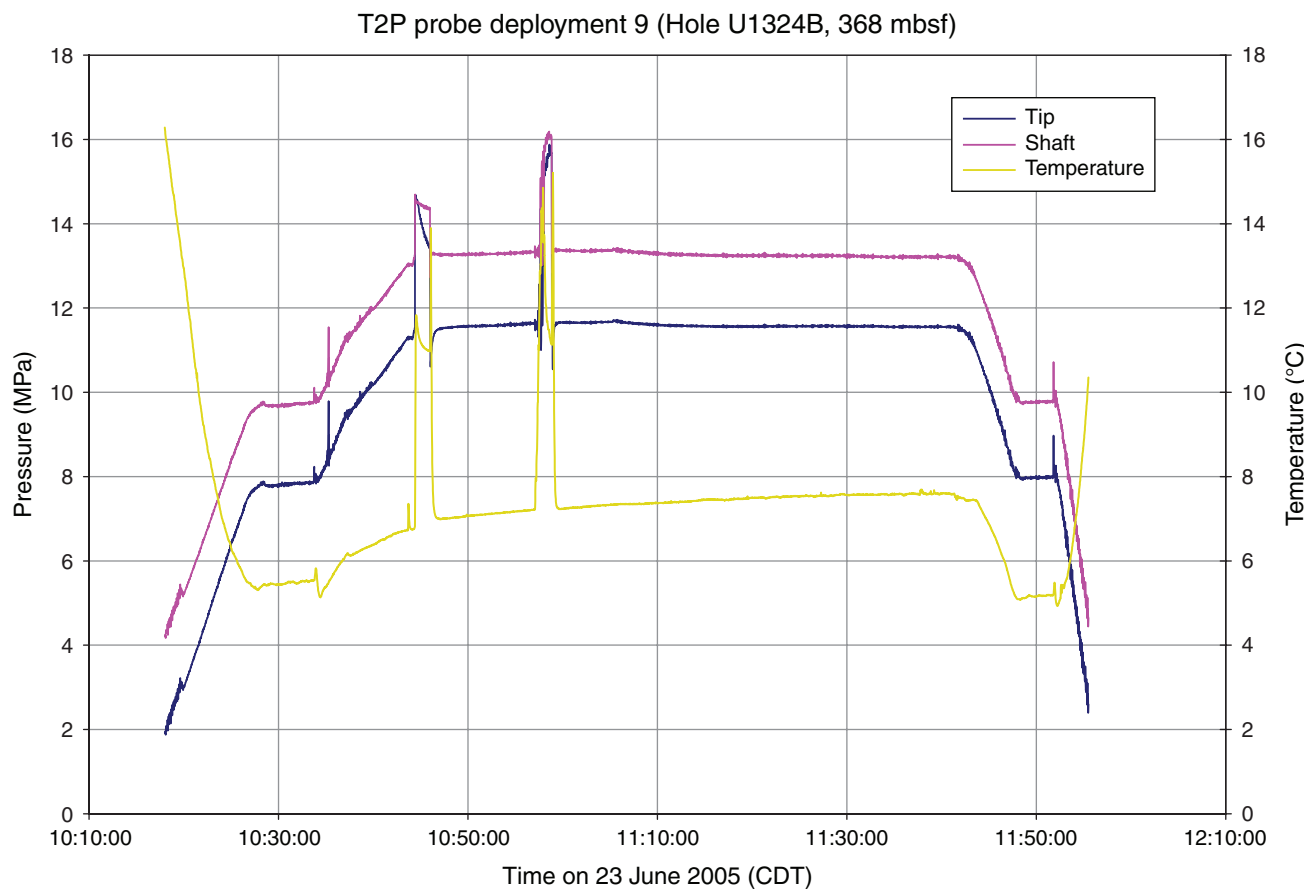
**Figure F58.** Fluid pressure and temperature measured by the temperature/dual pressure (T2P) probe during Deployment 7. CDT = central daylight time. See “Downhole” in “[Supplementary material](#).”



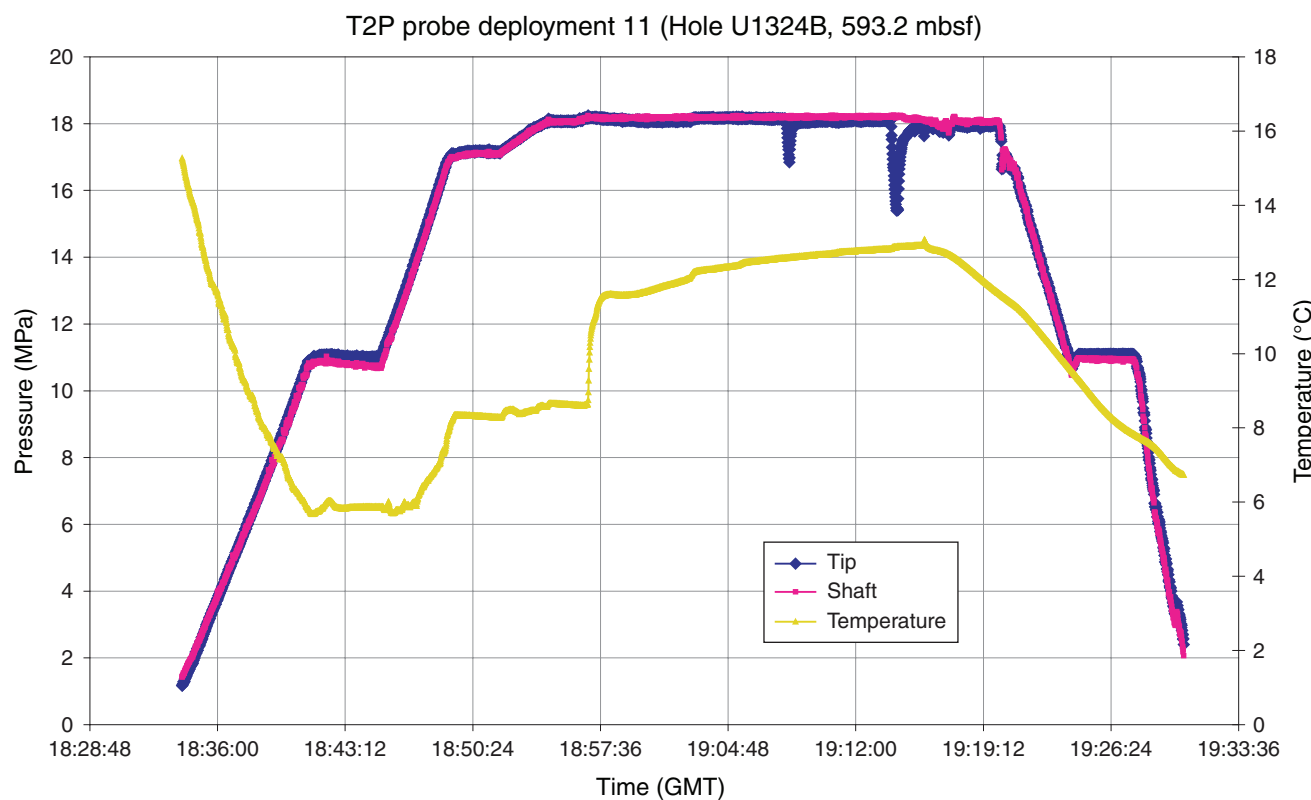
**Figure F59.** Fluid pressure and temperature measured by the temperature/dual pressure (T2P) probe during Deployment 8. CDT = central daylight time. See “Downhole” in “[Supplementary material](#).”



**Figure F60.** Fluid pressure and temperature measured by the temperature/dual pressure (T2P) probe during Deployment 9. CDT = central daylight time. See “Downhole” in “[Supplementary material](#).”



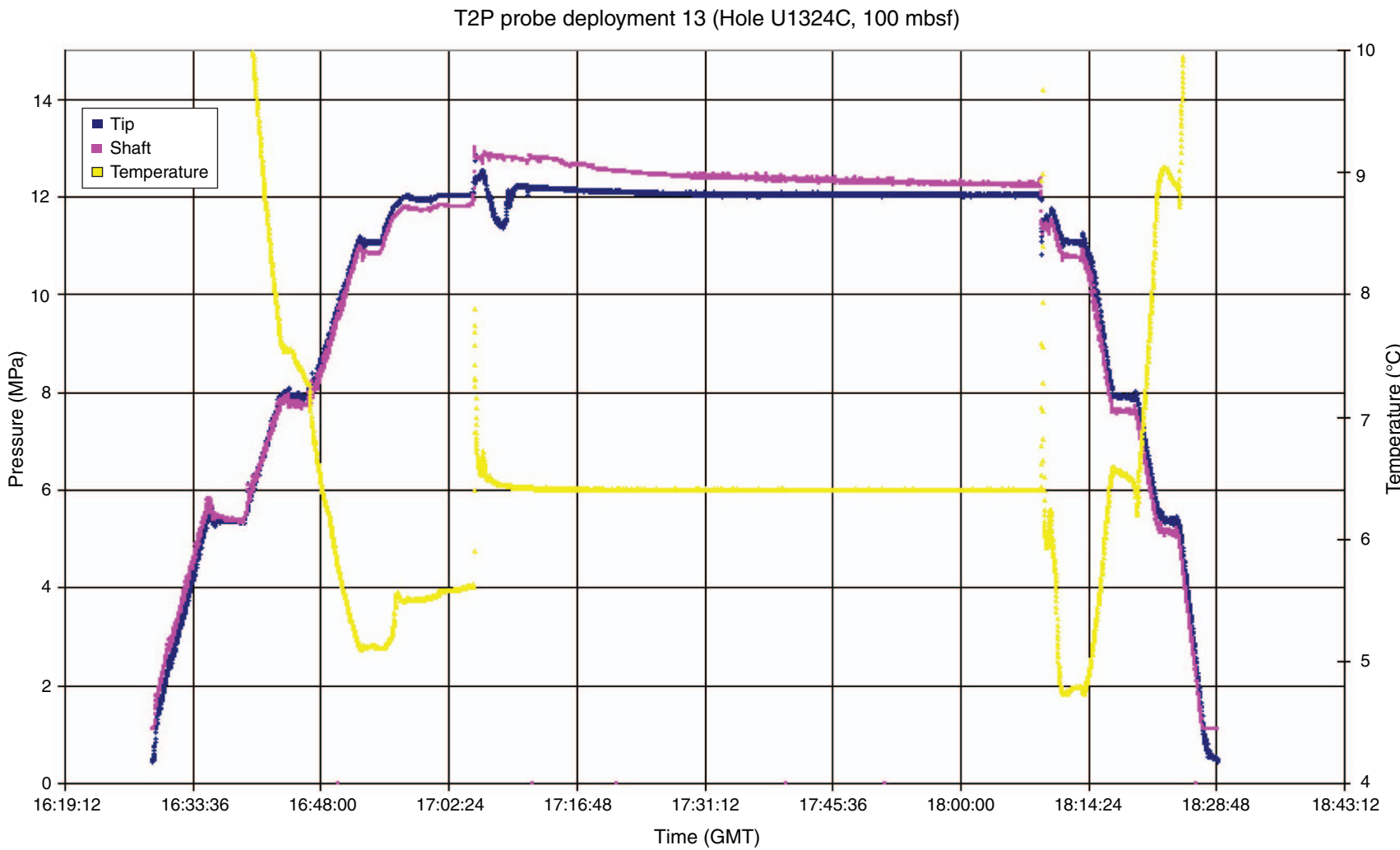
**Figure F61.** Fluid pressure and temperature measured by the temperature/dual pressure (T2P) probe during Deployment 11. CDT = central daylight time. See “Downhole” in “[Supplementary material](#).”



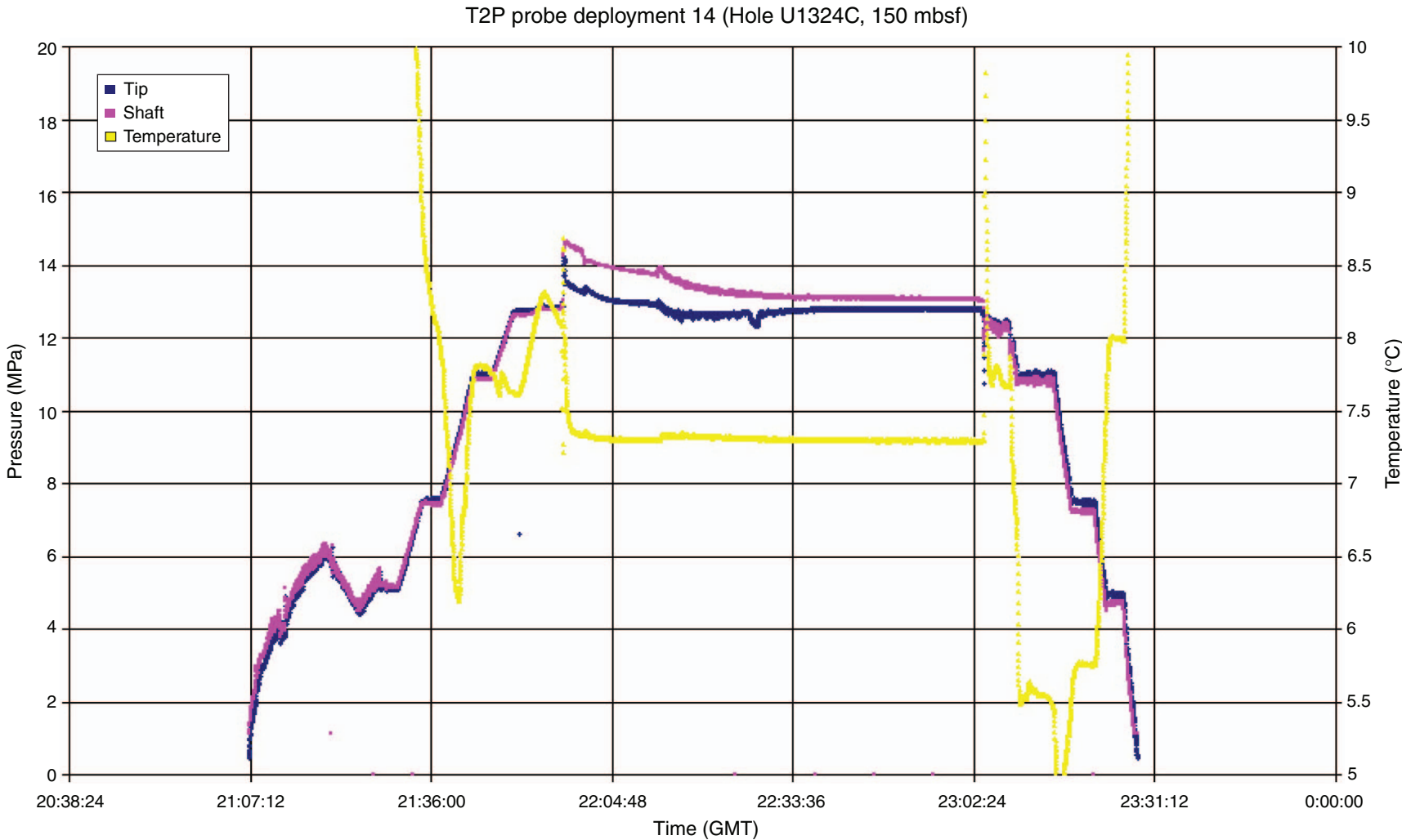
**Figure F62.** Fluid pressure and temperature measured by the temperature/dual pressure (T2P) probe Deployment 12. Ph\_500 = hydrostatic pressure at 500 mbsl, Ph\_750 = hydrostatic pressure at 75 mbsl, and Ph-mudline = hydrostatic pressure at seafloor. GMT = Greenwich Mean Time. See “Downhole” in [“Supplementary material.”](#)



Figure F63. Fluid pressure and temperature measured by the temperature/dual pressure (T2P) probe during Deployment 13. GMT = Greenwich Mean Time. See “Downhole” in “[Supplementary material](#).”



**Figure F64.** Fluid pressure and temperature measured by the temperature/dual pressure (T2P) probe during Deployment 14. GMT = Greenwich Mean Time. See “Downhole” in “[Supplementary material](#).”



**Figure F65.** Fluid pressure and temperature measured by the temperature/dual pressure (T2P) probe during Deployment 15. GMT = Greenwich Mean Time. See “Downhole” in “[Supplementary material](#).”

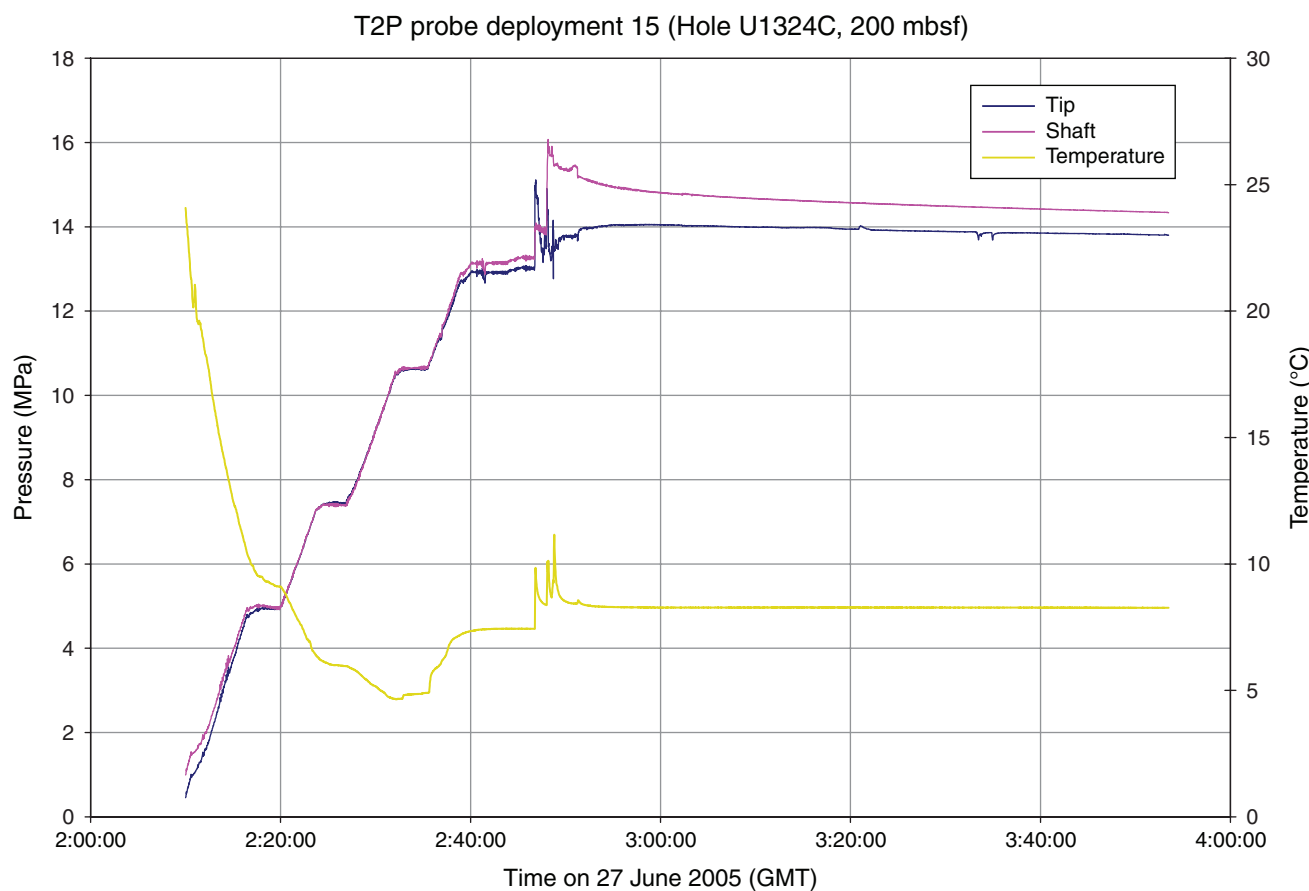


**Figure F66.** Fluid pressure and temperature measured by the temperature/dual pressure (T2P) probe during Deployment 16. GMT = Greenwich Mean Time. See “Downhole” in “[Supplementary material](#).”

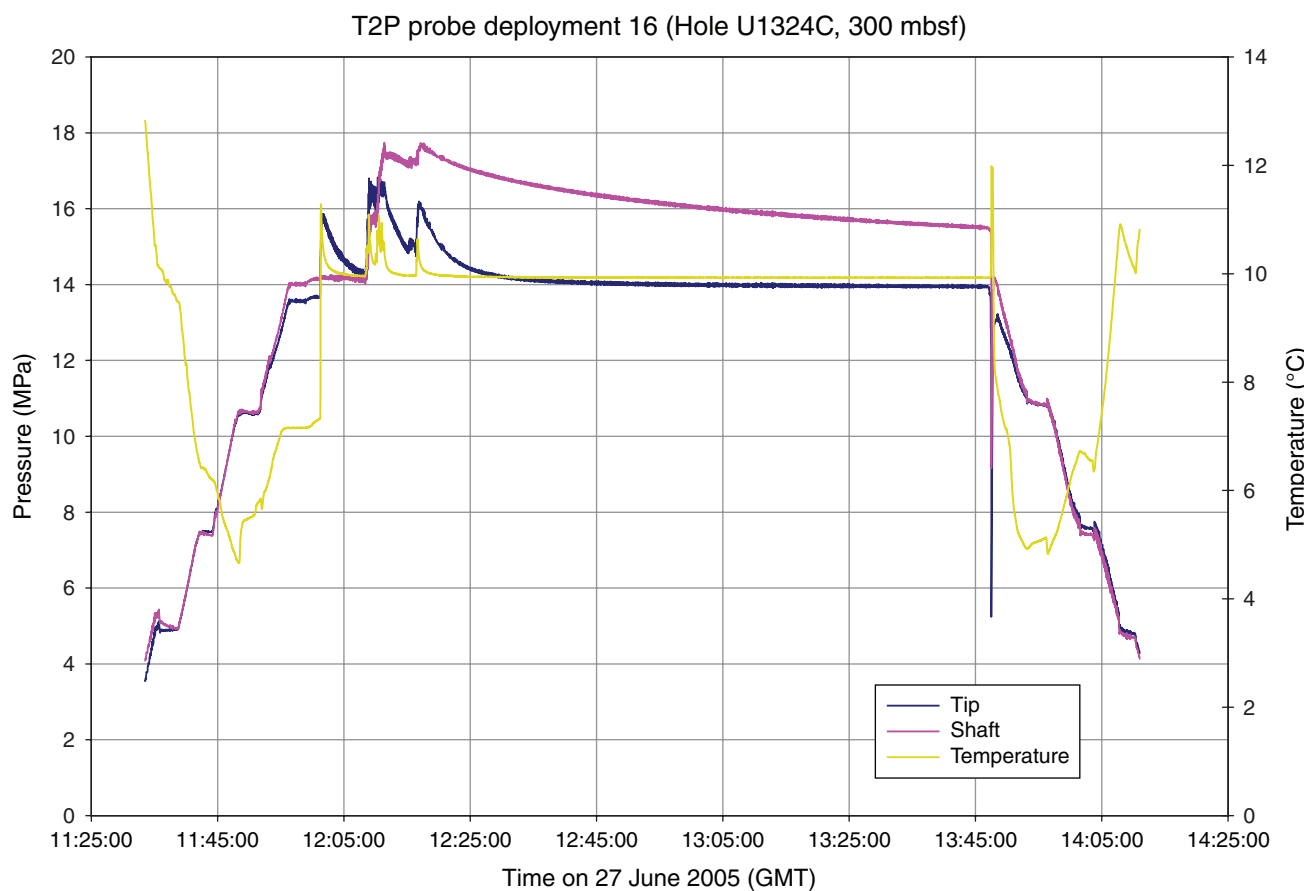


**Figure F67.** Fluid pressure and temperature measured by the Davis Villinger Temperature Pressure probe (DVTTP) during Deployment 3. GMT = Greenwich Mean Time. See “Downhole” in “[Supplementary material](#).”

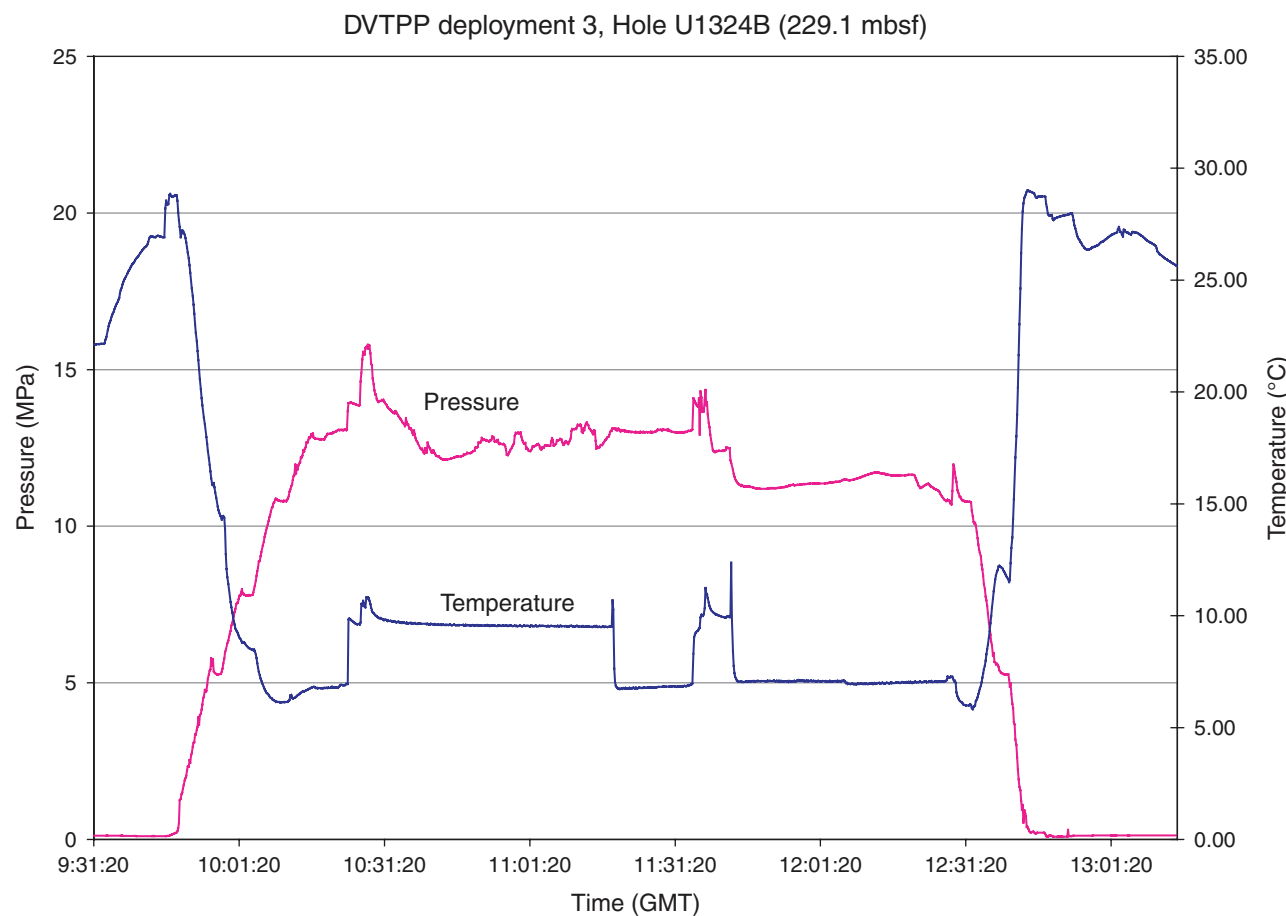


**Figure F68.** Fluid pressure and temperature measured by the Davis Villinger Temperature Pressure probe (DVTTP) during Deployment 4. GMT = Greenwich Mean Time. See “Downhole” in “[Supplementary material](#).”

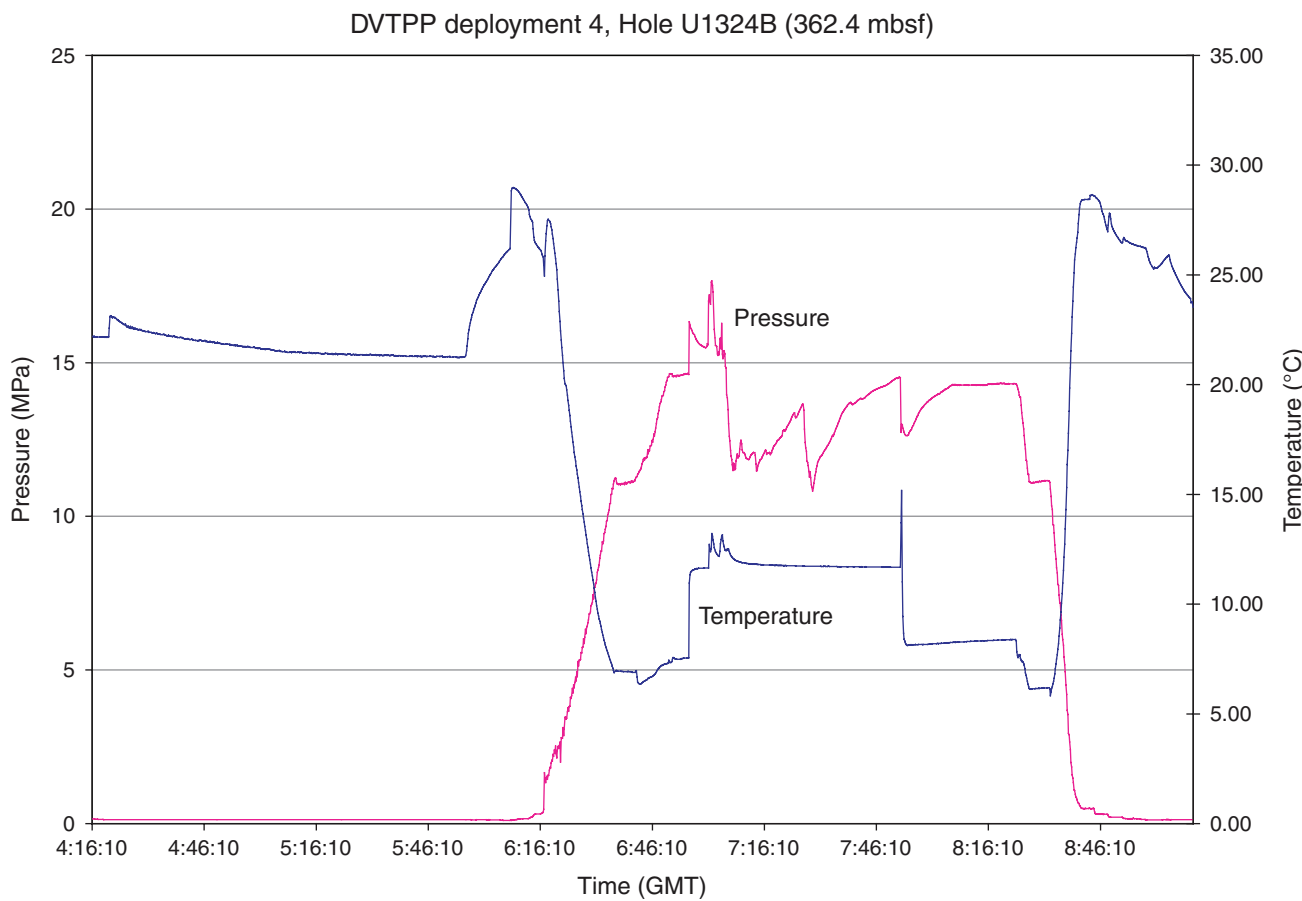


**Figure F69.** Fluid pressure and temperature measured by the Davis Villinger Temperature Pressure probe (DVTTP) during Deployment 6. GMT = Greenwich Mean Time. See “Downhole” in “[Supplementary material](#).”

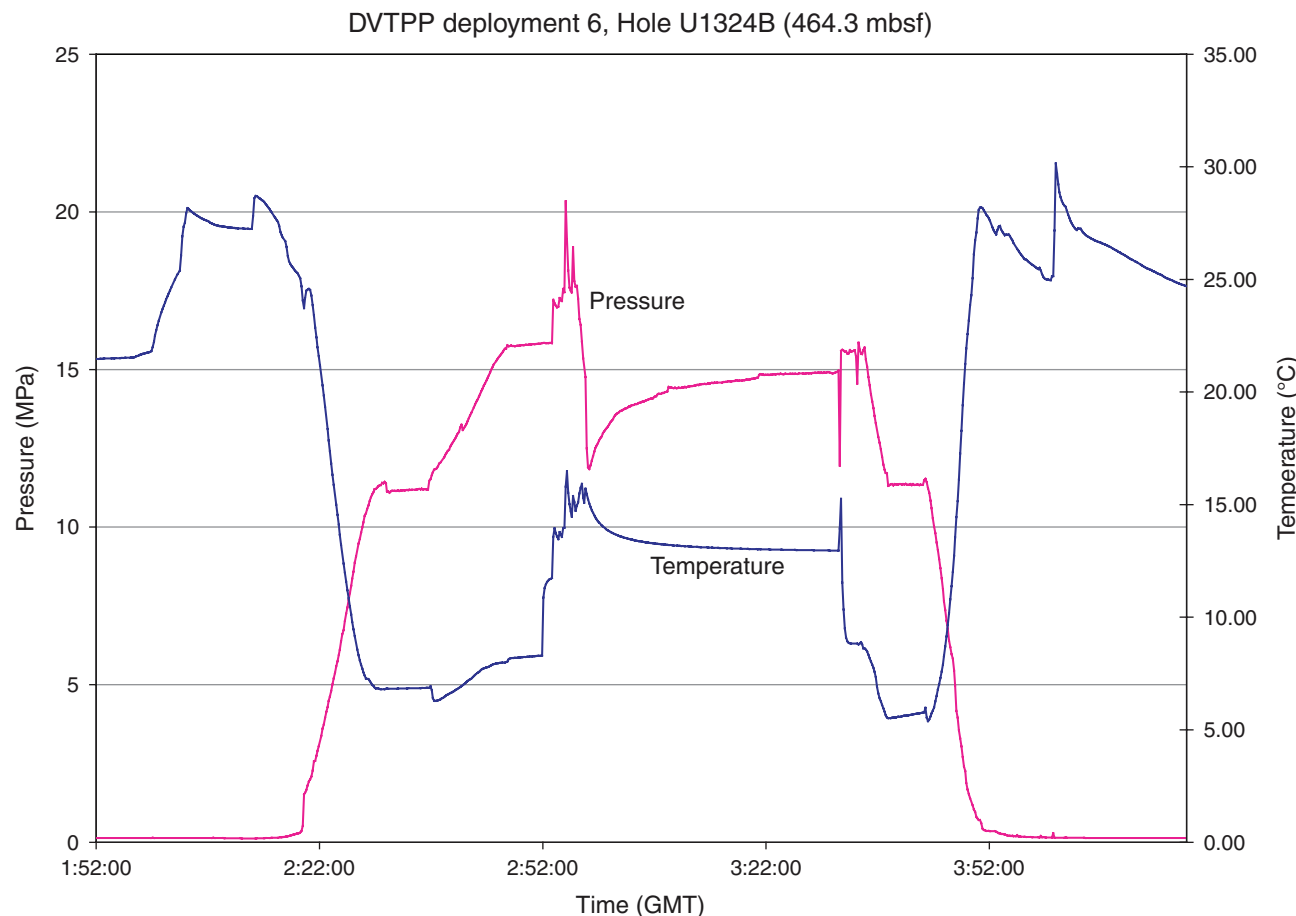


**Figure F70.** Fluid pressure and temperature measured by the Davis Villinger Temperature Pressure probe (DVTTP) during Deployment 7. GMT = Greenwich Mean Time. See “Downhole” in “[Supplementary material](#).”

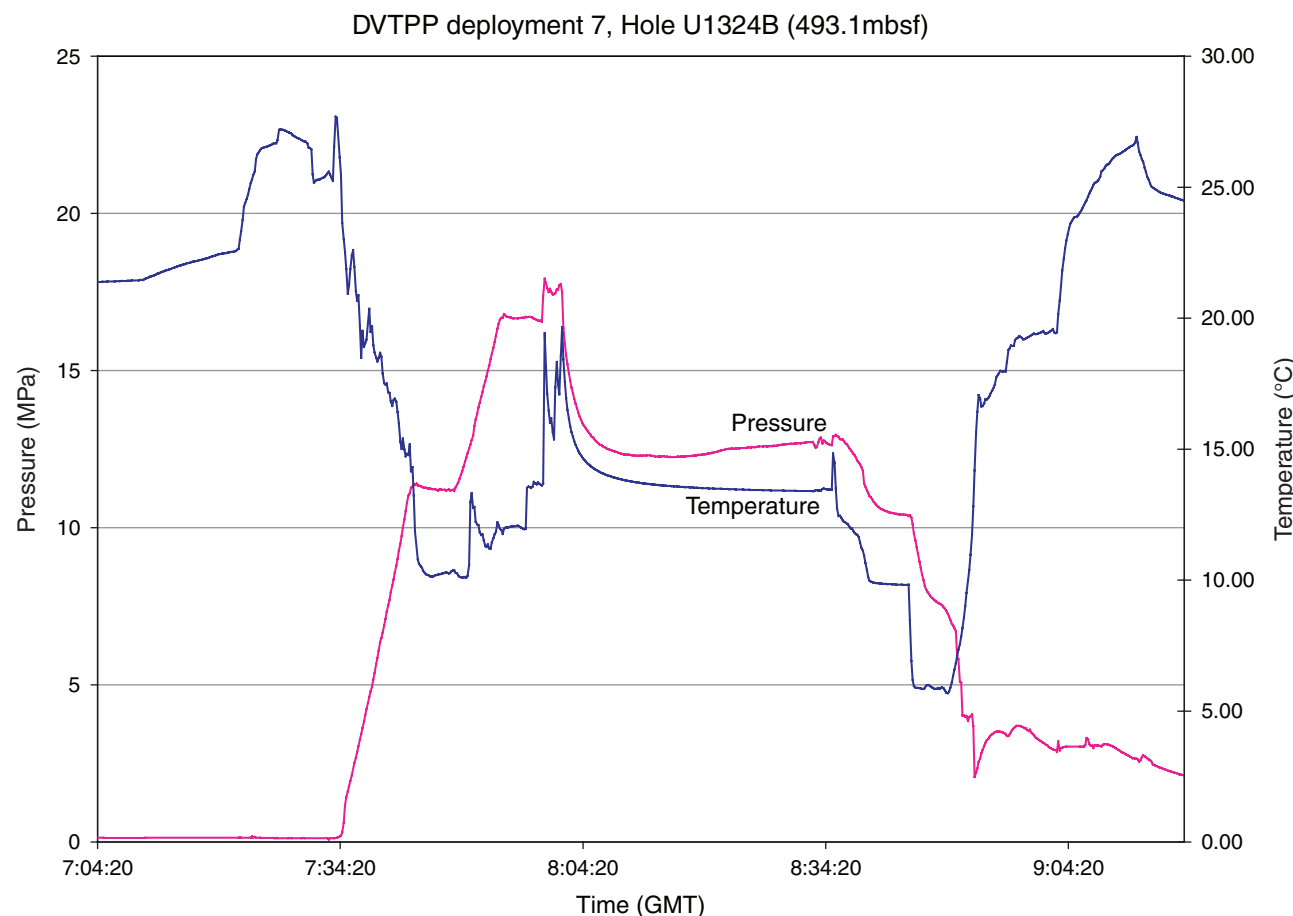


**Figure F71.** Fluid pressure and temperature measured by the Davis Villinger Temperature Pressure probe (DVTTP) during Deployment 8. GMT = Greenwich Mean Time. See “Downhole” in “[Supplementary material](#).”

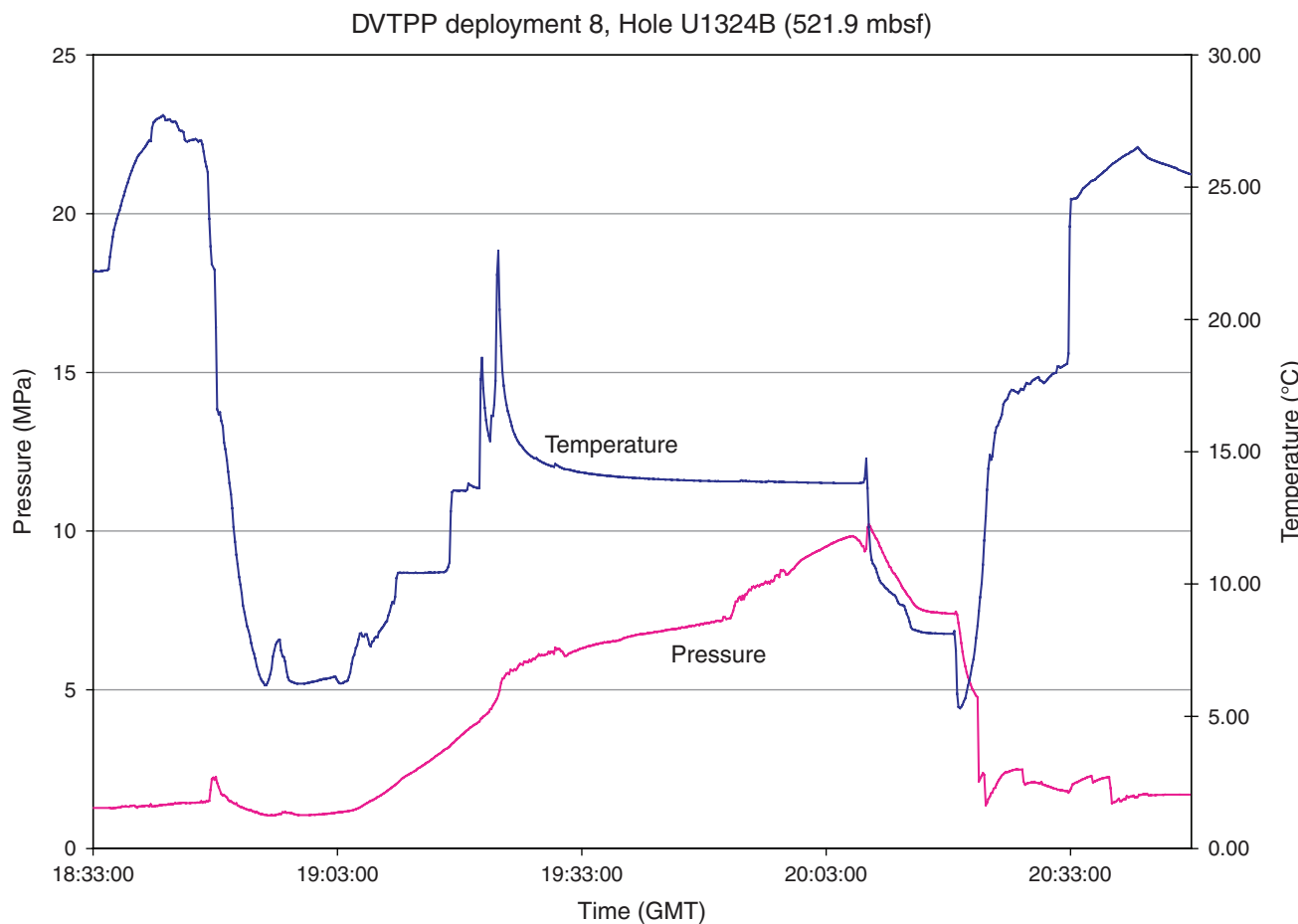


**Figure F72.** Fluid pressure and temperature measured by the Davis Villinger Temperature Pressure probe (DVTTP) during Deployment 10. GMT = Greenwich Mean Time. See “Downhole” in “[Supplementary material](#).”

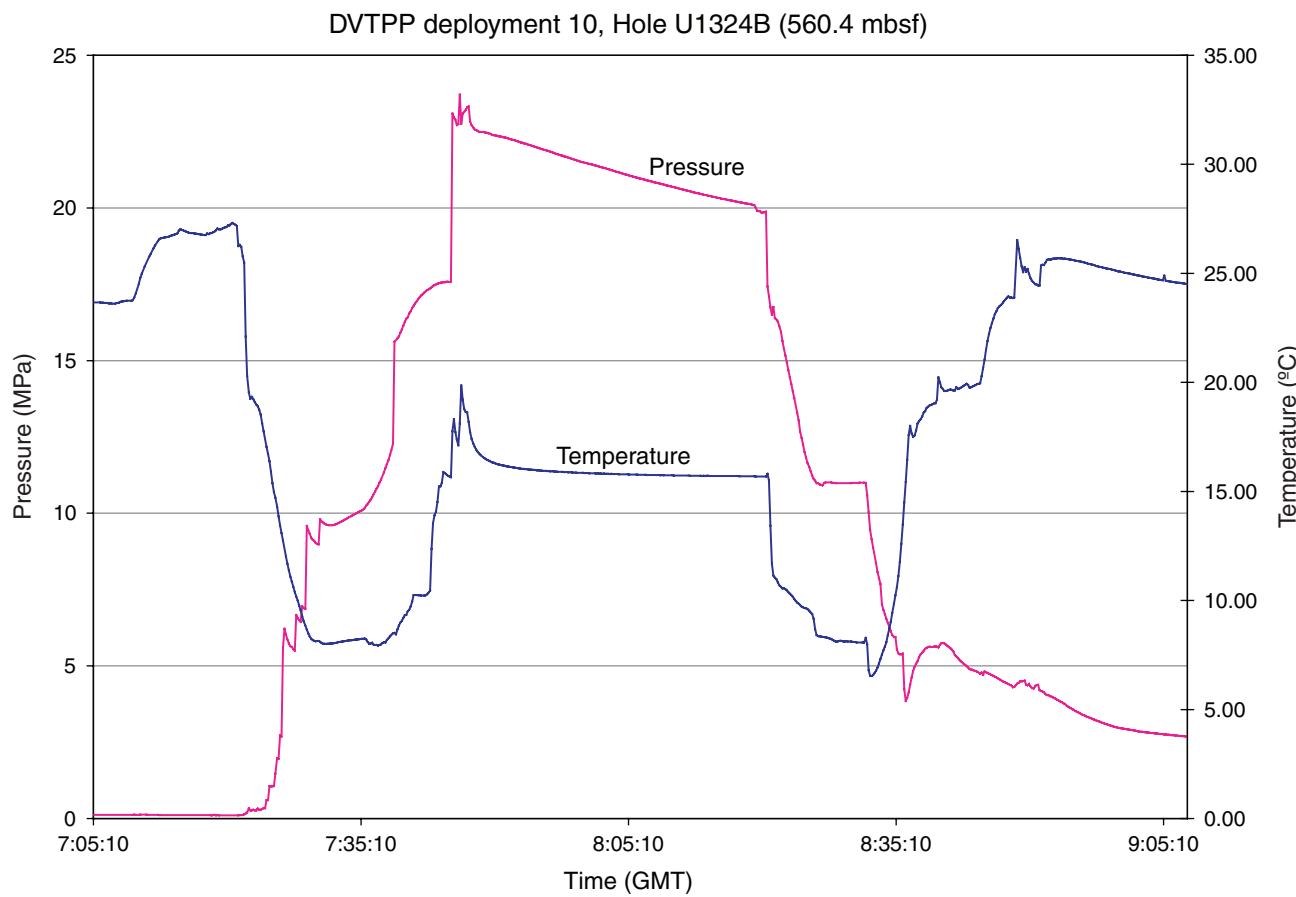


**Figure F73.** Fluid pressure and temperature measured by the Davis Villinger Temperature Pressure probe (DVTTP) during Deployment 11. GMT = Greenwich Mean Time. See “Downhole” in “[Supplementary material](#).”

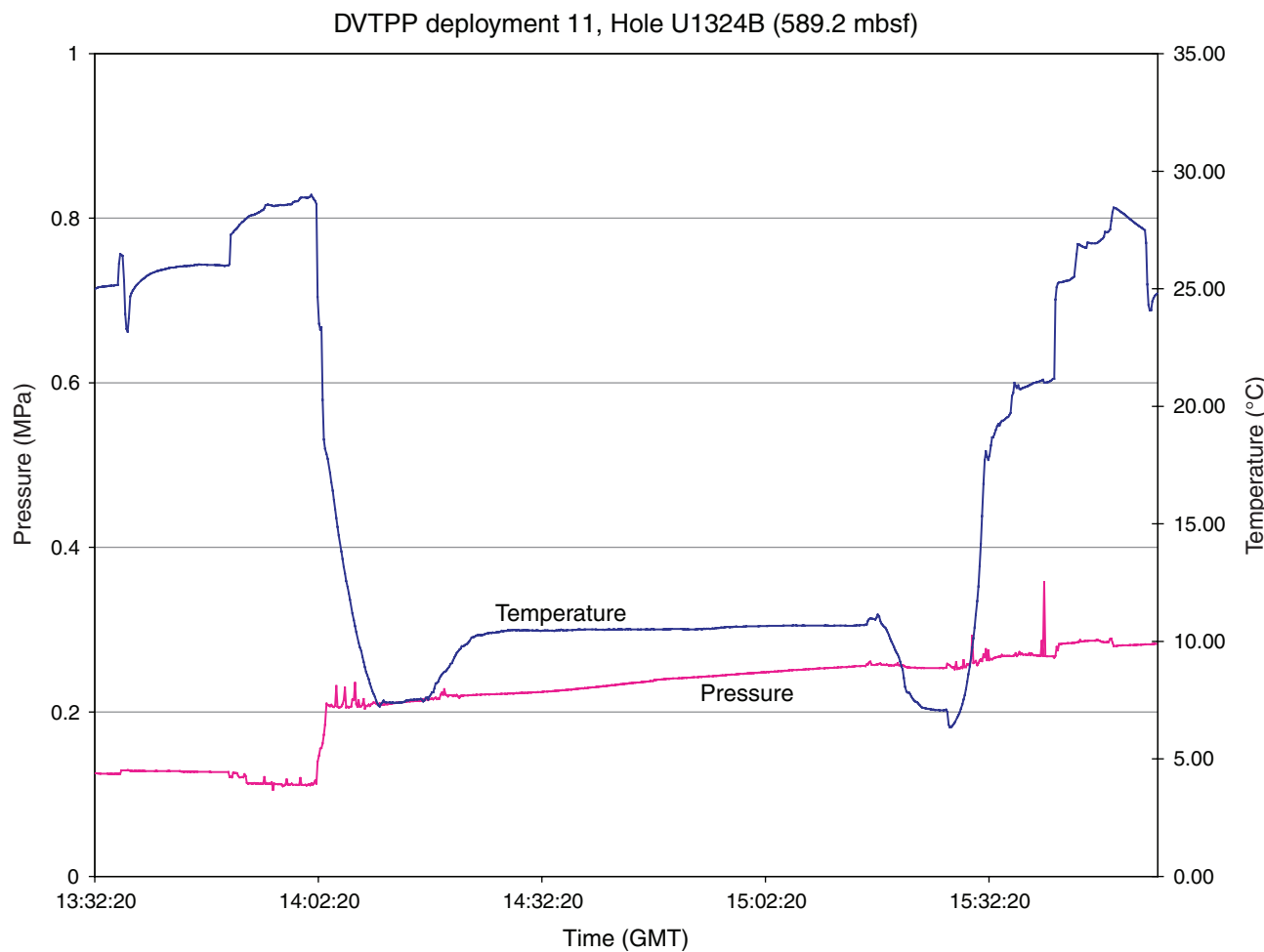


**Figure F74.** Fluid pressure and temperature measured by the Davis Villinger Temperature Pressure probe (DVTTP) during Deployment 12. GMT = Greenwich Mean Time. See “Downhole” in “[Supplementary material](#).”

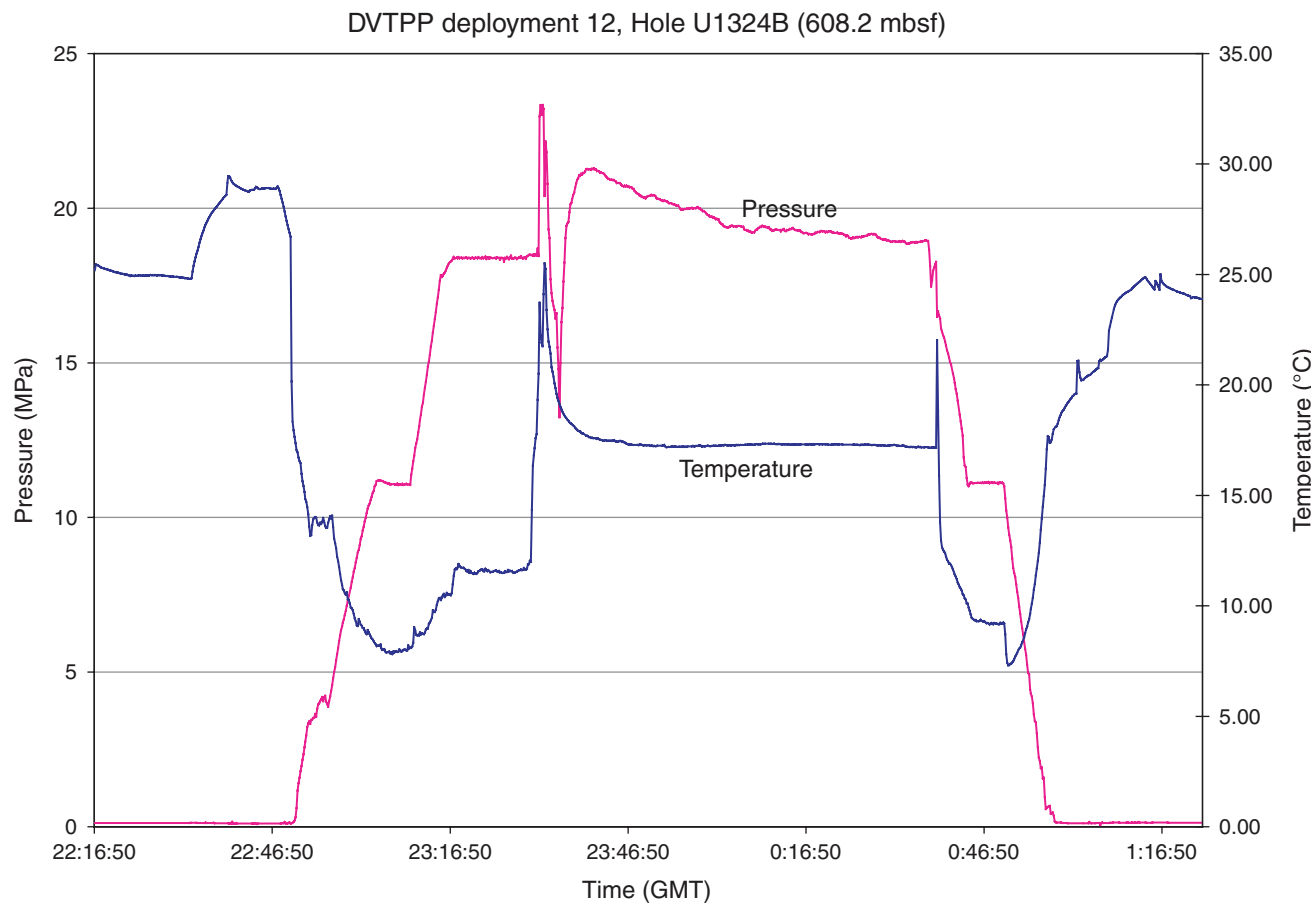


**Figure F75.** Fluid pressure and temperature measured by the Davis Villinger Temperature Pressure probe (DVTTP) during Deployment 13. GMT = Greenwich Mean Time. See “Downhole” in [“Supplementary material.”](#)

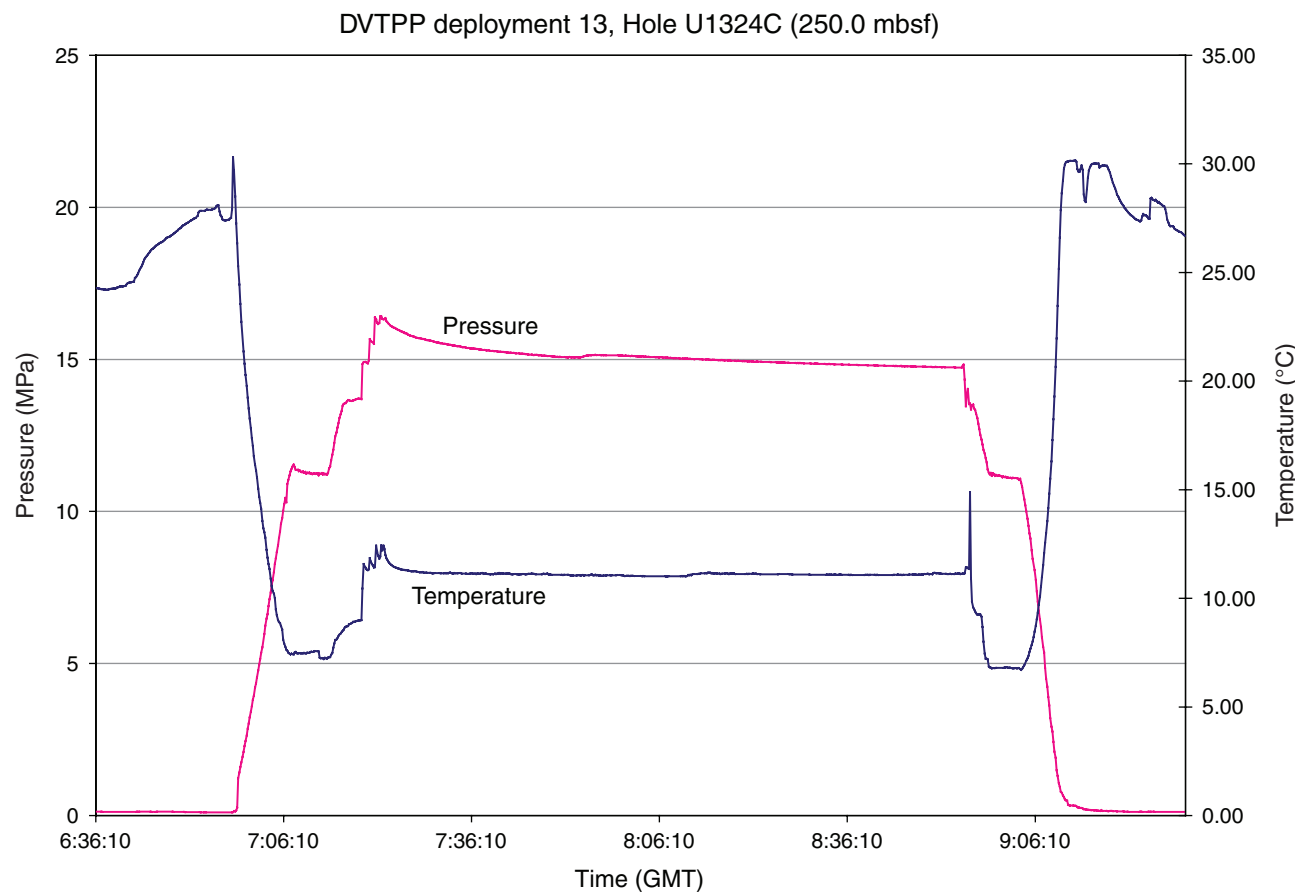


**Figure F76.** Fluid pressure and temperature measured by the Davis Villinger Temperature Pressure probe (DVTTP) during Deployment 14. GMT = Greenwich Mean Time. See “Downhole” in [“Supplementary material.”](#)

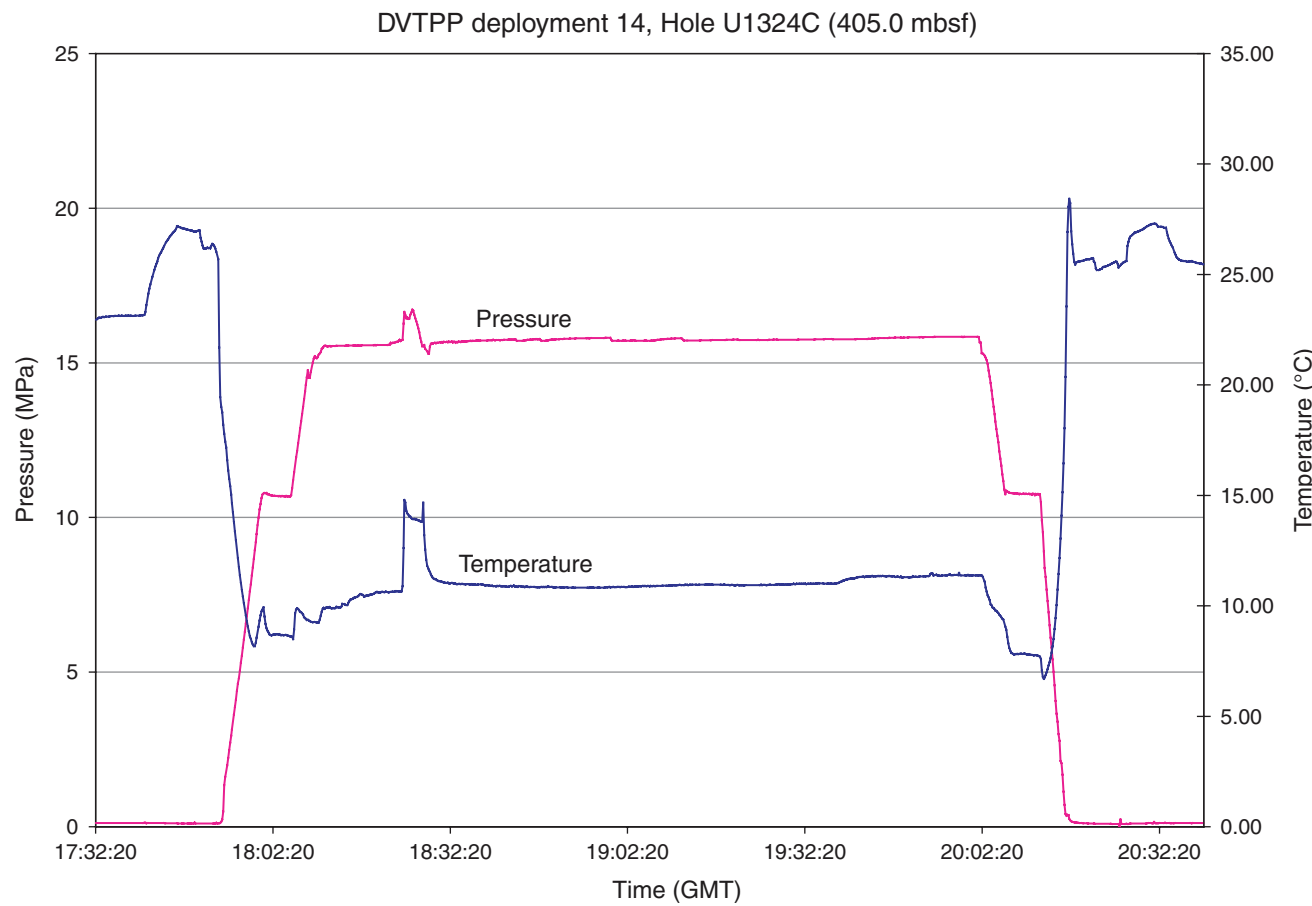


**Figure F77.** Fluid pressure and temperature measured by the Davis Villinger Temperature Pressure probe (DVTTP) during Deployment 15. GMT = Greenwich Mean Time. See “Downhole” in “[Supplementary material](#).”

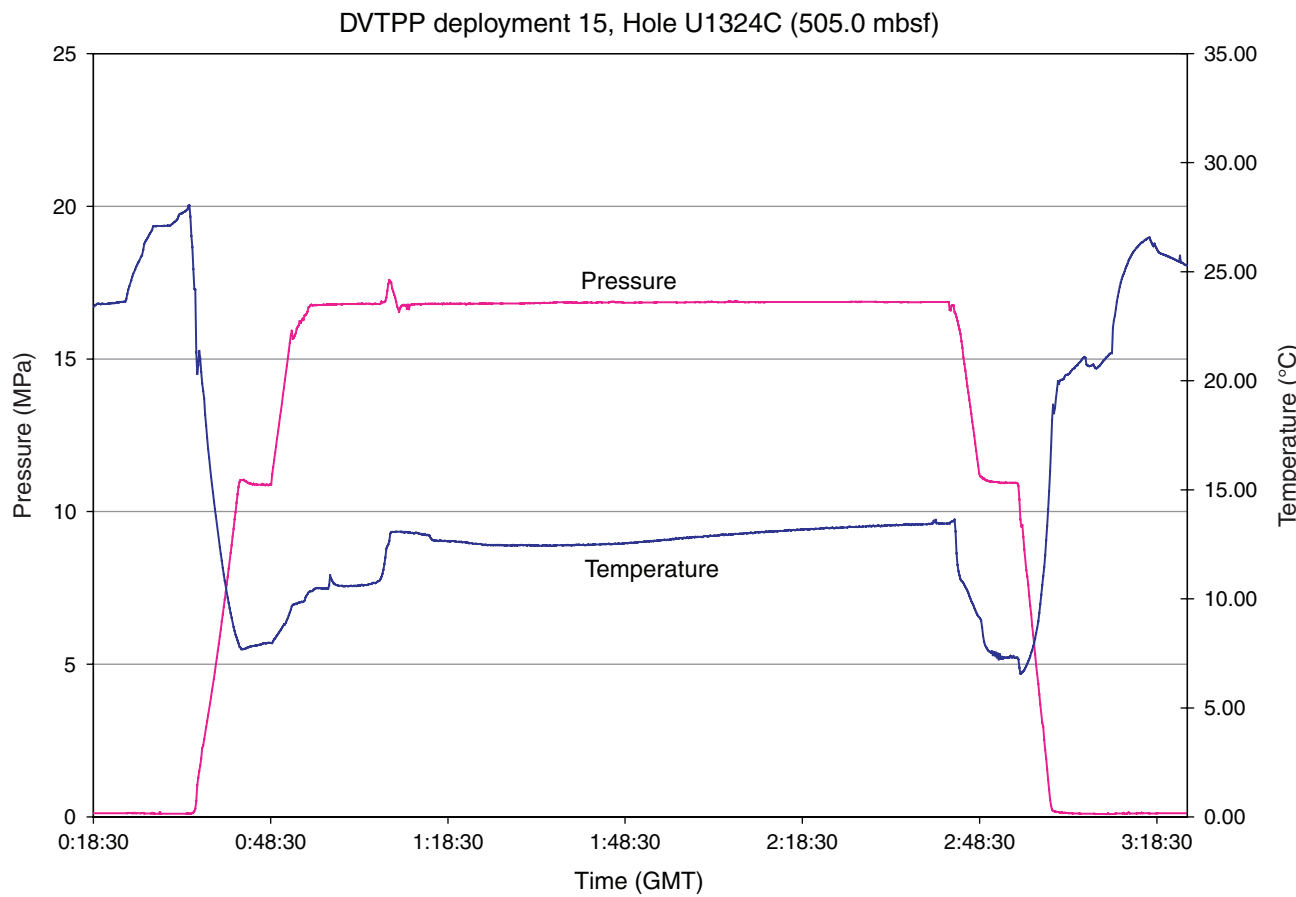


**Figure F78.** Equilibrium temperatures from the Advanced Piston Corer Temperature (APCT) tool, temperature/dual pressure (T2P) probe, and the Davis-Villinger Temperature-Pressure Probe (DVTTP). Black line = linear regression of the measured temperatures which provides an average gradient of  $18.4^{\circ}\text{C}/\text{km}$ .

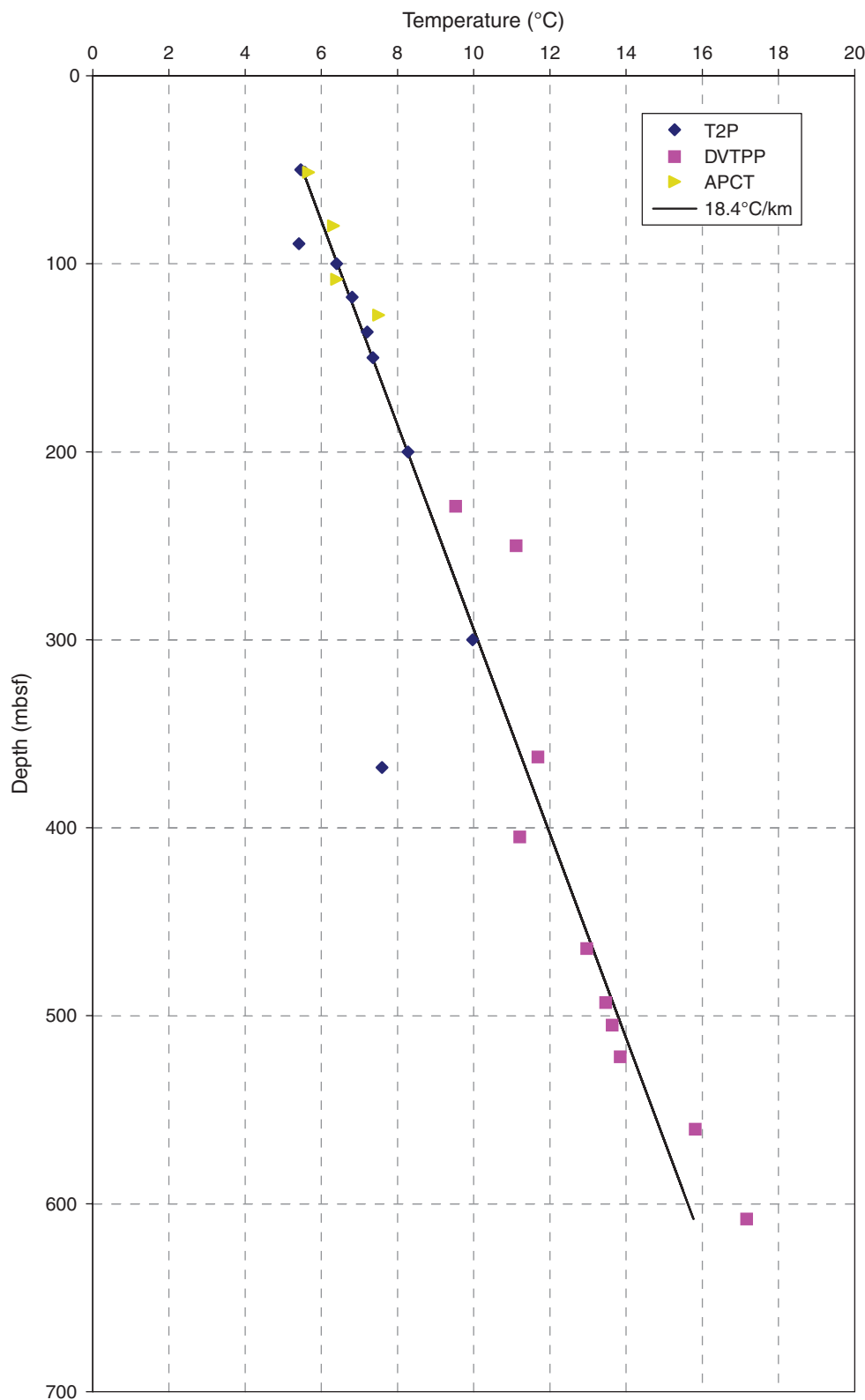


**Figure F79.** Maximum in situ pressures estimated from the last measurement on pressure dissipation curves from the temperature/dual pressure (T2P) probe and the Davis-Villinger Temperature-Pressure Probe (DVTTP). Hydrostatic pressure is calculated for an assumed water density of 1.024 g/cm<sup>3</sup>. Lithostatic stress is calculated for an assumed bulk density of 1.700 g/cm<sup>3</sup>. All pressure data are referenced to the seafloor.

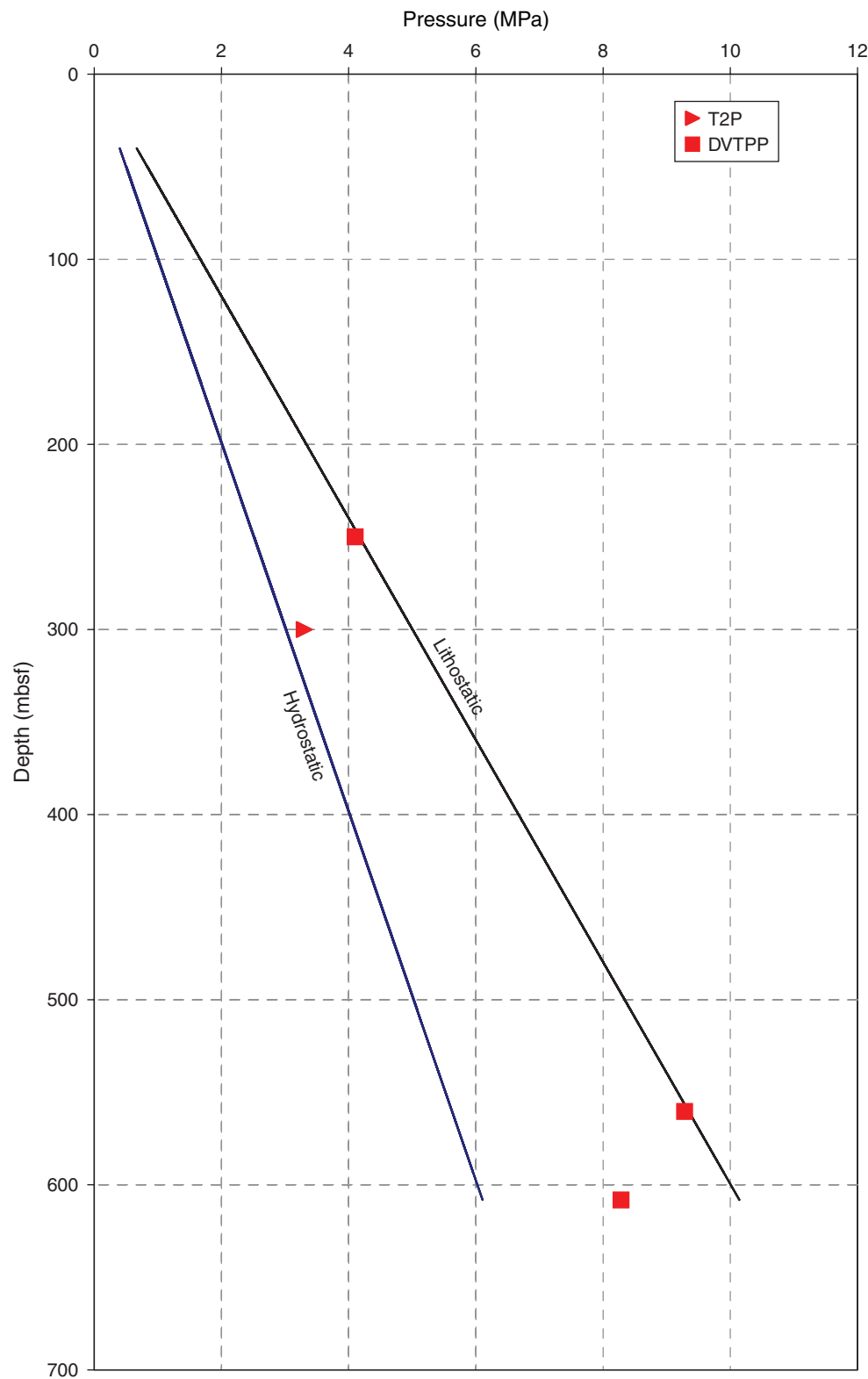


**Figure F80.** Pressures estimated from the last measurement on pressure dissipation curves from the temperature/dual pressure (T2P) probe and the Davis-Villinger Temperature-Pressure Probe (DVTTP). Pressures interpreted from pressure rebound curves are also shown. Hydrostatic pressure is calculated for an assumed water density of  $1.024 \text{ g/cm}^3$ . Lithostatic stress is calculated for an assumed bulk density of  $1.7 \text{ g/cm}^3$ . All pressure data are referenced to the seafloor.

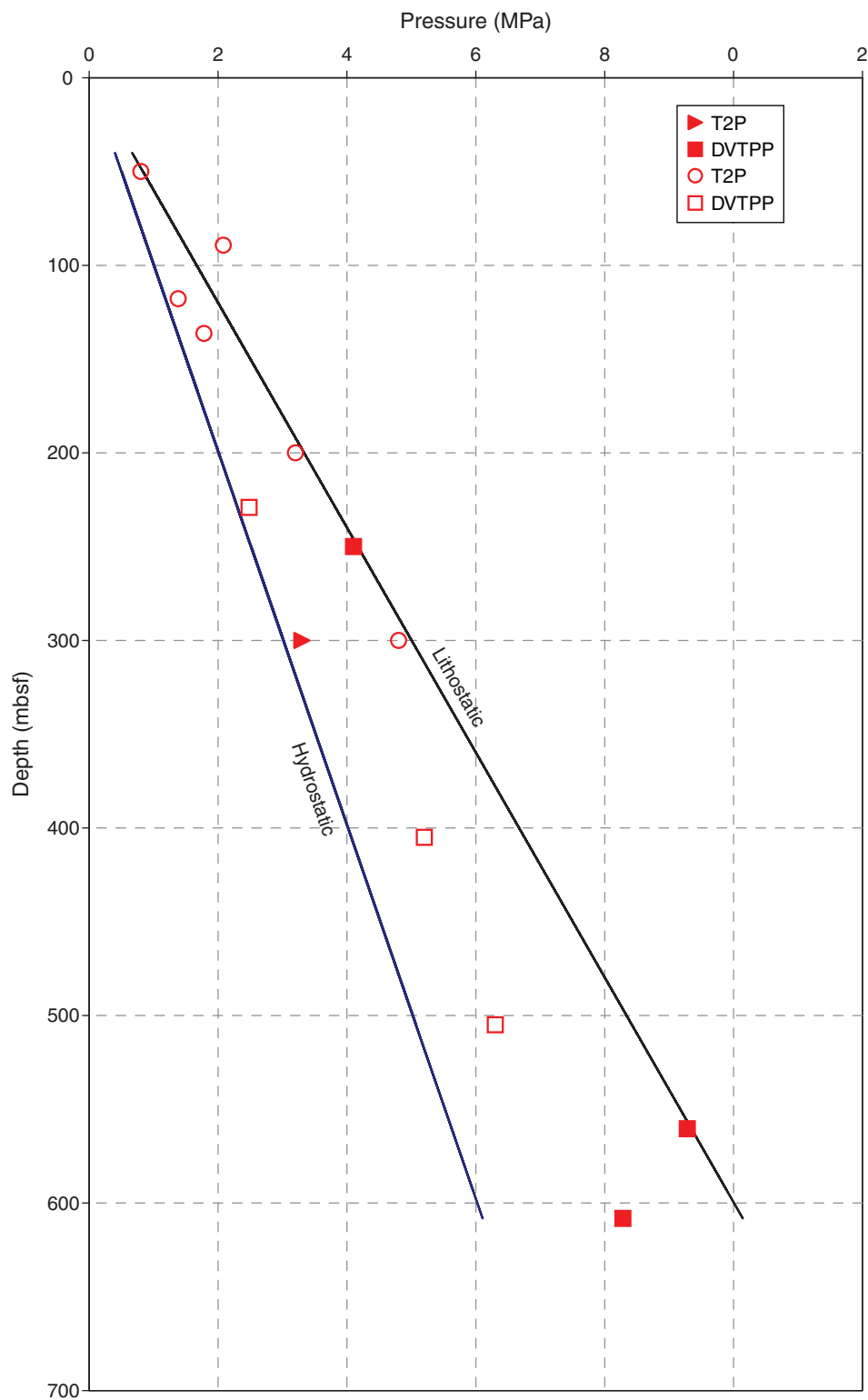


**Table T1.** Coring summary, Hole U1324A.

**Hole U1324A**  
 Latitude: 28°4.7856'N  
 Longitude: 89°8.3574'W  
 Time on site (h): 83.58  
 Seafloor (drill pipe measurement from rig floor, mbrf): 1066  
 Distance between rig floor and sea level (m): 10.5  
 Water depth (drill pipe measurement from sea level, m): 1055.5  
 Total depth (drill pipe measurement from rig floor, mbrf): 1678  
 Total penetration (meters below seafloor, mbsf): 612  
 Total length of cored section: 0  
 Total core recovered: 0  
 Core recovery (%): 0  
 Total number of cores: 0

Core	Date (Jun 2005)	Local time (h)	Depth (mbsf)		Length (m)		Recovery (%)
			Top	Bottom	Cored	Recovered	
308-U1324A-			0	612	0	0	0
1-0	19	0410			0	0	0
			Cored totals:		0	0	0

**Table T2.** Coring summary, Hole U1324B. (See table notes. Continued on next page.)

**Hole U1324B**  
 Latitude: 28°4.7845'N  
 Longitude: 89°8.3442'W  
 Time on site (h): 122.17  
 Seafloor (drill pipe measurement from rig floor, mbrf): 1067.5  
 Distance between rig floor and sea level (m): 10.7  
 Water depth (drill pipe measurement from sea level, m): 1056.8  
 Total depth (drill pipe measurement from rig floor, mbrf): 1675.7  
 Total penetration (meters below seafloor, mbsf): 608.2  
 Total length of cored section (m): 608.2  
 Total core recovered (m): 569.92  
 Core recovery (%): 94  
 Total number of cores: 74

Core	Date (Jun 2005)	Local time (h)	Depth (mbsf)		Length (m)		Comments
			Top	Bottom	Cored	Recovered	
308-U1324B-							
1H	21	0300	0.0	3.8	3.8	3.87	Fluorescent microspheres
2H	21	0400	3.8	13.3	9.5	9.79	Fluorescent microspheres
3H	21	0420	13.3	22.8	9.5	9.83	Fluorescent microspheres
4H	21	0500	22.8	32.3	9.5	10.03	Tensor on at 0420 h; fluorescent microspheres
5H	21	0530	32.3	41.8	9.5	10.04	105.68
6H	21	0625	41.8	51.3	9.5	10.06	105.89
7H	21	0900	51.3	60.8	9.5	9.98	105.05
8H	21	0935	60.8	70.3	9.5	9.84	103.58
9H	21	1025	70.3	79.8	9.5	10.05	105.79
10H	21	1105	79.8	89.3	9.5	9.79	103.05
11H	21	1415	89.3	98.8	9.5	9.48	99.79
12H	21	1510	98.8	108.3	9.5	9.76	102.74
13H	21	1545	108.3	117.8	9.5	9.91	104.32
14H	21	1900	117.8	127.3	9.5	8.07	84.95
15H	21	2025	127.3	136.3	9.0	9.06	100.67
16H	21	2325	136.3	144.9	8.6	8.63	100.35
17H	22	0100	144.9	153.7	8.8	8.84	100.45
18H	22	0150	153.7	162.0	8.3	8.35	100.60
19H	22	0240	162.0	170.8	8.8	8.81	100.11
20H	22	0330	170.8	179.0	8.2	8.19	99.88
21H	22	0430	179.0	186.9	7.9	7.92	100.25
22H	22	0510	186.9	193.8	6.9	6.99	101.30
23H	22	0600	193.8	200.4	6.6	6.70	101.52
24H	22	0655	200.4	207.5	7.1	7.15	100.70
25H	22	0740	207.5	216.1	8.6	8.60	100.00
26H	22	0830	216.1	222.5	6.4	6.48	101.25
							Advance by recovery; fluorescent microspheres
							Advance by recovery; Tensor out at 0240 h; fluorescent microspheres
							Advance by recovery; Tensor on at 0230 h
							Advance by recovery; fluorescent microspheres
							Advance by recovery; fluorescent microspheres
							Advance by recovery; fluorescent microspheres
							Advance by recovery; fluorescent microspheres

**Table T2 (continued).**

Core	Date (Jun 2005)	Local time (h)	Depth (mbsf)		Length (m)		Recovery (%)	Comments
			Top	Bottom	Cored	Recovered		
27H	22	0925	222.5	229.1	6.6	6.61	100.15	Tensor out at 0925 h; DVTTP at 1296.6 m
28H	22	1335	229.1	238.6	9.5	9.63	101.37	
29H	22	1435	238.6	247.3	8.7	8.73	100.34	Fluorescent microspheres
30H	22	1510	247.3	256.8	9.5	9.72	102.32	
31H	22	1555	256.8	264.6	7.8	7.80	100.00	
32H	22	1640	264.6	273.7	9.1	9.10	100.00	Changed all seals on APC after Core 32H; fluorescent microspheres
33H	22	1745	273.7	282.5	8.8	8.78	99.77	
34H	22	1825	282.5	290.4	7.9	7.92	100.25	
35H	22	1935	290.4	296.4	6.0	6.06	101.00	Fluorescent microspheres
36H	22	2015	296.4	305.6	9.2	9.30	101.09	
37H	22	2105	305.6	311.3	5.7	5.75	100.88	Changed inner and outer seals after Core 37H
38H	22	2205	311.3	319.2	7.9	7.98	101.01	Fluorescent microspheres
39H	22	2340	319.2	327.6	8.4	8.45	100.60	
40H	23	0025	327.6	333.5	5.9	5.97	101.19	Tensor on at 0025 h
41H	23	0135	333.5	339.0	5.5	5.52	100.36	Fluorescent microspheres
42H	23	0225	339.0	345.0	6.0	5.96	99.33	
43H	23	0325	345.0	352.7	7.7	7.79	101.17	
44H	23	0430	352.7	357.9	5.2	5.14	98.85	Fluorescent microspheres; Tensor out at 0500 h
45X	23	0550	357.9	362.4	4.5	4.57	101.56	DVTTP; sheared pin on overshot
46X	23	0945	362.4	368.0	5.6	5.33	95.18	T2P probe at 1435.9 m
47H	23	1300	368.0	373.2	5.2	5.26	101.15	Tensor at 1200 h; fluorescent microspheres
48H	23	1400	373.2	381.5	8.3	8.38	100.96	
49H	23	1445	381.5	387.9	6.4	6.36	99.38	DVTTP at 1455.4 m
50H	23	1715	387.9	394.5	6.6	6.64	100.61	T2P probe at 1462.0 m
51X	23	2055	394.5	396.8	2.3	2.31	100.43	
52X	23	2145	396.8	406.4	9.6	7.29	75.94	
53X	23	2225	406.4	416.0	9.6	7.39	76.98	
54X	23	2305	416.0	425.7	9.7	5.32	54.85	
55X	23	2350	425.7	435.3	9.6	9.68	100.83	
56X	24	0030	435.3	445.0	9.7	8.34	85.98	
57X	24	0110	445.0	454.6	9.6	8.75	91.15	
58X	24	0145	454.6	464.3	9.7	9.70	100.00	DVTTP at 1531.8 m (464.3 mbsf)
59X	24	0445	464.3	473.9	9.6	9.65	100.52	
60X	24	0535	473.9	483.5	9.6	9.84	102.50	
61X	24	0710	483.5	493.1	9.6	9.65	100.52	Core with 10.5 ppg mud; DVTTP
62X	24	1030	493.1	502.7	9.6	8.76	91.25	10.5 ppg mud, S/B out
63X	24	1155	502.7	512.4	9.7	7.28	75.05	10.5 ppg mud
64X	24	1310	512.4	521.9	9.5	4.98	52.42	10.5 ppg mud; DVTTP at 1589.4 m
65X	24	1810	521.9	531.6	9.7	8.41	86.70	10.5 ppg mud
66X	24	2030	531.6	541.1	9.5	1.62	17.05	10.5 ppg mud; DVTTP at 1608.6 m
67X	25	0015	541.1	550.7	9.6	8.42	87.71	10.5 ppg mud
68X	25	0200	550.7	560.4	9.7	7.86	81.03	10.5 ppg mud; DVTTP at 1627.9 m
69X	25	0525	560.4	570.0	9.6	4.02	41.87	10.5 ppg mud
70X	25	0650	570.0	579.6	9.6	8.55	89.06	10.5 ppg mud
71X	25	0840	579.6	589.2	9.6	8.39	87.40	10.5 ppg mud; DVTTP at 1656.7 m
72X	25	1215	589.2	593.2	4.0	3.94	98.50	10.5 ppg mud; T2P probe at 1660.7 m
73X	25	1530	593.2	598.6	5.4	2.68	49.63	10.5 ppg mud
74X	25	1720	598.6	608.2	9.6	8.12	84.58	10.5 ppg mud; DVTTP at 1675.7 m
Cored totals:			608.2	569.92	93.71			

Notes: T2P = temperature/dual pressure probe, DVTTP = Davis-Villinger Temperature-Pressure Probe. APC = advanced piston corer.



**Table T3.** Coring summary, Hole U1324C.

<b>Hole U1324C</b>							
Core	Date (Jun 2005)	Local time (h)	Depth (mbfs)		Length (m)		Recovery (%)
			Top	Bottom	Cored	Recovered	Comments
308-U1324C-							
1-0	26	0555	0.0	50.0			XCB center bit; T2P probe
1H	26	0840	50.0	59.5	9.5	9.66	101.68
2-1	26	1115	59.5	100.0			T2P probe
2H	26	1405	100.0	109.0	9.0	9.01	100.11 Advance by recovery
3-2	26	1545	109.0	150.0			T2P probe
3H	26	1910	150.0	155.5	5.5	5.52	100.36 Advance by recovery
4-3	26	2100	155.5	200.0			T2P probe
4H	26	2355	200.0	206.4	6.4	6.50	101.56 Advance by recovery
5-4	27	0200	206.4	250.0			DVTTP
5H	27	0450	250.0	258.3	8.3	8.38	100.96 Advance by recovery
6-5	27	0600	258.3	300.0			T2P probe
6H	27	0950	300.0	304.2	4.2	4.24	100.95 Advance by recovery
7-6	27	1300	304.2	405.0			DVTTP at 1471.5 m
7H	27	1600	405.0	410.4	5.4	5.41	100.19 Advance by recovery
8-7	27	1930	410.4	505.0			DVTTP
8H	27	2350	505.0	511.8	6.8	6.85	100.74
Cored totals:				55.1	55.57	100.85	

Notes: XCB = extended core barrel. T2P = pressure/dual pressure probe, DVTTP = Davis-Villinger Temperature-Pressure Probe.

**Table T4.** Lithostratigraphic units, Hole U1324B.

Unit	Top		Bottom		
	Core, section, interval (cm)	Depth (mbfs)	Core, section, interval (cm)	Depth (mbfs)	Thickness (m)
308-U1324B-					
I	1H-1, 0	0.0	46X-2, 75	364.7	364.7
IA	1H-1, 0	0.0	6H-2, 53	43.9	43.9
IB	6H-2, 53	43.9	7H-6, 81	59.7	15.8
IC	7H-6, 81	59.7	12H-6, 90	107.0	47.3
ID	12H-6, 90	107.0	13H-6, 80	151.0	44.0
IE	13H-6, 80	151.0	32H-1, 0	264.6	113.6
IF	32H-1, 0	264.6	34H-4, 100	288.0	23.4
IG	34H-4, 100	288.0	46X-2, 85	364.7	76.7
II	46X-2, 75	364.7	74X-7, 40	608.0	243.3
IIA	46X-2, 85	364.7	57X-1, 25	445.5	80.8
IIB	57X-1, 25	445.5	60X-6, 60	481.9	36.4
IIC	60X-6, 60	481.9	71X-2, 30	581.4	99.5
IID	71X-2, 30	581.4	74X-7, 40	608.0	26.6



**Table T5.** Summary of structural measurements, Hole U1324B.

Unit	Core, section, interval (cm)	Depth (mbsf)	Core strike (°)	Reference dip (°)	True strike (°)	Reference dip (°)	Feature/Remarks
IB	308-U1324B-6H-2, 53	43.83	124	NA			
	6H-4, 65	46.95	60	90	231	30SE	Fault
	6H-5, 105	48.85	60	NA			Fault, dip probably same as one above with same strike
	7H-3, 25	54.56					Possible fault, sediment disrupted
	7H-6, 60	59.41	16	NA			Reverse fault, steep, apparent offset 1 cm
	7H-6, 81	59.62					Steep reverse fault, disturbed bedding
	13H-1, 10–130	108.4–109.6	70	90	320	20SW	Bedding
ID	13H-2, 60	110.40	75	90	320	15SW	Bedding
	13H-2, 80–92	110.6–110.72					Fault zone, showing some small normal faults (riedel shears?) and some possible low-angle reverse faults
	13H-2, 110	110.90	70	90	320	20SW	Bedding
	13H-3, 25–120	111.55–112.0	70	90	320	20SW	Bedding
	13H-4, 20	113.00	70	90	320	20SW	Bedding
	13H-4, 130	114.10	66	90	320	24SW	Bedding
	13H-5, 20	114.50	70	90	320	20SW	Bedding
IE	13H-6, 30	114.60	70	90	320	20SW	Bedding
	13H-6, 80	116.80	75	90	320	15SW	Bedding
	15H-2, 5–50	128.85–129.3					Normal faults
	21H-4, 125	184.75	110	NA			Reverse fault
	22H-1, 25	187.15	60				Possible fault
	32H-1, 40	265.00	120	52NE	332	56NE	Bedding
	32H-2, 125	267.34	140	50NE	319	70NE	Bedding
IF	32H-3, 10	267.70	125	NA			Bedding
	32H-3, 20–150	267.8–269.10	~155	NA			Bedding, small reverse faults in this interval
	34H-1, 65–100	283.15–283.5					Bedding disrupted
	34H-1, 15	284.15	150	90	98	60S	Bedding
	34H-2, 22	284.22	115	90	98	25S	Bedding
	34H-4, 40	285.90	40	90	98	50N	Bedding
	34H-4, 100	288.00	90	90			Beds horizontal
IG	37H-2, 120	307.25	50	58NW	196	75NW	
	39H-2, 90	321.60					Possible fault
IIB	57X-1, 25–75	445.25–445.75					Possible slump fold
	58X–59X	454.6–473.95					Disruption of layering, mass transport deposit?
IID	71X-2, 30	581.40	65	75N			Dipping beds, biscuiting causes reversal of orientations in core on <5 cm interval, cannot be oriented
	72X-1, 20–130	589.4–590.3					Deformed zone, possible overturned folds, grain size reversals suggest overturned beds

Notes: Orientation convention: strike taken on cut core face, measured in a clockwise direction 0°–360°, dip taken from cut core face downward, with direction referred to compass quadrant with north being at top of core. APC cores can be oriented by reference to Tensor tool measurement taken during coring.

**Table T6.** Relative abundances of benthic foraminifers, Hole U1324B. This table is available in an [oversized format](#).

**Table T7.** Relative abundances of planktonic foraminifers, Hole U1324B. (See table notes. Continued on next page.)



**Table T7 (continued).**

Notes: Abundance: A = abundant, C = common, F = frequent, R = rare, VR = very rare, T = trace, B = barren. Preservation: VG = very good, G = good, M = moderate. PAL = paleontological sample.

**Table T8.** Datums used to plot Figure F23, Hole U1324B.

Code	Event	Top		Bottom		Age (ka)	Average depth (mbsf)	Average sedimentation rate (m/k.y.)
		Core, section, interval (cm)	Depth (mbsf)	Core, section, interval (cm)	Depth (mbsf)			
PF	LO <i>G. inflata</i>	308-U1324B-1H-CC, 15-20	3.80	308-U1324B-2H-CC, 22-27	13.54	10	8.65	0.86
MS	Tie point 3					26	10.00	
PF	Y2/Y3 boundary	16H-CC, 38-43	162.00	17H-CC, 33-38	164.02	24	163.00	10.00
PF	Y3/Y4 boundary	29H-CC, 50-55	247.28	30H-CC, 19-24	256.97	42	252.00	5.50
PF	Y4/Y5 boundary	38H-CC, 40-45	319.23	39H-CC, 40-45	327.60	48	323.00	12.00
MS	Tie point 4				470.00	52	470.00	
PF	No LO <i>P. obliquiloculata</i>			74X-CC, 36-43	606.65	65	606.65	>25.00

Notes: PF = planktonic foraminifer, MS = magnetostratigraphy. LO = last occurrence.

**Table T9.** Summary of pass-through cryogenic magnetometer measurements, Hole U1324B.

Measurement	Core, section
	308-U1324B-
NRM (0, 10, 20, 30 mT)	1H-1 through 12H-6
NRM (0, 10, 20 mT)	12H-7 through 13H-2
NRM (0, 20 mT)	13H-3 through 25H-4
NRM (0, 10, 20 mT)	26H-1 through 74X-2
Fugro cutting shoe	4H, 7H, 11H, 13H, 17H, 19H, 21H, 23H, 25H, 27H, 29H, 31H, 33H, 35H, 37H, 39H, 41H, 43H, 47H, and 49H
Skipped sections because of core flow-in	25H-5, 25H-6, 28H-5, 28H-6, 28H-7, 32H-4, 32H-5, 32H-6, 35H-4, 36H-5, 36H-6, 38H-5, 38H-6, 39H-4, 39H-5, 39H-6, 43H-5, 48H-6, 50H-4, and 50H-5
Skipped sections because of sandy lithology	37H-1
Skipped sections because of mechanical disturbance	64X-1, 64X-3, and all core catchers
Tensor tool	4H through 50H

Note: NRM = natural remanent magnetization.

**Table T10.** Magnetostratigraphic tie points, Site U1324.

Magnetostratigraphic tie point	MIS	Age (ka)
MTP1		1.1?
MTP2		2.2?
MTP3	3.1	30
MTP4	3.3	52

Note: MIS = marine isotope stage. Corresponding MIS and ages assigned according to Bassinot et al. (1994).



**Table T11.** Pore water chemistry, Holes U1324B and U1324C. (Continued on next page.)

Core, section, interval (cm)	Depth (mbsf)	Alkalinity (mM)	pH	Salinity (pph)	Chlorinity (mM)	$\text{SO}_4^{2-}$ (mM)	$\text{NH}_4^+$ ( $\mu\text{M}$ )	$\text{PO}_4^{3-}$ ( $\mu\text{M}$ )	$\text{H}_4\text{SiO}_4$ (nM)	$\text{Na}^+$ (mM)	$\text{K}^+$ (mM)	$\text{Mg}^{2+}$ (mM)	$\text{Ca}^{2+}$ (mM)	$\text{B}^{3+}$ (nM)	$\text{Li}^+$ ( $\mu\text{M}$ )	$\text{Sr}^{2+}$ ( $\mu\text{M}$ )	$\text{Ba}^{2+}$ ( $\mu\text{M}$ )	$\text{Fe}^{2+}$ ( $\mu\text{M}$ )	$\text{Mn}^{2+}$ ( $\mu\text{M}$ )	
308-U1324B-																				
1H-2, 135–140	2.85			3.7	557	30.6		315	467	11.3	53.3	13.2	453	29.1	84.9	1.4	94.5	22.9		
2H-1, 145–150	5.25			3.7	555	27.4	1109	0.0	323	432	9.7	49.7	12.7	490	30.1	93.0	1.0	137.6	14.4	
2H-3, 145–150	8.25	5.44	6.91	3.7	558	29.6	1209	3.4	430	449	9.0	53.6	14.5	592	35.7	109.4	0.9	435.8	14.3	
2H-5, 135–140	11.15			3.6	564	31.0	1423	0.5	463	472	9.2	56.7	15.5	647	36.3	117.1	0.8	458.5	15.1	
3H-1, 145–150	14.75	4.99	6.80	3.7	565	29.0	1698	0.0	457	428	7.5	52.7	14.3	677	35.8	127.5	1.2	325.5	8.3	
3H-3, 145–150	17.75	5.00	6.72	3.7	562	33.7	1417	0.5	490	490	8.0	60.6	16.9	729	38.8	133.1	0.8	479.1	7.3	
3H-5, 137–142	20.67	5.08	6.86	3.8	564	32.4	1155	0.0	515	473	7.5	59.3	18.3	779	41.4	137.2	0.9	433.9	7.4	
4H-1, 145–150	24.25	5.42	6.70	3.8	566	31.9	1758	0.0	469	456	6.9	56.9	17.2	838	45.2	139.2	1.7	364.4	5.6	
4H-3, 137–142	27.17	5.96	6.76	3.7	563	36.9	2260		494	508	7.6	63.5	20.0	886	49.3	141.0	1.7	427.8	6.0	
4H-5, 145–150	30.25	5.70	6.67	3.8	554	33.3	1483	0.5	475	473	7.4	58.3	19.5	903	55.0	141.2	1.2	284.3	5.8	
5H-1, 145–150	33.75	6.43	6.83	3.8	568	37.3	1691	0.0	441	525	8.0	65.2	22.7	917	59.8	145.0	1.4	228.6	5.9	
5H-3, 137–142	36.67	6.54	7.00	3.7	562	33.2	1905	2.3	481	470	6.6	60.5	21.4	866	58.4	138.5	1.3	216.5	7.5	
5H-5, 145–150	39.75	6.74	6.78	3.8	557	30.8	1329	0.0	497	427	5.8	55.6	20.3	881	59.3	143.1	1.1	245.3	9.0	
6H-1, 145–150	43.25	7.44	6.78	3.7	558	33.4	1329	2.3	465	491	6.7	63.3	23.6	842	57.1	143.5	1.0	191.7	10.4	
6H-3, 137–142	46.17	6.59	6.90	3.7	559	30.3	1584	2.3	411	456	7.0	57.2	21.4	825	56.7	136.7	1.0	61.3	9.4	
6H-5, 145–150	49.25	6.02	6.79	3.8	564	33.1	1738	2.3	450	500	7.0	63.2	24.1	822	53.3	137.9	0.9	95.9	10.5	
7H-3, 132–142	55.63	5.41	6.86	3.7	555	28.6	1571	1.7	433	495	6.8	59.7	23.5	759	45.3	137.1	0.9	164.9	7.5	
9H-3, 132–142	74.62	4.61	6.70	3.6	561	9.1	2079	1.1	431	447	5.9	50.8	17.9	641	33.1	123.4	1.2	191.8	7.4	
11H-3, 140–150	93.70	4.83	6.59	3.4	562	0.0	1925	0.5	568	476	5.1	50.2	19.3	666	21.5	117.4	3.1	353.6	7.5	
13H-3, 132–142	112.62	4.48	6.69	3.4	562	0.0	2950	3.4	484	446	4.4	45.9	12.0	597	24.8	117.6	23.2	223.0	7.7	
15H-3, 132–142	131.62	5.66	6.90	3.4	561	0.0	2595	0.0	506	471	4.2	46.8	12.1	487	13.6	105.5	10.9	229.6	5.8	
17H-3, 132–142	149.22	5.09	6.86	3.3	558	0.0	2796	0.0	476	416	4.3	42.2	9.6	477	11.1	98.7	9.9	138.2	4.6	
19H-3, 132–142	166.32			3.3	564	0.0	3010	3.4	452	427	5.0	42.8	10.8	467	15.4	100.5	12.7	97.8	9.1	
21H-3, 132–142	183.32	5.08	6.90	3.4	555	0.0	3050	2.3	535	503	5.3	47.3	12.8	495	14.7	96.9	13.0	69.5	5.4	
23H-3, 137–142	198.12	5.30	6.91	3.3	563	0.0	2943	1.1	601	427	4.6	41.3	9.0	515	15.2	89.8	13.2	228.3	6.4	
25H-3, 140–150	211.90	5.46	7.01	3.4	554	0.0	3559	1.1	521	459	5.5	46.5	8.6	541	16.1	89.2	12.7	89.5	3.5	
27H-3, 140–150	226.90	7.26	7.09	3.4	564	0.0	3077	4.0	514	480	6.0	50.2	10.7	546	30.6	95.3	12.2	112.3	6.2	
29H-3, 132–142	242.92	4.86	7.13	3.4	558	0.0	3579	0.5	391	505	4.9	51.6	11.9	422	15.0	103.2	10.0	54.0	3.7	
31H-3, 140–150	261.20	5.48	7.02	3.3	564	0.0	3693	2.3	338	478	4.3	48.7	11.5	461	25.7	109.8	10.2	44.0	3.4	
33H-3, 140–150	278.00	5.16	6.93	3.4		0.0	3244	0.0	461	435	3.5	43.1	10.5	497	14.0	106.6	10.7	114.7	4.6	
35H-3, 140–150	293.22	5.23	7.09	3.3	556	0.0	3405	0.0	426	449	3.8	45.1	9.6	423	18.5	99.0	12.6	48.2	4.1	
37H-3, 140–150	310.00	5.92	7.01	3.3	561	0.0	3921	0.0	478	424	3.5	42.7	7.9	415	20.9	97.8	10.8	112.8	4.8	
39H-3, 140–150	323.60				554	0.0	4229	4.0	429	447	4.2	46.6	8.3	371	29.2	96.7	11.1	22.2	4.1	
40H-3, 140–150	332.00	5.53	7.21	3.3	559	0.0	5273	4.0	276	449	4.5	44.1	7.8	358	26.2	93.5	9.7	12.8	3.1	
41H-3, 132–142	337.82			3.3	560	0.0	4952	2.8	393	457	4.0	46.4	8.4	364	18.7	98.6	9.7	33.8	3.8	
42H-3, 140–150	343.40	5.75	7.18	3.4	559	0.0	3740	0.0	355	474	4.0	48.0	9.0	366	19.3	100.8	10.4	20.1	3.4	
43H-3, 140–150	349.40				559	0.0	3619	0.0	361	428	3.6	44.7	8.1	359	19.1	98.5	9.7	22.9	4.2	
44H-2, 132–142	355.42	5.80	7.19	3.3	563	0.0	3586	0.0	389	472	3.8	47.9	9.2	379	20.2	103.4	10.8	26.2	4.1	
45X-2, 140–150	360.80	6.20	7.10	3.4	561	0.0	3947	0.0	502	492	3.8	50.9	9.5	419	18.2	103.3	10.8	95.5	4.2	
46X-3, 140–150	366.80	6.31	7.21	3.4	562	0.0	4624	0.5	409	450	3.8	45.5	8.7	382	19.4	103.3	12.2	32.9	3.8	
47H-3, 88–98	371.88	6.33	7.43	3.3	563	0.0	5092	1.7	299	475	4.0	48.5	9.3	370	25.2	102.7	12.8	11.8	4.2	
48H-3, 140–150	377.60	6.16	7.57	3.3	570	0.0	5400	0.0	185	437	4.0	42.1	8.3	351	32.1	100.0	14.1	7.8	2.8	
49H-3, 131–141	385.81	5.89	7.51	3.4	569	0.0	5126	0.0	193	464	4.2	45.3	8.7	349	26.1	99.9	13.1	7.9	3.0	
50H-3, 140–150	392.30	6.51	7.34	3.3	564	0.0	5153	0.0	312	484	4.2	47.9	8.8	398	20.1	104.2	12.5	7.2	3.3	
51X-1, 140–150	395.90				3.4	562	0.0	4550	4.0	398	474	4.0	50.0	9.3	357	26.3	103.3	12.8	7.2	3.8
52X-3, 140–150	401.20	7.93	7.18	3.3	561	0.0	4209	0.5	444	454	3.8	46.1	8.4	369	30.7	104.7	12.8	35.7	3.6	
53X-3, 140–150	410.80	8.97	7.31	3.3	563	0.0	5052	1.1	379	368	3.7	35.5	7.1	359	18.1	98.3	14.1	70.4	4.3	
54X-2, 140–150	418.90	7.63	7.48	3.3	556	0.0	5226	3.4	267	433	4.0	44.7	8.9	311	26.9	99.3	13.0	8.1	3.9	
55X-3, 140–150	430.10				3.3	557	0.0	4737	1.7	360	442	3.9	45.8	9.4	365	19.1	99.8	9.8	28.3	4.7
56X-2, 132–142	438.12	8.24	7.60	3.3	528	0.0	3981	1.7	465	475	4.7	48.1	11.1	395	17.0	104.5	9.8	38.1	4.4	

**Table T11 (continued).**

Core, section, interval (cm)	Depth (mbfs)	Alkalinity (mM)	pH	Salinity (pph)	Chlorinity (mM)	$\text{SO}_4^{2-}$ (mM)	$\text{NH}_4^+$ ( $\mu\text{M}$ )	$\text{PO}_4^{3-}$ ( $\mu\text{M}$ )	$\text{H}_4\text{SiO}_4$ (nM)	$\text{Na}^+$ (mM)	$\text{K}^+$ (mM)	$\text{Mg}^{2+}$ (mM)	$\text{Ca}^{2+}$ (mM)	$\text{B}^{3+}$ (nM)	$\text{Li}^+$ ( $\mu\text{M}$ )	$\text{Sr}^{2+}$ ( $\mu\text{M}$ )	$\text{Ba}^{2+}$ ( $\mu\text{M}$ )	$\text{Fe}^{2+}$ ( $\mu\text{M}$ )	$\text{Mn}^{2+}$ ( $\mu\text{M}$ )
57X-3, 140–150	449.40					0.0		281	440	3.6	46.6	10.2	485	30.2	99.2	13.6	15.5	5.1	
59X-3, 132–142	467.46	9.28	7.31	3.3	558	0.0	4644	1.1	325	449	4.2	45.9	9.3	416	26.3	100.0	18.9	6.6	3.6
61X-3, 140–150	487.90	6.96	7.25	3.3	563	0.0	4322	3.4	481	455	3.6	46.0	8.9	394	31.4	100.5	9.9	35.4	4.5
63X-3, 140–150	507.10	9.70	7.42	3.4	556	0.0	5374	9.2	384	448	3.8	45.1	8.7	379	17.5	102.8	14.0	25.1	4.4
65X-3, 140–150	526.30	8.24	7.24	3.3	557	0.0	4443	2.3	479	446	3.4	45.0	8.6	390	20.1	97.7	20.9	43.3	8.7
67X-3, 140–150	545.50	7.66	7.18	3.4	559	0.0	4845	0.5	493	462	3.6	47.0	10.5	412	30.6	98.0	19.3	25.5	9.5
69X-2, 140–150	563.30	7.84	7.50	3.4	559	0.0	3934	1.7	379	441	3.5	44.5	9.5	386	26.2	104.3	15.6	26.5	4.8
71X-3, 140–150	584.00	11.35	7.49	3.4	559	0.0	6820	1.7	371	444	4.0	44.7	9.6	437	22.3	105.8	16.8	29.0	5.1
73X-1, 140–150	594.60	9.48	7.44	3.4	556	0.0	6445	2.3	282	469	4.6	44.2	9.1	379	25.0	98.8	15.3	9.6	5.1
74X-3, 140–150	603.10				564	1.7	4443	1.7	306	351	3.7	36.7	8.0	337	46.1	70.8	3.1	10.5	25.2
308-U1324C-																			
1H-1, 140–150	51.40	6.422	6.68	3.7	557	30.7	629	2.3	595	492	5.6	60.5	23.6	851	51.7	141.1	0.8	362.3	12.9
2H-3, 140–150	104.40	5.326	6.76	3.4	559	0.0	1020	2.8	515	460	4.6	43.9	12.6	629	19.6	111.8	6.5	307.2	5.7
3H-3, 140–150	153.49	5.513	7.22	3.4	556	0.0	2646	2.3	474	449	4.9	41.6	8.5	547	11.5	98.5	18.2	52.1	2.8
4H-3, 140–150	204.40	5.593	7.14		557	0.0	1622	1.1	570	492	5.0	46.5	8.2	578	14.6	86.5	15.5	104.1	2.1
5H-3, 140–150	254.40	5.813	7.01	3.4	561	0.0	2344	2.3	547	466	4.1	46.5	9.0	484	11.9	104.5	10.0	183.6	4.0
6H-2, 140–150	302.90	6.063	7.25	3.4	552	0.0	2304	0.5	366	437	4.0	40.8	7.2	443	11.9	94.3	9.6	34.1	0.4
7H-2, 140–150	407.90				564	0.0	4823	6.3	263	451	4.5	43.2	7.5	355	16.9	95.8	13.7	5.0	1.2
8H-3, 140–150	509.40			3.4	545	0.0	2987	4.0	222	469	4.6	44.1	7.8	289	15.7	95.9	16.6	5.1	3.0

**Table T12.** Sediment elemental analysis, Holes U1324B and U1324C. (See table note. Continued on next page.)

Core, section, interval (cm)	Depth (mbsf)	Carbon (wt%)				TN (wt%)	TH (wt%)	C/N (mol:mol)
		Total	Inorganic	CaCO <sub>3</sub>	Organic			
<b>308-U1324B-</b>								
1H-1, 132–137	1.32	1.85	0.60	5.02	1.25	0.16	0.93	9.09
2H-1, 145–150	5.25	1.93	0.79	6.61	1.14	0.18	0.86	7.47
2H-3, 145–150	8.25	3.32	1.08	9.02	2.24	0.53	0.92	4.92
2H-5, 135–140	11.15	2.47	0.99	8.28	1.48	0.21	1.00	8.09
3H-1, 145–150	14.75	1.83	0.90	7.47	0.93	0.16	0.87	6.85
3H-3, 145–150	17.75	3.17	1.73	14.39	ND	0.16	0.67	
3H-5, 137–142	20.67	2.82	1.85	15.39	0.97	0.18	0.71	6.32
4H-1, 145–150	24.25	2.78	1.72	14.34	1.06	0.16	0.70	7.97
4H-3, 137–142	27.17	2.80	1.76	14.65	1.04	0.16	0.64	7.68
4H-5, 145–150	30.25	3.33	2.37	19.72	0.96	0.17	0.61	6.63
5H-1, 145–150	33.75	3.00	2.17	18.08	0.83	0.17	0.62	5.74
5H-3, 137–142	36.67	2.40	1.42	11.80	0.98	0.16	0.74	7.21
5H-5, 145–150	39.75	2.56	1.54	12.85	0.00	0.15	0.80	0.00
6H-1, 145–150	43.25	2.40	1.48	12.37	0.92	0.13	0.76	8.50
6H-3, 137–142	46.17	2.21	1.31	10.88	0.90	0.20	0.91	5.33
6H-5, 145–150	49.25	2.77	1.95	16.20	0.82	0.19	0.80	5.07
7H-3, 132–142	55.63	2.27	1.51	12.56	0.76	0.17	0.83	5.12
9H-3, 132–142	74.62	2.26	1.51	12.58	0.75	0.17	0.68	5.19
11H-3, 140–150	93.70	2.19	1.56	13.02	0.63	0.19	0.75	3.83
13H-3, 132–142	112.62	2.82	2.16	17.96	ND	0.18	0.62	
15H-3, 132–142	131.62	3.23	2.71	22.54	0.52	0.16	0.57	3.82
17H-3, 132–142	149.22	3.49	2.92	24.34	0.57	0.16	0.53	4.18
19H-3, 132–142	166.32	1.28	0.72	5.98	0.56	0.18	0.89	3.60
21H-3, 132–142	183.32	3.32	2.77	23.11	0.55	0.14	0.50	4.45
23H-3, 137–142	198.17	3.00	2.08	17.30	0.92	0.19	0.68	5.69
25H-3, 140–150	211.90	2.86	1.95	16.28	0.91	0.19	0.59	5.70
27H-3, 140–150	226.90	3.08	2.20	18.35	0.88	0.20	0.68	4.99
29H-3, 132–142	242.92	3.08	2.45	20.41	0.63	0.12	0.55	6.28
31H-3, 140–150	261.20	3.27	2.61	21.74	0.66	0.12	0.54	6.38
33H-3, 140–150	278.00	3.23	2.55	21.28	0.68	0.13	0.55	5.97
35H-2, 132–142	293.22	3.07	2.25	18.71	0.82	0.15	0.64	6.48
37H-3, 140–150	310.00	2.96	2.10	17.46	0.86	0.15	0.65	6.53
39H-3, 140–150	323.60	3.33	2.25	18.78	1.08	0.15	0.67	8.21
40H-3, 140–150	332.00	3.02	2.53	21.08	0.49	0.15	0.55	3.78
41H-3, 132–142	337.82	2.53	1.87	15.60	0.66	0.11	0.67	7.21
42H-3, 140–150	343.40	2.97	2.47	20.56	0.50	0.12	0.56	5.05
43H-3, 140–150	349.40	2.71	2.15	17.93	0.56	0.11	0.65	5.75
44H-2, 132–142	355.42	2.77	2.20	18.30	0.57	0.12	0.61	5.78
45X-2, 140–150	360.80	2.23	1.29	10.71	0.94	0.12	0.75	9.24
46X-3, 140–150	366.80	3.11	2.63	21.90	0.48	0.15	0.57	3.63
47H-3, 88–98	371.88	2.51	1.98	16.52	0.53	0.12	0.53	5.29
48H-3, 140–150	377.60	2.96	2.39	19.90	0.57	0.11	0.49	6.24
49H-3, 131–141	385.81	2.80	2.35	19.54	0.45	0.11	0.49	4.69
50H-3, 140–150	392.30	2.71	2.30	19.13	0.41	0.10	0.43	4.55
51X-1, 140–150	395.90	2.22	1.53	12.77	0.69	0.13	0.70	6.00
52X-3, 140–150	401.20	2.72	2.19	18.22	0.53	0.12	0.56	5.13
53X-3, 140–150	410.80	2.01	1.59	13.24	0.42	0.11	0.34	4.56
54X-2, 140–150	418.90	2.71	2.23	18.55	0.48	0.10	0.48	5.48
55X-3, 140–150	430.10	2.46	1.79	14.95	0.67	0.12	0.65	6.39
56X-2, 132–142	438.12	2.58	2.00	16.65	0.58	0.11	0.58	5.88
57X-3, 140–150	449.40	1.38	0.75	6.22	0.63	0.12	0.64	6.37
59X-3, 132–142	467.46	3.08	2.32	19.35	0.76	0.12	0.68	7.16
61X-3, 140–150	487.90	1.43	0.99	8.28	0.44	0.12	0.67	4.18
63X-3, 140–150	507.10	2.28	1.62	13.52	0.66	0.11	0.61	7.24
65X-3, 140–150	526.30	2.35	1.77	14.72	0.58	0.12	0.59	5.84
67X-3, 140–150	545.50	2.36	1.92	16.00	0.44	0.14	0.54	3.65
69X-2, 140–150	563.30	1.14	1.89	15.71	ND	0.16	0.60	
71X-3, 140–150	584.00	2.37	1.51	12.57	0.86	0.13	0.33	7.90
73X-1, 140–150	594.60	2.03	1.54	12.87	0.49	0.17	0.55	3.41

**Table T12 (continued).**

Core, section, interval (cm)	Depth (mbsf)	Carbon (wt%)				TN (wt%)	TH (wt%)	C/N (mol:mol)
		Total	Inorganic	CaCO <sub>3</sub>	Organic			
74X-3, 132–142	602.92	1.58	1.36	11.35	0.22	0.10	0.17	2.46
308-U1324C-								
1H-1, 140–150	51.50	2.53	1.54	12.86	0.99	0.17	0.38	6.73
2H-3, 140–150	104.50	2.53	1.91	15.93	0.62	0.17	0.48	4.19
3H-3, 140–150	153.59	3.66	3.21	26.74	0.45	0.12	0.39	4.38
4H-3, 140–150	204.50	2.67	2.10	17.51	0.57	0.17	0.27	3.86
5H-3, 140–150	254.50	3.13	2.63	21.91	0.50	0.16	0.57	3.65
6H-2, 140–150	303.00	2.82	2.46	20.47	ND	0.16	0.53	
7H-2, 140–150	408.00	1.62	1.31	10.88	0.31	0.10	0.32	3.49
8H-3, 140–150	509.50	2.19	1.78	14.85	0.41	0.14	0.52	3.46

Note: ND = not detected.

**Table T13.** Headspace gas analysis, Hole U1324B.

Core, section, interval (cm)	Depth (mbsf)	Headspace gas (ppmv)			C <sub>1</sub> /C <sub>2</sub> ratio
		Methane	Ethane	Ethylene	
<b>308-U1324B-</b>					
1H-2, 0–5	1.5	1.7	0.0	0.0	
2H-6, 0–5	11.3	1.7	0.0	0.0	
3H-6, 0–5	20.8	1.8	0.0	0.0	
4H-6, 0–5	30.3	4.0	0.0	0.0	
5H-6, 0–5	39.8	2.0	0.0	0.0	
6H-6, 0–5	49.3	1.9	0.0	0.0	
7H-6, 0–5	58.8	1.5	0.0	0.0	
8H-6, 0–5	68.3	1.7	0.0	0.0	
9H-4, 0–5	74.8	1.6	0.0	0.0	
10H-6, 0–5	87.3	1.7	0.0	0.0	
11H-4, 0–5	93.8	9.9	0.0	0.0	
12H-4, 0–5	103.3	123.1	0.0	0.0	
13H-4, 0–5	112.8	752.8	0.0	0.0	
14H-5, 0–5	121.7	3,062	0.9	0.0	3,402
15H-4, 0–5	131.8	3,109	0.0	0.8	
16H-4, 0–5	139.7	383.9	0.0	0.0	
17H-4, 0–5	149.4	212.2	0.0	0.0	
18H-5, 0–5	159.7	148.5	0.0	0.0	
19H-4, 0–5	166.5	8,905	0.0	0.0	
20H-5, 0–5	176.8	14,174	2.3	0.0	6,163
21H-4, 0–5	183.5	1,302	0.0	0.0	
22H-4, 0–5	191.4	3,154	0.0	0.0	
23H-4, 0–5	198.3	1,360	0.0	0.0	
24H-4, 0–5	204.9	39,540	4.2	0.0	9,414
25H-4, 0–5	212.0	40,340	4.0	0.0	10,085
26H-4, 0–5	220.6	13,664	1.5	0.0	9,109
27H-4, 0–5	227.0	6,437	0.0	0.0	
28H-4, 0–5	233.6	382.3	0.0	0.0	
29H-3, 0–5	241.6	32,062	3.1	0.0	10,342
30H-4, 0–5	251.8	37,786	2.6	0.0	14,533
31H-4, 0–5	261.3	41,621	3.5	0.0	11,892
32H-4, 0–5	269.1	6,586	0.0	0.0	
33H-4, 0–5	278.1	3,527	0.0	0.0	
34H-3, 0–5	285.5	1,575	0.0	0.0	

Core, section, interval (cm)	Depth (mbsf)	Headspace gas (ppmv)			C <sub>1</sub> /C <sub>2</sub> ratio
		Methane	Ethane	Ethylene	
35H-3, 0–5	293.4	1,371	0.0	0.0	
36H-5, 0–5	302.4	647.0	0.0	0.0	
37H-4, 0–5	310.1	592.3	0.0	0.0	
38H-5, 0–5	317.3	13,613	0.9	0.0	15,125
39H-4, 0–5	323.7	6,046	0.0	0.0	
40H-4, 0–5	332.1	17,041	0.0	0.0	
41H-4, 0–5	338.0	5,006	0.0	0.0	
42H-4, 0–5	343.5	5,231	0.0	0.0	
43H-4, 0–5	349.5	5,563	0.0	0.0	
44H-3, 0–5	355.6	4,387	0.0	0.0	
45X-3, 0–5	360.9	3,965	0.0	0.0	
46X-3, 0–5	365.4	3,239	0.0	0.0	
47H-4, 0–5	372.0	6,949	0.0	0.0	
48H-4, 0–5	377.7	7,597	0.0	0.0	
49H-4, 0–5	385.9	14,277	0.0	0.0	
50H-4, 0–5	392.4	4,754	0.0	0.0	
51X-2, 0–5	396.0	7,007	0.0	0.0	
52X-4, 0–5	401.3	4,311	0.0	0.0	
53X-4, 0–5	410.9	4,662	0.0	0.0	
54X-3, 0–5	419.0	5,060	0.0	0.0	
55X-4, 0–5	430.2	3,526	0.0	0.0	
56X-4, 0–5	439.8	4,703	0.0	0.0	
57X-4, 0–5	449.5	5,716	0.0	0.0	
58X-5, 0–5	460.6	2,789	0.0	0.0	
59X-4, 0–5	467.6	10,949	0.0	0.0	
60X-4, 0–5	478.4	4,795	0.0	0.5	
61X-5, 0–5	489.5	3,567	0.0	0.0	
62X-4, 0–5	497.5	10,451	0.0	0.0	
63X-4, 0–5	507.2	7,390	0.0	0.0	
65X-4, 0–5	526.4	5,834	0.0	0.0	
67X-4, 0–5	545.6	2,021	0.0	0.0	
68X-5, 0–5	556.7	3,297	0.0	0.0	
69X-3, 0–5	563.4	8,898	0.0	0.0	
70X-4, 0–5	574.5	4,921	0.0	0.0	
71X-4, 0–5	584.1	13,244	0.0	0.0	
72X-3, 0–5	592.2	13,653	1.4	1.5	9,752
73X-2, 0–5	594.7	12,016	0.0	0.0	
74X-4, 0–5	603.1	14,071	0.7	0.0	20,102

**Table T14.** Samples for microbiology, Hole U1324B.

Core, section, interval (cm)	Cell density (cells/mL)	Comments
308-U1324B-		
1H-2, 2.9–3.0	$2.0 \times 10^5$	
2H-2, 6.7–6.8	$3.3 \times 10^4$	
2H-5, 11.2–11.3	$1.5 \times 10^5$	
3H-2, 16.2–16.3	$6.6 \times 10^4$	
3H-5, 20.7–20.8	$2.5 \times 10^4$	
4H-3, 27.2–27.3	$2.5 \times 10^4$	
5H-3, 36.7–36.8	$1.9 \times 10^4$	
6H-3, 46.2–46.3	ND	
7H-3, 55.7–55.8	$1.5 \times 10^4$	
8H-3, 65.2–65.3	$1.0 \times 10^4$	
9H-3, 74.7–74.8	ND	
10H-3, 84.2–84.3	$1.0 \times 10^4$	
11H-3, 93.7–93.8	ND	
13H-3, 112.7–112.8	ND	
15H-3, 131.7–131.8	$2.8 \times 10^4$	
17H-3, 149.3–149.4	ND	
19H-3, 166.4–166.5	ND	
21H-3, 183.4–183.5	ND	
23H-3, 198.2–198.3	ND	
26H-3, 220.5–220.6	ND	
29H-3, 243.0–243.1	ND	
32H-3, 269.0–269.1	ND	
35H-2, 293.3–293.4	ND	
38H-3, 315.7–315.8	ND	
41H-3, 337.9–338.0	ND	
44H-2, 355.5–355.6	ND	
48H-3, 377.6–377.7	ND	No contamination test
50H-3, 392.2–392.3	ND	
53X-3, 410.7–410.8	ND	
56X-2, 438.2–438.3	ND	
59X-3, 467.6–467.6	ND	
64X-3, 515.6–515.6	ND	
66X-1, 532.8–532.9	ND	
68X-4, 556.6–556.7	ND	
70X-3, 574.4–574.5	ND	
72X-2, 592.1–592.2	ND	
74X-3, 603.02–603.1	ND	No contamination test

Note: ND = not detected or below significant levels.



**Table T15.** Check shot stack summary, Hole U1324A.

Gun azimuth: 0  
 Gun offset: 49  
 Gun depth from Schlumberger zero (m): 12.6  
 Hydrophone depth from Schlumberger zero (m): 12.6  
 SRD from Schlumberger zero (m): 10.6  
 Water depth (meters below rig floor, mbrf): 1066.1  
 Other check shot constants:  
 True vertical time correction: yes  
 Surface velocity (m/s): 1524.0

Stack number	Measured depth (mbrf)	Shots stacked (N)	Measured transit time (ms)	True vertical depth from SRD (mbsl)	Corrected two-way traveltime (ms)	Interval velocity (m/s)
16	1149.9	5	759.84	1139.3	1520.90	1582.64
15	1177.0	5	776.95	1166.4	1555.15	1602.26
14	1220.0	5	803.76	1209.4	1608.82	1654.27
13	1250.0	5	821.88	1239.4	1645.09	1689.34
12	1275.5	5	836.96	1264.9	1675.28	1642.15
11	1300.0	5	851.87	1289.4	1705.12	1596.43
10	1325.0	7	867.51	1314.4	1736.44	1645.45
9	1350.0	9	882.69	1339.4	1766.83	1702.81
8	1375.1	9	897.42	1364.5	1796.31	1708.40
7	1400.0	9	911.99	1389.4	1825.46	1688.26
6	1425.1	9	926.84	1414.5	1855.19	1777.93
5	1449.9	9	940.78	1439.3	1883.09	1802.80
4	1495.0	9	965.78	1484.4	1933.12	1827.46
3	1520.0	7	979.45	1509.4	1960.49	1832.37
2	1544.9	9	993.03	1534.3	1987.66	1851.97
1	1565.0	9	1003.87	1554.4	2009.37	0.00

Note: SRD = seismic reference depth.



**Table T16.** Downhole tool deployment, Site U1324.

Hole	Tool	Deployment	Depth		Date (Jun 2005)	Time in formation (min)
			(mbsf)	(mbsl)		
308-						
U1324B	T2P	5	51.3	1108.1	21	30
U1324B	T2P	6	89.3	1146.1	21	30
U1324B	T2P	7	117.8	1174.6	21	40
U1324B	T2P	8	136.3	1193.1	21	30
U1324B	T2P	9	368.0	1424.8	23	40
U1324B	T2P	10	394.5	1451.3	23	30
U1324B	T2P	11	593.2	1650.0	25	15
U1324C	T2P	12	50.0	1105.7	26	60
U1324C	T2P	13	100.0	1155.7	26	60
U1324C	T2P	14	150.0	1205.7	26	60
U1324C	T2P	15	200.0	1255.7	27	60
U1324C	T2P	16	300.0	1355.7	27	90
U1324B	DVTTP	3	229.1	1285.9	22	40
U1324B	DVTTP	4	362.4	1419.2	23	40
U1324B	DVTTP	5	387.9	1444.7	23	10
U1324B	DVTTP	6	464.3	1521.1	24	30
U1324B	DVTTP	7	493.1	1549.9	24	30
U1324B	DVTTP	8	521.9	1578.7	24	25
U1324B	DVTTP	9	541.1	1597.9	25	30
U1324B	DVTTP	10	560.4	1617.2	25	30
U1324B	DVTTP	11	589.2	1646.0	25	45
U1324B	DVTTP	12	608.2	1665.0	25	60
U1324C	DVTTP	13	250.0	1305.7	27	90
U1324C	DVTTP	14	405.0	1460.7	27	90
U1324C	DVTTP	15	505.0	1560.7	28	90
U1324B	APCT	2	51.3	1108.1	21	10
U1324B	APCT	3	79.8	1136.6	21	10
U1324B	APCT	4	108.3	1165.1	21	10
U1324B	APCT	5	136.3	1193.1	21	10

Note: T2P = temperature/dual pressure probe, DVTTP = Davis-Villinger Temperature-Pressure Probe, APCT = advanced piston corer temperature tool.



**Table T17.** Event summary of T2P Deployment 5, Hole U1324B.

Event	Time (CDT)	Event
1		Data logger started at 1 Hz
2	0640	T2P on rig floor
3	0647	Pressure response chamber removed from T2P tip
4	0647	Shroud in place over T2P tip
5	0648	T2P connected to spacer
6	0650	CDS connected to spacer
7	0655	Start lowering T2P downhole, pumps on
8	0704	Stop at 515 mbsl, pumps off
9	0708	Start lowering probe, pumps on
10	0712	Stop at 768 mbsl, pumps off
11	0714	Start lowering probe, pumps on
12	0719	Stop at 1066 mbsl, pumps off
13	0722	Start lowering probe, pumps on at 18 spm
14	0723	Bit is 0.5 m off BOH
15	0724	Start lowering probe to land in BHA
16	0725	CDS lands in BHA; pumps off
17	0725	Raising BHA to 2 m off BOH
18	0726	Start penetration of T2P into sediment, 2 m advance of BHA
19	0727	End of T2P penetration; bit 0.25 m off bottom of hole
20	0727	Raising BHA 2 m off bottom of hole
21	0732	Pumping at 11 spm
22	0757	Pulling T2P uphole slowly with wireline
23	0758	CDS clear of BHA
24	0800	Stop at 1067 mbsl, pumps off
25	0804	Pulling T2P uphole slowly with wireline
26	0809	Stop at 767 mbsl, pumps off
27	0811	Pulling T2P uphole slowly with wireline
28	0815	Stop at 516 mbsl, pumps off
29	0817	Pulling T2P uphole slowly with wireline
30	0825	Wireline disconnected from CDS
31	0825	CDS extended
32	0828	CDS disconnected from spacer
33	0828	Spacer disconnected from CDS
34	0830	T2P disconnected from spacer
35	0833	T2P out of pipe
36		Data downloaded from data logger

Notes: Depth = 51.3 mbsf. Date = 21 June 2005. T2P = temperature/dual pressure probe. CDS = colleted delivery system. BHA = bottom-hole assembly. CDT = central daylight time. SPM = strokes per minute. BOH = bottom of hole.

**Table T18.** Event summary of T2P Deployment 6, Hole U1324B.

Event	Time (CDT)	Event
1	09:17:00	Data logger started at 1 Hz
2	11:15:19	T2P on rig floor
3	11:47:09	Start lowering T2P downhole, pumps on
4	11:56:03	Stop at 511 mbsl, pumps off
5	11:57:57	Start lowering probe, pumps on
6	12:03:05	Stop at 761 mbsl, pumps off
7	12:04:57	Start lowering probe, pumps on
8	12:10:14	Stop at 1058 mbsl, pumps off
9	12:16:30	Start lowering probe
10	12:18:50	Stop at 1135 mbsl, pumps off
11	12:20:54	Start lowering probe to land in BHA
12	12:22:56	CDS lands in BHA; pumps off
13	12:31:02	Start penetration of T2P into sediment
14	12:33:43	End of T2P penetration; bit 1 m off bottom of hole
15	12:36:02	Raising BHA 2 m off bottom of hole
16	12:42:09	Pumping at 11 spm
17	13:08:17	Pulling T2P uphole slowly with wireline
18	13:11:30	CDS clear of BHA
19	13:13:40	Stop at 1058 mbsl, pumps off
20	13:15:47	Pulling T2P uphole slowly with wireline
21	13:18:55	Stop at 760 mbsl, pumps off
22	13:20:52	Pulling T2P uphole slowly with wireline
23	13:23:50	Stop at 511 mbsl, pumps off
24	13:25:46	Pulling T2P uphole slowly with wireline
25	13:31:24	Wireline disconnected from CDS
26	13:32:30	CDS retracted
27	13:35:22	CDS disconnected from spacer
28	13:37:31	Spacer disconnected from CDS
29	13:38:23	T2P out of pipe
30	13:50:30	Data downloaded from data logger

Notes: Depth = 89.3 mbsf. Date = 21 June 2005. T2P = temperature/dual pressure probe. CDS = colleted delivery system. BHA = bottom-hole assembly. CDT = central daylight time. SPM = strokes per minute.

**Table T19.** Event summary of T2P Deployment 7, Hole U1324B.

Event	Time (CDT)	Event
1	15:18:00	Data logger started at 1 Hz
2	15:56:13	T2P on rig floor
3	16:07:34	Start lowering T2P downhole, pumps on
4	16:15:37	Stop at 511 mbsl, pumps off
5	16:17:21	Start lowering probe, pumps on
6	16:20:55	Stop at 761 mbsl, pumps off
7	16:22:48	Start lowering probe, pumps on
8	16:26:40	Stop at 1058 mbsl, pumps off
9	16:30:00	Start lowering probe
10	16:33:23	Stop at 1164 mbsl, pumps off
11	16:40:04	Start lowering probe to land in BHA
12	16:44:27	CDS lands in BHA; pumps off
13	16:47:23	Start penetration of T2P into sediment
14	16:48:41	End of T2P penetration; bit 1 m off bottom of hole
15	16:52:24	Raising BHA 2 m off bottom of hole
16	16:58:15	Pumping at 14 spm
17	17:28:50	Pulling T2P uphole slowly with wireline
18	17:33:15	CDS clear of BHA
19	17:34:00	Stop at 1058 mbsl, pumps off
20	17:36:23	Pulling T2P uphole slowly with wireline
21	17:40:42	Stop at 760 mbsl, pumps off
22	17:42:49	Pulling T2P uphole slowly with wireline
23	17:46:02	Stop at 511 mbsl, pumps off
24	17:48:12	Pulling T2P uphole slowly with wireline
25	17:55:35	Wireline disconnected from CDS
26	17:56:39	CDS retracted
27	17:58:10	CDS disconnected from spacer
28	17:59:55	Spacer disconnected from CDS
29	18:01:00	T2P out of pipe
30	18:08:18	Data downloaded from data logger

Notes: Depth = 117.8 mbsf. Date = 21 June 2005. T2P = temperature/dual pressure probe. CDS = colleted delivery system. BHA = bottom-hole assembly. CDT = central daylight time. STM = strokes per minute.

**Table T20.** Event summary of T2P Deployment 8, Hole U1324B.

Event	Time (CDT)	Event
1	19:28:15	Data logger started at 1 Hz
2	20:45:41	T2P on rig floor
3	20:58:19	Start lowering T2P downhole, pumps on
4	21:08:05	Stop at 511 mbsl, pumps off
5	21:10:10	Start lowering probe, pumps on
6	21:14:29	Stop at 761 mbsl, pumps off
7	21:17:00	Start lowering probe, pumps on
8	21:21:21	Stop at 1058 mbsl, pumps off
9	21:23:35	Start lowering probe
10	21:27:07	Stop at 1151 mbsl, pumps off
11	21:32:50	Start lowering probe
12	21:34:35	Stop at 1181 mbsl, pumps off
13	21:38:25	Start lowering probe
14	21:43:12	CDS lands in BHA; pumps off
15	21:43:58	Start penetration of T2P into sediment
16	21:44:49	End of T2P penetration; bit at bottom of hole
17	21:45:21	Raising BHA 1.5 m off bottom of hole
18	22:16:41	Pulling T2P uphole slowly with wireline
19	22:18:30	CDS clear of BHA
20	22:20:50	Stop at 1058 mbsl, pumps off
21	22:23:50	Pulling T2P uphole slowly with wireline
22	22:27:26	Stop at 761 mbsl, pumps off
23	22:30:25	Pulling T2P uphole slowly with wireline
24	22:33:40	Stop at 511 mbsl, pumps off
25	22:36:00	Pulling T2P uphole slowly with wireline
26	22:42:35	Wireline disconnected from CDS
27	22:45:08	CDS disconnected from spacer
28	22:46:30	Spacer disconnected from CDS
29	22:47:15	T2P out of pipe
30	23:11:00	Data downloaded from data logger

Notes: Depth = 136.3 mbsf. Date = 21 June 2005. T2P = temperature/dual pressure probe. CDS = colleted delivery system. BHA = bottom-hole assembly. CDT = central daylight time.

**Table T21.** Event summary of T2P Deployment 9, Hole U1324B.

Event	Time (CDT)	Event
1	08:28:29	Data logger started at 1 Hz
2	09:57:35	T2P on rig floor
3	10:11:43	Start lowering T2P downhole, pumps on
4	10:28:24	Stop at 1058 mbsl, pumps off
5	10:33:36	Start lowering probe
6	10:45:14	Stop at 1432 mbsl, pumps off
7	10:49:43	Start lowering probe
8	10:53:27	CDS lands in BHA; pumps off
9	10:54:10	Start penetration of T2P into sediment
10	10:58:39	End of T2P penetration; bit at bottom of hole
11	10:59:31	Raising BHA 2 m off bottom of hole
12	11:40:15	Pulling T2P uphole slowly with wireline
13	11:48:13	Stop at 1058 mbsl, pumps off
14	11:51:35	Pulling T2P uphole slowly with wireline
15	12:01:39	Wireline disconnected from CDS
16	12:04:35	CDS disconnected from spacer
17	12:06:10	Spacer disconnected from CDS
18	12:08:23	T2P out of pipe
19	12:30:00	Data downloaded from data logger

Notes: Depth = 368.0 mbsf. Date = 23 June 2005. T2P = temperature/dual pressure probe. CDS = colleted delivery system. BHA = bottom-hole assembly. CDT = central daylight time.



**Table T22.** Event summary of T2P Deployment 10, Hole U1324B.

Event	Time (CDT)	Event
1	16:36:20	Data logger started at 1 Hz
2	17:26:10	T2P on rig floor
3	17:57:34	Start lowering T2P downhole, pumps on
4	18:10:58	Stop at 1058 mbsl, pumps off
5	18:14:18	Start lowering probe
6	18:24:55	CDS lands in BHA; pumps off
7	18:27:03	Start penetration of T2P into sediment
8	18:31:25	End of T2P penetration; bit at bottom of hole
9	18:33:20	Raising BHA 2.5 m off bottom of hole
10	19:06:01	Pulling T2P uphole slowly with wireline
11	19:13:40	Stop at 1058 mbsl, pumps off
12	19:16:47	Pulling T2P uphole slowly with wireline
13	19:30:04	Wireline disconnected from CDS
14	19:37:00	CDS disconnected from spacer
15	19:39:21	Spacer disconnected from CDS
16	19:40:11	T2P out of pipe
17	19:59:59	Data downloaded from data logger

Notes: Depth = 394.5 mbsf. Date = 23 June 2005. T2P = temperature/dual pressure probe. CDS = colleted delivery system. BHA = bottom-hole assembly. CDT = central daylight time.

**Table T23.** Event summary of T2P Deployment 11, Hole U1324B.

Event	Time (GMT)	Event
1	12:02:00	Data logger started at 1 Hz
2	12:18:13	T2P on rig floor
3	12:31:55	Start lowering T2P downhole, pumps on
4	12:42:00	Stop at 1068 mbsl, pumps off
5	12:45:46	Start lowering probe
6	12:50:23	Stop at 1510 mbsl, pumps off
7	12:56:38	Start lowering probe
8	12:58:11	CDS lands in BHA; pumps off
9	13:14:02	Pulling T2P uphole slowly with wireline
10	13:25:02	Stop at 1067 mbsl, pumps off
11	13:28:02	Pulling T2P uphole slowly with wireline
12	13:34:27	Wireline disconnected from CDS
13	13:38:21	CDS disconnected from spacer
14	13:40:15	Spacer disconnected from CDS
15	13:46:40	T2P out of pipe
16	14:10:36	Data downloaded from data logger

Notes: Depth = 593.2 mbsf. Date = 25 June 2005. T2P = temperature/dual pressure probe. CDS = colleted delivery system. BHA = bottom-hole assembly. GMT = Greenwich Mean Time.



**Table T24.** Event summary of T2P Deployment 12, Hole U1324C.

Event	Time (GMT)	Event
1		Data logger started at 1 Hz
2	10:44:26	T2P on rig floor
3	10:52:56	Start lowering T2P downhole, pumps on
4	11:09:00	Stop at 491 mbsl, pumps off
5	11:11:37	Start lowering probe
6	11:14:13	Stop at 741 mbsl, pumps off
7	11:19:00	Stop at 1057 mbsl, pumps off
8	11:22:09	Stop at 1095 mbsl, pumps off
9	11:28:08	Start lowering probe
10	11:29:20	CDS lands in BHA; pumps off
11	11:32:50	Start penetration of T2P into sediment
12	11:40:35	End of T2P penetration; bit on bottom of hole
13	11:40:36	Raising BHA 4.5 m off bottom of hole
14	12:41:05	Pulling T2P uphole slowly with wireline
15	12:44:52	Stop at 1057 mbsl, pumps off
16	12:48:00	Pulling T2P uphole slowly with wireline
17	12:54:09	Stop at 741 mbsl, pumps off
18	12:56:09	Pulling T2P uphole slowly with wireline
19	13:00:57	Stop at 491 mbsl, pumps off
20	13:02:57	Pulling T2P uphole slowly with wireline
21		Data downloaded from data logger

Notes: Depth = 50.0 mbsf. Date = 26 June 2005. T2P = temperature/dual pressure probe. CDS = colleted delivery system. BHA = bottom-hole assembly. GMT = Greenwich Mean Time.

**Table T25.** Event summary of T2P Deployment 13, Hole U1324C.

Event	Time (GMT)	Event
1	14:42:47	Data logger started at 1 Hz
2	16:18:30	T2P on rig floor
3	16:28:42	Start lowering T2P downhole, pumps on
4	16:44:22	Stop at 741 mbsl, pumps off
5	16:46:30	Start lowering probe
6	16:52:33	Stop at 1057 mbsl, pumps off
7	16:54:39	Start lowering probe
8	17:03:38	CDS lands in BHA; pumps off
9	17:04:34	Start penetration of T2P into sediment
10	17:05:22	End of T2P penetration; bit 1 m off bottom of hole
11	17:06:00	Raising BHA 2 m off bottom of hole
12	18:08:10	Pulling T2P uphole slowly with wireline
13	18:11:22	Stop at 1057 mbsl, pumps off
14	18:13:30	Pulling T2P uphole slowly with wireline
15	18:17:18	Stop at 741 mbsl, pumps off
16	18:19:36	Pulling T2P uphole slowly with wireline
17	18:22:53	Stop at 491 mbsl, pumps off
18	18:24:29	Pulling T2P uphole slowly with wireline
19	18:30:32	Wireline disconnected from CDS
20	18:34:39	CDS disconnected from spacer
21	18:36:28	Spacer disconnected from CDS
22	18:36:28	T2P out of pipe
23		Data downloaded from data logger

Notes: Depth = 100.0 mbsf. Date = 26 June 2005. T2P = temperature/dual pressure probe. CDS = colleted delivery system. BHA = bottom-hole assembly. GMT = Greenwich Mean Time.



**Table T26.** Event summary of T2P Deployment 14, Hole U1324C.

Event	Time (GMT)	Event
1		Data logger started at 1 Hz
2	21:28:16	Stop at 491 mbsl, pumps off
3	21:30:16	Start lowering probe
4	21:35:17	Stop at 741 mbsl, pumps off
5	21:37:29	Start lowering probe
6	21:43:36	Stop at 1057 mbsl, pumps off
7	21:45:49	Start lowering probe
8	21:49:31	Stop at 1195 mbsl, pumps off
9	21:52:07	Start lowering probe
10	21:55:00	CDS lands in BHA; pumps off
11	21:56:30	Start penetration of T2P into sediment
12	21:57:25	End of T2P penetration; bit on bottom of hole
13	21:57:44	Raising BHA 2.5 m off bottom of hole
14	23:02:47	Pulling T2P uphole slowly with wireline
15	23:09:44	Stop at 1057 mbsl, pumps off
16	23:14:53	Pulling T2P uphole slowly with wireline
17	23:18:53	Stop at 741 mbsl, pumps off
18	23:21:27	Pulling T2P uphole slowly with wireline
19	23:24:07	Stop at 491 mbsl, pumps off
20	23:26:07	Pulling T2P uphole slowly with wireline
21		Data downloaded from data logger

Notes: Depth = 150.0 mbsf. Date = 26 June 2005. T2P = temperature/dual pressure probe. CDS = colleted delivery system. BHA = bottom-hole assembly. GMT = Greenwich Mean Time.

**Table T27.** Event summary of T2P Deployment 15, Hole U1324C.

Event	Time (GMT)	Event
1	0:49:19	Data logger started at 1 Hz
2	1:56:31	T2P on rig floor
3	2:09:04	Start lowering T2P downhole, pumps on
4	2:17:40	Stop at 491 mbsl, pumps off
5	2:19:52	Start lowering probe
6	2:24:36	Stop at 741 mbsl, pumps off
7	2:26:51	Start lowering probe
8	2:32:55	Stop at 1057 mbsl, pumps off
9	2:35:34	Start lowering probe
10	2:40:23	Stop at 1245 mbsl, pumps off
11	2:43:42	Start lowering probe
12	2:47:37	CDS lands in BHA; pumps off
13	2:48:02	Start penetration of T2P into sediment
14	2:49:28	End of T2P penetration; bit 1 m off bottom of hole
15	2:52:20	Raising BHA 4.5 m off bottom of hole
16	3:53:17	Pulling T2P uphole slowly with wireline
17	3:56:56	Stop at 1057 mbsl, pumps off
18	3:59:23	Pulling T2P uphole slowly with wireline
19	4:02:52	Stop at 741 mbsl, pumps off
20	4:05:07	Pulling T2P uphole slowly with wireline
21	4:07:56	Stop at 491 mbsl, pumps off
22	4:10:05	Pulling T2P uphole slowly with wireline
23	4:15:55	Wireline disconnected from CDS
24	4:17:54	CDS disconnected from spacer
25	4:19:43	Spacer disconnected from CDS
26	4:21:51	T2P out of pipe
27		Data downloaded from data logger

Notes: Depth = 200.0 mbsf. Date = 27 June 2005. T2P = temperature/dual pressure probe. CDS = colleted delivery system. BHA = bottom-hole assembly. GMT = Greenwich Mean Time.



**Table T28.** Event summary of T2P Deployment 16, Hole U1324C.

Event	Time (GMT)	Event
1		Data logger started at 1 Hz
2	11:18:00	Start lowering T2P downhole, pumps on
3	11:37:22	Stop at 491 mbsl, pumps off
4	11:39:35	Start lowering probe
5	11:43:21	Stop at 741 mbsl, pumps off
6	11:45:21	Start lowering probe
7	11:49:33	Stop at 1057 mbsl, pumps off
8	11:52:30	Start lowering probe
9	11:57:30	Stop at 1345 mbsl, pumps off
10	11:59:30	Start lowering probe
11	12:05:15	Start penetration of T2P into sediment
12	12:17:12	End of T2P penetration; bit on bottom of hole
13	12:22:15	Raising BHA 4 m off bottom of hole
14	13:47:24	Pulling T2P uphole slowly with wireline
15	13:54:09	Stop at 1057 mbsl, pumps off
16	13:57:00	Pulling T2P uphole slowly with wireline
17	14:02:33	Stop at 741 mbsl, pumps off
18	14:04:30	Pulling T2P uphole slowly with wireline
19	14:09:10	Stop at 491 mbsl, pumps off
20	14:11:10	Pulling T2P uphole slowly with wireline
21		Data downloaded from data logger

Notes: Depth = 300.0 mbsf. Date = 27 June 2005. T2P = temperature/dual pressure probe. BHA = bottom-hole assembly. GMT = Greenwich Mean Time.